A FRACTAL TRANSPORT APPROACH TO HEAT TRANSFER THROUGH CELLULAR STRUCTURE

A thesis submitted to The University of Manchester for the degree of
PhD
in the Faculty of Engineering and Physical Sciences

2016

CHULIN JIANG

SCHOOL OF MECHANICAL, AEROSPACE AND CIVIL ENGINEERING

Contents

List of Figures

List of Tables

Nomenclature

D	Hausdorff fractal dimension
q	local heat flux density
κ	product of the intrinsic permeability of the medium
$\hat{E}_k$	a pre-fractal domain
$\hat{T}_k$	a corresponding tessellation
$\boldsymbol{P}_{ij}$	affine map for tessellations
$\boldsymbol{S}_{ij}$	affine map for pre-fractals
Ω	control volume
$\boldsymbol{F}$	Jacobean matrix
ℓ_0	edge length
$\boldsymbol{F}$	Jacobian matrix for the hole map
$\boldsymbol{K}_s$	conductivity tensor for a pre-fractal element
$\boldsymbol{K}_r$	corresponding conductivity tensor for a tile in the tessellation
h	convection heat transfer coefficient
T_{wat}	water temperature
T_∞	bulk temperature
$\dot{Q}$	velocity of thermal energy
d	hydraulic diameter
A	heat transfer surface area
P	wetted perimeter of the cross section

k	thermal conductivity of the coolant
μ	viscosity
j	mass flux
ρ	density
v	material velocity
c_p	specific heat capacity at constant pressure
L	pipe length
Δp	pressure difference
H	Heaviside step function
ψ	specific field variable
$\underline{n}$	outward unit normal
Γ	orientable boundary
W	weighting function
$\boldsymbol{D}_F$	diagonal matrix with eigenvalues on the principal diagonal
$\boldsymbol{Q}_F$	orthogonal matrix
$\boldsymbol{R}$	upper triangular matrix
$\boldsymbol{D}$	diagonal matrix
w	width

Abstract

The present thesis, entitled **A fractal transport approach to heat transfer through cellular structure**, was submitted in the alternative format, by **Chulin Jiang** to **The University of Manchester** for the degree of **Doctor of Philosophy** in the **Faculty of Engineering and Physical Sciences, School of Mechanical, Aerospace and Civil Engineering**, **18 September 2016**.

The transport of heat and mass through porous structures has been the focus of extensive research for many decades. Porous materials have excellent characteristics like large contact area, controllable pore sizes and low density, which are widely exploited in chemistry, biomechanics and fluid mechanics. Cellular heat exchangers utilise porous materials and are of particular interest in this research. These types of heat exchangers combine high conductivity materials with good enhancement of fluid mixing to increase heat transfer rates. However, the use of porous media presents challenges in the form of extremely complex geometries, which are difficult to accurately represent and analyse. This research focuses on the use of fractals (or more correctly pre-fractals) for the representation of porous media and a new numerical analysis method to enable the application of continuum thermal analysis. This is achieved by tessellating the continuum and extending classical continuum mechanics by a procedure coined tessellated continuum mechanics for the study of the thermo-mechanical response of porous media.

The new procedure for the representation of porous materials involves pre-fractals which can produce extraordinarily complex porous geometries using a relatively small number of linear affine contraction maps. This approach is mirrored by an almost identical approach for the creation of tessellations but in this case affine expansion maps are employed. Elements on a pre-fractal are placed in a one-to-one correspondence with tiles in a tessellation and the associated bijection map is termed a hole-fill map. With tiles doubling up as elements, numerical analysis can be performed on the tessellation and the results immediately "lifted" to the corresponding pre-fractals. The whole approach is shown to be extremely accurate with discontinuous physics on tessellations being accounted for with a new concept termed the discontinuity network. Results obtained by the new approach are contrasted with direct analysis using a commercial package and high accuracy is recorded.

Declaration

No portion of the work referred to in the thesis has been submitted in support of an application for another degree or qualification of this or any other university or other institute of learning.

Copyright

i.   The author of this thesis (including any appendices and/or schedules to this thesis) owns certain copyright or related rights in it (the "Copyright") and s/he has given The University of Manchester certain rights to use such Copyright, including for administrative purposes.

ii.   Copies of this thesis, either in full or in extracts and whether in hard or electronic copy, may be made **only** in accordance with the Copyright, Designs and Patents Act 1988 (as amended) and regulations issued under it or, where appropriate, in accordance with licensing agreements which the University has from time to time. This page must form part of any such copies made.

iii.   The ownership of certain Copyright, patents, designs, trade marks and other intellectual property (the "Intellectual Property") and any reproductions of copyright works in the thesis, for example graphs and tables ("Reproductions"), which may be described in this thesis, may not be owned by the author and may be owned by third parties. Such Intellectual Property and Reproductions cannot and must not be made available for use without the prior written permission of the owner(s) of the relevant Intellectual Property and/or Reproductions.

iv.   Further information on the conditions under which disclosure, publication and commercialisation of this thesis, the Copyright and any Intellectual Property and/or Reproductions described in it may take place is available in the University IP Policy (see http://www.campus.manchester.ac.uk/medialibrary/policies/intellectualproperty.pdf), in any relevant Thesis restriction declarations deposited in the University Library, The University Library's regulations (see http://www.manchester.ac.uk/library/aboutus/regulations) and in The University's policy on presentation of Theses

Acknowledgement

Thanks are given first and foremost to my supervisors Dr. K. Davey and Dr. R. Prosser for all their help, comments, criticisms, feedback and inspiration. Their unfaltering guidance and support is much appreciated. The project would not be what it is today without their guidance, inspiring discussions, and encouragement. Working with them has been a great privilege.

Finally, and not least, thanks my family, friends and tutors in School of Mechanical, Aerospace and Civil Engineering of the University of Manchester who have supported me through my research.

Chapter 1.

Introduction

This research is concerned with continuum mechanics for porous materials and its application to cellular heat exchangers [1]. A fractal or a pre-fractal is introduced to represent a porous material. In order to apply continuum mechanics, relative tessellated structures are created to investigate thermal behaviour of pre-fractals. This thesis has explored the analysis of heat transfer for porous materials through analysis of an appropriately related continuous construction.

1. 1   Background

Porous materials have many great qualities like low density, large contact area, high heat resistance, etc [2]. A large number of engineering, biological and geological materials such as ceramics, concrete, wood, bricks, rocks, polymers, biological tissues and bones are characterised by porous materials [3]. Due to the ability of enhancement of the heat transfer, they are always considered in heat exchangers.

Heat exchangers are a piece of equipment with the primary responsibility of transferring energy from one medium to another. They are used in all manner of devices, industries and applications including heating, refrigeration, air conditioning, power plants, petroleum refineries, natural gas processing, and sewage treatment. Many types of heat exchangers can be distinguished from their composition like plate heat exchanger, shell and tube heat exchanger [4]. Cellular heat exchangers as an application of porous materials are of particular interest in this thesis. An alternative but similar configuration is the plate-fine heat exchanger design [5].

Porous materials with cellular structures provide high efficiency exploiting a complex geometrical structure to maximise fluid contact area and flow tortuosity. Many cellular heat exchangers embody this geometry through high thermal conductivity metallic foams such as copper and aluminium. Boomsma et al. [6] explored the

thermal performance of cellular heat exchangers and reported on the advantages offered by these types of design. Similar conclusions were drawn by Bhouri et al. [7] where metallic honeycomb heat exchanger designs were shown to be suitable for enhanced thermal management in hydrogen storage systems.

Although cellular designs provide effective cooling and enhance heat transfer, their analysis is difficult arising principally from the complex geometry involved. The transport of heat and mass through porous structures has been the focus of extensive research for many decades. Tarasov [8][9] and Ostraja-Starzewski [10][11] for example investigated the use of fractional derivatives in an attempt to analyse transport behaviour of irregular structures. However, there is scant practical evidence for theoretical work of this ilk. The vast majority of practical analysis to date is founded on continuum equations and assumptions, with the indirect representation of geometry using parameters such as permeability, porosity and fractal dimension [12][13]. Such approaches have severe limitations and are unlikely to capture the complex flow and heat transfer physics involved in practical cellular designs.

An alternative approach adopted in this thesis is the direct representation of the complex geometries involved. Such an approach is not without controversy, as practical cellular designs are very complex. Cellular metal structures can be classified into two broad classes; one with stochastic topology, and the other with a periodic structure [14]. Commercial metal foams with open cells typically have a stochastic structure; they provide good compact heat exchangers and are relatively cheap. Nonetheless, as cross-flow heat exchangers, they can provide a high thermal conduction path for heat transport, a very high surface area for dissipation into a cooling fluid (typically located in the pores) and a contiguous path for forcing the coolant through the structure. The complexities involved in the modelling of cellular heat exchanger systems means that presently there exist no realistic means of coupling cells to the macro behaviour of the structure.

The research presented here is concerned with the application and development of a recently discovered general transport theory for fractals/pre-fractals. The cellular structures are represented using pre-fractals and collapsed using a hole-fill map concept. The hole-fill maps can be generated as part of the fractal construction process, which is relatively simple and involves only the repeated application of a

number of affine maps. The approach returns the analysis to the continuum but in this case the continuum is tessellated and each tile in the tessellation possesses thermal properties arising from the hole-fill map.

1. 2   Objective of the Research

The hypothesis underpinning the research is that thermal analysis for a porous material can be achieved on a tessellated continuum. In order to test out the hypothesis the following four measurable objectives form the focus of the proposed research:

i.   Obtain analytical solutions for pre-fractals to provide a means to test the accuracy of the tessellated approach.

     Simple fractals such as Cantor dust is first considered to test the hypothesis through the analytical solution. The hole-fill map concept is applied to construct a relative tessellation. The results will confirm that the tessellated approach can be used to demonstrate the thermal analysis for pre-fractals. Hence, the accuracy of the tessellated approach is established.

ii.   Develop a Galerkin finite element method (applicable to tessellations) to describe the thermal response of porous material when cooled by a highly conductive coolant.

     A Galerkin finite element method is introduced to the tessellated approach to explore thermal behaviour for porous materials with a prefect conductive matrix in cooling system. The analytical solution and numerical solution from the Galerkin finite element method are first used to demonstrate the temperature distribution of Cantor dust. Then, numerical results of thermal behaviour for a series of non-product fractals are obtained to prove the accuracy of the method.

iii.   Develop a Galerkin Finite Element Method with discontinuity networks to cater for discontinuities that arise on a tessellation with more realistic cooling of the porous material.

Discontinuity networks are introduced to the tessellated approach in order to better describe the discontinuous behaviour for fractals. The Galerkin finite element method with discontinuity networks is then applied to investigate thermal analysis for porous materials. The mapped results from both analytical and numerical solutions using tessellated approach with discontinuity networks is first tested on 1-D Cantor dust. The numerical solutions from tessellated approach with and without discontinuity networks on several typical non-product fractals are investigated. Accuracy for tessellated approach with and without discontinuity networks are then explored to demonstrate the influence of the discontinuity networks.

iv. Test the robustness of the tessellated approach and in particular its insensitivity to alternative hole-fill maps.

The tessellation is not unique or arbitrary. This tessellation variability is reflected by changes in the maps defined on the original set. The construction of the hole-fill maps may induce problems for numerical analysis. Thus, it is important to explore the accuracy and robustness of the tessellated approach.

1. 3   Outline of the Thesis

The thesis will start with a general literature review in Chapter 2, which introduces the basic knowledge, analysis and how to characterise the porous material. Cellular heat exchangers provide a focus in this thesis as an application example involving a porous material and heat transfer. In order to analyse and design a cellular heat exchanger, the porous material has to be represented by a mathematical model with a similar geometric structure or described by real geometry through CT-micro scanning. Then, transport theory, Partial Differential Equations, Darcy's Law, Lattice Method and Lattice Boltzmann Method can be involved in the analysis of the thermal response of porous materials. It is thus important to consider these approaches along with existing analytical and numerical methods.

Exploring the ideas and concepts on relatively simple fractals is the focus of Chapter 3. A feature of some simple fractals considered in this chapter is the existence of analytical solutions, which can be used to test out the tessellated approach. The cellular structures of porous materials are represented using pre-fractals. The hole-fill maps concept is proposed to construct the corresponding tessellations. Transport equations and partial differential equations are introduced to link the transport phenomenon on the fractal to a corresponding tessellation. Complex thermal conductivity distributions on corresponding tessellations are presented for a series of non-product fractals. Other material properties such as density, specific heat and heat coefficient on tessellations are illustrated. Analytical solutions on fractal dusts and rings in 1-D and 2-D are obtained for a range of thermal loading conditions.

The Galerkin finite element method is applied to the tessellated continuum to capture the energy transfers for pre-fractal structures in Chapter 4. The relationship between the principal directions of thermal conductivity on each tile and the principal stretch directions of hole-filling maps are investigated. A weighted transport equation is introduced via the Galerkin finite element method for the tessellated constructions to demonstrate numerical analysis of cellular designs. The analytical and numerical solutions of simple Cantor dust are explored to analyse the accuracy of the tessellated approach. A series of pre-fractals to represent porous materials are tested with respect to heat transfer in order to extend the work. Modelling error is illustrated to establish the accuracy of the approach.

Discontinuity networks are introduced in Chapter 5 to the tessellations in order to present the discontinuous behaviour of pre-fractals. The procedure for construction of pre-fractals and corresponding tessellations with complex networks is described. Weighted transport equations are applied to the tessellations with discontinuity networks to obtain steady state and transient solutions via a finite element method. The mapped results for discontinuity networks of simple 1-D fractals are obtained from analytical and numerical solutions. Heat transfer analysis of classical fractals is carried out on the corresponding tessellations both with and without discontinuity networks. The importance of discontinuity networks for the tessellated approach is demonstrated in this chapter. The modelling error for tessellations with discontinuity network is investigated to show the advantage of the complex networks.

As the fluid is assumed as a perfect conduct, limitations of the tessellated approach in the presentation of thermally complex matrix materials are examined in Chapter 6. Analytical solution and numerical solution on simple 2-D Cantor Dust from tessellated approach without discontinuity network are investigated. Tessellations with and without discontinuity networks are considered to investigate the effect of the discontinuity networks. A series of classical non-product pre-fractals are tested by considering the matrix material. The temperatures at the vicinity of relatively large matrix domains are focused on demonstrating the accuracy of the tessellated approach. A further test is applied to explore the impact on the mapped temperature with temperature boundary condition for alternative expansion maps.

In Chapter 7, the research is summarised, and conclusions are drawn. This thesis only considers classical fractals, simplified heat transfer coefficients for cooling channels and manually constructed hole-fill maps. Thus, some future work is proposed which could enhance further the tessellation.

Chapter 2.

Literature Review

This thesis explores the analysis of heat transfer through porous materials. Porous materials with cellular structures should be represented in order to be described in the analysis. Advanced porous materials have been explored for mechanical properties, heat transfer, and fluid mechanics for decades. Some typical theories are considered in its research such as transport theory, partial differential equations and Darcy's law. Analytical methods and numerical methods for solving porous materials problems are discussed in this chapter.

2. 1   Porous Materials

Many porous materials underlying cellular structures have been studied for engineering applications [15]. Classic porous materials include organic materials and polymeric foams. Recently, a large number of inorganic materials like metal foams and ceramics have been developed for areas such as insulation, cushioning, impact and construction materials [16]. The past decade has seen significant development in the ability to manufacture new porous materials.

2. 1. 1   Porous Material Concept

Because of the controllable dimensions for the ordered or irregular arrangement of pores, porous materials are of scientific and technological importance in biology, chemistry and mechanics [17]. They are composed of a matrix and a porous space, latter being typically filled by a fluid like liquid or gas [18][19]. There are some examples of porous materials depicted in Figure 2.1. The internal structure of many porous materials involves multiple scales which hinders research on the relation

between structure and transport properties [20]. Due to their special structure, they embody decreased density and increased specific surface area. The true density of the porous materials excludes pores, and the surface area is the accessible area of the solid surface per unit mass of the material [2].

Because porous materials are abundant both in nature and industry, they have been focused by researchers for many decades. Porous materials are considered in diverse branches of applied science and engineering such as solid mechanics [21], fluid mechanics [22], and thermal mechanics [23]. The heat transfer performance is defined as the ratio of heat transfer rate enhancement to pressure drop increment [24], and it has been shown that high heat transfer performance values can be achieved by porous inserts. In this thesis, the thermal behaviour of porous materials is focused on fluid flowing through the pores.
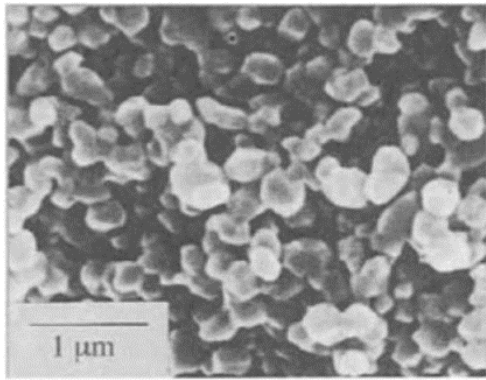
(a) porous titania sintered fine power
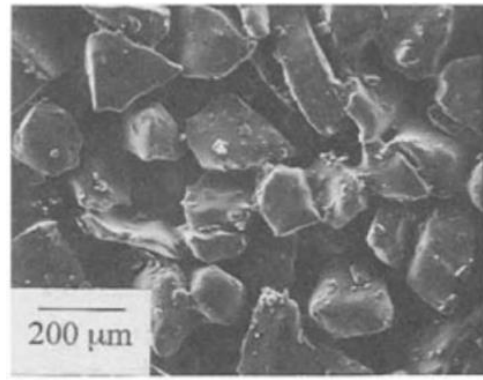
(b) grinding wheel, abrasive grains with a vitrified bonding agent
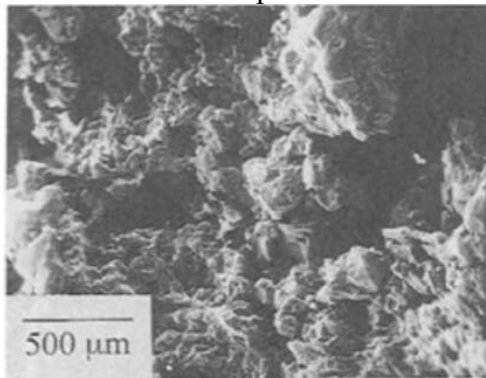
(c) sponge titamium
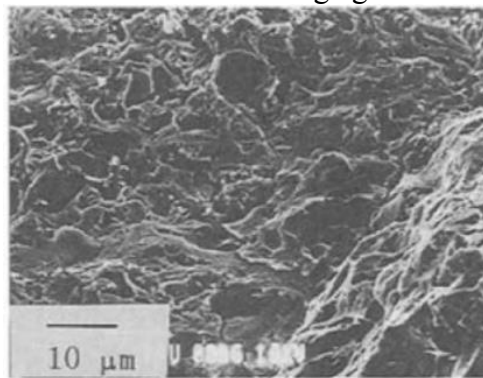
(d) a traditional ceramic
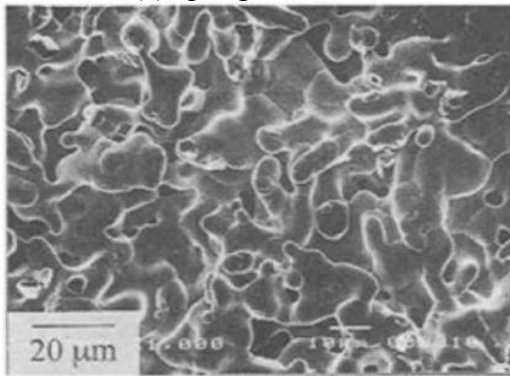
(e) porous copper sintered electrolytic powder
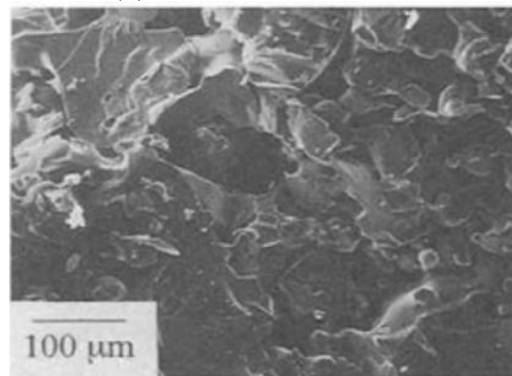
(f) porous silicon carbide produced by reaction sintering
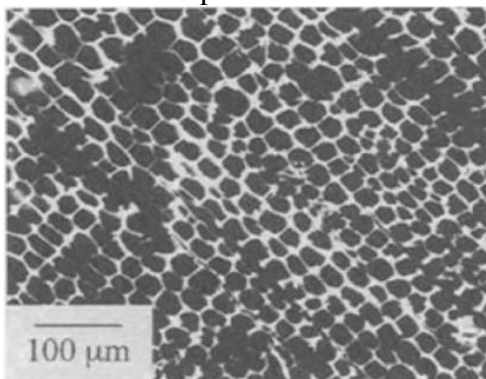
(g) charcoal
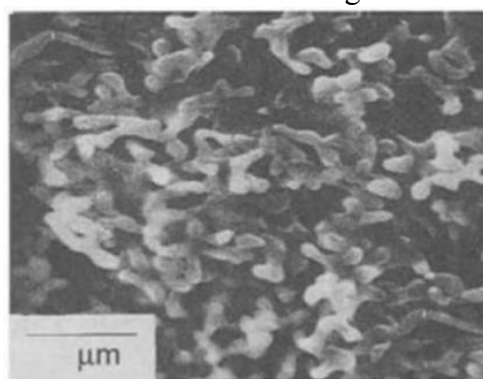
(h) porous glass prepared by leading method

Figure 2.1. Examples of porous materials [25]

2. 1. 2 Porous Material Applications

According to accessibility, porous materials usually are classified into open porous materials (which connect to the outside of the material) and closed pores (which are isolated from the outside) [25], shown in Figure 2.2. Open pores are required for most industrial applications such as filters, catalysts and bioreactors [25]. However, close pores are used mainly in thermal insulators, heaters and heat exchangers [25].
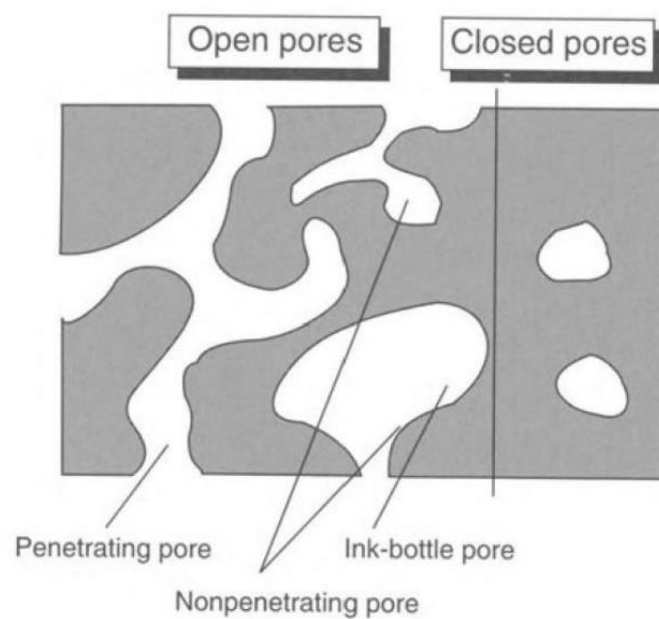
Figure 2.2. Different morphology of pores [25]

Because porous materials have a positive effect on the heat transfer enhancement but a negative impact on the pressure drop [26], they are often considered in heat exchangers which have been studied in the past. The enhancement of heat transfer in a straight channel fully filled with porous materials is investigated through a series of experiments in [27][28][29][30]. Printed circuit heat exchanger (PCHE) [1] concept allows simultaneous high temperature and high pressure operation with relatively thin wall thicknesses between the primary and secondary coolants. At the same time, the thermal behaviour of foam structure has been investigated by Mancin [31] and Boomsma [6]. They illustrated that the open-cell foams in heat exchangers can

enhance heat transfer. The structure of porous heat exchangers is also considered in this research. The honeycomb structure is a second class of cellular materials which is suitable for heat exchanger to improve thermal management [7]. Honeycomb ceramic materials can additionally be for thermal storage under high temperature operation with high heat transfer rate [32]. In this thesis, the cellular heat exchanger design is focused on considering both open and closed pores as the two typical structures.

2. 2   Representation of Porous Materials

As a random process material, each sample in a population will be different from others in a point-to-point sense for porous materials, so it is difficult to use a traditional geometry for their representation [33]. Therefore, experimental and theoretical tools have been developed for the description of porous materials in order to investigate different capabilities. As a demonstration of the sufficiency of parameters extracted from a porous material, explicit (using a mathematical tool) and implicit (using the geometry itself) methods are commonly applied to represent the cellular structures for porous materials in order to create a model for the analysis.

2. 2. 1   Fractals

A fractal was first suggested by Mandelbrot in 1982 to represent a new kind of geometry for many of the irregular self-similar patterns [34]. It provides a mathematical set exhibiting a repeating pattern at multiple scales. As a class of self-similar objects, fractals are exactly the same at every scale or nearly the same at different scales [35]. With these characteristics, they can be used to describe coastlines, porous media, turbulent flows and even the surface of the human brain [36][37]. Fractal mechanics is applied in research since it can generate an elegant model where continuum mechanics will fail, particularly for highly irregular geometries [38][39][40]. Because the pore space of real media is characterised by an extremely complex and irregular geometry [41], the fractal can be used to better describe and investigate the permeability of unsaturated media [42].

In addition, fractals can be used to represent a set of cellular structures like porous materials; a pre-fractal as a finite subset can be used to demonstrate one porous/cellular structure. For example, the role of pore structure on liquid flow behaviour in porous media has been investigated on a classical fractal model Sierpinski carpet [43]. Other cases have investigated the relationship between the thermal conductivity and the pore size for porous materials on a pre-fractal Sierpinski carpet [44][45]. Although these research works only use Sierpinski carpet in their approaches, they confirm that fractals can be used to describe the geometry structure of porous materials. In this thesis, fractals are chosen to describe the cellular structure of porous materials.

Fractal dimensions are always considered in the fractal analysis, because they can be defined in connection with the real-world data and measured approximately by means of experiments [46]. The concept of fractal dimension gives a provisional mathematical definition of a fractal as a set [47]. Box counting as a method of gathering data for complex geometry is always applied to determine fractal dimensions. It presents better analytical properties since the definition is based on a measure; and it can connect each level of a pre-fractal to the original set to present the property of each pre-fractal. Using the fractal dimensions, the material properties of the kth pre-fractal can be linked to the original set. In reference [48], the conductivity K_k of pre-fractal elements scale as given by the relationship $K_k / K_0 = \left(\ell_k / \ell_0 \right)^{1-D}$ on the kth pre-fractal, where ℓ_k is pre-fractal length and D is the fractal dimension for Cantor dust.

2. 2. 2   X-ray computed micro-tomography (micro-CT)

Micro-CT scanning has become a non-destructive and truly 3D imaging technique [49]. It provides a direct way to image the pore space as a volumetric (3D) representation of structures and a three-dimensional image of the pore space at a resolution of several microns [50]. Micro-CT can be used to investigate characteristics of porous media. It is an effective technology to study the cellular structure of porous materials [51]. Thus, it cannot only be used in experiments but also create three-

dimensional models for numerical analysis by importing data into commercial simulation packages.

Micro-scanning is applied in a number of previous research works. In reference [52], the ability to present porous material from micro-CT scanning is clearly shown. Micro-CT diameters can describe blocks of porous material with different diameters and illustrate the bones with porous structures, as shown in Figure 2.3 and 2.4. In Liu's numerical study on fluid flow and heat transfer through porous media, the porous geometry is reconstructed using micro-tomography images from micro-CT scanner [53]. Micro-CT scanning is also utilised to investigate 3D microstructure of porous magnesium composite reinforced by multi-walled carbon nanotubes [54]. All these studies illustrate that X-ray computed micro-tomography (micro-CT) can be used to represent the structure of porous materials. It provides another method of presenting more realistic models for porous materials in the analysis.
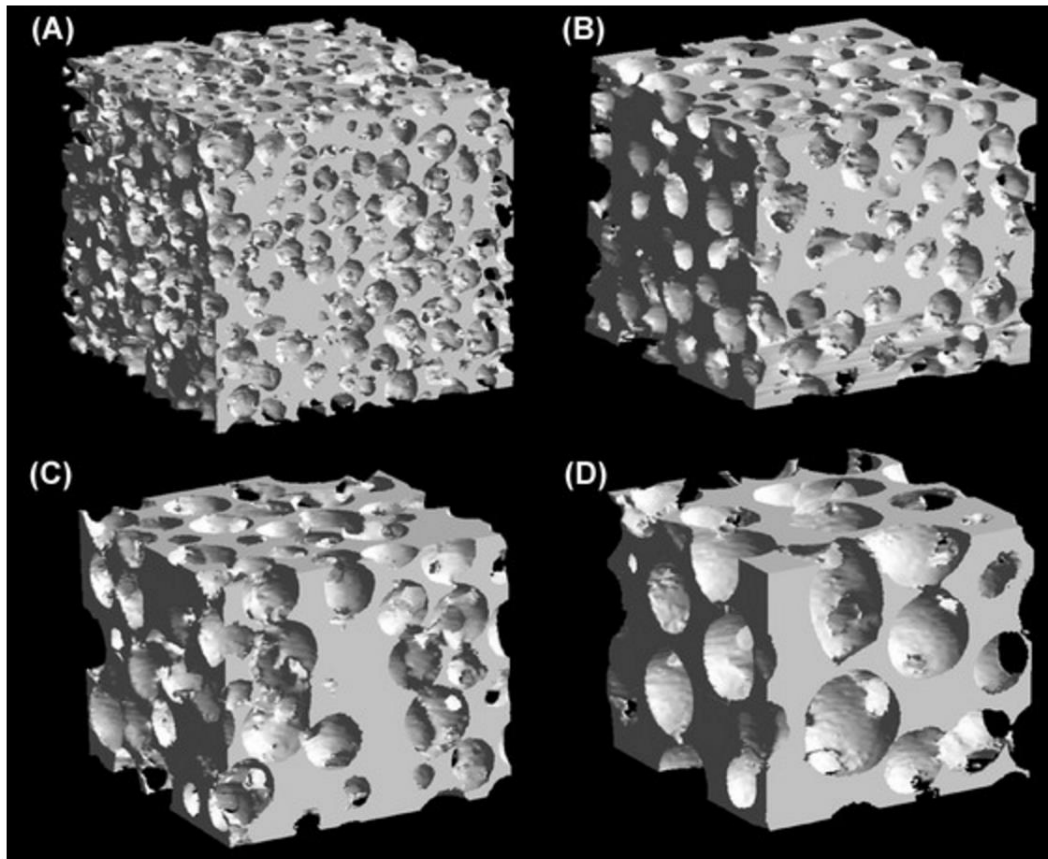
Figure 2.3. Micro-CT reconstruction of the four types of porous blocks [52]
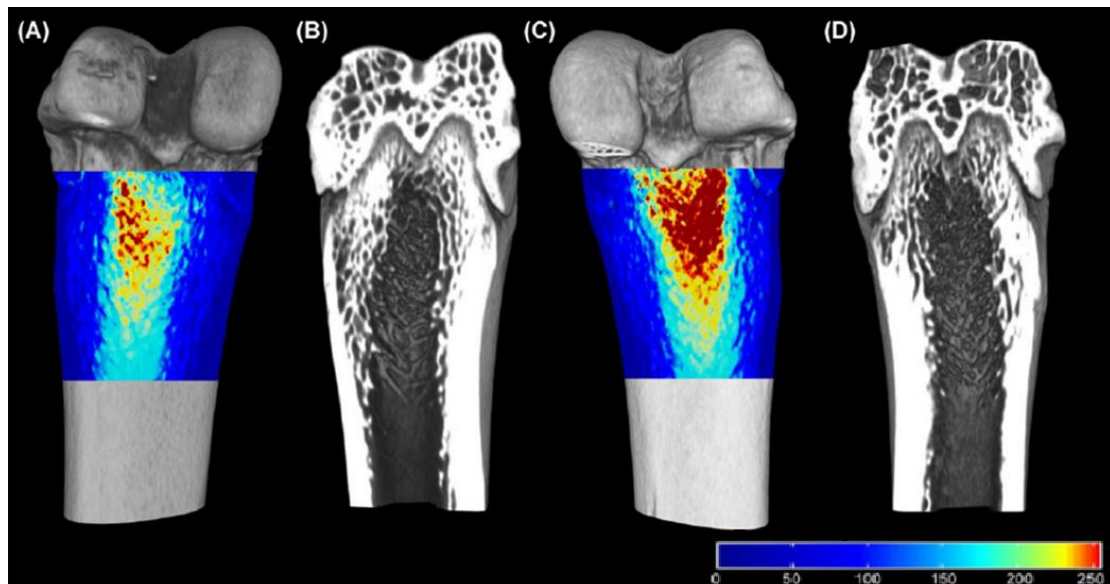
Figure 2.4. Projected porosity on the periosteal surface of the femur cortex [52]

2. 3   Analysis of Porous Materials

Different methods are used to explore porous media such as transport theory, fractional derivatives, fractional integrals and partial differential equations. They are always applied on fractals to do the investigation with analytical methods. Darcy's law is always used to investigate fluid flow through a porous medium. As water coolant flowing through the channels of the cellular heat exchanger is considered, Darcy's law can be used to demonstrate heat transfer coefficients in the channel. Due to the complex geometry of the fractal, the Lattice Boltzmann method (LBM) can be chosen to do further analysis of the fluid flow in the voids of the porous materials.

2. 3. 1   Transport Theory

In engineering, the exploration of transport phenomena involves the exchange of mass, energy and momentum between systems [55][56]. In particular, the analysis of transport phenomena in porous materials is encountered in many natural processes and technological applications [57]. Transport theory is used to refer to the mathematical description of the transport of particles [58] and has been applied to study fluid flowing through porous media [59]. Because the direct derivation of the governing partial differential equations is not straightforward, the integral form of the governing transport equations is introduced. The transport equations for momentum, energy, heat transfer and mass can be constructed in different forms.

The transport theory has been applied to the analysis of porous material in different areas. The seepage mechanics of fluid in fractal porous media has been studied in [60] by introducing fractional order derivative to establish a new mathematical flow model. Transport approaches involving fractals and fractional derivatives can be introduced to link the fractals to a relatively continuous structures. Ostoja-Starzewski [10][11][61] created a continuum-like transport equation for mass momentum and energy for a fractal porous media. Tarasov has described fractal media using fractional integrals to define the medium mass for a continuum media in [8]. He [9] again considered a fractional continuous medium model for the fractal media and derived a fractional

generalisation of the balance equations of mass density, momentum density and internal energy. Because they are founded upon transport forms that do not readily arise from the underpinning physics, their approaches are untested and physically unrealisable. Nevertheless, all these researches confirm that the transport theory can be applied to obtain relative material properties for corresponding continuous constructions in order to investigate behaviour for fractals.

2. 3. 2   Partial differential equations

Partial differential equations in a multidisciplinary sense have a special emphasis on applications to the problems in civil engineering, mechanical engineering, theoretical and applied mechanics [62]. It covers the topics such as fluid flow, diffusion and mass transport in porous media and heat conduction in solid [62]. A set of partial differential equations with a set of algebraic relations can solve multiphase flow in porous media for the basic mathematical models [63]. The heat transfer problems for porous materials can also be explored through governing partial differential equations in numerical methods [64].

Although transport phenomena in porous materials bring a challenge to mathematical problems in the field of partial differential equations, partial differential equations involving partial derivatives can be applied to solve transport equations. The framework of continuum hypothesis is used to obtain the numerical solution for transport phenomena in porous media through partial differential equations [65]. Several pressure distributions are illustrated as the solution of flow problem for porous media. However, all the results are only shown for the continuous construction. Partial differential equations can be introduced to explore the behaviour for porous materials. In Davey's research [48], partial differential equations are combined with transport equations to connect fractals and their relative continuous structure in order to investigate the thermal analysis for fractals. This approach proves that the partial differential equations can be used to obtain the results for porous materials from continuum structures.

2. 3. 3 Darcy's Law

Darcy's law is able to represent the complex physics involved in a wide variety of porous geometrical structures with great accuracy. Convection in porous media governed by Darcy's law has been used to study nonlinear dynamics and pattern formation of convective flow [66]. In recent research for either free or combined convection in porous materials, the boundary layer treatments have mainly been based on Darcy's law [67][68]. However, it is well known that Darcy's law is an empirical formula relating the pressure gradient, the bulk viscous resistance and the gravitational force in a porous medium [67]. Thus, the formulation of convective heat transfer problems based on Darcy's law completely neglects the viscous force acting along a surface. Heat transfer coefficient can be determined by Darcy-Weisbanch equation and Dittus-Boelter equation through the size of the channel and the conditions of the flow [69].

Darcy's law is always used as a basic law to explore the fluid flow in porous media. In Li's research, the temperature dependent fluid properties (variable fluid viscosity and thermal conductivity) are taken into account in the modified Darcy's law to describe the constitutive relations of highly coupled velocity and temperature fields in porous medium through computational fluid dynamics [70]. Based on Darcy's law, Chevalier has investigated yield stress fluid of flowing through a porous medium in the experiment [71]. These research works confirm that Darcy's law can be combined with other methods to investigate fluid mechanics of porous materials.

2. 3. 4 Lattice Method

Lattice method generates a model with regular structure and tessellations on a unit cell along independent periodic vectors in the space continuum [72]. It is quite popular amongst the theoretical methods because the discretization of any continuum model can be turned into a lattice model [72]. Therefore, lattice method can be used to establish continuum structures for porous materials. The early studies of porous structures were carried out to investigate lattice structures [73]. Later, 3D lattice models were established as a kind of tessellated constructions [74]. In addition,

Lattice methods including its derivative are powerful alternatives to traditional numerical methods for solving partial differential equations, particularly in simulating fluid flow for porous media [75].

Lattice methods are used to investigate different capabilities for porous materials. Stiffness and strength of periodic cellular materials have been explored for both 3D open and closed cell lattices by Vigliotti [76]. This unprecedented research illustrates that Lattice model can be used to obtain the mechanical properties of cellular structures. Xiao applied Lattice models to represent the random structure of porous media by using tessellations, and the Lattice Boltzmann method was introduced to solve the fluid flow problem [77]. This confirmed that the Lattice method could be used to establish a relative continuous structure for a porous media. Other research works carried out are on the stress [78] and flow[79] for porous media where results have been obtained by analysing the problem along the independent periodic vectors. All these studies show the Lattice methods can be used to solve the heat transfer problem for porous materials by combining it with other methods.

2. 3. 5   Lattice Boltzmann Method

The Lattice Boltzmann Method (LBM) is a powerful technique for the computational simulation of a wide variety of complex fluid flow problems with complex geometries [80]. It does not require re-meshing and can overcome the limitations of the conventional and Finite Element Methods by using a fixed, non-adaptive (Eulerian) grid system to represent the flow field [81]. Because some discrete distribution functions on the fluid boundary cannot be solved directly like internal particles, macroscopic boundary conditions are required. Bounce-back boundary conditions are applied in LBM due to its ability of readily simulating complex boundaries. However, LBM is recognised to be particularly attractive for low Reynold number flows involving complex boundary conditions [82].

With some development, the LBM is widely used in fluid mechanics for porous media. High resolution with large eddy simulation by LBM is applied to the porous medium structures to describe turbulent transport processes inside porous media by Y. Kuwata

[83]. D3Q27 Lattice Boltzmann model has been created for four different three dimensional fractals. In another research, a lattice Boltzmann model for two dimensional fractal Sierpinski gasket is introduced [84] to investigate the influences of porosity on fluid flows and the effect of thermal conductivity ratio of solid matrix to fluid on heat transfer in fractal porous medium. An improved Non-Dimensional Lattice Boltzmann Method [85] is developed to perform comparison studies between direct and porous medium model heat exchangers. D2Q9 Lattice Boltzmann model has built in these two researches. All these studies show that simple Lattice Boltzmann model can be used to solve the fluid flow problem for porous materials and fractals. Despite the popularity of the LBM in simulating fluid mechanics in complex porous media, this approach has some limitations. The LBM is restricted to simulate fluid-fluid multiphase flows and fluid-fluid interfaces [86] [87]; hence, this approach needs to be improved in order to investigate the complex fluid flow and heat transfer in a porous medium.

In this thesis, porous materials are represented by fractals and analysed for relative tessellations. Due to the continuous structure and perfect thermal conductivity for the matrix, the LBM is not considered for the thermal analysis of porous materials. However, LBM can be applied in the future work in order to bring more accuracy to the analysis of fluid flow through the pores.

2. 4 Solving the Porous Materials Problem

Analytical solution, experimental solution and numerical solutions are the three main general solutions for solving problems. In this section, analytical methods and numerical methods for solving porous materials problem are focussed. In analytical methods, fractals are mainly used as a mathematical model in order to better describe porous materials. The thermodynamic orthogonality as a general framework in which to formulate constitutive laws in continuum mechanics of elastic/dissipative media been established for fifty years [11]. A relative continuous structure is constructed to analyse fractal problems. For numerical methods, both explicit and implicit models

for porous materials can be considered. Finite element method is focused on in order to investigate porous media in this section.

2. 4. 1   Analytical Methods

Mathematical modelling of porous materials as an analytical method usually needs to apply a simplified effective concept such as continuum construction. However, porous media with points and domains, which cannot be filled with the medium particles, cannot be considered as a continuous media directly in general cases [88][89]. Most of analytical solutions will first introduce fractals to represent porous media and then, select a relative continuum structure to do the analysis. Fractal with self-similar geometry as one of the most important development structures is worthwhile for the exploration of porous materials, which brings an alternative approach to the mathematics. Finally, porous media can be represented by a special continuous media through fractals [8][9]. The difference between the real fractal medium and fractional continuous medium model is analogous to the difference between the real atomic structure (fractal medium) and usual continuous models for that medium.

Continuous structures have been chosen to analyse porous materials problems. Tarasov has tried to create continuous medium model for fractal media in [8], but he has focused on the properties of the fractal media. Again in 2015, he introduced continuum models with non-integer dimensional space to describe isotropic fractal materials [90], but still no physical solution was obtained. His research pays too much attention to the analysis on the fractal media but not with realistic continuous model for mechanical analysis. Other studies like [91][92][93][94] are based on the application of fractional derivatives. Similar to Tarasov, these theories are untested and unrealisable in the physical field, because fractional derivatives do not readily come from the governing physics.

More realistic problems have been investigated. For example, Balankin has discussed the mapping of constitutive equations for mechanical behaviour into the fractal continuum framework by using Menger sponge as an example depicted in Figure 2.5 [95]. Although this research confirms that the fractal problem can be solved with the

exploration of a relative continuum model, it does not provide any accurate theory for the continuous fractal model. A new concept of hole-fill maps, is provided by Davey to create a relative tessellation for a pre-fractal [48] which is used to represent one shape of porous material. This research has shown that the analysis of fractals can be achieved through the analysis of the corresponding continuous structure and has established the accuracy of the tessellated approach through comparing analytical and numerical solutions shown in Figure 2.6. This research provides an excellent approach for solving cellular structures, but it only considers simple Cantor dust as an example which should be extended.
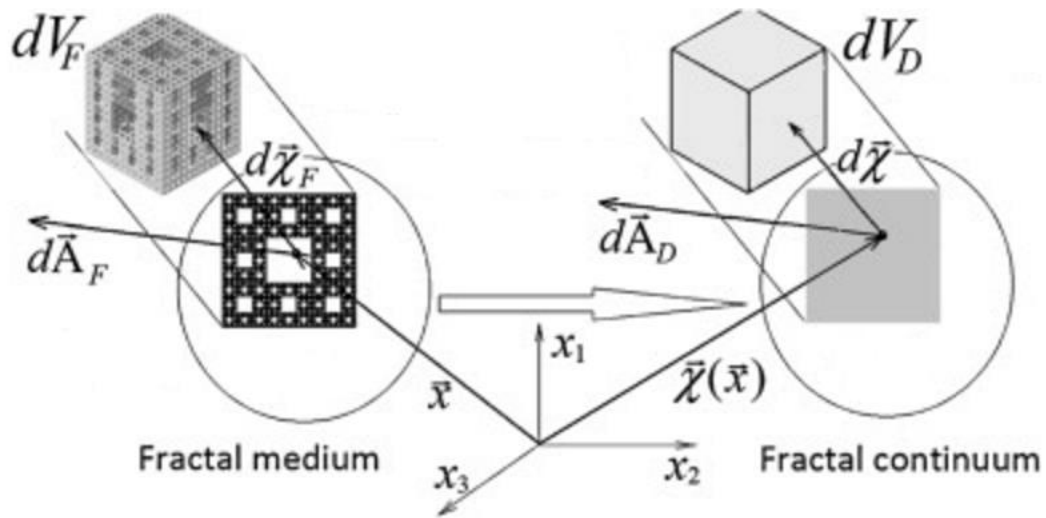
Figure 2.5. Mapping of essentially discontinuous Menger sponge into the fractal continuum
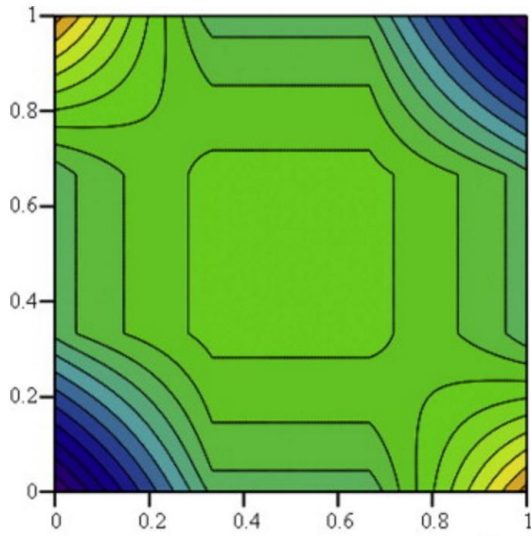
(a) temperature contours on $\hat{E}_1^2$ (b) contours on continuum for $\hat{E}_1^2$
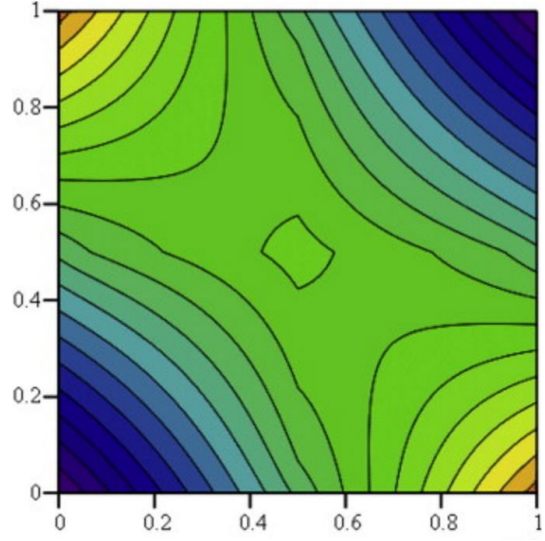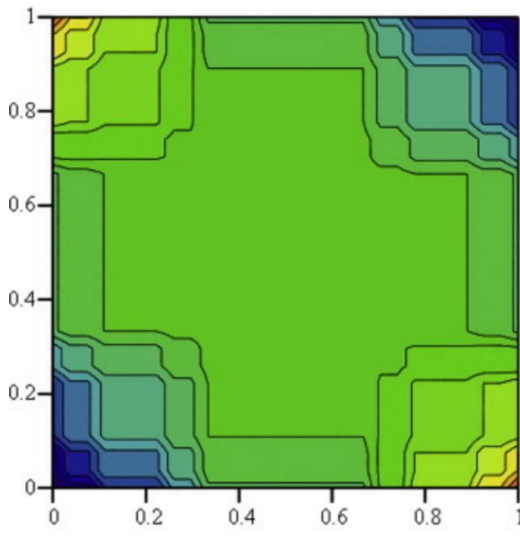
(c) temperature contours on $\hat{E}_3^2$ (d) contours on continuum for $\hat{E}_3^2$
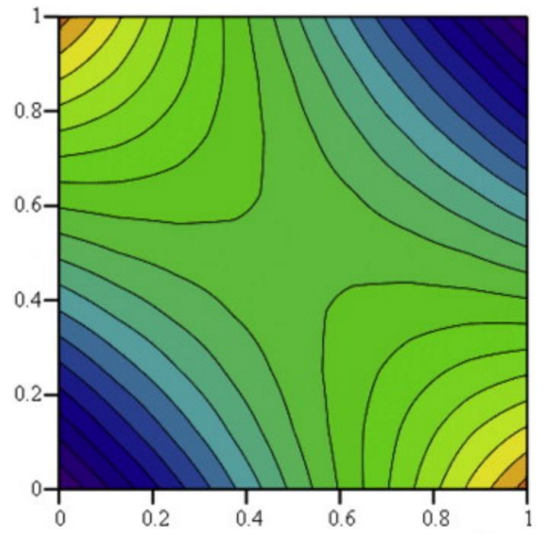
Figure 2.6. Contour temperature plots for pre-fractal and corresponding continuum

[48]

2. 4. 2　Numerical Methods

The finite element method (FEM) is the most common numerical method applied to complex geometries in different application areas [96]. FEM can be applied to explore complex elasticity, structural and thermal problems by using commercially developed packages such as Matlab, ABAQUS and ANSYS.

The FEM began to be used to predict the response of structures involving porous materials in the 1990s [97]. Different characteristics of porous materials have been explored through FEM. Tensile behaviour of fibrous porous material is investigated using finite element analysis (FEA); an optimised FEA model is obtained from the calculated results' dependence on the quantity of numerical samples, mesh density and model size [98]. Lu investigated the compressive behaviour using a FE model with ANSYS [99]. The microstructure of real material is reconstructed in the numerical model by extracting the primary features of bonded networks of the porous Si_3N_4 ceramics, as shown in Figure 2.7. Although these research works illustrate the capability of FEM for solving porous materials problems, their FE models are always represented by the materials themselves in order to obtain the analytical solution. Another example is that of Cantor dust which was chosen to demonstrate the thermal behaviour in Davey's study for the temperature distribution illustrated in Figure 2.6 [48]. This research does thermal analysis on a relative continuum structure through finite element method using Mathcad. This research also provides a simple approach to represent cellular structures.
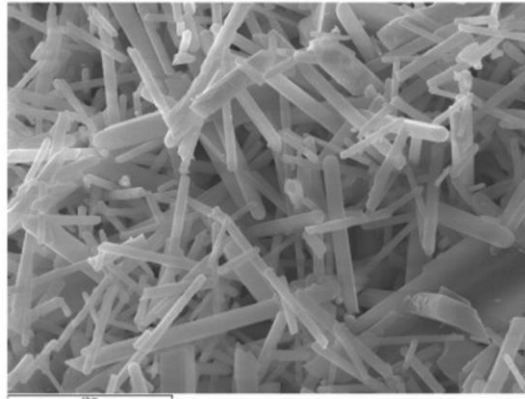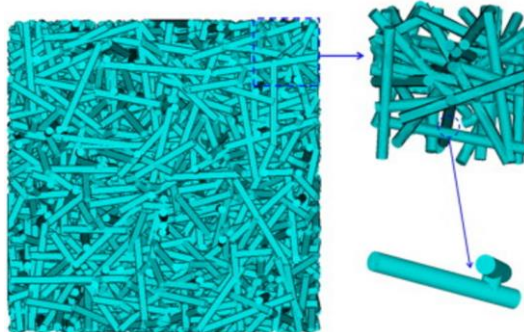
(a) Porous Si$_3$N$_4$ ceramics   (b) The representative FE model

Figure 2.7. Porous Si$_3$N$_4$ ceramics and its FE model [99]

Other numerical methods with and without elements as in [100][101] (the Generalized Finite Element Method) [102] (a development of the Runge–Kutta discontinuous Galerkin methods) could, in principle, be applied to solve porous media problems. These methods performing a numerical analysis can be divided into two ways: i) the continuous tessellation which is then mapped on the fractal; ii) the porous media directly. All these approaches have the limitation of representing complex geometries.

Chapter 3.

Paper 1: HEAT TRANSFER THROUGH FRACTAL-LIKE POROUS MEDIA: A TESSELLATED CONTINUUM APPROACH

This chapter presents a tessellated continuum approach to demonstrate heat transfer analysis of porous materials. Hole-fill maps are introduced to build a relative tessellation for pre-fractal representation of the porous material. The tessellation is linked to the pre-fractal through the transport equation and partial differential equations. Thermal analysis on pre-fractals can be then performed through the analysis of the tessellation.

Simple Cantor dust and rings are considered to test the hypothesis. The thermal behaviour of different fractals is obtained from the analytical solution. All these results provide a means of testing the accuracy of the tessellated approach. In addition, the most complex material property, thermal conductivity, is obtained from the distribution on a series of non-product fractals.

The theory presented in this chapter follows that found in reference [48]. The hole-filling maps were created by K. Davey. The tests were designed to validate the fundamental equations. The distributions of thermal conductivity and thermal behaviour were obtained by C. Jiang. The manuscript was written by K. Davey, with technical and editorial supervision and proofing provided by R. Prosser and C. Jiang.

Published in Computers & Structures

Heat transfer through fractal-like porous media: A tessellated continuum approach

K. Davey *, R. Prosser, C. Jiang

School of Mechanical, Aerospace and Civil Engineering, The University of Manchester, United Kingdom

ABSTRACT

This paper tests the hypothesis that the analysis of heat transfer through a cellular structure represented by a fractal or a pre-fractal can be achieved through analysis on a tessellated continuum. A transport theory for fractals is introduced, which is coupled to a hole-fill mapping strategy, to facilitate the analysis of transport problems on a tessellated continuum. The hole-fill maps are constructed by means of an iterated function scheme similar to that applied in the fractal generation process. The method enables known analytical and numerical continuum solutions to be immediately transferred to the fractal medium. A feature of the approach is that complex fractal structures result in continuum transport equations with material properties that are inhomogeneous, anisotropic and discontinuous.

It is demonstrated that a measurable temperature is possible on fractal structures, along with finite measures of heat flux and energy. Analytical steady-state thermal solutions are presented incorporating convective heat transfer.

© 2015 Elsevier Ltd. All rights reserved.

1. Introduction

Heat exchangers find widespread application in areas as diverse as refrigeration, natural gas processing and engine cooling. The increasing power densities encountered in these applications motivates the development of improved heat exchanger design. The *cellular* heat exchangers used to cool printed circuit boards provide an example of this [1], exploiting a complex geometrical structure to maximise the fluid contact area; many cellular heat exchangers embody this geometry through metallic foam materials [2]. Metallic foam heat exchangers utilise high conductivity materials such as aluminium or copper alloys. They are recognised to be a good option for enhancing heat transfer, since they possess both a large fluid–solid contact surface area, and provide good enhancement of fluid mixing [3]. These designs have been shown to be useful in thermal management devices for high power density applications [4].

Although cellular designs provide effective cooling, their analysis is beset with difficulties arising principally from the complex geometry involved. The transport of heat and mass through porous structures has been the focus of extensive research for many decades [5–9]. The research has led to approaches founded on modifications to continuum equations which account for the effects of complex geometry indirectly through variables such as

permeability and porosity. One of the founding studies by Darcy revealed an empirical expression relating pressure drop across a porous medium to average-flow velocity, material permeability and viscosity. Suggestions for improvements to Darcy's law (as it is now know) have been made with ever increasing complexity, from Brinkmann's [10] relatively simply quadratic modification, to more recent elaborate formulations [11]. It is unlikely that these empirical approaches will be able to represent completely the complex physics involved in the vast variety of porous geometrical structures that exist, nor to meet increasing demand for greater accuracy.

The idea that *fractals* could be applied to represent better cellular geometry is more recent and was first suggested by Mandelbrot in 1982 [12]. Transport approaches involving fractals have been considered by Tarasov [13,14] and more recently by Ostoja-Starzewski [15,16]. Their approach (like others [17–20]) is founded on the application of fractional derivatives. These theories are untested and physically unrealisable in many respects since fractional derivatives do not readily arise from the governing physics. An alternative approach that avoids the need for fractional derivatives is the indirect use of fractal quantities; such approaches also have severe limitations akin to those arising with the employment of parameters in empirical expressions, so is not considered further here [21,22].

The transport methodology presented in this paper is founded on the existence of mappings between pre-fractals and the

continuum. These maps are termed *hole-fill* maps because they close the holes in the fractal to create a tessellated continuum. In view of the extraordinary complexity involved in fractal geometry, it might be anticipated that hole-fill maps are equally difficult to construct. However, a novel procedure is introduced here that readily facilitates the construction of these maps. This involves constructing a tessellated continuum in a manner that mirrors the generation of a fractal. Thus, a fractal constructed through the iteration of *n* contraction maps also has *n* maps for the iterated construction of the tessellated continuum. The hole-fill maps can then be formed either by means of function composition or—more directly—by identifying corresponding elements of the fractal with the tessellation. While the hole-fill maps allow the analysis of heat transfer on the tessellated continuum, the precise form of the governing partial differential equations on the tessellation is not obvious. One of the novel contributions of this paper is to derive the transport forms for both the fractal and the tessellated continuum, and to relate both through the hole-fill maps; from these transport equations, the governing partial differential equations may then be obtained. Interestingly, the physics of heat transfer from fractal to fluid manifests itself through the appearance of heat sources at the edges of elements in the tessellation. These distribution terms can readily be taken into account by integration of the governing partial differential equations.

This paper establishes the equivalence of the new hole-filling method with an earlier approach developed by the authors [23]; background material is presented in Section 2 to establish the idea that analytical heat solutions on a continuum can be applied to fractal dusts. Section 3 is concerned with hole-filling maps which provide the formal link between pre-fractals, fractals and the tessellated continua. A general transport theory is presented in Section 4, thereby establishing the relationship between the governing partial differential equations on a fractal to those on the associated tessellation. A specific application to heat transfer is given. The general theory is applied to heat transfer in Section 5, where material properties on the tessellated continuum are established for fractal dusts and rings. The non-linear hole-fill maps involved in the creation of fractal rings manifest themselves in inhomogeneous and anisotropic material properties. Thermal solutions on fractal dusts and rings in 1-D and 2-D are presented in Sections 6 and 7; analytical solutions are obtained for thermal loads, through which heat sources arising from the fluid manifest themselves as Dirac delta distributions at the edges of tessellated elements in the continuum. New analytical solutions are established. In Section 8, the spatial distribution of thermal conductivity is calculated for the three non-product fractals. The paper ends with a discussion and conclusions.

2. Background theory

The analysis outlined in Ref. [23] is concerned with the solution of a partial differential equation $\partial_k \theta_k = 0$ on a pre-fractal domain $\widehat{E}_k$, where ∂_k is a differential operator and θ_k represents the temperature on the kth generation pre-fractal. The solution to this equation is obtained indirectly by first obtaining a continuum analytical solution to $\partial \theta(\boldsymbol{x}, t) = 0$ (where ∂ is a differential operator identical in form to ∂_k), and second establishing a piecewise-linear mapping $\boldsymbol{x}_k(\boldsymbol{s})$ between the pre-fractal $\widehat{E}_k$ and the continuum $\widehat{E}_0$. The solution on $\widehat{E}_k$ for a binary composite consisting of two isotropic materials with extreme thermal properties was shown to be $\theta_k(\boldsymbol{s}) = \theta \circ \boldsymbol{x}_k(\boldsymbol{s})$. The solution strategy outlined in Ref. [23] is limited to product dusts so could not be applied to non-product fractals such as the Sierpinski gasket, for example. To illustrate the approach consider the embedding of a Cantor set [24] in a bar of

initial length ℓ_0. The required Cantor set is generated by the self-similar contraction mappings

$$S_1(x) = \frac{x}{3} \text{ and } S_2(x) = \frac{2\ell_0 + x}{3} \tag{1}$$

where $\widehat{E}_0 = [0, \ell_0]$.

The initial pre-fractals are shown in Fig. 1 and the null regions contained in $\widehat{E}_0 \setminus \widehat{E}_k$ are loosely associated with $\widehat{E}_k$ to avoid the introduction of unnecessary notation. The *support* μ_k on $\widehat{E}_0$ is

$$\mu_k(s) = \begin{cases} 1 & \text{if } s \in \widehat{E}_k \\ 0 & \text{if } s \in \widehat{E}_0 \setminus \widehat{E}_k \end{cases} \tag{2}$$

and the piecewise-linear mapping $x_k : \widehat{E}_0 \to \widehat{E}_0$ central to the theory is

$$x_k(s) = \left(\frac{3}{2}\right)^k \int_0^s \mu_k(r) dr. \tag{5}$$

The mapping is depicted in Fig. 2 for $k = 1, 2, \ldots, 5$, and is denoted here to be a *hole-fill map*. It is evident that x_k is continuous and maps regions of $\widehat{E}_k$ to corresponding regions in the continuum $\widehat{E}_0$, which is effectively subdivided into $N_k = 2^k$ regions of length $N_k^{-1}\ell_0$. The null regions associated with $\widehat{E}_k$ are mapped to the corresponding internal boundaries of $\widehat{E}_o$. It is important to note that because x_k is piecewise linear its derivative is piecewise constant, i.e.

$$\frac{dx_k}{ds}(s) = \left(\frac{3}{2}\right)^k \mu_k(s) = \left(\frac{\ell_k}{\ell_0}\right)^{D_1 - 1} \mu_k(s) \tag{6}$$

where ℓ_k is the length of an element of $\widehat{E}_k$ and D_1 is the Hausdorff fractal dimension.

Although it is possible to invoke mappings whose derivatives are not piecewise constant these can suffer the disadvantage of changing the form of the continuum partial differential equation $\partial \theta = 0$ when contrasted against $\partial_k \theta_k = 0$. The transient heat equation on $\widehat{E}_k$ is

$$\rho_k c_k \frac{\partial \theta_k}{\partial t} = K_k \frac{\partial^2 \theta_k}{\partial s^2} \tag{7}$$

where-as explained in [23]-on the basis of heat, mass and energy considerations, thermal conductivity satisfies $K_k = K_0(\ell_k/\ell_0)^{1-D_1}$, density satisfies $\rho_k = (\ell_k \ell_0^{-1})^{D_1 - 1} \rho_0$ and $c_k = c_0$.

Under the assumption that $\theta_k(s) = \theta \circ x_k(s)$, then

$$\frac{\partial \theta_k}{\partial s} = \frac{dx_k}{ds} \frac{\partial \theta}{\partial x} = \left(\frac{3}{2}\right)^k \mu_k \frac{\partial \theta}{\partial x} = \left(\frac{\ell_k}{\ell_0}\right)^{D_1 - 1} \mu_k \frac{\partial \theta}{\partial x} \tag{8}$$
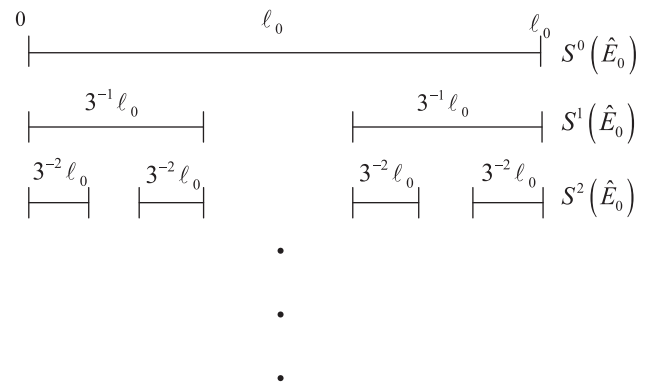

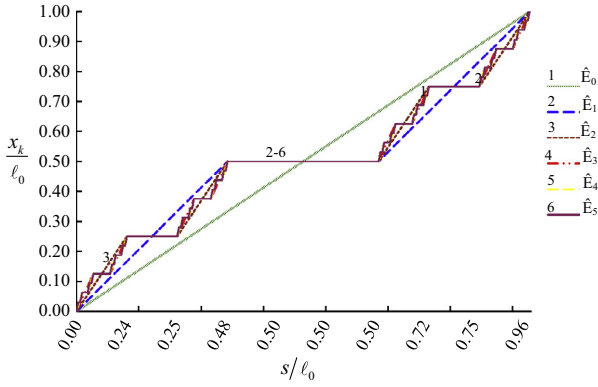Fig. 1. Pre-fractals for the Cantor dust.

Fig. 2. Mapping x_k for different values of k.

and

$$\frac{\partial^2 \theta_k}{\partial s^2} = \frac{d^2 x_k}{ds^2}\frac{\partial \theta}{\partial x} + \left(\frac{dx_k}{ds}\right)^2 \frac{\partial^2 \theta}{\partial x^2} = \left[\left(\frac{\ell_k}{\ell_0}\right)^{D_1-1}\mu_k\right]^2 \frac{\partial^2 \theta}{\partial x^2} \qquad (9)$$

Substitution into Eq. (7) gives

$$\rho_k c_k \frac{\partial \theta_k}{\partial t} - K_k \frac{\partial^2 \theta_k}{\partial s^2} = \left(\frac{\ell_k}{\ell_0}\right)^{D_1-1}\mu_k\left(\rho_0 c_0 \frac{\partial \theta}{\partial t} - K_0 \frac{\partial^2 \theta}{\partial x^2}\right) = 0 \qquad (10)$$

and it follows that θ satisfying the continuum heat equation ensures that $\theta_k(s) = \theta \circ x_k(s)$ is a solution to the heat equation on $\widehat{E}_k$.

It is important to appreciate that the theory is founded on the existence of a continuous hole-fill map, which is recognised to be singular. The map gives rise to the differential relationship $dV_k = (\ell_k \ell_0^{-1})^{D_1-1}\mu_k dV_D$, where dV_D is a differential measure of volume on the pre-fractal and $dV_k = A dx_k$.

3. Hole-fill maps

One of the principal difficulties with the approach outlined in Section 2 (and [23]) is the determination of the hole-fill map. The map is readily determinable for product dusts through the integration of the support. However, this approach cannot easily be applied to non-product sets (e.g. the Sierpinski gasket/carpet), so an alternative method involving two sets of maps, is presented in this section.

The basic idea is to create a tessellation for the structure under consideration using the exact same number of maps used in construction of the original porous fractal. A pre-fractal formed by the union $\widehat{E}_k = \cup S_i(\widehat{E}_{k-1})$ has a corresponding tessellation (should this exist) produced by $\widehat{T}_k = \cup P_i(\widehat{T}_{k-1})$. A *hole-fill map* identifies a coordinate $s \in \widehat{E}_k \subset \widehat{E}_0$ with a coordinate $x \in \widehat{T}_k = \widehat{E}_0$; should the point $s \in \widehat{E}_0 \setminus \widehat{E}_k$, then x belongs to an internal edge of the tessellation. The map $x : \widehat{E}_0 = \widehat{E}_k \cup (\widehat{E}_0 \setminus \widehat{E}_k) \to \widehat{T}_k$ by design is continuous and surjective (onto) but not injective (one-to-one).

Two approaches for the formation of the maps are considered: (1) indirectly via the formation of correspondence points $\boldsymbol{x}^{(i)} = \boldsymbol{x}(s^{(i)})$, where the bracketed superscripts are used to index the points; (2) directly via a function composition $P_i \circ P_j \circ \cdots \circ P_k \circ S_k^{-1} \circ \cdots \circ S_j^{-1} \circ S_i^{-1}$. Restricting attention to piecewise linear maps is a convenience used to simplify the analysis, but introduces additional internal boundaries and constrains the shape of the tessellating maps. However, by assembling the tessellating maps, each of the P_j can easily be formed in parts; this observation allows the extension of the hole filling approach from the 3 point tessellations of the Sierpinski gasket to (for example) the 4 point tessellations of the Sierpinski carpet.

3.1. Cantor dust

3.1.1. Construction of maps by method of corresponding points

The two contraction maps for the dust are defined in Eq. (1). One of the features of the Cantor dust is that the interval end points in $\widehat{E}_k$ are fixed points and are generated from the two-point set $\widehat{E}_0^S = \{0, \ell_0\}$; observe for example that

$$\widehat{E}_1^S = S_1\widehat{E}_0^S \cup S_2\widehat{E}_0^S = \left\{0, \frac{\ell_0}{3}\right\} \cup \left\{\frac{2\ell_0}{3}, \ell_0\right\} \qquad (11a)$$

and

$$\widehat{E}_2^S = S_1\widehat{E}_1^S \cup S_2\widehat{E}_1^S = \left\{0, \frac{\ell_0}{9}, \frac{2\ell_0}{9}, \frac{\ell_0}{3}\right\} \cup \left\{\frac{2\ell_0}{3}, \frac{7\ell_0}{9}, \frac{8\ell_0}{9}, \ell_0\right\} \qquad (11b)$$

It is apparent that $\widehat{E}_0^S \subset \widehat{E}_1^S \subset \widehat{E}_2^S \subset \cdots$, i.e. the points in the sets are fixed points.

The maps $\{P_1, P_2\}$ that provide the tessellation/cover for $\widehat{E}_0$ are

$$P_1(x) = \frac{x}{2} \quad \text{and} \quad P_2(x) = \frac{\ell_0 + x}{2} \qquad (12)$$

and observe that, for $\widehat{E}_0^P = \{0, \ell_0\}$,

$$\widehat{E}_1^P = P_1\widehat{E}_0^P \cup P_2\widehat{E}_0^P = \left\{0, \frac{\ell_0}{2}\right\} \cup \left\{\frac{\ell_0}{2}, \ell_0\right\} \qquad (13a)$$

and $\widehat{E}_2^P = P_1\widehat{E}_1^P \cup P_2\widehat{E}_1^P = \left\{0, \frac{\ell_0}{4}, \frac{\ell_0}{4}, \frac{\ell_0}{2}\right\} \cup \left\{\frac{\ell_0}{2}, \frac{3\ell_0}{4}, \frac{3\ell_0}{4}, \ell_0\right\}$ (13b)

where it is again apparent that $\widehat{E}_0^P \subset \widehat{E}_1^P \subset \widehat{E}_2^P \subset \cdots$.

Note that by stitching together the holes in the original fractal, the interior boundaries in the set $\widehat{E}_k^P$ are counted twice (this can be seen explicitly by $x_1^{(1)} = x_1^{(2)}$ in Eq. (13a), say). Thus, by counting interior points twice, a one-to-one correspondence exists between the set $\widehat{E}_k^S$ and $\widehat{E}_k^P$.

In view of the correspondence between $\widehat{E}_k^S$ and $\widehat{E}_k^P$ the hole-filling map is readily obtained, i.e.

$$
x_k(s) = x_k^{(i)} + \left\{\frac{x_k^{(i+1)} - x_k^{(i)}}{s^{(i+1)} - s^{(i)}}\right\}(s - s^{(i)})
$$
$$
= x_k^{(i)} + \begin{cases} 0 & \text{if } x_k^{(i+1)} = x_k^{(i)} \\ \left(\frac{\ell_k}{\ell_0}\right)^{D_1-1}(s - s^{(i)}) & \text{if } x_k^{(i+1)} \neq x_k^{(i)} \end{cases} \qquad (14)
$$

where $s \in [s^{(i)}, s^{(i+1)}]$ and it is assumed here that $\widehat{E}_k^S \subset \widehat{E}_k$ is enumerated from left to right, so that $s^{(i+1)} - s^{(i)} = \ell_k$ if $x_k^{(i+1)} \neq x_k^{(i)}$.

Observe that the derivative dx_k/ds is piecewise continuous with finite discontinuities occurring at the points $x_k^{(i)}$ in the continuum; any solution must be therefore considered in a weak sense, which lends itself to an integral transport approach.

3.1.2. Construction of maps by function composition

The alternative function–composition approach makes use of the inverse maps $S_1^{-1}(s) = 3s$ and $S_2^{-1}(s) = 3s - 2\ell_0$. Thus, on $\widehat{E}_1$, the hole-fill map is $P_1 \circ S_1^{-1}(s) = 2^{-1}3s$, $s \in [0, 3^{-1}\ell_0]$ and $P_2 \circ S_2^{-1}(s) = -2^{-1}\ell_0 + 2^{-1}3s$, $s \in [3^{-1}2\ell_0, \ell_0]$. Likewise on $\widehat{E}_2$ the hole-fill map is obtained by pre and post mapping operations on $P_1 \circ S_1^{-1}$ and $P_2 \circ S_2^{-1}$ to give,

$$
\begin{cases}
P_1 \circ (P_1 \circ S_1^{-1}) \circ S_1^{-1} \\
P_1 \circ (P_2 \circ S_2^{-1}) \circ S_1^{-1} \\
P_2 \circ (P_1 \circ S_1^{-1}) \circ S_2^{-1} \\
P_2 \circ (P_2 \circ S_2^{-1}) \circ S_2^{-1}
\end{cases}
= \begin{cases}
(2^{-1}3)^2 s & \text{if } s \in [0, \ell_0 9^{-1}] \\
-4^{-1}\ell_0 + (2^{-1}3)^2 s & \text{if } s \in [2\ell_0 9^{-1}, 3\ell_0 9^{-1}] \\
-\ell_0 + (2^{-1}3)^2 s & \text{if } s \in [6\ell_0 9^{-1}, 7\ell_0 9^{-1}] \\
-4^{-1}5\ell_0 + (2^{-1}3)^2 s & \text{if } s \in [8\ell_0 9^{-1}, 9\ell_0 9^{-1}]
\end{cases}
$$
$$(15)$$

and similarly for $\widehat{E}_3$ the four identified components of the maps in (15) give rise to 8 components $P_i \circ (P_n \circ P_m \circ S_m^{-1} \circ S_n^{-1}) \circ S_i^{-1}$, $i \in \{1, 2\}$.

Although this approach appears a little cumbersome it has the distinct advantage that the maps can be generated directly as part of the Fractal/Tessellation formation process.

3.2. Cantor product dust

Product fractals of the type $\widehat{E}_k \times \widehat{F}_k$, where $\widehat{E}_k$ and $\widehat{F}_k$ are dust-like fractals, are considered in reference [23]. Here, consideration is given to the set $\widehat{E}_k^2 = \widehat{E}_k \times \widehat{E}_k$ where $\widehat{E}_k$ is the Cantor dust pre-fractal discussed in previous sections. Thus, $\widehat{E}_0^2 = [0 \ \ell_0]^2 = \{(x, y) : 0 \leqslant x \leqslant \ell_0, 0 \leqslant y \leqslant \ell_0, \}$ and $\widehat{E}_k^2 = W^{\circ k}(\widehat{E}_0) \times W^{\circ k}(\widehat{E}_0)$, with $W(\widehat{E}_0) = \bigcup_{i=1}^2 S_i(\widehat{E}_0)$ and the superscript $\circ k$ denotes the kth composition. Examples of $\widehat{E}_k^2$ for $k = 1, 2, 3$ are depicted in Fig. 3 along with the corresponding tessellated continua. The approach adopted in [23] gives the hole-fill map to be

$$(r, s) \mapsto (x_k(r), y_k(s)) = \left(\left(\frac{\ell_k}{\ell_0}\right)^{D_1 - 1} \int_0^r \mu_k(r') dr', \left(\frac{\ell_k}{\ell_0}\right)^{D_1 - 1} \int_0^s \mu_k(s') ds' \right) \tag{16}$$

Interest here however is on the points $(x_k^{(i)}, y_k^{(j)}) = (x_k(r^{(i)}), y_k(s^{(j)}))$, which can be generated directly by identifying appropriate maps. Note that the four contraction maps employed to create the dust fractal are $\boldsymbol{S}_{ij}(x, y) = (S_i(x), S_j(y))$ where the S_i are defined in Eq. (1). Similarly, the corresponding maps used to cover $\widehat{E}_0^2$ are $\boldsymbol{P}_{ij}(x, y) = (P_i(x), P_j(y))$ with P_i defined in Eq. (12). Observe that

$$\widehat{E}_1^{2S} = \bigcup_{i,j} \boldsymbol{S}_{ij} \widehat{E}_0^{2S} = \bigcup_{i,j} S_i \widehat{E}_0^S \times S_j \widehat{E}_0^S \tag{17}$$

and similarly $\widehat{E}_1^{2P} = \bigcup_{i,j} \boldsymbol{P}_{ij} \widehat{E}_0^{2P} = \bigcup_{i,j} P_i \widehat{E}_0^P \times P_j \widehat{E}_0^P$ and the hole-fill map readily follows, i.e.

$$(r, s) \mapsto \left(x_k^{(i)} + \frac{x_k^{(i+1)} - x_k^{(i)}}{r^{(i+1)} - r^{(i)}} (r - r_i), y_k^{(j)} + \frac{y_k^{(j+1)} - y_k^{(j)}}{s^{(j+1)} - s^{(j)}} (s - s^{(j)}) \right) \tag{18}$$

where $(r, s) \in [r^{(i)}, r^{(i+1)}] \times [s^{(j)}, s^{(j+1)}]$.

In terms of function composition the map of interest on $\widehat{E}_1$ is

$$\begin{cases} \boldsymbol{P}_{11} \circ S_{11}^{-1} \\ \boldsymbol{P}_{12} \circ S_{12}^{-1} \\ \boldsymbol{P}_{21} \circ S_{21}^{-1} \\ \boldsymbol{P}_{22} \circ S_{22}^{-1} \end{cases} = \begin{cases} (P_1 \circ S_1^{-1}(r), P_1 \circ S_1^{-1}(s)) & \text{if } r, s \in [0, 3^{-1}\ell_0] \\ (P_1 \circ S_1^{-1}(r), P_2 \circ S_2^{-1}(s)) & \text{if } r \in [0, 3^{-1}\ell_0], s \in [3^{-1}2\ell_0, \ell_0] \\ (P_2 \circ S_2^{-1}(r), P_1 \circ S_1^{-1}(s)) & \text{if } r \in [3^{-1}2\ell_0, \ell_0], s \in [0, 3^{-1}\ell_0] \\ (P_2 \circ S_2^{-1}(r), P_2 \circ S_2^{-1}(s)) & \text{if } r, s \in [3^{-1}2\ell_0, \ell_0] \end{cases} \tag{19}$$
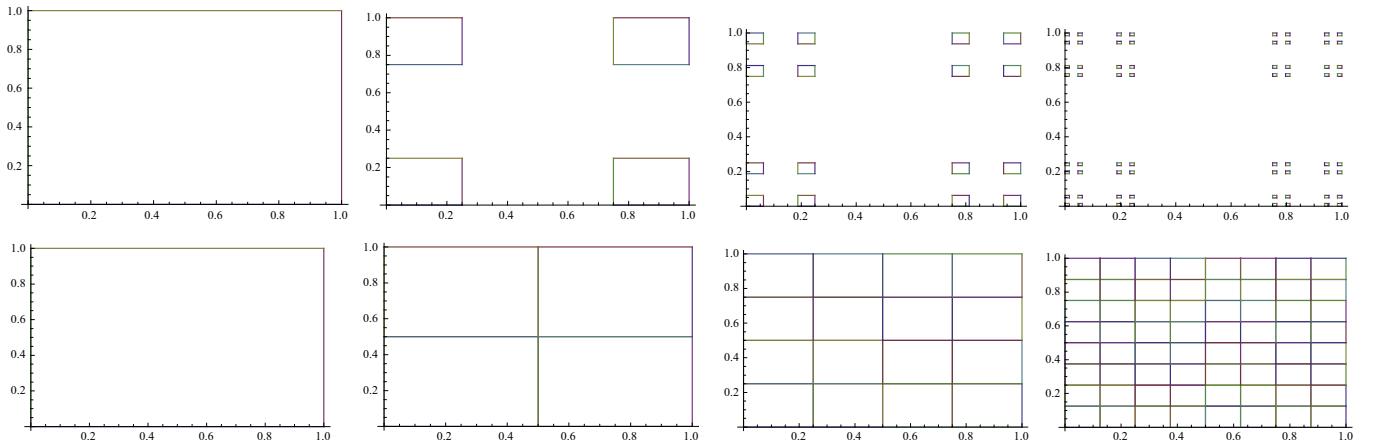
and similarly for $\widehat{E}_2$, $\boldsymbol{P}_{ij} \circ (\boldsymbol{P}_{nm} \circ \boldsymbol{S}_{nm}^{-1}) \circ \boldsymbol{S}_{ij}^{-1}$ gives rise to sixteen components of the hole-fill map.

Observe further that the map gives rise to volume and area differential relationships $dV_k = (\ell_k \ell_0^{-1})^{D_2 - 2} \mu_k^2 dV_D$ and $dA_k = (\ell_k \ell_0^{-1})^{D_1 - 1} \mu_k dA_D$ with Hausdorff dimension $D_2 = 2D_1$, where $D_1 = \ln 2 / \ln 3$, and where μ_k^2 and μ_k are support functions.

3.3. Other fractals

Extensions of this approach to the Sierpinski gasket and carpet have been developed to demonstrate the power of the method; the mappings for these latter fractals are more involved algebraically but add nothing substantially new to the observations already made. Consequently, the mappings and tessellations associated with these fractals relegated to an Appendix A at the end of this paper.

4. Transport equations for a fractal

When considering physical processes on a fractal structure, direct derivation of the governing partial differential equations is not straightforward; a simpler approach is to start with the integral forms governing transport, and then proceed to the strong form.

4.1. Integral form of transport equation

The starting points are the continuum transport equations applied to: (1) a stationary control volume Ω_s (within which $\widehat{E}_k$ is embedded) and (2) a stationary control volume Ω_r (within which $\widehat{T}_k$ is embedded):

$$\frac{d}{dt} \int_{\Omega_s} \rho_s \psi_s \, dV_s + \int_{\Gamma_s} \rho_s \psi_s \underline{v}_s \cdot \underline{n}_s \, d\Gamma_s = -\int_{\Gamma_s} \underline{J}_s \cdot \underline{n}_s \, d\Gamma_s + \int_{\Omega_s} \rho_s b_s \, dV_s, \tag{20}$$

$$\frac{d}{dt} \int_{\Omega_r} \rho_r \psi_r \, dV_r + \int_{\Gamma_r} \rho_r \psi_r \underline{v}_r \cdot \underline{n}_r \, d\Gamma_r = -\int_{\Gamma_r} \underline{J}_r \cdot \underline{n}_r \, d\Gamma_r + \int_{\Omega_r} \rho_r b_r \, dV_r, \tag{21}$$

where ρ is density, $\underline{v}$ is the material velocity, $\underline{J} \cdot \underline{n}$ is a flux, b is a source term. The k indicating the kth generation of pre-fractal has been dropped for convenience.

Equation (20) can be related to Eq. (21) via the hole-fill map; geometrical considerations give rise to Nanson's differential relationships: $dV_r = |\boldsymbol{F}| \mu_k dV_s$, $d\Gamma_r = |\boldsymbol{F}| \mu_k^{\Gamma} d\Gamma_s \cdot \boldsymbol{F}^{-1}$, where $F_{ij} = \partial x_i / \partial s_j$, $d\Gamma_s = \underline{n}_s d\Gamma_s$ and $d\Gamma_r = \underline{n}_r d\Gamma_r$. Substitution of these into Eq. (21) gives

Fig. 3. Pre-fractals for the Cantor product dust and corresponding tessellation.

(a) Pre-fractals
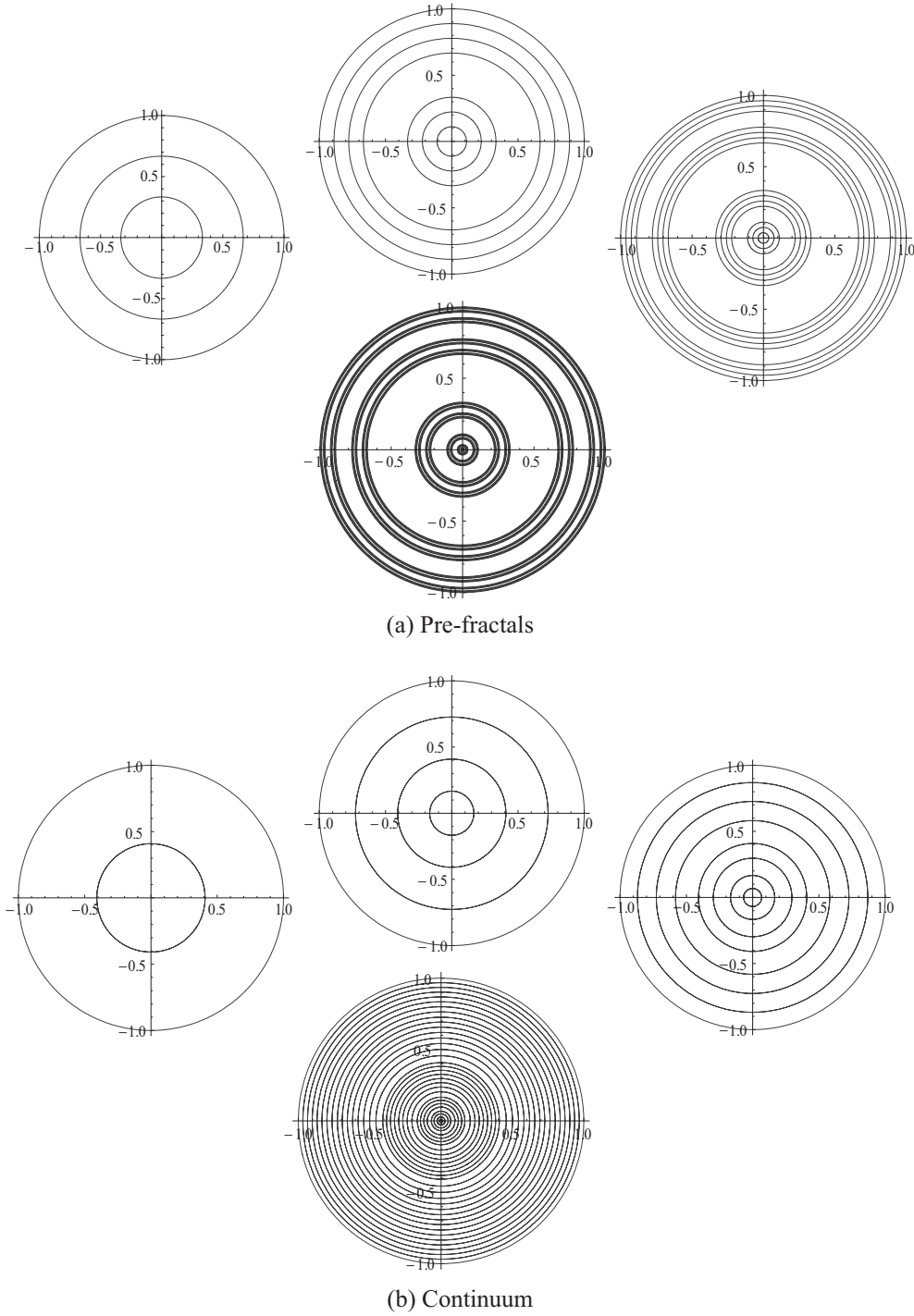
(b) Continuum

Fig. 4. Rotated Cantor dust pre-fractals and corresponding continuum.

$$\frac{d}{dt} \int_{\Omega_s} \rho_r \psi_r |\boldsymbol{F}| \mu_k \, dV_s + \int_{\Gamma_s} \rho_r |\boldsymbol{F}| \psi_r \mu_k \boldsymbol{F}^{-1} \cdot \underline{v}_r \cdot d\boldsymbol{\Gamma}_s$$
$$= - \int_{\Gamma_s} |\boldsymbol{F}_X^*| \mu_k \boldsymbol{F}^{-1} \cdot \underline{J}_r \cdot d\boldsymbol{\Gamma}_s + \int_{\Omega_s^*} \rho_r |\boldsymbol{F}| \mu_k b_r \, dV_s \qquad (22)$$

Recognising that a mass conserving map satisfies $\rho_r dV_r = \rho_s dV_s$ it follows that $\rho_r |\boldsymbol{F}| = \rho_s$ and matching of the two terms on the left hand-side of Eqs. (20) and (22) is achieved with $\psi_r = \psi_s$ and $\boldsymbol{F}^{-1} \cdot \underline{v}_r = \underline{v}_s$. Similarly, the right-hand sides of Eqs. (20) and (22) match with the definitions $|\boldsymbol{F}|\boldsymbol{F}^{-1} \cdot \underline{J}_r = \underline{J}_s$ and $b_r = b_s$.

4.2. Differential form of transport equation

By direct inspection, the associated partial differential equation for the transport Eq. (21), say, is

$$\rho_r \frac{\partial \psi_r}{\partial t} + \rho_r \underline{v}_r \cdot \nabla \psi_r = -div_r(\underline{J}_r) + \rho_r b_r, \qquad (23)$$

To relate quantities appearing on the fractal to those appearing on the tessellation, guidance is sought from the integral transport forms. As an example, consider the problem of heat transfer. Setting $\underline{v}_s = \underline{v}_r = \underline{0}$ gives rise to

$$\rho_r \frac{\partial h_r}{\partial t} = div_r(\boldsymbol{K}_r \cdot \nabla_r \theta_r) + \rho_r Q_r \tag{24}$$

where $\boldsymbol{K}_r$ is the conductivity tensor, h_r is specific enthalpy and Q_r is a heat source. Now, from the scaling identified for the transport equations, it follows that the conditions $b_r = b_s$, $\varphi_r = \varphi_s$, $\rho_r |\boldsymbol{F}| = \rho_s$ and $|\boldsymbol{F}|\boldsymbol{F}^{-1} \cdot \underline{J}_r = \underline{J}_s$ give rise to $Q_r = Q_s$, $h_r = h_s$, $\rho_r = |\boldsymbol{F}|^{-1}\rho_s$ and $\dot{q}_r = |\boldsymbol{F}|^{-1}\boldsymbol{F} \cdot \dot{q}_s$, where the heat flux $\dot{q}_s = -\boldsymbol{K}_s \cdot \nabla_s \theta_s$. From the observations $c_r \partial \theta_r / \partial t = c_s \partial \theta_s / \partial t$ and $\theta_s = \theta(\boldsymbol{x}(\boldsymbol{s}), t)$, it follows that $\nabla_s \theta_s = \boldsymbol{F}^T \cdot \nabla_r \theta_r$, which leads to $\dot{q}_r = -\boldsymbol{K}_r \cdot \nabla_r T_r$, where $\boldsymbol{K}_r = |\boldsymbol{F}|^{-1}\boldsymbol{F}\boldsymbol{K}_s\boldsymbol{F}^T$.

5. Thermal transport on Cantor dusts

It is instructive to re-examine the examples presented in Section 2 in the light of the new theory.

The hole-fill map for the 1-D Cantor dust is $x(s) = (\ell_k \ell_0^{-1})^{D_1-1} \int_0^s \mu_k(s')ds'$ and the associated deformation gradient tensor is simply a scalar, i.e. $|\boldsymbol{F}| = F = (\ell_k \ell_0^{-1})^{D_1-1}$; the support μ_k is not included as calculations are performed on the continuum domain Ω_r, for which $\mu_k = 1$ almost everywhere. It immediately follows that $\rho_r = |\boldsymbol{F}|^{-1}\rho_s = (\ell_k \ell_0^{-1})^{1-D_1}\rho_s$ and $K_r = |\boldsymbol{F}|^{-1}FK_sF^T = (\ell_k \ell_0^{-1})^{D_1-1}K_s$, where K_s and K_r in this case are scalars. The relationships between densities and conductivities are exactly those stipulated in Section 2.

The isotropic product fractal dust with $x(r) = (\ell_k \ell_0^{-1})^{D_1-1} \int_0^r \mu_k(r')dr'$ and $y(s) = (\ell_k \ell_0^{-1})^{D_1-1} \int_0^s \mu_k(s')ds'$ gives rise to $|\boldsymbol{F}| = (\ell_k \ell_0^{-1})^{2D_1-2}$ and

$$\begin{aligned}
\boldsymbol{K}_r &= |\boldsymbol{F}|^{-1}\boldsymbol{F}\boldsymbol{K}_s\boldsymbol{F}^T \\
&= |\boldsymbol{F}|^{-1} \begin{bmatrix} (\ell_k/\ell_0)^{D_1-1} & 0 \\ 0 & (\ell_k/\ell_0)^{D_1-1} \end{bmatrix} \begin{bmatrix} K_s & 0 \\ 0 & K_s \end{bmatrix} \begin{bmatrix} (\ell_k/\ell_0)^{D_1-1} & 0 \\ 0 & (\ell_k/\ell_0)^{D_1-1} \end{bmatrix} \\
&= \begin{bmatrix} K_s & 0 \\ 0 & K_s \end{bmatrix}
\end{aligned} \tag{25}$$

which establishes that $\boldsymbol{K}_r = \boldsymbol{K}_s$ in complete agreement with the results of reference [23].

The simplicity of these relationships is a consequence of the piecewise linear maps being employed as well as their homogeneity in this case. The same simplicity is not found, however, for curvilinear (or other intrinsically non-linear) systems.

5.1. Spherical fractal forms

Differential expressions arising from a curvilinear system gives rise to non-linear hole-fill maps. As an example, consider the hole filling maps that take as their input the circular swept Cantor dust shown in Fig. 1. The associated explicit hole-filling maps the rotation of the Cantor dust appearing in Fig. 1 through an angle of 2π is considered. The initial pre-fractals are depicted in Fig. 4(a) and the Hausdorff dimension D_2 of the construction is $1 + D_1$, where $D_1 = \ln 2 / \ln 3$. To ensure that mass is conserved the following identity must hold:

$$dM_k = 2\pi \rho_k \mu_k(s)sds = 2\pi \rho_0 r_k dr_k = dM_0 \tag{26}$$

Integrating this provides

$$r_k^2(s) = \frac{\rho_k}{\rho_0} \int_0^s 2\mu_k(s')s' \, ds' \tag{27}$$

Which, setting $s = \ell_0$ gives $\ell_0^2 = \rho_k \rho_0^{-1} \int_0^{\ell_0} 2\mu_k s' \, ds'$. The radial symmetry implies $\mu_k(\ell_0 - s) = \mu_k(s)$, so

$$\begin{aligned}
\int_0^{\ell_0} 2\mu_k(s')s' \, ds' &= \int_0^{\ell_0} 2\mu_k(\ell_0 - s')(\ell_0 - s') \, ds' \\
&= \ell_0 \int_0^{\ell_0} 2\mu_k(s')ds' - \int_0^{\ell_0} 2\mu_k(s')s' \, ds'
\end{aligned} \tag{28}$$

which yields $\int_0^{\ell_0} 2\mu_k s' \, ds' = \ell_0 \int_0^{\ell_0} \mu_k ds' = \ell_0^2(\ell_k/\ell_0)^{1-D_1}$ and it immediately follows that the required continuum map is

Fig. 6. Temperature plot for a finite bar fixed bar with fixed wall temperatures for $\frac{\dot{Q}_0 \ell_0^2}{K_0 \Delta \theta_0} = 5$, $\dot{Q}_1 = 0$ and $\frac{\dot{Q}_2 \ell_0^2}{K_0 \Delta \theta_0} = 0.5$ and $\dot{Q}_0 = \dot{Q}_1 = \dot{Q}_2$ with $\frac{\dot{Q}_0 \ell_0^2}{K_0 \Delta \theta_0} = 1$.

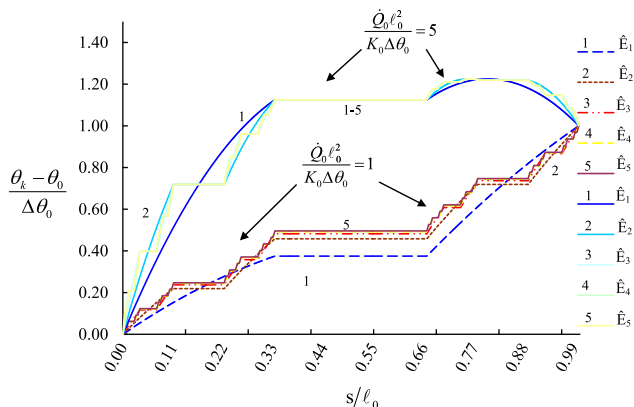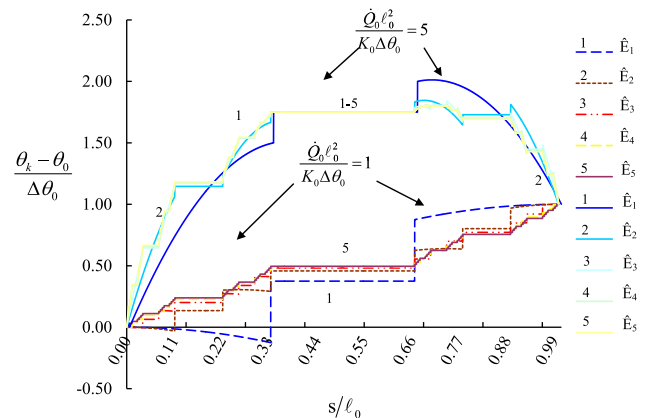**Fig. 5.** Temperature plot for a finite bar fixed bar with fixed wall temperatures for $\frac{\dot{Q}_0 \ell_0^2}{K_0 \Delta \theta_0} = 5$ & $\dot{Q}_1 = 0$ and $\dot{Q}_0 = \dot{Q}_1$ with $\frac{\dot{Q}_0 \ell_0^2}{K_0 \Delta T_0} = 1$.
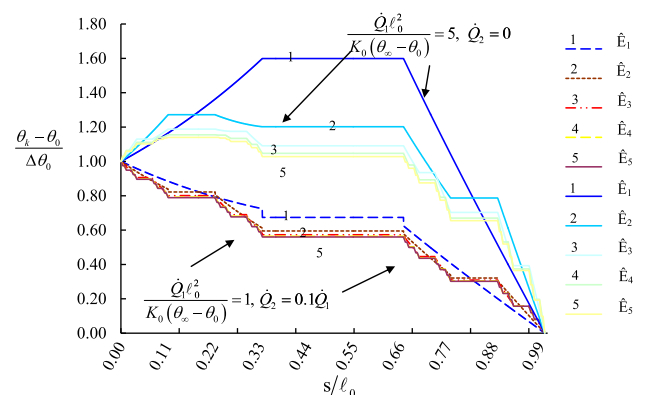
Fig. 7. Temperature plot for a finite bar fixed bar with fixed wall temperatures for $2h_0 \ell_0^2 / wK_0 = 1$ and $(\theta_r - \theta_\infty)(\theta_0 - \theta_\infty) = 0$.
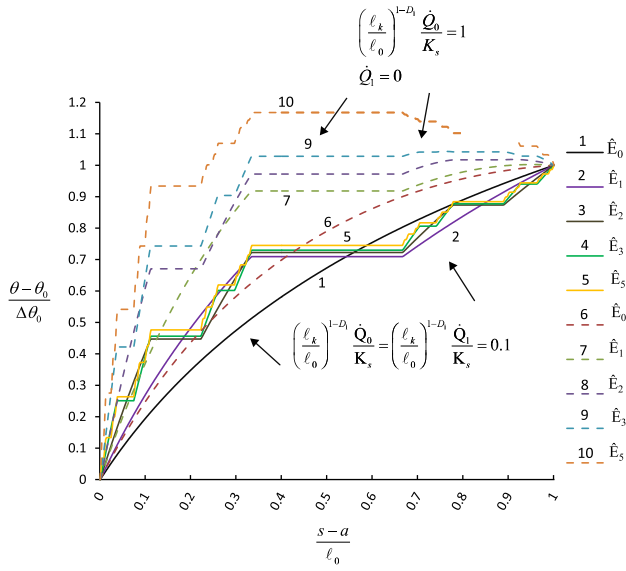
Fig. 8. Temperature plot for per-fractal rings in steady state with heat sources for different values of k.

$$r_k(s) = \left(\frac{\ell_k}{\ell_0}\right)^{\frac{D_1-1}{2}} \left[\int_0^s 2\mu_k(s')s'\,ds'\right]^{1/2} \qquad (29)$$

where density is $\rho_k = (\ell_k\ell_0^{-1})^{D_1-1}\rho_0$ as previously derived for the dust embedded in a 1-D continuum.

It is evident from the analysis above that $\rho_r = (\ell_k\ell_0^{-1})^{1-D_1}\rho_s$ implies $|\boldsymbol{F}| = (\ell_k\ell_0^{-1})^{D_1-1}$. Given that $x_1 = r\cos\phi$, $x_2 = r\sin\phi$, $s_1 = s\cos\phi$ and $s_2 = s\sin\phi$, it follows that

$$\boldsymbol{F} = \begin{bmatrix} \frac{\partial x_1}{\partial s_1} & \frac{\partial x_1}{\partial s_2} \\ \frac{\partial x_2}{\partial s_1} & \frac{\partial x_2}{\partial s_2} \end{bmatrix} = \begin{bmatrix} r'\cos^2\phi + \left(\frac{r}{s}\right)\sin^2\phi & \left(r' - \left(\frac{r}{s}\right)\right)\sin\phi\cos\phi \\ \left(r' - \left(\frac{r}{s}\right)\right)\sin\phi\cos\phi & r'\sin^2\phi + \left(\frac{r}{s}\right)\cos^2\phi \end{bmatrix} \qquad (30)$$

where $r' = dr/ds$. Following some algebraic manipulation, the Jacobean reduces to $|\boldsymbol{F}| = (r/s)r'$, which is the expected result since direct differentiation of Eq. (29) gives $(r/s)r' = (\ell_k\ell_0^{-1})^{D_1-1}$.

A somewhat more straightforward expression for $\boldsymbol{F}$ is obtained when the polar coordinate system is applied directly to give

$$\boldsymbol{F} = \begin{bmatrix} \dfrac{\partial r}{\partial s} & \dfrac{1}{s}\dfrac{\partial r}{\partial\phi} \\ r\dfrac{\partial\phi}{\partial s} & \dfrac{r}{s}\dfrac{\partial\phi}{\partial\phi} \end{bmatrix} = \begin{bmatrix} r' & 0 \\ 0 & \dfrac{r}{s} \end{bmatrix}. \qquad (31)$$

The conductivity tensor for the continuum is

$$\boldsymbol{K}_r = |\boldsymbol{F}|^{-1}\boldsymbol{F}\boldsymbol{K}_s\boldsymbol{F}^T = |\boldsymbol{F}|^{-1}\boldsymbol{K}_s\boldsymbol{F}^2 = |\boldsymbol{F}|^{-1}\boldsymbol{K}_s\begin{bmatrix} r'^2 & 0 \\ 0 & \left(\frac{r}{s}\right)^2 \end{bmatrix} = \boldsymbol{K}_s\begin{bmatrix} \left(\frac{r's}{r}\right) & 0 \\ 0 & \left(\frac{r's}{r}\right)^{-1} \end{bmatrix} \qquad (32)$$

which yields $K_r = K_s(\ell_k\ell_0^{-1})^{D_1-1}(s/r)^2$ and $K_\theta = K_s(\ell_k\ell_0^{-1})^{1-D_1}(r/s)^2$.

The key lesson here is that an inhomogeneous, anisotropic and piecewise continuous material conductivity in the tessellated continuum emerges as a consequence of the non-linear map (29).
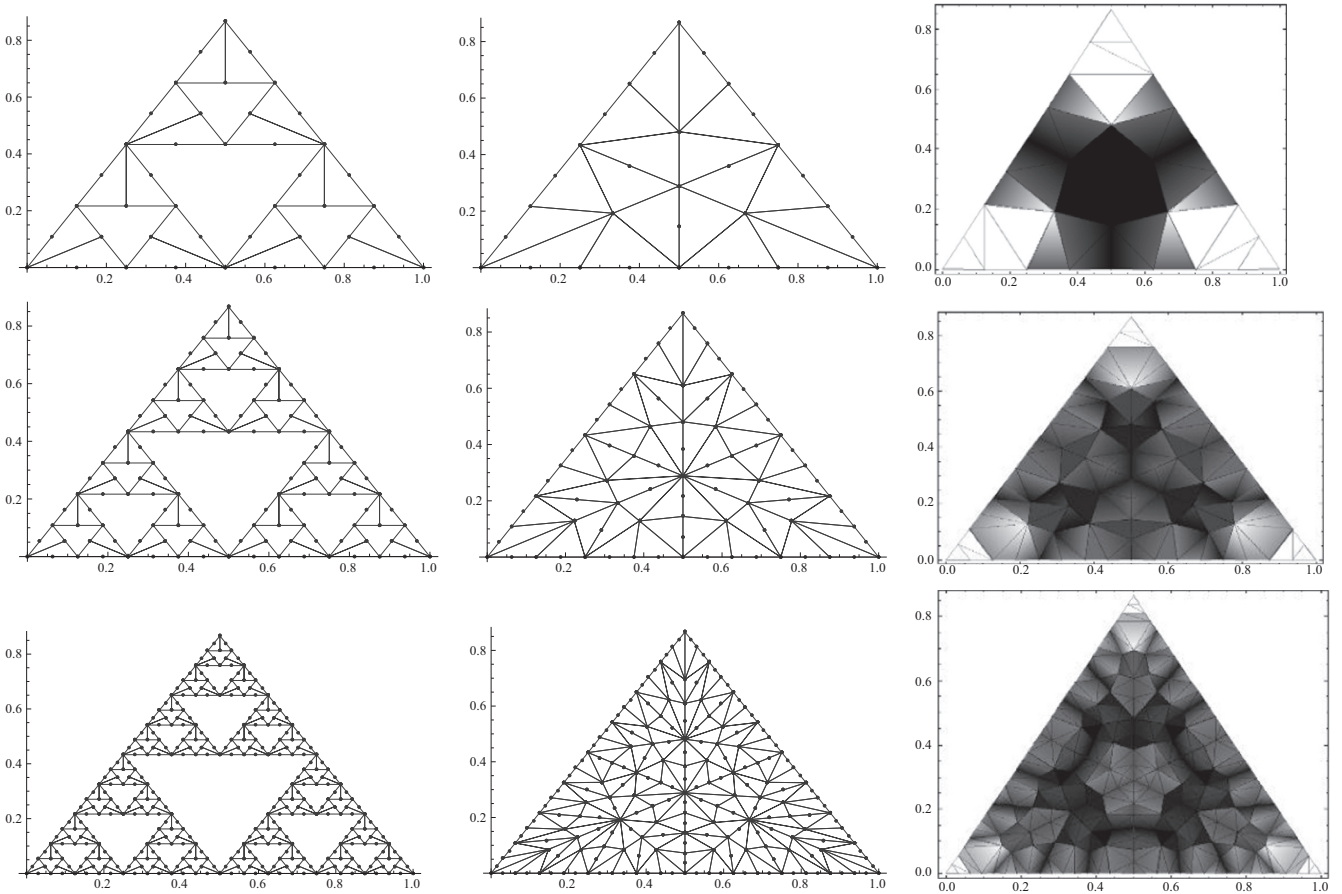
Fig. 9. Thermal conductivity (K_r/K_s) distribution on tessellation for pre-fractals of the Sierpinski gasket.

6. Analytical solutions for Cantor dusts

This section focuses on solutions for the Cantor dust depicted on Fig. 1, whose continuum model is a bar $\widehat{E}_0$ of length ℓ_0 with thermal conductivity K_0 subject to various types of thermal loading but constrained by temperatures at $x = 0$ and $x = \ell_0$ of θ_0 and θ_ℓ, respectively. The fractal/pre-fractal can be thermally loaded in a variety of ways, with varying degrees of complexity. Setting $K_r = K_0 = (\ell_k \ell_0^{-1})^{D_1-1} K_s$ (see Section 5.1) has the effect of producing different values for K_s, depending on whichever pre-fractal $\widehat{E}_k$ the analysis is being performed.

Consider a model problem, in which a fluid is assumed to flow through the voids of a pre-fractal Cantor dust model. Elements in the fractal are assumed to contain a uniformly distributed internal heat source, defined such the total load per unit volume $\dot{Q}_0$ appears uniform on the tessellated continuum. An alternative possibility also considered is fluid flowing over elements of width w to provide thermal loads through convective heat transfer, in which the bar is subjected to a heat flux of the form $q_0 = h_0(\theta - \theta_\infty)$, where h_0 is a (constant) heat transfer coefficient, and θ_∞ is viewed as the ambient temperature of the of the surrounding medium.

Additional thermal loading arising from the fluid flowing through the voids is assumed to manifest as a set of source terms of the form $(2^k - 1)^{-1} \dot{Q}_1 \delta(\ell_0^{-1} x - 2^{-k} i)$, $1 \leqslant i \leqslant 2^k - 1$, where $2^k - 1$ is the number of holes associated with $\widehat{E}_k$ and δ is the Dirac delta distribution function.

If the fluid is viewed as a perfect conductor, the edge temperatures of any two adjacent solid components are common. A wider variety of thermal loading problems can be analysed by allowing the model fluid itself to support a temperature gradient, wherein the temperature gradient induced by conductive heat transfer would manifest itself as discontinuous behaviour across adjacent element edges. Such behaviour can be replicated by the inclusion of source terms of the form $(2^k - 1)^{-1} \dot{Q}_2 \ell_0 \delta'(\ell_0^{-1} x - 2^{-k} i)$, where δ' represents the x derivative of the Dirac delta distribution.

6.1. 1-D bar subject to uniform heat loading

The governing differential equation applicable to the tessellation $\widehat{T}_1$ incorporating the heat sources alluded to above is $K_0 \theta^{1''} + \dot{Q}_0 - \dot{Q}_1 \delta(x/\ell_0 - 1/2) - \dot{Q}_2 \ell_0 \delta'(x/\ell_0 - 1/2) = 0$, which can be integrated to give

$$\theta^1(x) = -\frac{\dot{Q}_0}{2K_0} x^2 + \frac{\dot{Q}_1 \ell_0^2}{K_0} \left\{ \frac{x}{\ell_0} - \frac{1}{2} \right\} + \frac{\dot{Q}_2 \ell_0^2}{K_0} H\left(\frac{x}{\ell_0} - \frac{1}{2} \right)$$
$$+ \left(\frac{\theta_\ell - \theta_0}{\ell_0} + \frac{\dot{Q}_0 \ell_0}{2K_0} - \frac{\dot{Q}_1 \ell_0}{2K_0} - \frac{\dot{Q}_2 \ell_0}{K_0} \right) x + \theta_0 \quad (33)$$

where H is the Heaviside step function or more generally the governing equation on the tessellation $\widehat{T}_k$ is

$$K_0 \theta^{k''} + \dot{Q}_0 - \frac{\dot{Q}_1}{2^k - 1} \sum_{i=1}^{2^k-1} \delta\left(\frac{x}{\ell_0} - \frac{i}{2^k} \right) - \frac{\dot{Q}_2 \ell_0}{2^k - 1} \sum_{i=1}^{2^k-1} \delta'\left(\frac{x}{\ell_0} - \frac{i}{2^k} \right) = 0$$
$$(34)$$

with solution

$$\theta^k = -\frac{\dot{Q}_0}{2K_0} x^2 + \frac{\dot{Q}_1 \ell_0^2}{K_0(2^k - 1)} \sum_{i=1}^{2^k-1} \left\{ \frac{x}{\ell_0} - \frac{i}{2^k} \right\}$$
$$+ \frac{\dot{Q}_2 \ell_0^2}{K_0(2^k - 1)} \sum_{i=1}^{2^k-1} H\left(\frac{x}{\ell_0} - \frac{i}{2^k} \right)$$
$$+ \left[\frac{\theta_\ell - \theta_0}{\ell_0} + \frac{\dot{Q}_0 \ell_0}{2K_0} - \frac{\dot{Q}_1 \ell_0}{2K_0} + \frac{\dot{Q}_2 \ell_0}{K_0} \right] x + \theta_0 \quad (35)$$
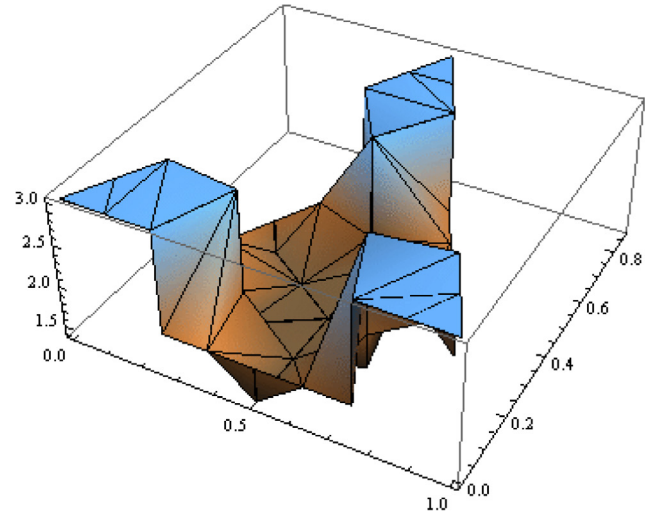
(a)　　Conductivity (K_r K_s) on $\widehat{T}_{k=2}$
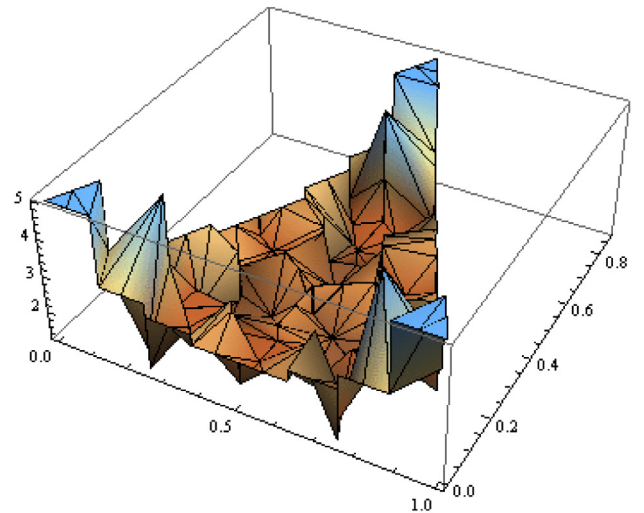
(b)　　Conductivity (K_r K_s) on $\widehat{T}_{k=3}$
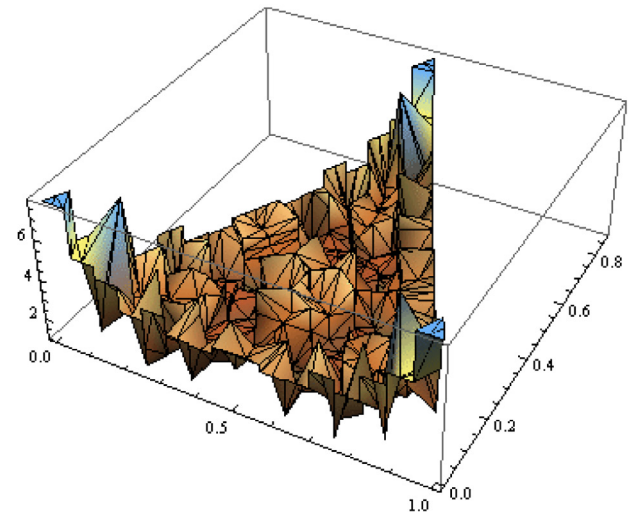
(c)　　Conductivity (K_r K_s) on $\widehat{T}_{k=4}$

Fig. 10. Thermal conductivity (K_r/K_s) distribution on tessellation for pre-fractals of the Sierpinski gasket.
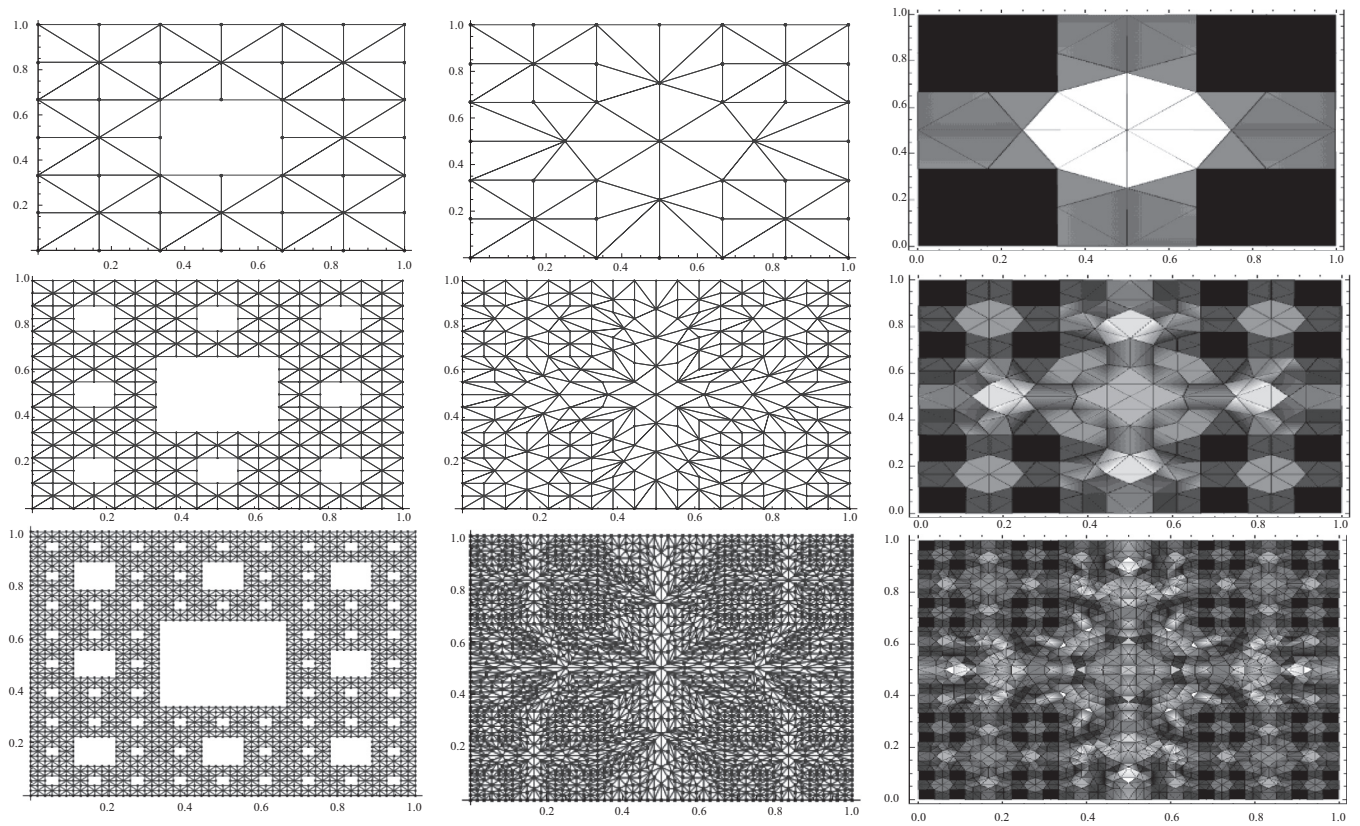
Fig. 11. Thermal conductivity (K_r/K_s) distribution on tessellation for pre-fractals of the Sierpinski carpet.
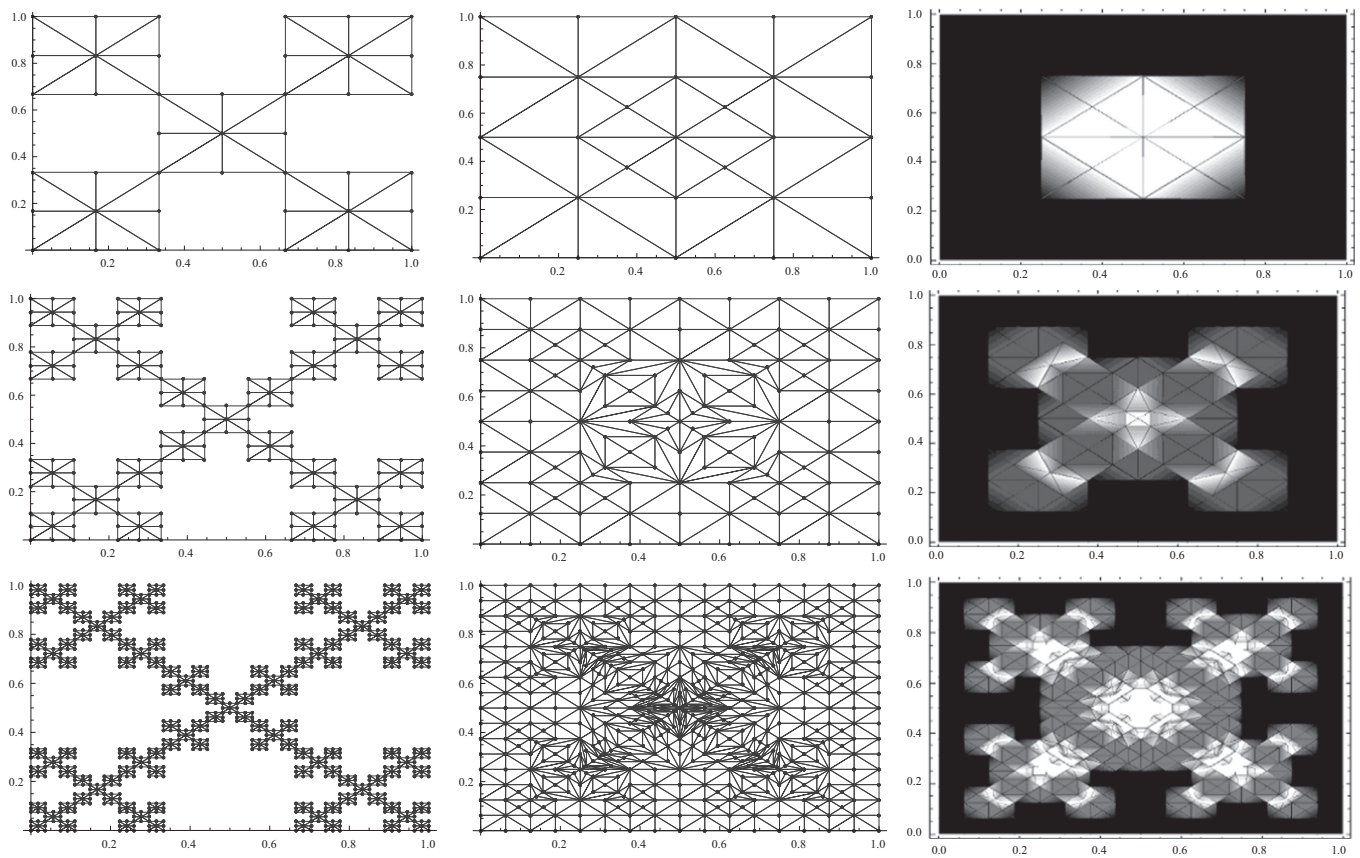
Fig. 12. Thermal conductivity (K_r/K_s) distribution on tessellation of a finger-like porous fractal.
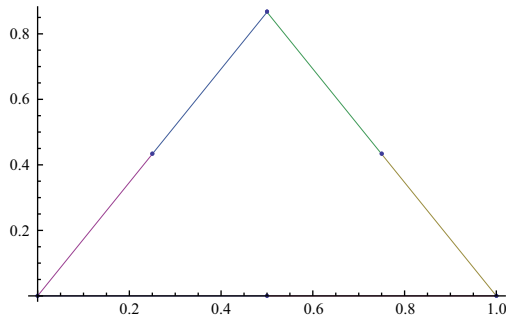
Fig. 13. Initial Points and domain for the Sierpinski Gasket.

where {•} is a Macaulay bracket, which returns the contents if positive.

The solution $\theta_k = \theta^k \circ x_k$ with θ^k given by Eq. (35) with $\dot{Q}_2 = 0$ is presented in Fig. 5 for two different values of $\dot{Q}_0$ and $\dot{Q}_1$. Observe from Fig. 5 that all temperatures are continuous and are set at constant values across holes despite not being truly representative of the temperature there. Moreover, note the effect of the heat sink $\dot{Q}_1$ which has the effect of producing different temperature plateaus when non-zero. It is apparent for this case however, that any change in plateau temperature reduces with increase in k as a consequence of finer adjustments being made to the pre-fractals. Temperature of the case $\dot{Q}_2 \neq 0$ are presented in Fig. 6, where discontinuous behaviour is now apparent at holes. In the case where $\dot{Q}_1 = 0$ the temperature of the largest plateau is invariant for each $\widehat{E}_k$ although slight changes appear at other plateaus. For $\dot{Q}_1 \neq 0$ (as in Fig. 5) large changes in plateau temperatures are apparent along with temperature discontinuities as a consequence of $\dot{Q}_2 \neq 0$.

6.2. 1-D bar subject to convective heat loading

In this case and with regards to $\widehat{E}_1$ for example, the governing equation for the temperature θ^1 on $\widehat{T}_1$ is thus given by

$$K_0\theta^{1\prime\prime} + \frac{2h_0}{w}(\theta_\infty - \theta^1) - \dot{Q}_1\delta\left(\frac{x}{\ell_0} - \frac{1}{2}\right) - \dot{Q}_2\ell_0\delta'\left(\frac{x}{\ell_0} - \frac{1}{2}\right) = 0 \quad (36)$$

where w is width.

Eq. (36) can be solved by assuming a solution of the form $\theta_G = \theta_{cf} + \theta_P + \theta_\infty$, where the complementary function $\theta_{cf}(x) = a\cosh(\alpha x) + b\sinh(\alpha x)$ with $\alpha = (2h_0/wK_0)^{\frac{1}{2}}$, and where a and b are integration constants. The particular integral θ_P is obtained by setting $\theta_P = Ze^{\alpha x}$, which on substitution into Eq. (36) and integrating yields

$$Z' = \frac{\dot{Q}_1\ell_0}{K_0}e^{\frac{\alpha\ell_0}{2}}e^{-2\alpha x}H\left(\frac{x}{\ell_0} - \frac{1}{2}\right)$$
$$+ \frac{\dot{Q}_2\ell_0}{K_0}\left(e^{-\alpha x}\delta\left(\frac{x}{\ell_0} - \frac{1}{2}\right) - \alpha\ell_0 e^{\frac{\alpha\ell_0}{2}}e^{-2\alpha x}H\left(\frac{x}{\ell_0} - \frac{1}{2}\right)\right). \quad (37)$$

One further integration and multiplication with $e^{\alpha x}$ gives

$$\theta_P = \left[-\frac{\dot{Q}_1\ell_0}{K_0\alpha}\sinh\left(\alpha\left(\frac{\ell_0}{2} - x\right)\right) + \frac{\dot{Q}_2\ell_0^2}{K_0}\left(\cosh\left(\alpha\left(\frac{\ell_0}{2} - x\right)\right)\right)\right]H\left(\frac{x}{\ell_0} - \frac{1}{2}\right). \quad (38)$$

Extending the analysis to $\widehat{T}_k$ provides

$$K_0\theta^{k\prime\prime} + \frac{2h_0}{w}(\theta_\infty - \theta^k) - \frac{\dot{Q}_1}{2^k - 1}\sum_{i=1}^{2^k-1}\delta\left(\frac{x}{\ell_0} - \frac{i}{2^k}\right) - \frac{\dot{Q}_2\ell_0}{2^k - 1}\sum_{i=1}^{2^k-1}\delta'\left(\frac{x}{\ell_0} - \frac{i}{2^k}\right) = 0 \quad (39)$$

Which, following a similar procedure as above gives

$$\theta^k(x) = (\theta_0 - \theta_\infty)\cosh(\alpha x) + b\sinh(\alpha x)$$
$$- \frac{\dot{Q}_1\ell_0}{K_0\alpha(2^k - 1)}\sum_{i=1}^{2^k-1}\sinh\left(\alpha\left(\frac{i\ell_0}{2} - x\right)\right)H\left(\frac{x}{\ell_0} - \frac{i}{2^k}\right)$$
$$+ \frac{\dot{Q}_2\ell_0^2}{K_0(2^k - 1)}\left(\sum_{i=1}^{2^k-1}\cosh\left(\alpha\left(\frac{i\ell_0}{2^k} - x\right)\right)H\left(\frac{x}{\ell_0} - \frac{i}{2^k}\right)\right) + T_\infty, \quad (40)$$

where b is determined on setting $\theta^k(\ell_0) = \theta_\ell$.

Fig. 7 gives the temperature $\theta_k = \theta^k \circ x_k$ with θ^k given by Eq. (40) for small values of k. Fixed end temperatures are applied and (for demonstration purposes) $2h_0\ell_0^2/wK_0 = 1$ and $(\theta_\ell^k - \theta_\infty)(\theta_0 - \theta_\infty) = 0$. The temperatures are continuous in the case of $\dot{Q}_2 = 0$ but discontinuous when $\dot{Q}_2 \neq 0$.
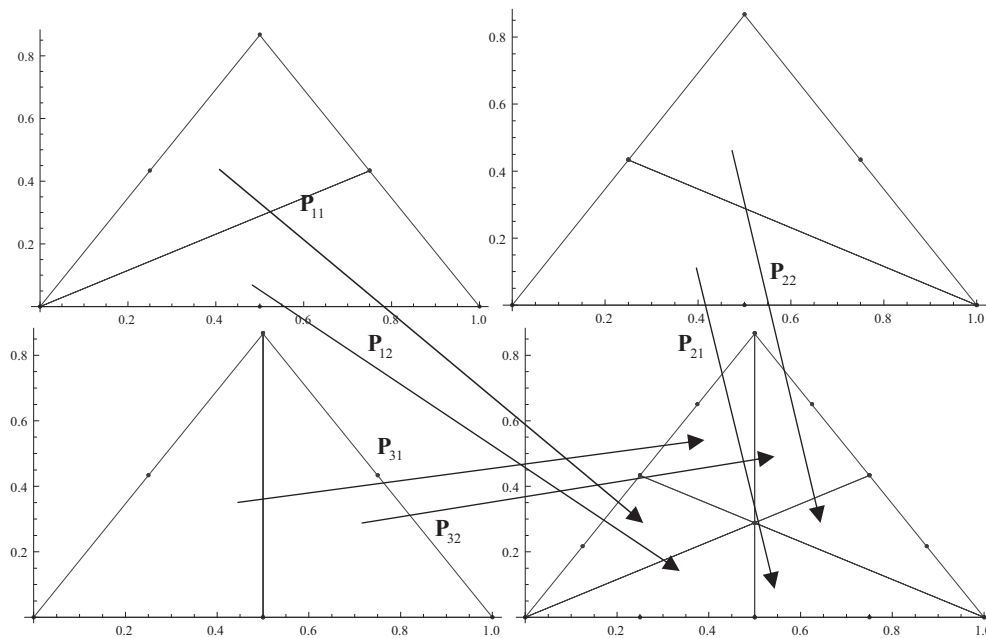
Fig. 14. Maps used to tessellate the triangle.
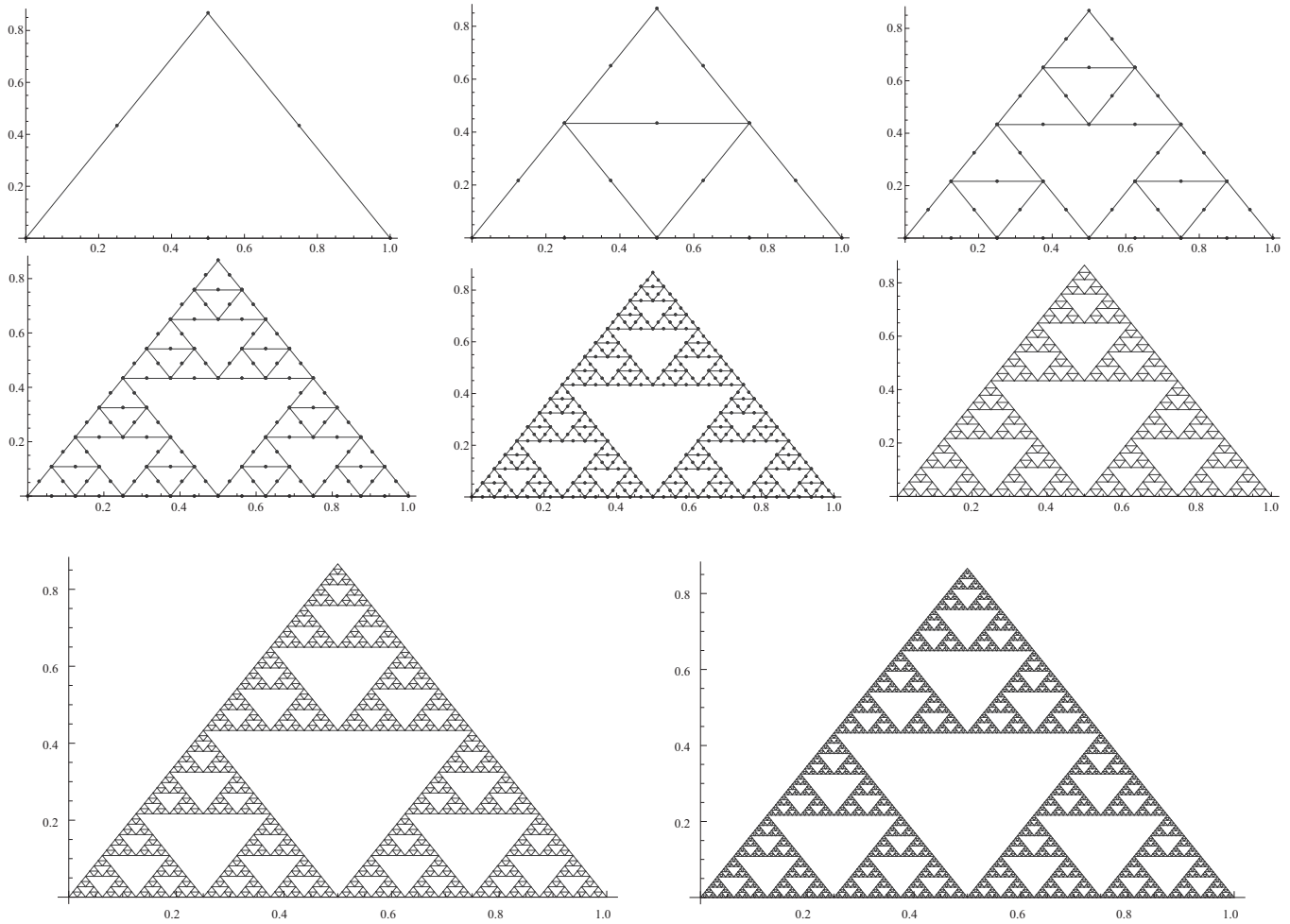
Fig. 15. Pre-fractals for the Sierpinski Gasket.

7. Analytical solutions for circular dusts

In the foregoing analyses, the mappings between the continuum and fractal have been relatively straightforward to identify, and essentially transparent in their application. In the swept ring Cantor set, the coordinate system itself impacts on the mapping and, through this, the fractal description itself. Consider the governing steady-state partial differential equation on a cylindrical continuum;

$$div_r(\underline{q}) = \frac{1}{r}\left(\frac{\partial}{\partial r}(rq_r) + \frac{\partial}{\partial \theta}(q_\phi)\right) = 0, \tag{41}$$

where $\underline{q} = -\boldsymbol{K}_r \cdot \nabla_r \theta_r$, and $\nabla_r \theta_r = (\partial \theta/\partial r)\underline{e}_r + r^{-1}(\partial \theta/\partial \phi)\underline{e}_\phi$.

The axi-symmetric problem reduces to $d(s^2 r^{-1}(d\theta_r/dr))/dr = 0$ and integrates readily to give $(d\theta_r/dr) = Ars^{-2}$, where A is an integration constant. The absence of piecewise linearity presents a difficulty through the appearance of s in the differential equation, and to proceed further requires the inverse map for $r(s)$.

The map from the cylindrical pre-fractal to the continuum is obtained in a similar way to Eq. (29), and takes the form $r^2 - a^2 = (\ell_k/\ell_0)^{D_1-1}\int_a^s 2\mu_k(s')s'\,ds'$, where a is the internal radius. Applying this map to an annular element of the pre-fractal with inner radius s_j gives $r^2 - r_j^2 = (\ell_k/\ell_0)^{D_1-1}(s^2 - s_j^2)$ and the governing differential equation integrates to give

$$\theta_r = A\frac{1}{2}\left(\frac{\ell_k}{\ell_0}\right)^{D_1-1}\ln\left(\left(\frac{\ell_k}{\ell_0}\right)^{1-D_1}(r^2 - r_j^2) + s_j^2\right) + B_j \tag{42}$$

for $r_j \leqslant r \leqslant r_{j+1}$; the integration constants A and B_j are determined by boundary and temperature compatibility conditions.

It is readily confirmed that the solution to the governing equation $d(s(d\theta_s/ds))/ds = 0$ is given by $\theta_s = \theta_r \circ r$, since $s(d\theta_s/ds) = sr'(d\theta_r/dr) = Ar'r/s$ but $(r/s)r' = (\ell_k\ell_0^{-1})^{D_1-1}$, so it immediately follows that $d(s(d\theta_s/ds))/ds = d(A(\ell_k\ell_0^{-1})^{D_1-1})/ds = 0$.

Heat sources and sinks can in principle be incorporated into the governing steady-state equations; on $\hat{T}_1$ for example, the internal sources and edge loadings described in preceding sections can be included:

$$\left(\frac{\ell_k}{\ell_0}\right)^{1-D_1}\frac{1}{r}\frac{d}{dr}\left(\frac{s^2}{r}\frac{d\theta_r}{dr}\right) + \frac{\dot{Q}_0}{K_s} - \frac{\dot{Q}_1}{K_s}\delta\left(\frac{r}{r_1} - 1\right) = 0, \tag{43}$$

and integrated once to give

$$\left(\frac{\ell_k}{\ell_0}\right)^{1-D_1}\frac{d\theta_r}{dr} + \frac{\dot{Q}_0}{2K_s}\frac{r^3}{s^2} - \frac{\dot{Q}_1 r_1}{K_s}\frac{r^2}{s^2}H\left(\frac{r}{r_1} - 1\right) = A\frac{r}{s^2} \tag{44}$$

The second integration is rendered more difficult through the presence of the s-coordinate and thus involves the inverse map mentioned above:
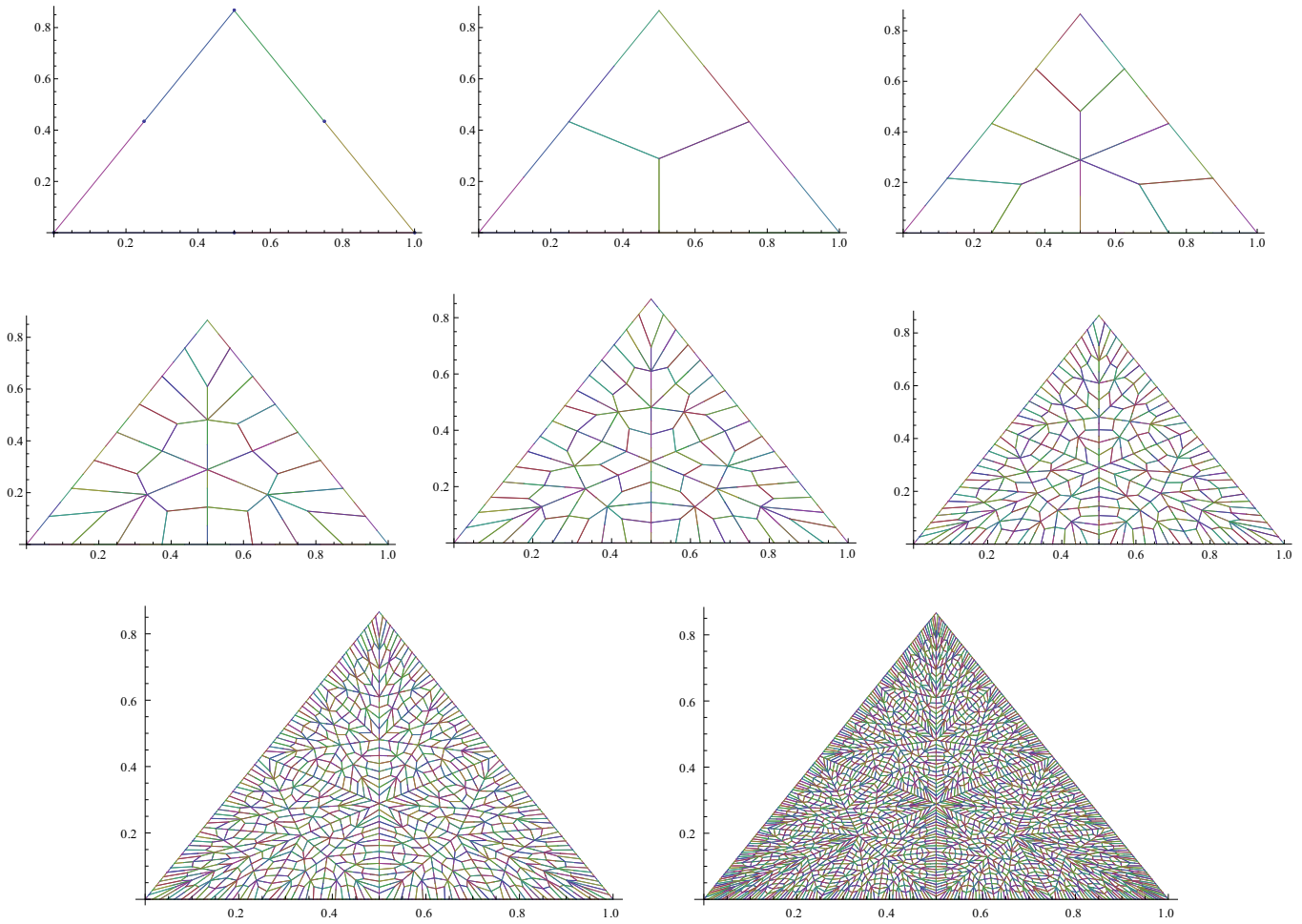
Fig. 16. Corresponding tessellated domains for the Sierpinski Gasket.

$$\left(\frac{\ell_k}{\ell_0}\right)^{1-D_1}\theta_r + \frac{\dot{Q}_0}{2K_s}\int_a^r \frac{\rho^3}{s(\rho)^2}d\rho - \frac{\dot{Q}_1 r_1}{K_s}\int_a^r \frac{\rho^2}{s(\rho)^2}H\left(\frac{\rho}{r_1}-1\right)d\rho$$

$$= A\int_a^r \frac{\rho}{s(\rho)^2}d\rho + B \tag{45}$$

The governing equation on the tessellation $\widehat{T}_k$ is

$$\left(\frac{\ell_k}{\ell_0}\right)^{1-D_1}\frac{1}{r}\frac{d}{dr}\left(\frac{s^2}{r}\frac{d\theta_r}{dr}\right) + \frac{\dot{Q}_0}{K_s} - \frac{\dot{Q}_1}{K_s\left(2^k-1\right)}\sum_{i=1}^{2^k-1}\delta\left(\frac{r}{r_i}-1\right) = 0 \tag{46}$$

whose solution mirrors that on $\widehat{T}_1$. Corresponding temperature plots are depicted in Fig. 8 for difference magnitudes of heat source.

8. Material properties in 2-D

On a tessellated continuum the material conductivity satisfies the relationship $\boldsymbol{K}_r = |\boldsymbol{F}|^{-1}\boldsymbol{F}\boldsymbol{K}_s\boldsymbol{F}^T$ as discussed in Section 5. The behaviour of a thermal conductivity is thus well defined but can be inhomogeneous, anisotropic and discontinuous. These properties are apparent with the ring fractal but are also evident in the non-product fractals presented in Appendix A. Fig. 9 for example shows the distribution of the point-wise maximum thermal conductivity in the form of contour plots on tessellated continua for pre-fractals of the Sierpinski gasket. Threefold rotational symmetry is apparent in the plots, as is the increasing complexity as the level of detail is increased on the pre-fractals. The results are also

displayed in 3-D in Fig. 10 where the piecewise continuous behaviour of the conductivity is readily visible.

Similar results pertaining to the Sierpinski carpet are presented in Fig. 11, where the excessive shear present in the maps is revealed in the distribution of the thermal conductivity. Likewise, results for a finger-like fractal depicted in Fig. 12 reveal similar intricate spatial variation in the thermal conductivity. All the plots reveal how the geometric complexity present in the pre-fractals manifests in the material properties on the tessellated continuum.

The ability to determine thermal conductivity on a tessellation—which can form the basis for a finite element mesh—opens up the approach to numerical analysis. The incorporation of element-edge sources/sinks in a standard continuous Galerkin finite element method corresponds to the situation where Dirac-delta terms are included in the governing differential equations. Moreover, the discontinuous Galerkin finite element method facilitates inclusion of asymmetric element-edge sources/sinks, which is equivalent to the inclusion of derivative-type Dirac-delta terms in the governing differential equations as discussed above.

9. Conclusions

This paper tests the hypothesis that heat transfer analysis on fractals/pre-fractals can be performed on an associated tessellated continuum. The results presented in Sections 6–8 confirm that, for the simple fractals considered, it is feasible to perform heat transfer analysis on a tessellated continuum. This is achieved by two
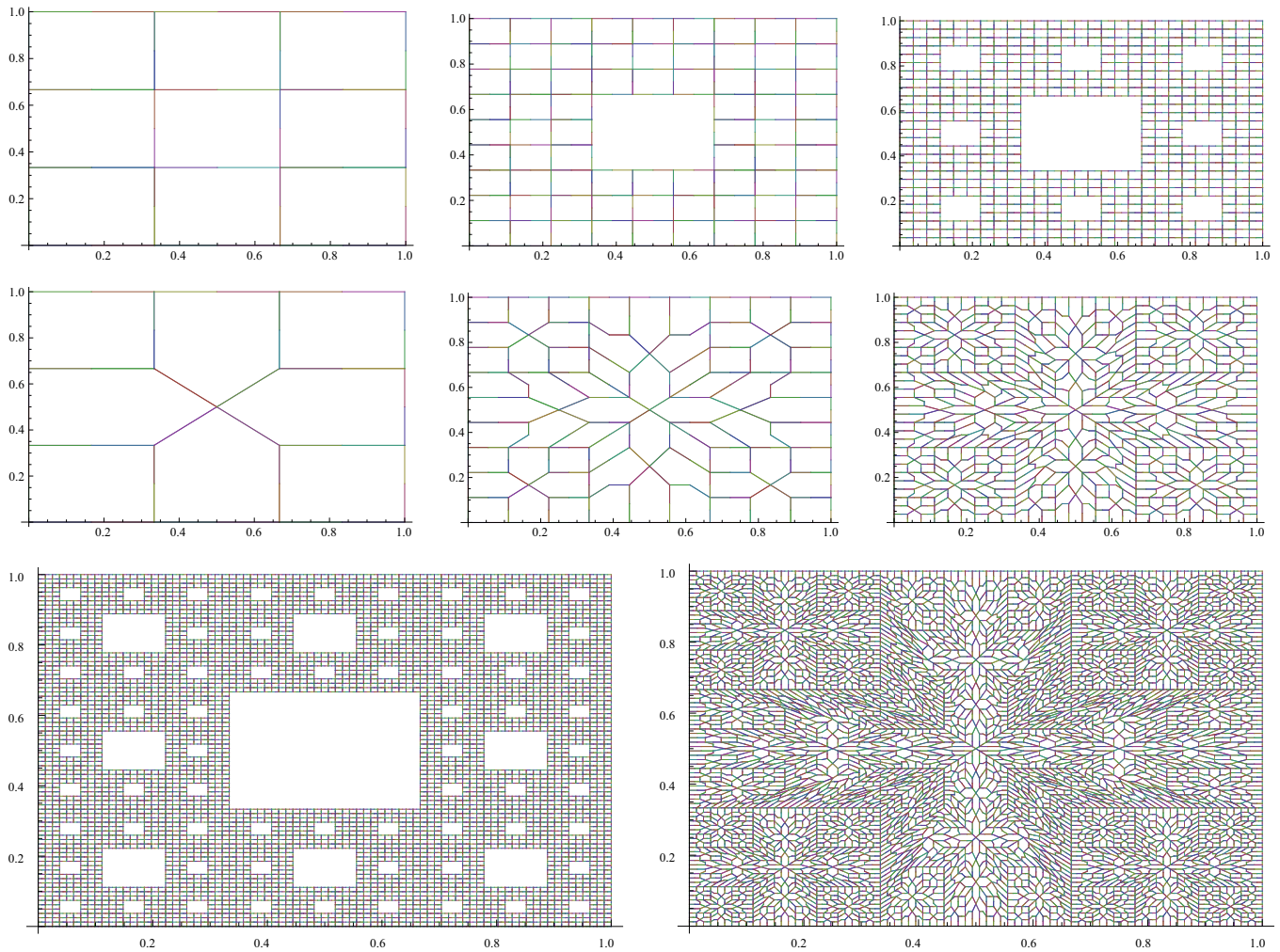
Fig. 17. Pre-fractals for the Sierpinski carpet along with corresponding tessellated domains.

distinct techniques: the hole-fill maps themselves and—equally important—the representation of the governing physics via integral forms of the transport equations. The transport equations provide a description of the underlying physics in the weak sense, and hence are particularly suitable for analysis on inherently discontinuous pre-fractals. The generality of the approach provides its key attractiveness but, as discussed in Section 8, the simplifications arising from the transfer of the analysis to the continuum are somewhat offset by the complexity arising in the material property spatial distribution.

In establishing the validity of the approach for the types of fractals considered, a number of advances have been made, which are:

- A procedure similar to the generation process for a fractal has been established for the generation of the associated tessellated continuum.
- Two procedures have been presented for formulation of a hole-fill map between a pre-fractal and its associated tessellated continuum.
- Transport equations linking transport phenomenon on a fractal to a tessellation has been established.
- Partial differential equations have been defined on the tessellated continuum and along with material properties by application of the transport theory.
- Analytical temperature solutions on fractal dusts and rings have been established for a range of thermal loading conditions principally involving heat sinks and sources.

- Complex material distributions have been presented on tessellated continua for a selection of non-product fractals.

Appendix A. Examples of hole-fill maps

A.1. Sierpinski gasket

Things are somewhat more involved with non-product sets and the Sierpinski gasket is an example where extra points are required to facilitate the construction of a piecewise linear hole-filling map. Depicted in Fig. 13 is an equilateral triangle with identifiable corner and mid-points; the domain and points are denoted respectively $\widehat{E}_0$ and $\widehat{E}_0^S$, where

$$\widehat{E}_0^S = \left\{ (0,0), \left(\frac{\ell_0}{2},0\right), (\ell_0,0), \left(\frac{3}{4}\ell_0, \frac{\sqrt{3}}{4}\ell_0\right), \left(\frac{1}{2}\ell_0, \frac{\sqrt{3}}{2}\ell_0\right), \left(\frac{\ell_0}{4}, \frac{\sqrt{3}}{4}\ell_0\right) \right\}$$

(47)

In forming $\widehat{E}_1$ or more notably $\widehat{E}_1^S$ three maps are employed, i.e.

$$\boldsymbol{S}_1(x,y) = \left(\frac{x}{2}, \frac{y}{2}\right), \boldsymbol{S}_2(x,y) = \left(\frac{\ell_0}{2} + \frac{x}{2}, \frac{y}{2}\right) \text{ and } \boldsymbol{S}_3(x,y)$$

$$= \left(\frac{\ell_0}{4} + \frac{x}{2}, \frac{\sqrt{3}\ell_0}{4} + \frac{y}{2}\right)$$

(48)

Similarly, three corresponding cover maps are

$$P_1(x,y) = \begin{cases} P_{11}(x,y) \text{ if } \sqrt{3}y \leqslant x, \\ P_{12}(x,y) \text{ if } \sqrt{3}y > x \end{cases},$$

$$P_2(x,y) = \begin{cases} P_{21}(x,y) \text{ if } \sqrt{3}y \leqslant \ell_0 - x \\ P_{22}(x,y) \text{ if } \sqrt{3}y > \ell_0 - x \end{cases} \text{ and} \qquad (49)$$

$$P_3(x,y) = \begin{cases} P_{31}(x,y) \text{ if } 2x \leqslant \ell_0 \\ P_{32}(x,y) \text{ if } 2x > \ell_0 \end{cases}$$

where

$$P_{11}(x,y) = \left(\frac{x}{2} + \frac{y}{2\sqrt{3}}, \frac{2y}{3}\right), \quad P_{12}(x,y) = \left(\frac{3x}{4} - \frac{y}{4\sqrt{3}}, \frac{x}{4\sqrt{3}} + \frac{5y}{12}\right),$$

$$P_{21}(x,y) = \left(\frac{x}{2} - \frac{y}{2\sqrt{3}} + \frac{\ell_0}{2}, \frac{2y}{3}\right),$$

$$P_{22}(x,y) = \left(\frac{3x}{4} + \frac{y}{4\sqrt{3}} + \frac{\ell_0}{4}, -\frac{x}{4\sqrt{3}} + \frac{5y}{12} + \frac{\ell_0}{4\sqrt{3}}\right),$$

$$P_{31}(x,y) = \left(\frac{x}{2} + \frac{\ell_0}{4}, -\frac{x}{2\sqrt{3}} + \frac{2y}{3} + \frac{\sqrt{3}\ell_0}{4}\right) \quad \text{and}$$

$$P_{32}(x,y) = \left(\frac{x}{2} + \frac{\ell_0}{4}, \frac{x}{2\sqrt{3}} + \frac{2y}{3} + \frac{\ell_0}{4\sqrt{3}}\right).$$

The six maps in Eq. (49) send the triangular shapes identified in Fig. 14 to the tessellation identified in the same figure. In forming maps by the composition approach it is possible to indentify how individual components compose without explicit reference to the inequalities identified in (49). For example (with reference to Fig. 14) in forming $\widehat{T}_2$ (say) the application P_1 is achieved through compositions $P_{11} \circ P_{11}$, $P_{11} \circ P_{21}$, $P_{11} \circ P_{22}$ and $P_{12} \circ P_{12}$ $P_{12} \circ P_{31}$ $P_{12} \circ P_{32}$ and similarly on application of P_2 and P_3.

The pre-fractal and the corresponding continuum domain produced by the maps in Eq. (48) and (49) are depicted in Figs. 15 and 16, respectively. Observe from Figs. 15 and 16 that the boundaries of the triangles are not fractal and $dA_k = dA_D$. The hole-fill maps in this case are much more involved and evidently inhomogeneous.

A.2. Sierpinski carpet

Similarly for the carpet the contraction maps are of the form:

$$S_i(x,y) = (x_i, y_i) + \left(\frac{x}{3}, \frac{y}{3}\right) \qquad (50)$$

where (x_i, y_i) refers to the coordinates of the bottom left corner points for $i = 1, \ldots, 8$.

Four of the continuum maps are identical to those defined in (50) apart from

$$P_2(x,y) = \begin{cases} P_{21}(x,y) & \text{if } y \geqslant 2x \text{ and } 2x \leqslant 1 \\ P_{22}(x,y) & \text{if } y \geqslant 2(1-x) \text{ and } 2x > 1 \\ P_{23}(x,y) & \text{otherwise} \end{cases}$$

$$P_4(x,y) = \begin{cases} P_{41}(x,y) & \text{if } 2y \leqslant x \text{ and } 2y \leqslant 1 \\ P_{42}(x,y) & \text{if } 2y \geqslant (2-x) \text{ and } 2y > 1 \\ P_{43}(x,y) & \text{otherwise} \end{cases}$$

$$P_5(x,y) = \begin{cases} P_{51}(x,y) & \text{if } 2y \leqslant 1-x \text{ and } 2y \leqslant 1 \\ P_{52}(x,y) & \text{if } 2y \geqslant 1-x \text{ and } 2y > 1 \\ P_{53}(x,y) & \text{otherwise} \end{cases}$$

$$P_7(x,y) = \begin{cases} P_{71}(x,y) & \text{if } y \leqslant 2-2x \text{ and } 2x \leqslant 1 \\ P_{72}(x,y) & \text{if } y \leqslant -1+2x \text{ and } 2x > 1 \\ P_{73}(x,y) & \text{otherwise} \end{cases} \qquad (51)$$

where

$$P_{21}(x,y) = \left(\frac{1}{3} + \frac{x}{3}, \frac{1}{3} + \frac{y}{3}\right), \ P_{22}(x,y) = \left(\frac{1}{3} + \frac{x}{3}, \frac{1}{3} - \frac{x}{3} + \frac{y}{3}\right),$$

$$P_{23}(x,y) = \left(\frac{x}{2}, \frac{1}{3} + \frac{y}{3}\right)$$

$$P_{41}(x,y) = \left(\frac{1}{3} + \frac{x}{3}, \frac{1}{3} + \frac{y}{3}\right), \ P_{42}(x,y) = \left(\frac{1}{3} + \frac{x}{3} - \frac{y}{3}, \frac{1}{3} + \frac{y}{3}\right),$$

$$P_{43}(x,y) = \left(\frac{x}{2}, \frac{1}{3} + \frac{y}{3}\right)$$

$$P_{51}(x,y) = \left(\frac{2}{3} + \frac{x}{3} - \frac{y}{3}, \frac{1}{3} + \frac{y}{3}\right), \ P_{52}(x,y) = \left(\frac{1}{3} + \frac{x}{3} + \frac{y}{3}, \frac{1}{3} + \frac{y}{3}\right),$$

$$P_{53}(x,y) = \left(\frac{1}{2} + \frac{x}{2}, \frac{1}{3} + \frac{y}{3}\right)$$

$$P_{71}(x,y) = \left(\frac{1}{3} + \frac{x}{3}, \frac{2}{3} - \frac{x}{3} + \frac{y}{3}\right), \ P_{72}(x,y) = \left(\frac{1}{3} + \frac{x}{3}, \frac{1}{3} - \frac{x}{3} + \frac{y}{3}\right),$$

$$P_{73}(x,y) = \left(\frac{1}{3} + \frac{x}{3}, \frac{1}{2} + \frac{y}{2}\right) \qquad (52)$$

It is apparent from the definition of the continuum maps that the four maps in Eq. (51) are constructed with three linear parts. The effect of the maps is illustrated in Fig. 17, where it is apparent that significant element shearing is necessary to hole-fill and create a continuum. As with the Sierpinski Gasket the boundary is not Fractal and $dA_k = dA_D$.

References

[1] Li Q, Flamant G, Yuan X, Neveu P, Luo L. Compact heat exchangers: a review and future applications for a new generation of high temperature solar receivers. Renew Sustain Energy Rev 2011;15(9):4855–75.
[2] Mancin S, Zilio C, Cavallini A, Rossetto L. Pressure drop during air flow in aluminum foams. Int J Heat Mass Transf 2010;53(15–16):3121–30.
[3] Boomsma K, Poulikakos D, Zwick F. Metal foams as compact high performance heat exchangers. Mech Mater 2003;35(12):1161–76.
[4] Bhouri M, Goyette J, Hardy BJ, Anton DL. Honeycomb metallic structure for improving heat exchange in hydrogen storage system. Int J Hydrog Energy 2011;36(11):6723–38.
[5] Teamah MA, El-Maghlany WM, Dawood MMK. Numerical simulation of laminar forced convection in horizontal pipe partially or completely filled with porous material. Int J Therm Sci 2011;50:1512–22.
[6] Dorea FT, de Lemos MJS. Simulation of laminar impinging jet on a porous medium with a thermal non-equilibrium model. Int J Heat Mass Transf 2010;53:5089–101.
[7] Bejan A. Porous media. Heat Mass Transf Handb 2003:1131–80.
[8] Cai J, Huai X. Study on fluid–solid coupling heat transfer in fractal porous medium by lattice Boltzmann method. Appl Therm Eng 2010;30(6–7): 715–23.
[9] H. Darcy. Les fontaines publiques de la ville de dijon, 1856.
[10] Brinkmann HC. On the permeability of media consisting of closely packed porous particles. Appl Sci Res 1948;A1:81–6.
[11] Nithiarasu P, Seetharamu KN, Sundararajan T. Natural convective heat transfer in an enclosure filledwith fluid saturated variable porosity medium. Int J Heat Mass Transf 1997;40:3955–67.
[12] Mandelbrot BB. The fractal geometry of nature. W.H. Freeman & Co Ltd.; 1982.
[13] Tarasov VE. Continuous medium model for fractal media. Phys Lett, Sect A: Gener Atom Solid State Phys 2005;336(2–3):167–74.
[14] Tarasov VE. Fractional hydrodynamic equations for fractal media. Ann Phys 2005;318(2):286–307.
[15] Ostoja-Starzewski M. Towards thermomechanics of fractal media. Zeitschrift fur Angewandte Mathematik und Physik 2007;58(6):1085–96.
[16] Ostoja-Starzewski M. Towards thermoelasticity of fractal media. J Therm Stress 2007;30(9–10):889–96.
[17] Ostoja-Starzewski M. Extremum and variational principles for elastic and inelastic media with fractal geometries. Acta Mech 2009;205(1–4):161–70.
[18] Carpinteri A, Cornetti P. A fractional calculus approach to the description of stress and strain localization in fractal media,. Chaos Solitons Fractals 2001;13(1):85–94.
[19] Carpinteri A, Cornetti P, Sapora A. Static-kinematic fractional operators for fractal and non-local solids. ZAMM Zeitschrift fur Angewandte Mathematik und Mechanik 2009;89(3):207–17.

[20] Carpinteri A, Chiaia B, Cornetti P. The elastic problem for fractal media: basic theory and finite element formulation. Comput Struct 2004;82(6): 499–508.

[21] Li S, Wang Y, Liu Y, Sun W. Estimation of thermal conductivity of porous material with FEM and fractal geometry. Int J Modern Phys C 2009;20(4):513–26.

[22] Zhi X, Yong W, Yimin W. Prediction of the effective thermal conductivity of graphitic foam using a fractal model. Cell Polym 2008;27(5):313–21.

[23] Davey K, Prosser R. Analytical solutions for heat transfer on fractal and pre-fractal domains. Appl Math Model 2013;37(1–2):554–69.

[24] Barnsley PM. Fractals everywhere, 2nd revised edition. AP Professional; 1993.

Chapter 4.
Paper 2: TESSELLATED CONTINUUM MECHANICS: A GALERKIN FINITE ELEMENT METHOD

In this chapter, hole-fill concept is applied to create relative tessellations for pre-fractals. Transport theory and partial differential equations are applied to connect the pre-fractal to its corresponding tessellated construction. Thus, the material properties for the tessellations can be obtained. Weighted transport equations are introduced in order to use the Galerkin finite element method on the tessellations. Simple Cantor dust and several non-product fractals are all considered to test the approach.

Mapped temperature distributions on pre-fractals are obtained from the temperature distributions on the corresponding tessellations. Mesh refinement is achieved through increasing the number of tiles on the original set of the pre-fractal. Despite of a small modelling error, all the results show high accuracy for the tessellated approach.

The hole-filling maps were improved upon by C. Jiang who also generated the thermal-conductivity distributions presented here. The tests performed were designed by K. Davey and C. Jiang. The thermal responses portrayed in the chapter were obtained by C. Jiang. The manuscript was written by K. Davey and C. Jiang, with technical and editorial supervision and proofing provided by R. Prosser.

Tessellated continuum mechanics: A Galerkin finite element method

K. Davey *, C. Jiang, R. Prosser

School of Mechanical, Aerospace and Civil Engineering, The University of Manchester, United Kingdom

ARTICLE INFO

ABSTRACT

This paper tests the hypothesis that the tessellation used in tessellated continuum mechanics can form a mesh in a continuous Galerkin finite element method. Although the tessellation is not unique, neither is it arbitrary, and its construction imposes constraints on any numerical analysis. A distinctive feature of the tessellation is that it can possess highly distorted elements yet—as a consequence of associated anisotropy in material properties—can still return accurate results.

The numerical procedure is tested on classical fractal porous geometries to demonstrate the potential of the method, and also illustrate the capability for analysis of disparate porous materials on continua.

© 2016 Elsevier Ltd. All rights reserved.

1. Introduction

Porous materials are widespread in nature and can take on various forms; examples include biological tissue such as wood, cork and bone. Rocks and soils also often contain natural porous structures that may act as gas and oil reservoirs; as such, these structures are of particular interest to petrochemical industry, where there is currently much activity driving developments in *fracking*. Porous materials are also studied in diverse branches of modern engineering such as impact mechanics [1], fluid mechanics [2], poromechanics [3] and Printed Circuit Board (PCB) heat exchanger design [4]. This latter application exploits the porous structure to maximise the fluid contact area, and many porous heat exchangers embody this geometry through high thermal conductivity metallic foams such as copper and aluminium [5]. These are recognised to be an excellent choice for enhancing heat transfer, since they possess a large fluid-solid contact surface area, high thermal conductivities and provide good enhancement of fluid mixing [6]. Heat transfer provides a strong driver for the work described in this paper.

Although heat exchanger performance is enhanced by exploiting porous material, the heat transfer analysis itself faces serious difficulties arising principally from the complex geometry involved. The transport of heat and mass through porous media has received much attention for many decades in a wide variety of fields [7,8]; such approaches are indirect in that a continuum approach is retained, with the influence of the cellular structure relegated to coarse grained parameters such as permeability and porosity. Clearly such models are unable to capture any effects arising from refined changes in cellular designs. To incorporate more refined structures, Lattice Boltzmann Methods have been proposed as a possible way around the purely classical continuum description; Yan Su et al. [9] for example has performed comparison studies between direct and porous medium model heat exchangers. The coupling of discrete lattice models—which account for interactions between voids or particles via local potentials—with continuum models (e.g. quasi-continuum models [10]) is an area of active research [11]. The idea underpinning these types of approaches is the establishment of an appropriate continuum representation, where the material-constitutive response is informed by the lattice model. Although such approaches advance the analysis they are evidently restricted by the extraordinarily complex geometries involved, and are therefore unlikely to capture the complex flow and heat transfer physics in practical porous medium heat exchanger designs.

An alternative approach is to utilise the mathematics of fractal geometry [12] and/or involve extensions to traditional calculus by involving fractional derivatives or other such mathematical devices. Transport approaches involving fractals and fractional derivatives have been considered by Tarasov [13,14] and Ostoja-Starzewski [15,16]. Their approaches are untested and physically unrealisable, since they are founded upon transport forms that do not readily arise from the underpinning physics. More recently, a fractional differential equation has been investigated by Salvatore et al. [17] with the aim of establishing a more definitive connection between fractional calculus and fractal geometry. Similarly, Gianluca et al. [18] investigated fractal-porous materials founded on classical fractals, including the Cantor dust, Sierpinski carpet and the Sierpinski gasket using a fractional-order transport

equation. It is transparent from the literature that most theories involving fractional derivatives have limited physical basis and offer little advance on classical parameter-continuum theory.

The approach adopted in this paper has at its foundation a classical control volume representation of the underlying physics. Transport equations in an integral (Euler) form are used in the analysis since integration—if correctly defined—readily caters for the discontinuous physics associated with fractals. The transport methodology is based on the existence of maps linking pre-fractals with the continuum which, in turn, is founded on the continuum hypothesis. These maps are named *hole-fill* maps due to the role they play in closing the pores in any fractal cellular representation to produce a tessellated continuum. We term the whole procedure of hole-fill, tessellated continua and subsequent analysis with transport equations as *tessellated continuum mechanics.*

Although the task of establishing hole-fill maps appears complex, a novel procedure introduced in Ref. [19] (and improved upon here) provides a straightforward route to obtain such constructions. The tessellated continuum—which forms an associated mesh in a Galerkin finite element analysis—is constructed in a process that essentially mirrors the fractal construction process itself. Thus, a fractal constructed through the iteration of *n* contraction maps also has *n* maps for the iterated construction of the tessellated continuum. The hole-fill maps can be constructed either by means of function composition or (more directly) by identifying the corresponding elements of a fractal with elements in the tessellated continua. The former is more suited for analytical work, with the latter suited to numerical analysis. For analytical work, the former approach is more suitable, since the requirement for the precise form of the governing partial differential equations can be elegantly established by means of the hole-fill map and the integral transport equations. For numerical analysis however, weighted forms of the transport equations can be established and immediately applied using the second approach, without recourse to partial differential equations. One of the novel contributions of this paper is to establish a finite element method on a tessellated continuum. We limit attention in this paper to a Galerkin formulation as this permits a commercial code to be readily employed. However, the appearance in the new approach of energy flux related terms at element edges—when coupled to the Galerkin formulation—limits the choice of fluid to those that are highly conducting and unable to support a temperature difference perpendicular to the direction of fluid flow. This does mean however that a modelling error [20,21] is present, which cannot be removed by means of mesh refinement. It is demonstrated in the paper that for the heat-exchanger problems considered that the modelling error is relatively small.

Other numerical methods (with or without elements [22–25]) could in principle be applied to solve the problems considered here. This could be done in one of two ways, i.e. by performing a numerical analysis on the tessellation (and mapping the results) or on the porous medium directly. No papers presently exist for analysis on a tessellation (as this paper is the first) but many methods have been applied to porous media [26–30], although these are limited to the solution of equations involving indirect representations of the geometry. There also exists a range of computational techniques for the efficient analysis of problems where the physical response is characterised by the size of the structure and the size of some underlying localised microscopic phenomena. The homogenisation approach [31] (which also capture the effect of geometry indirectly) can often be employed to analyse these types of problems and a computationally efficient approach can typically involve decomposition methods (see for example Refs. [32,33]).

This paper demonstrates an application of the Galerkin finite element method to a tessellated continuum to capture the energy transfers taking place on pre-fractal structures with applications to cellular heat exchangers. To achieve this, the general transport theory for pre-fractals and tessellated continua is presented in Section 2, where the physics of the two domains are related by the assumed existence of a hole-fill map. This is followed by the introduction to weighted transport equations in Section 3 and the establishment of the Galerkin finite element method for tessellated continua providing a convenient vehicle for numerical analysis of cellular designs. The whole procedure depends intimately on the tessellated continuum structure which is generated by means of a recursive method closely replicating the fractal generation process. Material properties for non-product fractals are considered in Section 4 along with corresponding tessellations. Of particular focus is the relationship between material properties on a tessellation and its relationship between corresponding pre-fractals. The tessellated finite element analysis method is introduced in Section 5 via some simple 1-D fractals; analytical 1-D solutions are obtained and contrasted against numerical predictions on different (but equivalent) tessellations. The process is repeated in Section 6 for product tessellations. In Section 7, thermal analysis is performed on non-product sets and predictions are contrasted with results obtained from the commercial package ABAQUS.

2. Tessellated continuum mechanics

The idea underpinning the tessellated approach is the assumed existence of a map (a *hole-fill* map) from a pre-fractal $\widehat{E}_k$ (which can be formed by the kth iterations of an Iteration Function Scheme (IFS) [34]) to a tessellation $\widehat{T}_k$ (which also can be formed in a similar fashion). Typical tessellations for some classical fractals are depicted in Figs. 1 and 2. The arrows depicted in the figures identify a corresponding selection of pre-fractal elements and tiles and it is important to appreciate that all pre-fractal elements have corresponding tiles. Physics taking place on $\widehat{E}_k$ is best represented in a weak sense using transport equations in integral form as these readily capture the highly discontinuous nature of the problem under consideration. Transport equations apply physical conservation laws to a control volume (identified here by Ω_s), within which the pre-fractal $\widehat{E}_k$ is at least in part embedded. A control volume is a continuous open set of points whose closure includes a continuous orientable boundary Γ_s. A typical transport equation for a stationary control volume takes the form

$$\frac{d}{dt}\int_{\Omega_s}\rho_s\psi_s dV_s + \int_{\Gamma_s}\rho_s\psi_s\underline{v}_s\cdot d\Gamma_s = -\int_{\Gamma_s}\underline{J}_s\cdot d\Gamma_s + \int_{\Omega_s}\rho_s b_s dV_s, \quad (1)$$

where ψ is a specific field variable, ρ is density, $\underline{v}$ is the material velocity, $\underline{n}$ is an outward pointing unit normal, $d\Gamma = \underline{n}d\Gamma$, $\underline{J}\cdot\underline{n}$ is a flux, b is a source term and subscript s is used to indicate quantities in the physical space. It is assumed here that the fractal $\widehat{E}_k$ is not deforming although it is noted in passing that transport theory can readily account for such a scenario.

The pre-fractal $\widehat{E}_k$ is assumed to support mass and given that Ω_s can be made arbitrarily small it is possible that $\widehat{E}_k \cap \Omega_s = \Phi$, i.e. the intersection of the control volume and pre-fractal can under certain conditions be empty. This can happen in a situation where a control volume fits in a pore for example. Thus, in order to ensure the validity of Eq. (1) for arbitrary Ω_s some care is required particularly with flux terms; the absence of mass readily removes domain integrals but not necessarily the flux integral.

With the assumed existence of a tessellation $\widehat{T}_k$ it can be assumed further that there exists a similar transport equation for the stationary control volume Ω_r in which the tessellation $\widehat{T}_k$ is embedded. The transport equation for Ω_r is
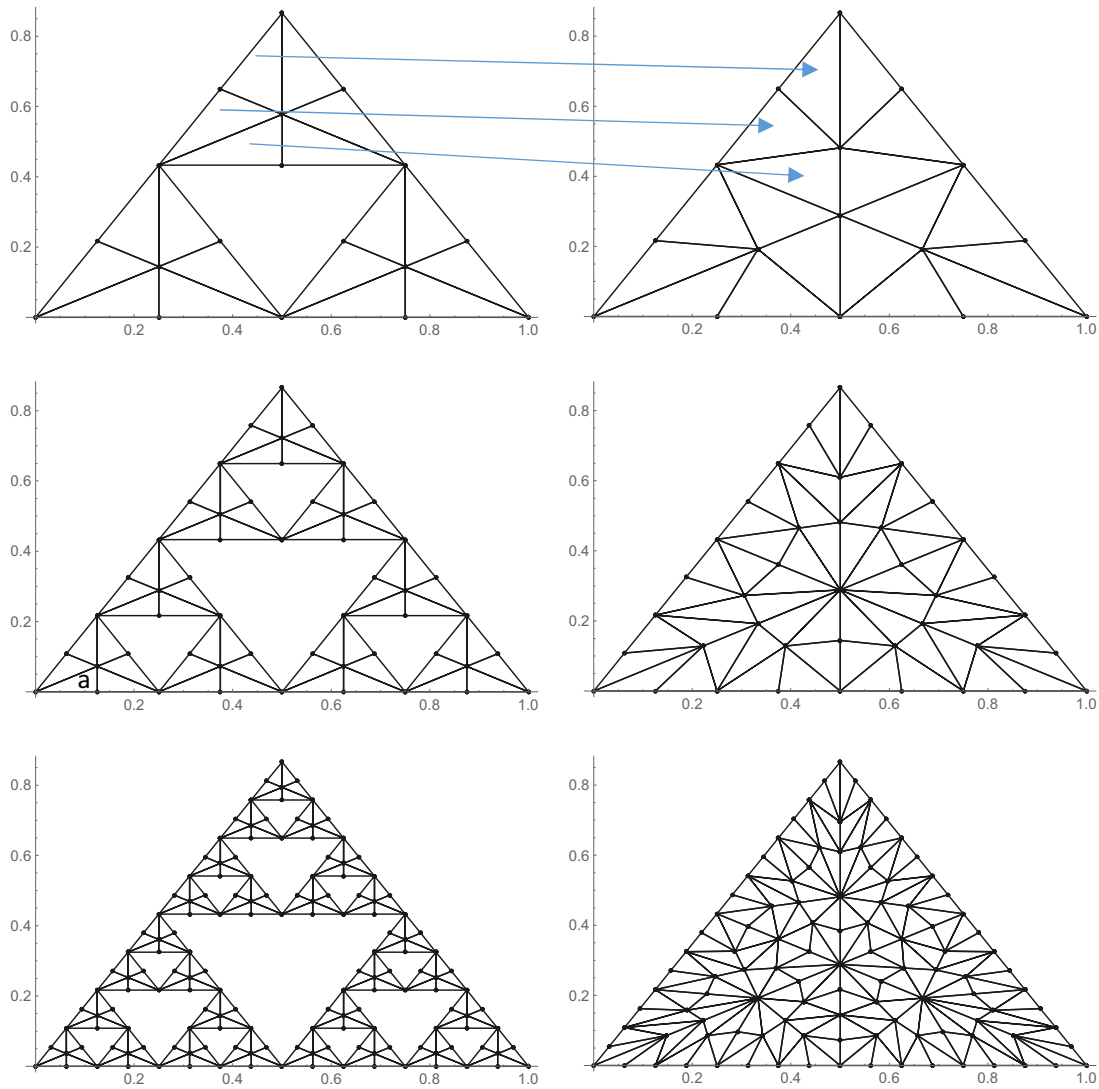
Fig. 1. Pre-fractal and corresponding tessellated domains for the Sierpinski Gasket.

$$\frac{d}{dt} \int_{\Omega_r} \rho_r \psi_r dV_r + \int_{\Gamma_r} \rho_r \psi_r \underline{v}_r \cdot d\Gamma_r = - \int_{\Gamma_r} \underline{J}_r \cdot d\Gamma_r + \int_{\Omega_r} \rho_r b_r dV_r \quad (2)$$

where subscript r is used to indicate quantities in the tessellation space.

Eq. (1) can be related to Eq. (2) via the hole-fill map $\boldsymbol{x} : \boldsymbol{s} \mapsto \boldsymbol{x}$. Geometrical considerations give rise to Nanson's differential relationships: $dV_r = |\boldsymbol{F}| \mu_k dV_s$, $d\Gamma_r = |\boldsymbol{F}| \mu_k^\Gamma d\Gamma_s \cdot \boldsymbol{F}^{-1}$, where $F_{ij} = \partial x_i / \partial s_j$, $d\Gamma_s = \underline{n}_s d\Gamma_s$ and $d\Gamma_r = \underline{n}_r d\Gamma_r$, and where μ_k is a support on $\widehat{E}_k$ and μ_k^Γ is a support on Γ_s. It is important to appreciate that certain fluxes do not involve mass (e.g. radiation heat transfer), so μ_k^Γ is not necessarily equal to μ_k on Γ_s. Support functions generally take on values of 1 or 0, with 1 identifying elements belonging to the set of interest. In this analysis control volumes Ω_s and Ω_r are related by an identity map $\boldsymbol{i} : \boldsymbol{s} \mapsto \boldsymbol{s}$ and by design conserved quantities are required to match on the sets $\widehat{E}_k \cap \Omega_s$ and $\widehat{T}_k \cap \Omega_s$, where $\widehat{T}_k = x(\widehat{E}_k)$. To achieve this, consider the substitution of Nanson's identities into Eq. (1):

$$\frac{d}{dt} \int_{\Omega_s} \rho_r \psi_r |\boldsymbol{F}| \mu_k dV_s + \int_{\Gamma_s} \rho_r |\boldsymbol{F}| \psi_r \mu_k (\boldsymbol{F}^{-1} \cdot \underline{v}_r) \cdot d\Gamma_s$$

$$= - \int_{\Gamma_s} |\boldsymbol{F}| \mu_k^\Gamma (\boldsymbol{F}^{-1} \cdot \underline{J}_r) \cdot d\Gamma_s + \int_{\Omega_s} \rho_r |\boldsymbol{F}| \mu_k b_r dV_s \quad (3)$$

Greater generality can be obtained on multiplication of Eq. (3) by a scalar (or by a matrix if ψ_r is a vector); this is not required for analysis limited to heat transfer, so is not considered further here. Thus, in view of the requirement for mass conservation, which takes the form $\rho_r dV_r = \rho_s dV_s$, it follows that $\rho_r |\boldsymbol{F}| = \rho_s$ and matching of the two terms on the left hand-side of Eqs. (3) and (1) is achieved with $\psi_r = \psi_s$ and $(\boldsymbol{F}^{-1} \cdot \underline{v}_r) = \underline{v}_s$. Similarly, the right-hand sides of Eqs. (3) and (1) match with the definitions $|\boldsymbol{F}| \boldsymbol{F}^{-1} \cdot \underline{J}_r = \underline{J}_s$ and $b_r = b_s$. The support functions are dropped for convenience since by design a tessellation is free of porosity, so $\mu_k = 1$ almost everywhere on a tessellation. In the subsequent development of the approach, the general theory presented is restricted to the case of heat transfer, where the field variable is specific enthalpy (i.e. $\psi_s = h_s$) and the flux term is heat flux (i.e. $\dot{q}_s \cdot \underline{n}_s = \underline{J}_s \cdot \underline{n}_s$). To keep the presentation as clear as possible with reference to cellular systems, convection is not considered in this work (i.e. $\underline{v}_s = \underline{0}$).

2.1. Heat transfer through a tessellation

The transport equation for transient heat transfer is

$$\frac{d}{dt} \int_{\Omega_s} \rho_s h_s dV_s = - \int_{\Gamma_s} \dot{\underline{q}}_s \cdot d\Gamma_s + \int_{\Omega_s} \rho_s \dot{Q}_s dV_s, \quad (4)$$
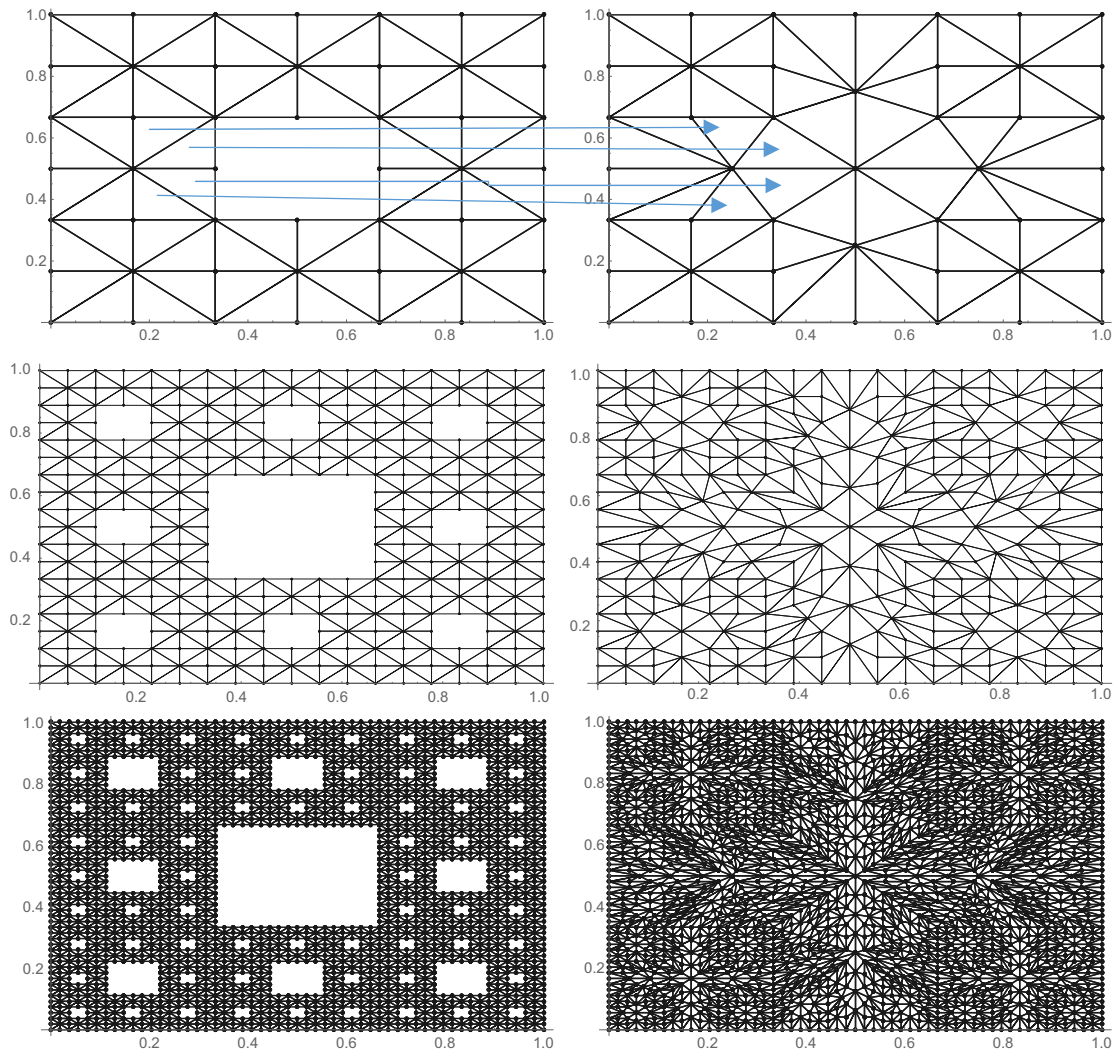
Fig. 2. Pre-fractal and corresponding tessellated domains for the Sierpinski Carpet.

$$K_s = \begin{bmatrix} 1 & 0 \\ 0 & 1 \end{bmatrix}$$

$$K_r = \begin{bmatrix} 1.5833 & 1.3472 \\ 1.3472 & 1.7778 \end{bmatrix}$$

Fig. 3. Stretching and change of thermal conductivity in hole-filling map for triangle "a" in Fig. 1.

where $\dot{Q}_s$ is a heat source and the heat flux is defined here (given its practical ubiquity) as $\underline{\dot{q}}_s \cdot n_s = \hat{h}_s(T_s - T_\infty)$, and where $\hat{h}_s$ is a heat transfer coefficient and T_∞ is the bulk temperature of the cooling/heating medium.

The equivalent equation on the tessellated domain is

$$\frac{d}{dt}\int_{\Omega_r} \rho_r h_r dV_r = -\int_{\Gamma_r} \underline{\dot{q}}_r \cdot d\Gamma_r + \int_{\Omega_r} \rho_r \dot{Q}_r dV_r \tag{5}$$

where $\rho_r = |\boldsymbol{F}|^{-1}\rho_s$, $h_r = h_s$, $\dot{Q}_r = \dot{Q}_s$ and $\underline{\dot{q}}_r = |\boldsymbol{F}|^{-1}\boldsymbol{F}\cdot\underline{\dot{q}}_s$. The latter definition provides convective heat transfer boundary conditions of the form:

$$\underline{\dot{q}}_r \cdot d\Gamma_r = \hat{h}_r(T_r - T_\infty)d\Gamma_r = |\boldsymbol{F}|^{-1}(\boldsymbol{F}\cdot\underline{\dot{q}}_s)\cdot(|\boldsymbol{F}|d\Gamma_s\cdot\boldsymbol{F}^{-1})$$
$$= \hat{h}_s(T_s - T_\infty)d\Gamma_s, \tag{6}$$

which is satisfied for $T_r = T_s$ and $\hat{h}_r d\Gamma_r = \hat{h}_s d\Gamma_s$.

Note that the equality $T_s = T_r$ means $T_s(\boldsymbol{s},t) = T_r(\boldsymbol{x}(\boldsymbol{s}),t)$, which gives $\nabla_s T_s = \boldsymbol{F}^T \cdot \nabla_r T_r$, and in view of the identity $\underline{\dot{q}}_r = |\boldsymbol{F}|^{-1}\boldsymbol{F}\cdot\underline{\dot{q}}_s$ leads to $\underline{\dot{q}}_r = -\boldsymbol{K}_r\cdot\nabla_r T_r$ where the associated conductivity tensor $\boldsymbol{K}_r$ on the tessellated domain is

$$\boldsymbol{K}_r = |\boldsymbol{F}|^{-1}\boldsymbol{F}\boldsymbol{K}_s\boldsymbol{F}^T \tag{7}$$

which, for isotropic (or indeed, orthotropic) $\boldsymbol{K}_s$, gives rise to an orthotropic $\boldsymbol{K}_r$.

This property arises from the fact that $\boldsymbol{K}_r$ is evidently symmetric and positive definite, hence giving rise to at most three distinct positive conductivities in orthogonal directions.

3. The tessellated finite element method

The finite element method can be derived in one of three ways: direct minimisation of a functional (e.g. minimisation of potential energy); A variational statement, provided one exists for the problem (e.g. Hamilton's principle) and; the weighted residual method applied to the governing partial differential equations. A fourth approach has arisen in the literature [35], which avoids the use of the governing partial differential equation, *provided* a transport equation is available. The approach involves the direct weighting of the transport equation which, on application to Eq. (4) gives

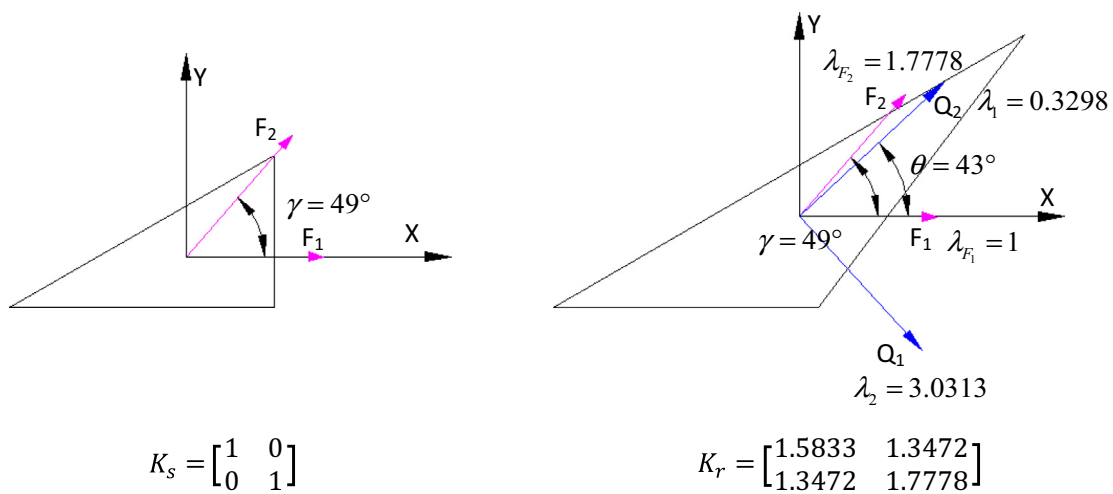$$\frac{d}{dt}\int_{\Omega_s} W_s \rho_s h_s dV_s = -\int_{\Gamma_s} W_s \underline{\dot{q}}_s \cdot d\Gamma_s + \int_{\Omega_s} \nabla_s W_s \cdot \underline{\dot{q}}_s dV_s$$
$$+ \int_{\Omega_s} W_s \rho_s \dot{Q}_s dV_s, \tag{8}$$

where W_s is a weighting function which in the first instance is assumed continuous at least up to the first derivative, i.e. $W_s \in C^1(\Omega_s)$ and is independent of time, i.e. $\partial W_s/\partial t = 0$. A similar equation is assumed to exist for the tessellation

$$\frac{d}{dt}\int_{\Omega_r} W_r \rho_r h_r dV_r = -\int_{\Gamma_r} W_r \underline{\dot{q}}_r \cdot d\Gamma_r + \int_{\Omega_r} \nabla_r W_r \cdot \underline{\dot{q}}_r dV_r$$
$$+ \int_{\Omega_r} W_r \rho_r \dot{Q}_r dV_r \tag{9}$$

which, after substitution of Nanson's identities and $\rho_r = |\boldsymbol{F}|^{-1}\rho_s$, $h_r = h_s$, $\dot{Q}_r = \dot{Q}_s$, $\underline{\dot{q}}_r = |\boldsymbol{F}|^{-1}\boldsymbol{F}\cdot\underline{\dot{q}}_s$ and $\nabla_s \equiv \boldsymbol{F}^{-T}\cdot\nabla_r$ gives

$$\frac{d}{dt}\int_{\Omega_s} W_r \rho_s h_s \mu_k dV_s = -\int_{\Gamma_s} W_r \mu_k^\Gamma \underline{\dot{q}}_s \cdot d\Gamma_s$$
$$+ \int_{\Omega_s} \nabla_s W_r \cdot \boldsymbol{F}^{-1}\boldsymbol{F}\cdot\underline{\dot{q}}_s \mu_k dV_s + \int_{\Omega_s} W_r \mu_k \dot{Q}_s dV_s \tag{10}$$

which is identical to Eq. (8) on setting $W_r = W_s$.

The finite element method applied to an element in the tessellation $\widehat{T}_k$ immediately follows, i.e.

$$\frac{d}{dt}\int_{\Omega_r^e} N_i \rho_r h_r dV_r = -\int_{\Gamma_r^e} N_i \underline{\dot{q}}_r \cdot d\Gamma_r - \int_{\Omega_r^e} \nabla_r N_i \cdot \boldsymbol{K}_r \cdot \nabla_r T_r dV_r$$
$$+ \int_{\Omega_r^e} N_i \rho_r \dot{Q}_r dV_r \tag{11}$$

where N_i is a shape function and Ω_r^e is an element in $\widehat{T}_k$; tessellated elements and finite elements are assumed identical in this paper.

While it is usual for $N_i \in C^\infty(\Omega_r^e)$, the weight function typically satisfies $W_r \in H^1(\Omega_r)$ if approximated using shape functions. This means that continuity of the first derivative is only weakly enforced at element boundaries. Continuity at element boundaries is assumed to apply for both the weighting and the temperature field. This assumption is convenient because it permits analysis with classical Galerkin finite elements but places limitations on the types of analysis that can be reasonably attempted. Any cooling medium passing through a porous structure is required to be a perfect conductor, which essentially means no temperature gradients are permitted perpendicular to the channel flow direction. If temperature gradients are present in the cooling medium, then the analysis becomes approximate. A feature of performing any analysis on a tessellation is the absence of pores; heat sources or sinks appear at element edges/surfaces in the tessellation to replicate their effect. This aspect is captured by the first term on the right hand side of Eq. (11).

In the following sections, the behaviour of thermal conductivity on individual tiles and tessellations is examined. The geometric complexity apparent in the fractal is manifestly absent on a tessellation, yet is found to re-emerge in the distribution of thermal conductivity. This finding is then exploited through heat transfer exemplars on relatively simple classical fractals embedded in 1-D and 2-D spaces.

4. Understanding material behaviour on tessellations

As a consequence of $h_r = h_s$ and $T_r = T_s$ (as established in Section 2) it follows that the specific heat satisfies $c_r = c_s$. Density follows $\rho_r = |\boldsymbol{F}|^{-1}\rho_s$ and therefore, for corresponding pre-fractals and tiles, scales in accordance with their volumes (in 3D) and areas (in 2D).

The behaviour of the conductivity (Eq. (7)) is less straightforward and depends on the principal stretch directions associated with the deformation tensor $\boldsymbol{F}$. The conductivity tensor $\boldsymbol{K}_r$ is positive definite and symmetric, so can be represented by a Schur decomposition $\boldsymbol{K}_r = \boldsymbol{Q}\boldsymbol{D}\boldsymbol{Q}^T$, where $\boldsymbol{Q}$ has eigenvectors as columns and is orthogonal (i.e. $\boldsymbol{Q}^T\boldsymbol{Q} = \boldsymbol{I}$) and $\boldsymbol{D}$ is a diagonal matrix whose eigenvalues (principal values of thermal conductivity) lay on the principal diagonal. Suppose now that $\boldsymbol{F}$ can decomposed into: the eigen-decomposition $\boldsymbol{F} = \boldsymbol{S}\boldsymbol{D}_F\boldsymbol{S}^{-1}$ (assuming $\boldsymbol{F}$ is diagonalisable) and; the $\boldsymbol{Q}_F\boldsymbol{R}$ decomposition (which always exists), where $\boldsymbol{S}$ has eigenvectors as columns, $\boldsymbol{D}_F$ is a diagonal matrix with eigenvalues on the principal diagonal, $\boldsymbol{Q}_F$ is an orthogonal matrix and $\boldsymbol{R}$ is an upper triangular matrix. Direct substitution of each decomposition into the definition of the conductivity tensor gives $\boldsymbol{K}_r = |\boldsymbol{R}|^{-1}\boldsymbol{Q}_F[\boldsymbol{R}\boldsymbol{K}_s\boldsymbol{R}^T]\boldsymbol{Q}_F^T$ and $\boldsymbol{K}_r = |\boldsymbol{D}_F|^{-1}(\boldsymbol{S}\boldsymbol{D}_F)[\boldsymbol{S}^{-1}\boldsymbol{K}_s\boldsymbol{S}^{-T}](\boldsymbol{S}\boldsymbol{D}_F)^T$, which simplifies significantly if $\boldsymbol{D}_F = \lambda\boldsymbol{I}$ to $\boldsymbol{K}_r = \lambda\boldsymbol{K}_s$ with λ being identified as a stretch ratio. Thus, for isotropic stretching with $\lambda > 1$, thermal conductivity increases in proportion to the amount of stretching taking place. In effect, thermal conductivity increases to mitigate increasing thermal resistance due to the presence of additional material. If however, $\boldsymbol{F} = \boldsymbol{Q}_F\boldsymbol{\mathcal{D}}$, where $\boldsymbol{\mathcal{D}}$ is a diagonal matrix, then $\boldsymbol{K}_r = |\boldsymbol{\mathcal{D}}|^{-1}\boldsymbol{Q}_F[\boldsymbol{\mathcal{D}}\boldsymbol{K}_s\boldsymbol{\mathcal{D}}^T]\boldsymbol{Q}_F^T$, which is nothing more than
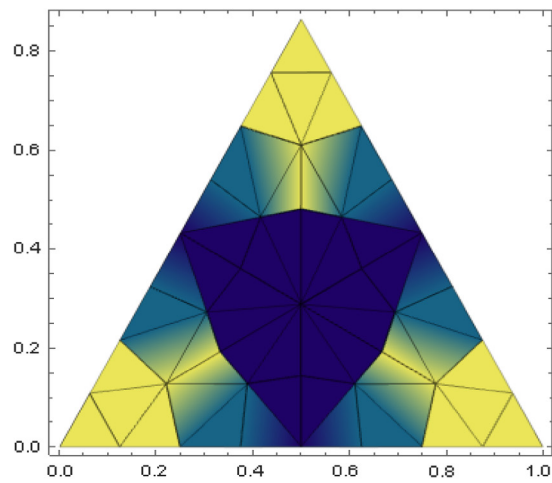
(i) Contours on $\hat{T}_2$
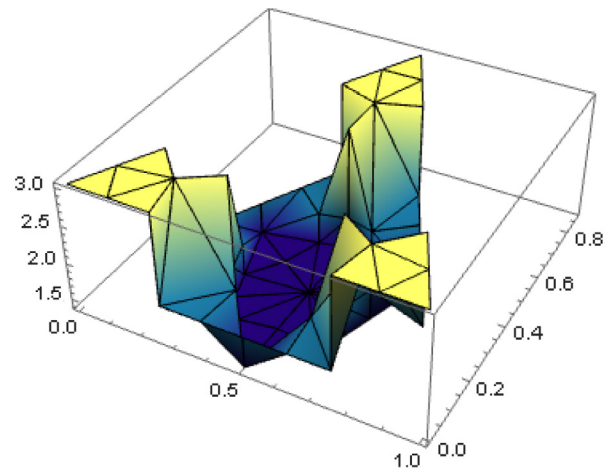
(ii) Graph on $\hat{T}_2$
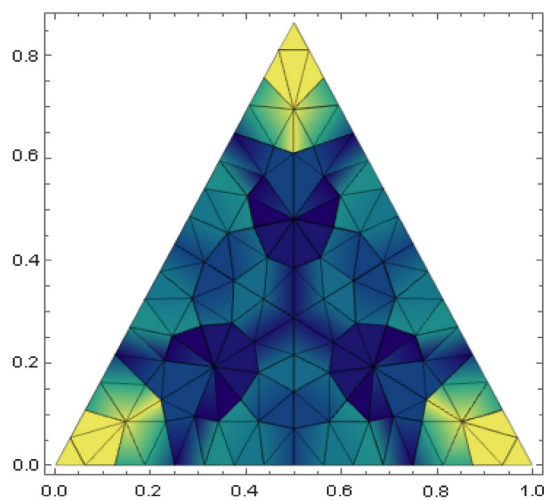
(iii) Contours on $\hat{T}_3$
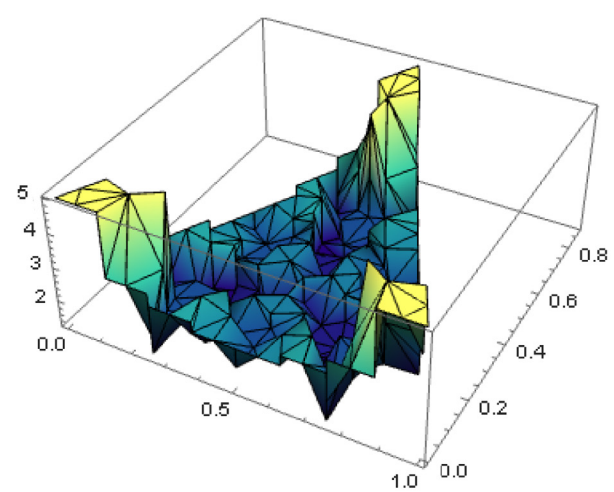
(iv) Graph on $\hat{T}_3$
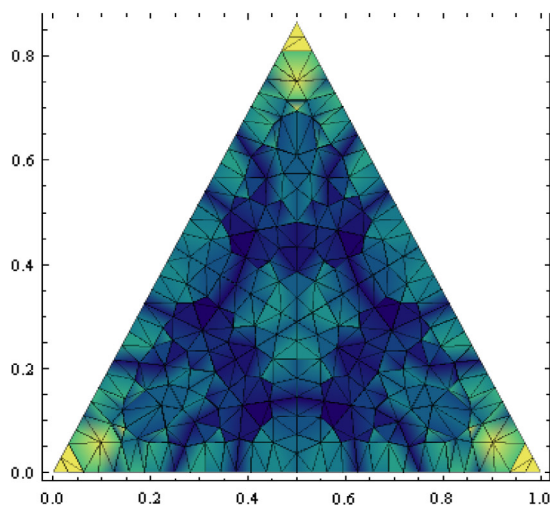
(v) Contours on $\hat{T}_4$
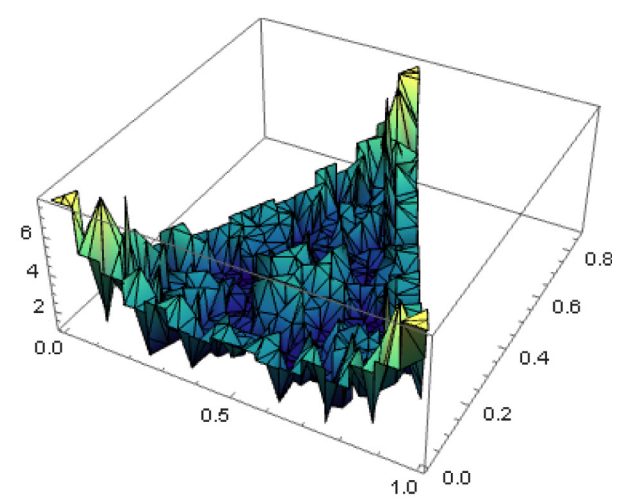
(vi) Graph on $\hat{T}_4$

Fig. 4. Principal thermal conductivity ratio (K_r/K_s) distribution on Sierpinski-gasket tessellations.
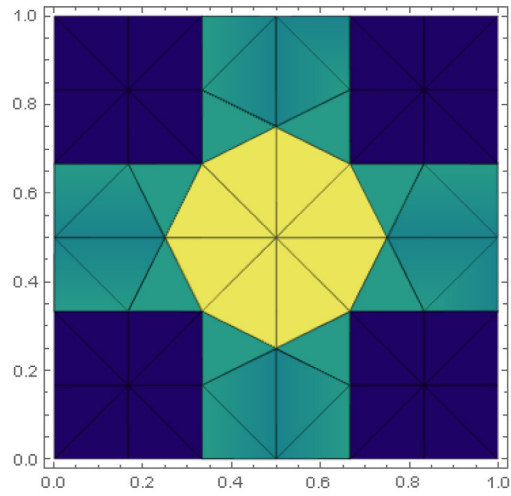
(i) Contours on $\hat{T}_1$
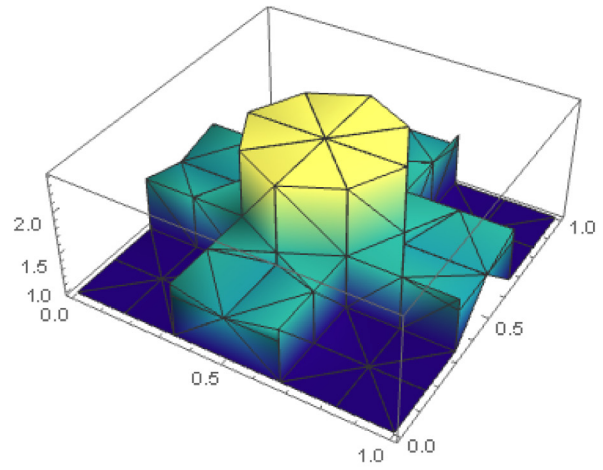
(ii) Graph on $\hat{T}_1$
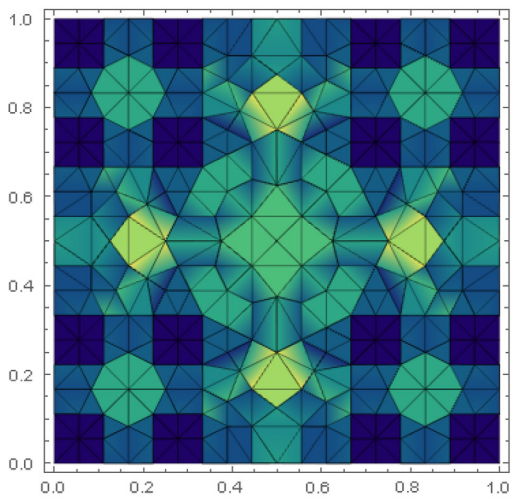
(iii) Contours on $\hat{T}_2$
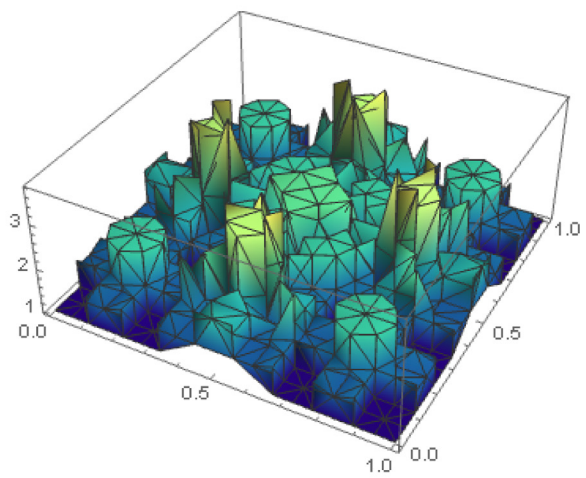
(iv) Graph on $\hat{T}_2$
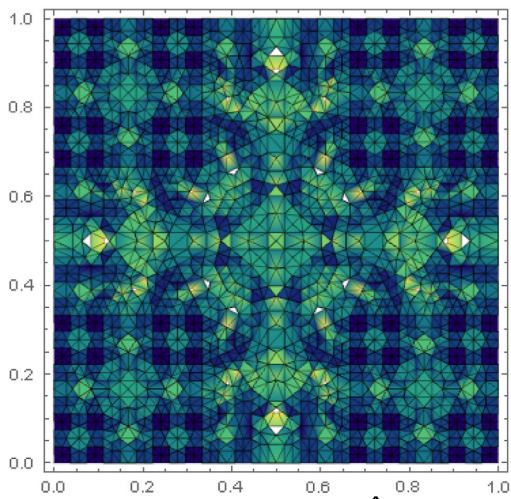
(v) Contours on $\hat{T}_3$
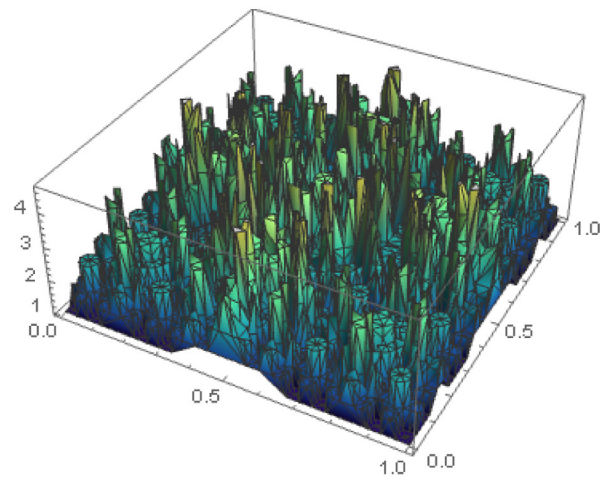
(vi) Graph on $\hat{T}_3$

Fig. 5. Principal thermal conductivity ratio (K_r/K_s) distribution on Seirpinski-carpet tessellations.
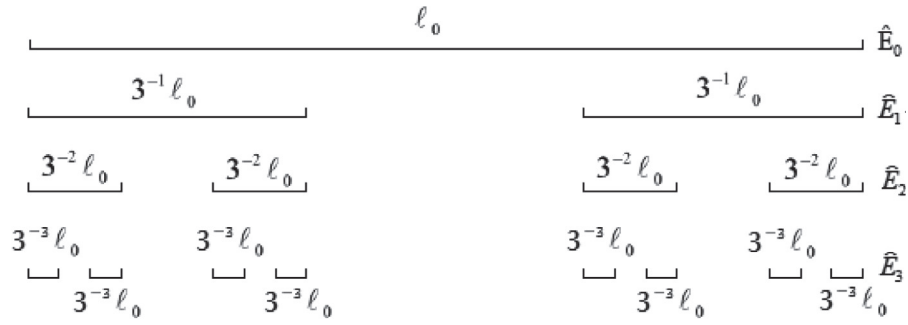
(a) Coarse Pre-fractals
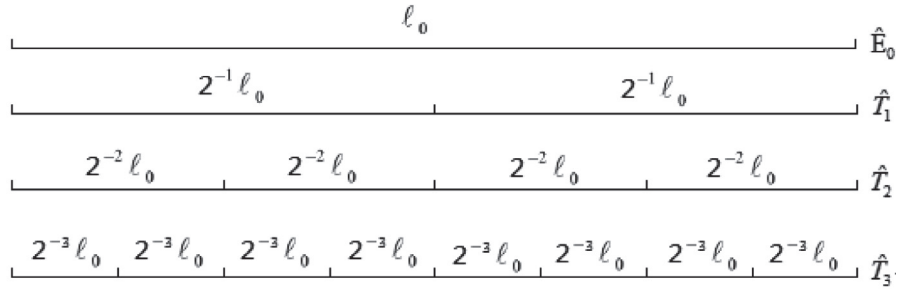
(b) Coarse Tessellations
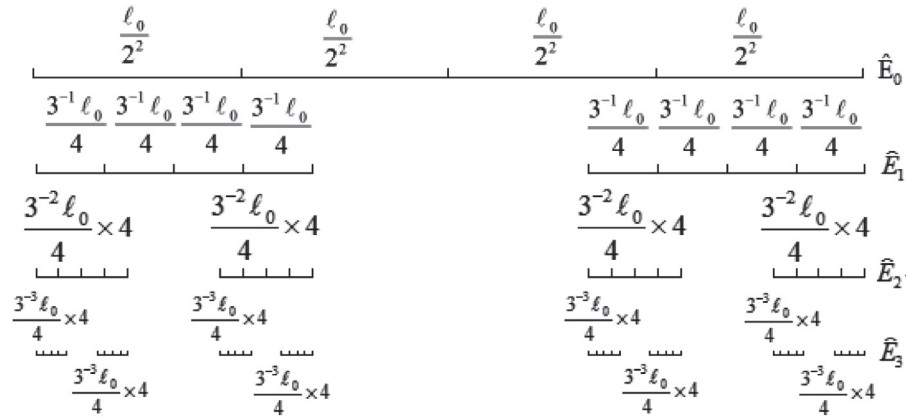
(c) Fine Pre-fractals
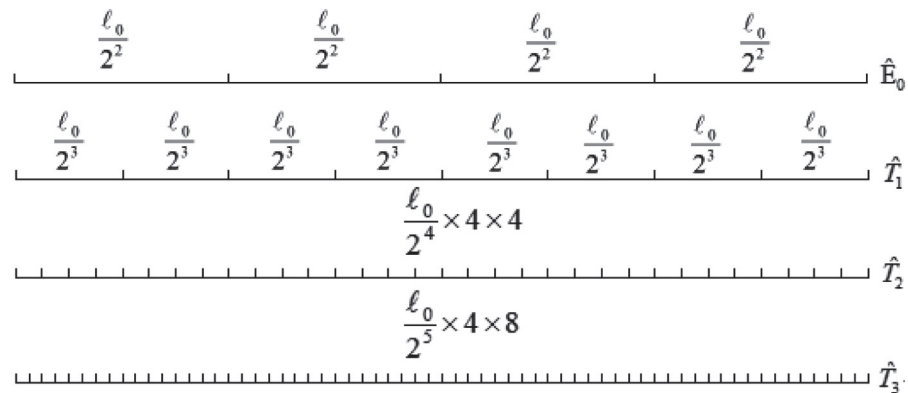
(d) Fine Tessellations

Fig. 6. Pre-fractals and Tessellation for the Cantor Dust.

the Schur decomposition (since $|\mathcal{D}|^{-1}\left[\mathcal{D}K_s\mathcal{D}^T\right]$ is a diagonal matrix). This confirms for this case that principal conductivity directions are immediately known to be the columns of $\mathbf{Q}_F$ and hence the normalised columns of $\mathbf{F}$. Moreover, principal conductivities are related by $(K_r)_i = \lambda_i K_s$ for an isotropic pre-fractal material, where $\mathcal{D} = diag(\lambda_1, \lambda_2)$ (in 2D).

To illustrate the behaviour when $\mathbf{D}_F = diag(\lambda_1, \lambda_2)$ with $\lambda_1 \neq \lambda_2$ it is convenient to consider a particular pre-fractal element (labelled "a") and corresponding tile as depicted in Fig. 1. The deformation tensor $\mathbf{F} = [F_1 \quad F_2]$, with $F_1 = \lfloor 1 \quad 0 \rfloor^T$ and $F_2 = \lfloor 1.3472 \quad 1.7778 \rfloor^T$. For this element, $\mathbf{F}$ happens to be upper triangular, so $\mathbf{F} = \mathbf{R}$ and $\mathbf{Q}_F = \mathbf{IF}$ is diagonalisable with $\mathbf{D}_F = diag(1.7778, 1)$ and $\mathbf{S} = [S_1 \quad S_2]$ with eigenvectors $S_1 = \lfloor 0.866 \quad 1 \rfloor^T$ and $S_2 = \lfloor 1 \quad 0 \rfloor^T$. The hole-fill map when applied to the pre-fractal element depicted in Fig. 1 stretches the element by a factor of 1.788 in the S_1 direction but providing no elongation in the S_2 direction. This can be contrasted this with the thermal conductivity tensor $\mathbf{K}_r = [K_1 \quad K_2]$ with $K_1 = \lfloor 1.5833 \quad 1.3472 \rfloor^T$ and $K_2 = \lfloor 1.3472 \quad 1.7778 \rfloor^T$, represented by the Schur decomposition with $\mathbf{D} = diag(0.3298, 3.0313)$ and orthogonal tensor $\mathbf{Q} = [Q_1 \quad Q_2]$, $Q_1 = \lfloor -0.7321 \quad 0.6812 \rfloor^T$, $Q_2 = \lfloor -0.6812 \quad -0.7321 \rfloor^T$. The Schur decomposition indicates that the maximum thermal conductivity is in the direction of Q_2, which is towards the direction of maximum stretch S_1. It is appreciated of course that principal values of thermal conductivity act along mutually perpendicular directions, so in general will not align with principal stretch directions, as this example illustrates. The situation is illustrated graphically in Fig. 3.

It is also of interest to observe typical spatial distributions of thermal conductivity on tessellations for classical pre-fractals to provide some indication of how the loss of geometrical complexity (present on pre-fractals but absent on tessellations) transforms into an increase in material complexity. Contour plots showing how the maximum principal value of thermal conductivity varies spatially for a selection of tessellations is depicted in Figs. 4 and 5. Larger values of thermal conductivity can be expected at areas of severe distortion. These distributions, although complex in appearance, do not provide a barrier to numerical analysis, particularly for a tessellation doubling up as a finite element mesh. The element stiffness matrices in the finite element method are readily obtained and in the case of a linear triangular element (used throughout this paper for 2D analysis) the thermal conductivity tensor is spatially invariant on each element domain.

5. Solutions on 1-D cantor dusts

In this section, analytical solutions to heat transfer problems with convection boundary conditions are defined on Cantor dusts in one and two dimensions. The analysis begins with the governing partial differential equation, which for Eq. (5) is of the form

$$\rho_r \frac{\partial h_r}{\partial t} = div_r(\mathbf{K}_r \cdot \nabla_r T_r) + \dot{Q}_0 + \dot{Q}_1, \tag{12}$$

where $\dot{Q}_0$ and $\dot{Q}_1$ are heat sources associated with elements and edges, respectively.

Table 1
Heat transfer coefficient (HTC) for pre-fractal holes.

d_s^{hole} Hydraulic diameter (m)	0.1667	0.0222	0.0026	3.0111×10^{-4}
$\hat{h}_{i\ell_0/2^k}$ (W/m^2 K)	574.6	46.9	3.7	0.3

5.1. Pre-fractal and tessellation construction

The pre-fractals $\widehat{E}_k$ and corresponding tessellation $\widehat{T}_k$ for the Cantor dust depicted in Fig. 6(a) are generated respectively by the self-similar contraction maps

$$S_1(x) = \frac{x}{3} \quad \text{and} \quad S_2(x) = \frac{2\ell_0 + x}{3} \tag{13}$$

and affine-tessellation maps

$$P_1(x) = \frac{x}{2} \quad \text{and} \quad P_2(x) = \frac{\ell_0 + x}{2} \tag{14}$$

with both initiated on the set $\widehat{E}_0 = [0, \ell_0]$.

Although the affine-tessellation maps are not unique, the ones selected in Eq. (14) are a natural choice producing tessellated elements of equal size. In any numerical method this choice corresponds to one finite element per pre-fractal element. A finer mesh can be obtained by simple function composition of the original map, i.e.

$$P_1 \circ P_1(x) = \frac{x}{4}, P_1 \circ P_2(x) = \frac{\ell_0 + x}{4},$$
$$P_2 \circ P_1(x) = \frac{2\ell_0 + x}{4} \quad \text{and} \quad P_2 \circ P_2(x) = \frac{3\ell_0 + x}{4} \tag{15}$$

which is a technique that can be employed for more complex structures.

The corresponding pre-fractal and tessellation generated by Eqs. (13) and (15) are presented in Fig. 6(b). Note that the pre-fractal and tessellation are constructed recursively using $\widehat{E}_k = \bigcup_i S_i(\widehat{E}_{k-1})$ and $\widehat{T}_k = \bigcup_i P_i(\widehat{T}_{k-1})$, respectively; complex structures can be created/represented with this approach and the associated data efficiently captured [19]. Splitting the domain according to $\widehat{E}_0 = \widehat{E}_k \cup (\widehat{E}_0 \setminus \widehat{E}_k)$ (i.e. elements and holes), then a *hole-fill map* is designed, which identifies a coordinate $s \in \widehat{E}_0 = \widehat{E}_k \cup (\widehat{E}_0 \setminus \widehat{E}_k)$ with a coordinate $\mathbf{x} \in \widehat{T}_k = \widehat{E}_0$; if $s \in \widehat{E}_0 \setminus \widehat{E}_k$ then $\mathbf{x}$ belongs to an internal edge of the tessellation. The hole-fill map in for the case is simply

$$x_k(s) = x_k^{(i)} + \frac{x_k^{(i+1)} - x_k^{(i)}}{s_k^{(i+1)} - s_k^{(i)}}(s - s_k^{(i)}), \tag{16}$$

where $s \in [s^{(i)}, s^{(i+1)}]$ and $s_k^{(i)}$ and $x_k^{(i)}$ are corresponding end-points of elements in the pre-fractal and tessellation, respectively. The graph for the map x_k is depicted in [36] and can be written in terms of support μ_k, i.e.

$$x_k(s) = \left(\frac{3}{2}\right)^k \int_0^s \mu_k(r)dr = \left(\frac{\ell_k}{\ell_0}\right)^{D_1-1} \int_0^s \mu_k(r)dr, \tag{17}$$

where ℓ_k is the length of an element of $\widehat{E}_k$ and D_1 is the Hausdorff fractal dimension [37] (see Ref. [20] for derivation). Eq. (16) provides a definition suitable for use in numerical analysis, and Eq. (17) provides the same definition for analytical work.

The associated deformation gradient tensor for this case is a scalar and is of the form $|F| = F = (\ell_k \ell_0^{-1})^{D_1-1}$, so $\rho_r = |F|^{-1}\rho_s = (\ell_k \ell_0^{-1})^{1-D_1}\rho_s$ with scalar K_s and K_r related by $K_r = |F|^{-1}FK_sF^T = (\ell_k \ell_0^{-1})^{D_1-1}K_s$. Since the length ℓ_k of each element of the kth pre-fractal for the Cantor dust is constant, the thermal conductivity is homogeneous on the tessellation; this is however not generally the case. It is important to appreciate also that any solution obtained for a fractal by means of a tessellation must be independent of the hole-fill map.

5.2. Analytical solution for a 1-D Cantor-dust model

In order to represent conditions met in a cellular heat exchanger, fluid is assumed to flow normal to the voids of the pre-fractal Cantor-dust model depicted in Fig. 6. Elements in the fractal are loaded uniformly with an internal heat source, defined such the total load per unit volume $\dot{Q}_0$ appears uniform on the tessellated continuum. Thermal cooling arising from the fluid flowing through the voids is assumed to manifest as a set of source terms of the form $2\ell_0^{-1}\hat{h}_x(T - T_{wat})\delta(\ell_0^{-1}x - 2^{-k}i)$ $1 \leqslant i \leqslant 2^k - 1$, where $2^k - 1$ is the number of holes associated with $\widehat{E}_k$, $\delta(\cdot)$ is the Dirac delta distribution function, $\hat{h}_x$ is a heat transfer coefficient, and T_{wat} is the bulk coolant temperature. If the fluid is viewed as a perfect conductor, the edge temperatures of any two adjacent solid components are common. External surfaces (the faces) are assumed to be exposed to a heat flux of the form $\dot{q}_0 = \hat{h}_0(T - T_\infty)$, where T_∞ is the ambient temperature of the of the surrounding medium and h_0 is the heat transfer coefficient of the surrounding medium.

5.2.1. Steady-state solution for a 1-D Cantor-dust

Eq. (12) expressed on the single element $\widehat{E}_1$ yields the governing equation

$$K_r T'' + \dot{Q}_0 - \frac{2\hat{h}_0}{w}(T - T_\infty) - \frac{2\hat{h}_{\ell_0/2}}{\ell_0}(T - T_{wat})\delta\left(\frac{x}{\ell_0} - \frac{1}{2}\right) = 0 \quad (18)$$

on $\widehat{T}_1$, where w is the width of the bar (i.e. depth in the flow direction).

Eq. (18) can be solved by assuming a solution of the form $T = T_{cf} + T_{hole} + T_{source}$, where the complementary function $T_{cf}(x) = a\cosh(\alpha x) + b\sinh(\alpha x)$ satisfies $K_r T''_{cf} - 2\hat{h}_0 w^{-1} T_{cf} = 0$ for $\alpha = (2\hat{h}_0/wK_r)^{\frac{1}{2}}$, and where a and b are integration constants. The term T_{source} satisfies $K_r T''_{source} + \dot{Q}_0 - 2\hat{h}_0 w^{-1}(T_{source} - T_\infty) = 0$ and is simply $T_{source} = T_\infty + 2^{-1}\hat{h}_0^{-1}w\dot{Q}_0$ (provided $\hat{h}_0 \neq 0$). The term T_{hole} is a little more involved; substituting $T = T_{cf} + T_{hole} + T_{source}$ into Eq. (18) gives

$$T''_{hole} + \alpha^2 T_{hole} - \frac{2}{K_r \ell_0}\hat{h}_{\ell_0/2}(T - T_{wat})\delta\left(\frac{x}{\ell_0} - \frac{1}{2}\right) = 0 \quad (19)$$

which can be solved by setting $T_{hole} = Ze^{\alpha x}$ and noting that

$$T''_{hole} + \alpha^2 T_{hole} = (Z'' + 2\alpha Z')e^{\alpha x} = \frac{d}{dx}(Z'e^{2\alpha x})e^{-\alpha x}$$

$$= \frac{2}{K_r \ell_0}\hat{h}_{\ell_0/2}(T - T_{wat})\delta\left(\frac{x}{\ell_0} - \frac{1}{2}\right) \quad (20)$$

integrates to give

$$Z' = \frac{2}{K_r}\hat{h}_{\ell_0/2}(T_{\ell_0/2} - T_{wat})e^{\frac{\alpha\ell_0}{2}}e^{-2\alpha x}H\left(\frac{x}{\ell_0} - \frac{1}{2}\right). \quad (21)$$

One further integration and multiplication with $e^{\alpha x}$ gives

$$T_{hole} = -\frac{2}{\alpha K_r}\hat{h}_{\ell_0/2}(T_{\ell_0/2} - T_{wat})\sinh\left(\alpha\left(\frac{\ell_0}{2} - x\right)\right)H\left(\frac{x}{\ell_0} - \frac{1}{2}\right) \quad (22)$$

Extending the analysis to $\widehat{T}_k$ provides

$$K_r T'' - \frac{2\hat{h}_0}{w}(T - T_\infty) - \frac{2}{\ell_0}\sum_{i=1}^{2^k-1}\hat{h}_{i\ell_0/2^k}(T_{i\ell_0/2^k} - T_{wat})\delta\left(\frac{x}{\ell_0} - \frac{i}{2^k}\right) = 0 \quad (23)$$

which, following a similar procedure as above gives

$$T(x) = a\cosh(\alpha x) + b\sinh(\alpha x) + \frac{2}{\alpha K_r}\sum_{i=1}^{2^k-1}\hat{h}_{i\ell_0/2^k}(T_{i\ell_0/2^k} - T_{wat})$$

$$\times \sinh\left(\alpha\left(x - \frac{i\ell_0}{2^k}\right)\right)H\left(\frac{x}{\ell_0} - \frac{i}{2^k}\right) + T_{source} \quad (24)$$

where a and b are determined by setting $\hat{h}_{wall}(T_{x=0} - T_{wall}) = K_r(\partial T/\partial x)|_{x=0}$ and $\hat{h}_0(T_{\ell_0} - T_\infty) = -K_r(\partial T/\partial x)|_{x=\ell_0}$, and where it is assumed that at $x = 0$ the medium is in contact with a wall of specified temperature T_{wall} through a conductance measured in the form of a heat transfer coefficient $\hat{h}_{wall}$. Some algebraic manipulation is required to take account of the initially unknown temperatures $T_{i\ell_0/2^k}$, which arise with through the application of the end condition at $x = \ell_0$. This is achieved through Eq. (24), which at $x = i\ell_0/2^k$ reduces to

$$T\left(\frac{i\ell_0}{2^k}\right) = a\cosh\left(\alpha\frac{i\ell_0}{2^k}\right) + b\sinh\left(\alpha\frac{i\ell_0}{2^k}\right)$$

$$+ \frac{2}{\alpha K_r}\sum_{j<i}\hat{h}_{j\ell_0/2^k}(T_{j\ell_0/2^k} - T_{wat})\sinh\left(\frac{\alpha\ell_0}{2^k}(i-j)\right) + T_{source} \quad (25)$$

and is defined sequentially for $i = 1, 2, \ldots, 2^k - 1$.
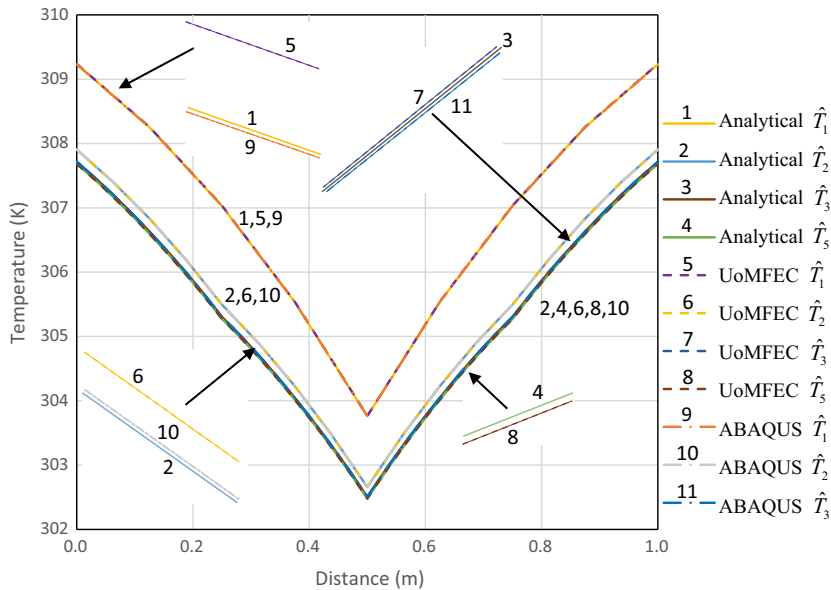
Fig. 7. Temperature plots for Cantor-dust with steady-state solution on tessellated continua.

5.2.2. Steady-state validation tests

In this section the analytical solution is compared with results obtained via the commercial package ABAQUS and a purpose-built finite element code developed at the University of Manchester (UoM). The material for the Cantor dust is chosen to be copper and the length of the test specimen is set to $\ell_0 = 1$ m with width $w = 1$ m. The air flowing around the Cantor dust is assumed to have a bulk temperature $T_{wall} = T_\infty = 323\,K$ and heat transfer coefficient $\hat{h}_{wall} = \hat{h}_0 = 200\,\mathrm{W/m^2}$. The bar is subjected to a uniform heat loading of $\dot{Q}_0 = 400\,\mathrm{J/m^3}$ to account for the thermal loading from an external heat source. For the Cantor set the heat transfer coefficients $\hat{h}_{i_{\ell_0}/2^k}$ for the holes are identical for both tessellations and pre-fractals and are tabulated in Table 1. The coefficients are determined using the Dittus-Boelter empirical relationship, the details of which are given in Appendix A (see also Refs. [38–40]).

Temperature plots from analytical, UoM finite element code (UoMFEC) and ABAQUS for the tessellated structure $\widehat{T}_k$ and corresponding pre-fractal $\widehat{E}_k$ are depicted in Figs. 7 and 8 for different

values of k. The first thing to appreciate is that the pre-fractal temperatures for analytical and the UoMFEC are indirect: they are determined first on the tessellation and then mapped onto the pre-fractal. Evidently therefore correspondence of results on tessellations gives correspondence on pre-fractals for the analytical and the UoMFEC. The principal reason for the development of the UoMFEC is to provide a convenient platform for the determination of element-conductivity (stiffness) matrices, which generally involve orthotropic conductivity tensors (Eq. (7)). Two options are available to ABAQUS, i.e. direct temperature determination on pre-fractals (which involves problematic geometry definitions) and temperature determination on tessellations (which involves problematic material property specifications). The former is easier to apply in ABAQUS but, more importantly, is also the most critical to the validation trials. The UoMFEC predictions provided in Fig. 8 are performed on different tessellations as depicted in Fig. 6. It transpires that different tessellations have little impact on the results, principally in this case, because of near-linear temperature distributions over pre-fractal elements. It is evident on close examination of Fig. 8 that the maximum deviation between UoMFEC and

(a) On pre-fractal $\hat{E}_1$
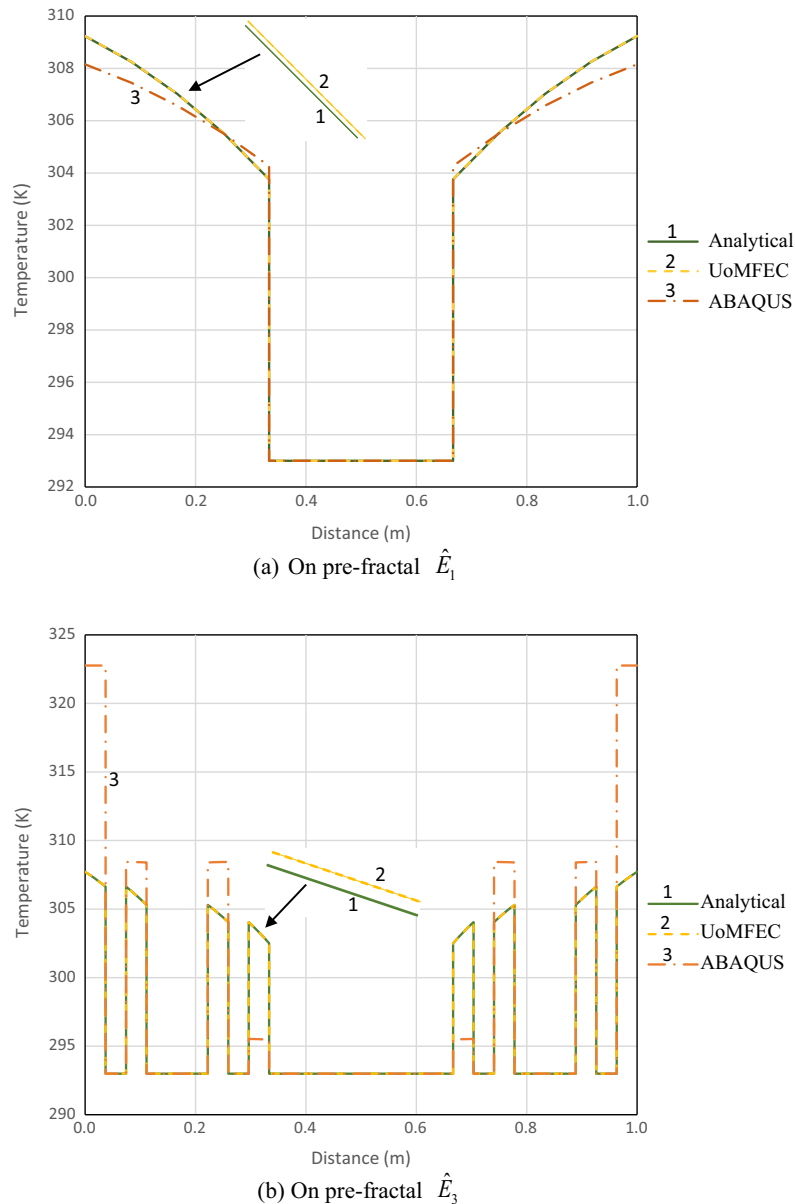
(b) On pre-fractal $\hat{E}_3$

Fig. 8. Temperature plots for Cantor-dust with steady-state solution on pre-fractal $\hat{E}_k$.

ABAQUS results arise at pre-fractal holes. Note that differences can be expected as continuity (Galerkin) assumptions are enforced on the tessellation. This means that temperatures on the two sides of any hole in a pre-fractal are identical for the UoMFEC and analytical predictions. This is not the case for ABAQUS and identical temperatures would only be achieved for high cooling-channel heat transfer coefficients. Despite this observation, it is apparent on examination of Table 2 (which provides average temperature differences) that reasonably high accuracy is returned. The averages $\overline{D}$ and $\overline{D}_\%$ appearing in Table 2 are obtained with the relationships

$$\overline{D} = \frac{1}{n}\sum_{i=1}^{n}|T_i^{(a)} - T_i^{(b)}| \qquad (26)$$

and

Table 2
Steady-state temperature differences for 1-D Cantor dust.

| k | Tessellation $\hat{T}_k$ | | | | | | Pre-fractal $\hat{E}_k$ | |
| | Analytical vs UoMFEC (coarse) | | Analytical vs UoMFEC (fine) | | Analytical vs ABAQUS (fine) | | Analytical vs ABAQUS (fine) | |
	$\overline{D}$ on $\hat{E}_k$ (K)	$\overline{D}_\%$ on $\hat{E}_k$ (%)	$\overline{D}$ on $\hat{E}_k$ (K)	$\overline{D}_\%$ on $\hat{E}_k$ (%)	$\overline{D}$ on $\hat{E}_k$ (K)	$\overline{D}_\%$ on $\hat{E}_k$ (%)	$\overline{D}$ on $\hat{E}_k$ (K)	$\overline{D}_\%$ on $\hat{E}_k$ (%)
1	0.0050	0.0016	0.0050	0.0016	0.0004	0.0001	0.5722	0.1862
2	0.0012	0.0004	0.0012	0.0004	0.0003	0.0001	9.5596	3.0977
3	0.0003	0.0001	0.0003	0.0001	0.0003	0.0001	7.3826	2.3891
4	0.0015	0.0005	0.0015	0.0005	0.0003	0.0001	8.9782	2.9279
5	0.0014	0.0005	0.0014	0.0005	0.0002	0.0001	12.9905	4.1606

(a) At point 0.25 on $\hat{E}_1$

(b) At point 0.0625 on $\hat{E}_3$
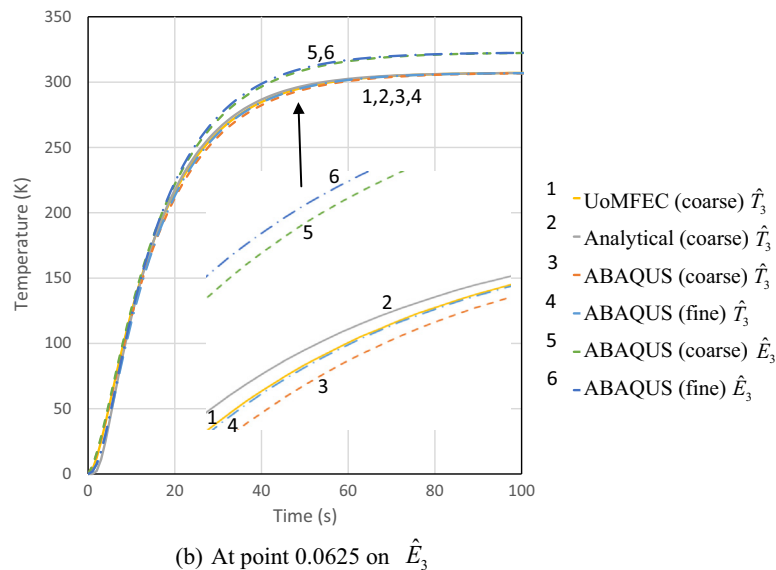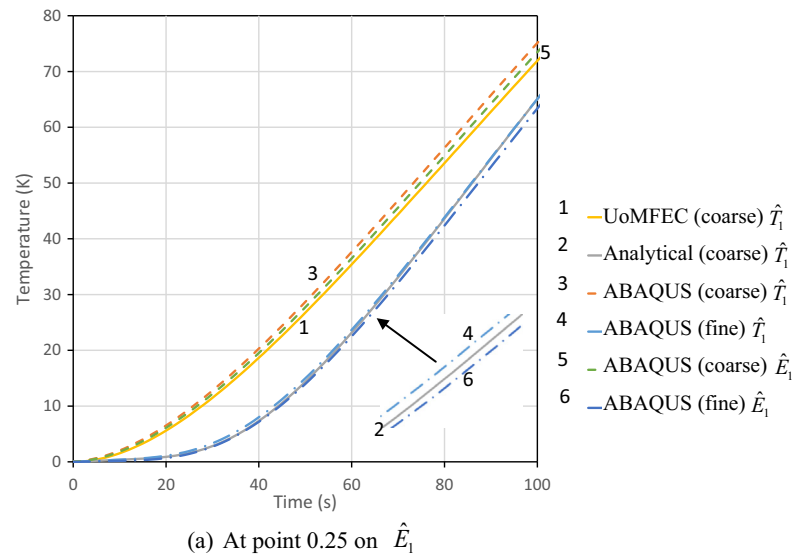
Fig. 9. Transient temperature plots for a Cantor Dust.

Table 3
Average temperature differences on $\widehat{E}_k$ and $\widehat{T}_k$.

	$x = 0.25$ and $k = 1$		$x = 0.125$ and $k = 2$		$x = 0.0625$ and $k = 3$	
	$\overline{D}$ (K)	$\overline{D}_\%$ (%)	$\overline{D}$ (K)	$\overline{D}_\%$ (%)	$\overline{D}$ (K)	$\overline{D}_\%$ (%)
Analytical vs UoMFEC(coarse) on $\widehat{T}_k$	16.2782	44.1550	9.4507	13.4720	2.3379	3.1508
Analytical vs UoMFEC (fine) on $\widehat{T}_k$	5.7731	23.9875	3.3168	8.1821	0.7144	1.8801
Analytical vs ABAQUS (fine) on $\widehat{T}_k$	0.2901	1.9369	0.6455	2.5640	0.6283	1.4462
Analytical vs ABAQUS (fine) on $\widehat{E}_k$	1.8335	6.4139	8.8444	5.4921	14.1051	5.7719

Table 4
Edge-boundary temperatures on $\widehat{T}_k$ (unit-tessellated continuum).

Boundary edge (m)	$x = 0$	$y = 0$	$x = 1$	$y = 1$
Temperature (K)	$T_r(0, y) = y$	$T_r(x, 0) = y$	$T_r(1, y) = 1 - y$	$T_r(x, 1) = 1 - x$

$$\overline{D}_\% = \frac{2 \times 100}{n} \sum_{i=1}^{n} \left| \frac{T_i^{(a)} - T_i^{(b)}}{T_i^{(a)} + T_i^{(b)}} \right| \qquad (27)$$

where superscripts (a) and (b) distinguish the method and n is the number of the data points.

5.2.3. Transient solution for a 1-D Cantor-dust

Following the approach adopted for the steady state solution, the transient equation on the tessellated continuum $\widehat{T}_k$ is given by

$$\rho_r c_r \frac{\partial T}{\partial t} = K_r \frac{\partial^2 T}{\partial x^2} + \dot{Q}_0 - \frac{2\hat{h}_0}{w}(T - T_\infty)$$
$$- \frac{2}{\ell_0} \sum_{i=1}^{2^k - 1} \hat{h}_{i\ell_0/2^k}(S_{i\ell_0/2^k} - T_{wat})\delta\left(\frac{x}{\ell_0} - \frac{i}{2^k}\right), \qquad (28)$$
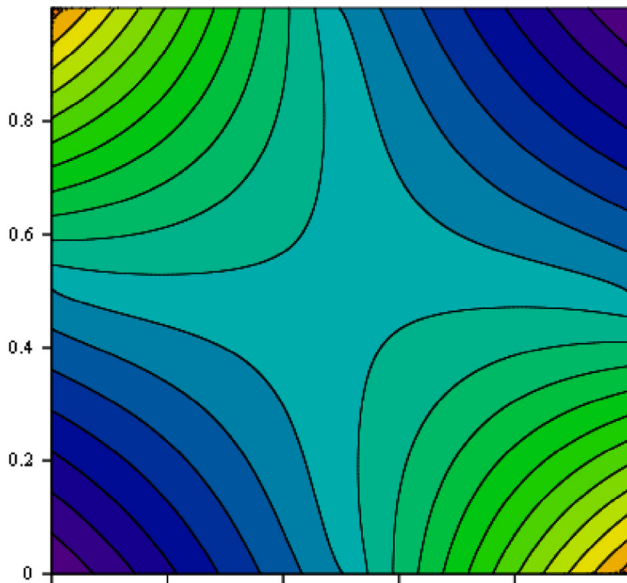
(i) Analytical
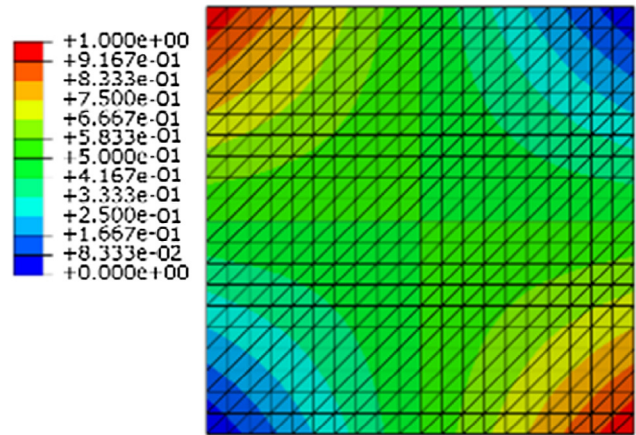
(ii) ABAQUS
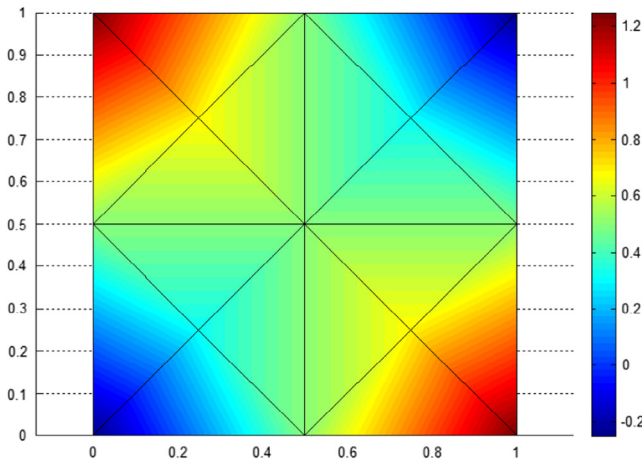
(iii) UoMFEC with 16 elements
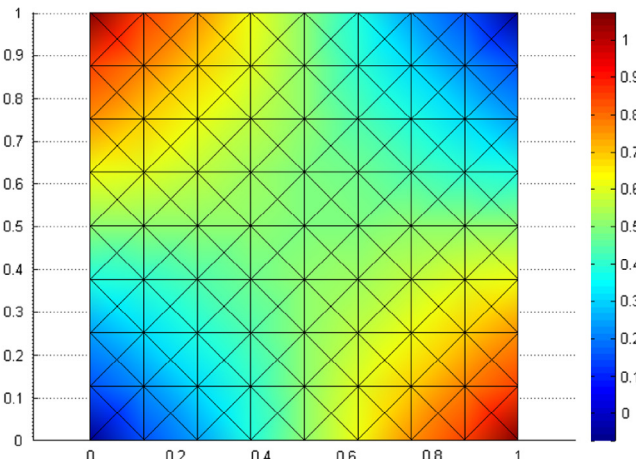
(iv) UoMFEC with 256 elements

Fig. 10. Temperatures on $\hat{T}_k$ for product Cantor dust without heat sources.

where it is assumed that steady state temperatures are attained at pre-fractal holes, consistent with the application of very high heat transfer coefficients there.

Consider a solution of the form $T(x,t) = \mathcal{F}(x,t) + S(x)$, where S satisfies Eqs. (18) and $\mathcal{F}(x,t)$ satisfies

$$\rho_r c_r \frac{\partial \mathcal{F}}{\partial t} = K_r \frac{\partial^2 \mathcal{F}}{\partial x^2} - \frac{2\hat{h}_0}{w}\mathcal{F}, \qquad (29)$$

which, assuming that $\mathcal{F}(x,t) = X(x)\tau(t)$ reduces to

$$\frac{\rho_r c_r}{K_r} \frac{\dot{\tau}}{\tau} + \frac{2\hat{h}_0}{wK_r} = \frac{X''}{X} = -\omega^2 \qquad (30)$$

A solution to the transient part of the equation is

$$\tau(t) = \exp(-\beta(\omega^2 + \alpha^2)t) \qquad (31)$$

where $\beta = K_r/\rho_r c_r$ and $\alpha = (2\hat{h}_0/wK_r)^{\frac{1}{2}}$ and similarly for the spatial part the solution is

$$X(x) = A\cos(\omega x) + B\sin(\omega x). \qquad (32)$$

Specified temperature end conditions return $A = 0$ and $\omega_n = n\pi/\ell_0$ and to match an arbitrary initial condition, a solution of the form

$$T(x,t) = S(x) + \sum_{n=1}^{\infty} B_n \sin(\omega_n x)\exp(-\beta(\omega_n^2 + \alpha^2)t) \qquad (33)$$

is required. Setting $T(x,0) = 0$ for example gives the requirement that

$$\sum_{n=1}^{\infty} B_n \sin(\omega_n x) = -S(x) \qquad (34)$$

which is simply a Fourier Sine series representation of $-S(x)$ and the Euler formulae are obtained from

$$B_n = -\frac{2}{\ell_0} \int_0^{\ell_0} S(x)\sin(\omega_n x)dx \qquad (35)$$

5.2.4. Transient validation tests

The validation trials for the transient theory follow those for the steady state, with comparisons made between the analytical solution, the UoMFEC and ABAQUS. The initial temperature on the tessellation and pre-fractals is assumed to be zero. Two tessellations are employed (fine and coarse, as depicted in Fig. 6), with the coarse tessellation having an identical number of tiles as pre-fractal elements. The ABAQUS meshes are set to match the tessellations, which is relatively straightforward for a 1-D structure. The transient temperature plots for a selection of points on $\widehat{E}_k$ are presented in Fig. 9 along with average differences calculated through Eqs. (26) and (27) appearing in Table 3.

One aspect of interest in this work is the appropriateness of a coarse tessellation when contrasted with more refined meshes. This is of interest because a coarse tessellation has—by construction—the identical number of elements as pre-fractal elements, and thus is the starting point for any analysis. It is evident on examination of Table 3 and Fig. 9 that errors can be quite large for low values of k but reduce as k increases. This reflects the fact that as the pre-fractals becomes more complex, involving more pre-fractal elements, the number of corresponding tiles increases. With tiles doubling up as finite elements, the mesh refines as k increases but the downside is that the geometry is more involved along with energy transfers. However, accuracy improvements with an increase in k can generally be expected due to the diminishing effect of geometry refinement. It is apparent from Table 3 that the coarse UoMFEC provides reasonable accuracy on $\widehat{T}_k$. Contrasting results on $\widehat{E}_k$ with the direct application of ABAQUS show larger errors arising as a direct result of the Galerkin assumption being employed resulting in the presence of a modelling error.

6. Solutions on 2-D product cantor dusts

Although not as straightforward as in 1-D, analytical solutions can also be found on product dusts [20] in 2D (and possibly in 3D), so it of interest to contrast the tessellated approach on these relatively simple structures before examining more complex geometries. The thermal problem considered here is slightly artificial in that it involves constant heat sources appearing at the internal edges of tiles, whose intensity is such that the *total* rate (per

Table 5
Temperature differences along $x = y$ on a 2-D Cantor Dust.

	No. of elements	Maximum difference (K)	Maximum difference (%)	Average difference (K)	Average difference (%)
UoMFEC	16	0.2499	24.9900	0.1250	16.6627
	64	0.1428	14.2800	0.0571	5.7120
	256	0.0721	7.2100	0.0290	2.9267
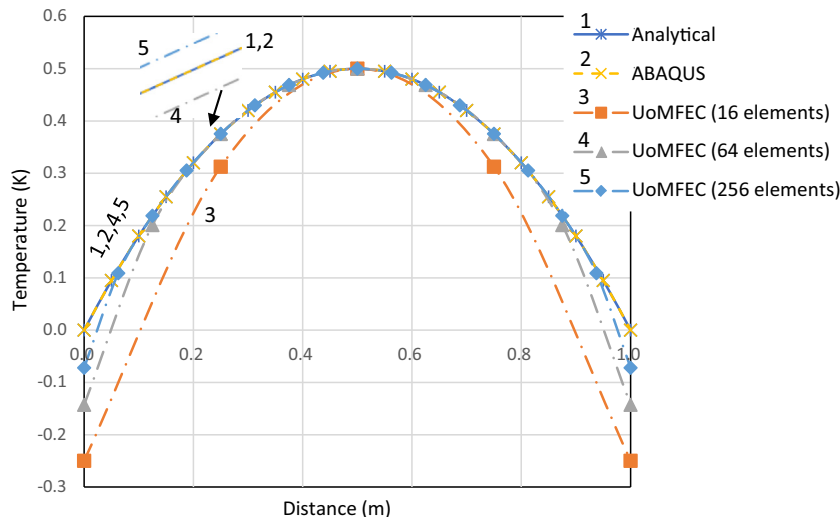
Fig. 11. Temperature plots on $\hat{T}_k$ along $x = y$ for product dust (no heat sources).

unit volume) of heat supplied by them takes a constant value $\dot{Q}$. This problem is selected because it matches the problem considered in Ref. [36] for which an analytical solution exists. The starting point is again Eq. (12), where it is readily confirmed that $\boldsymbol{K}_r = |\boldsymbol{F}|^{-1}\boldsymbol{FK}_s\boldsymbol{F}^T = \boldsymbol{K}_s$ confirming that the tessellated continuum is isotropic, permitting a scalar K_r in Eq. (12) related by $K_r = K_s$ [36]. It is assumed here that Cantor Dust is a material with thermal conductivity $K_s = 400$ W/mK, density $\rho_s = 400$ kg/m³, specific heat $c_s = 1000$ J/kg K and edge length $\ell_0 = 1$ m, i.e. the analysis is performed on a unit square domain. The edge temperatures are fixed on $\widehat{T}_k$ and the chosen values consistent with Ref. [36] are defined in Table 4.

6.1. Steady state and different tessellations

Product fractals are relatively easy to produce and involve the same contraction maps used in 1D. Thus, the four contraction maps employed to create the Cantor product-dust fractal are $\boldsymbol{S}_{ij}(x,y) = (S_i(x), S_j(y))$, where the S_i are defined in Eq. (13). The tessellation similarly involves the four affine maps $\boldsymbol{P}_{ij}(x,y) = (P_i(x), P_j(y))$ with P_i defined in Eq. (14). The tessellation produced by $\boldsymbol{P}_{ij}(x,y)$ is the coarsest when taken as a mesh for analysis purposes. Refinement however is relatively straightforward and mathematically represented by function (consistent with Eq. (15)) and takes the form $\boldsymbol{P}_{ijkm}(x,y) = \boldsymbol{P}_{ij} \circ \boldsymbol{P}_{km}(x,y) = (P_i \circ P_k(x), P_j \circ P_m(y))$. In a numerical setting there is no requirement to determine composition functions, since the process is a recursive application of $\boldsymbol{P}_{ij}(x,y) = (P_i(x), P_j(y))$ to an initial tessellation created by the same map in the first place. An additional facet of the numerical analysis is the use of triangular tiles, which is simply achieved on subdivision of the rectangular tiles produced by $\boldsymbol{P}_{ij}$.

The steady state equation on $\widehat{T}_k$ involves distribution terms to capture heat input at tile edges and is of the form

$$K_r\left(\frac{\partial^2 T}{\partial x^2} + \frac{\partial^2 T}{\partial y^2}\right) + \frac{\dot{Q}}{2(2^k-1)}\sum_{i=1}^{2^k-1}\left(\delta\left(\frac{x}{\ell_0} - \frac{i}{2^k}\right) + \delta\left(\frac{y}{\ell_0} - \frac{i}{2^k}\right)\right) = 0 \tag{36}$$
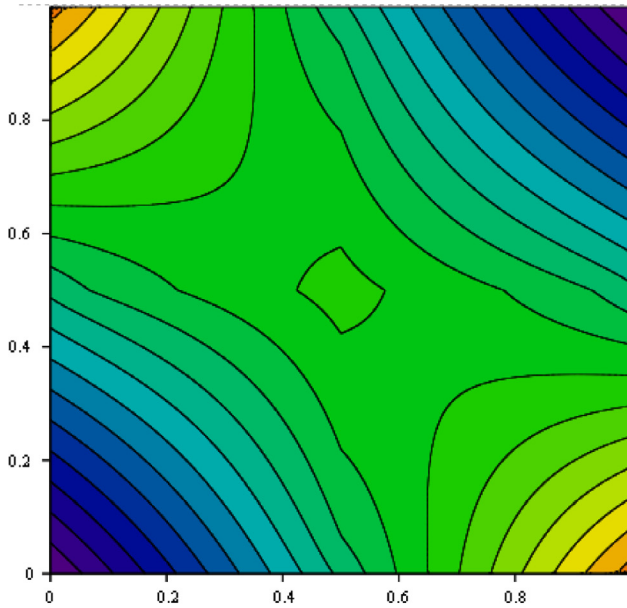
(i) Analytical on $\widehat{T}_1$
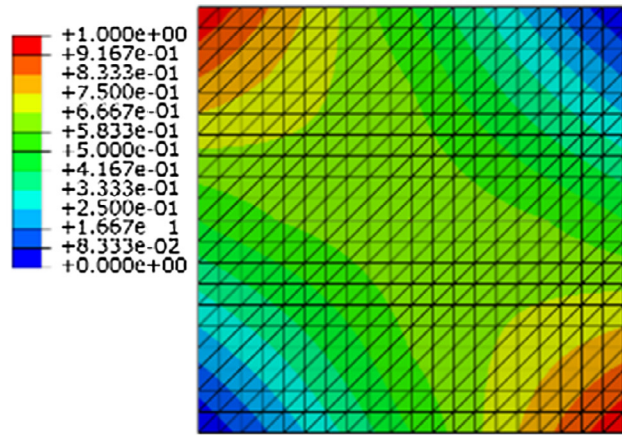
(ii) ABAQUS on $\widehat{T}_1$
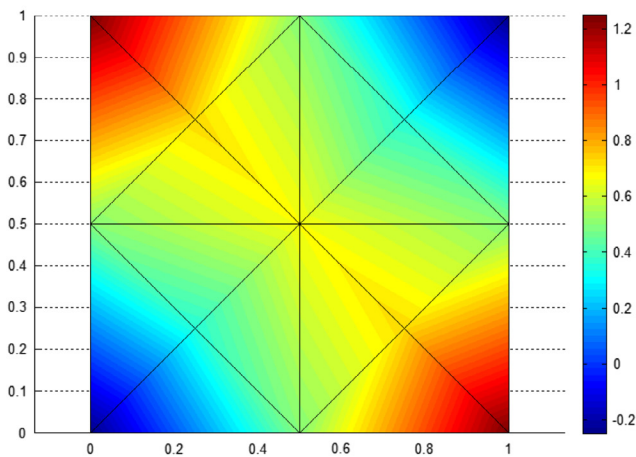
(iii) UoMFEC on $\widehat{T}_1$ (4 tiles on $\widehat{E}_0$)
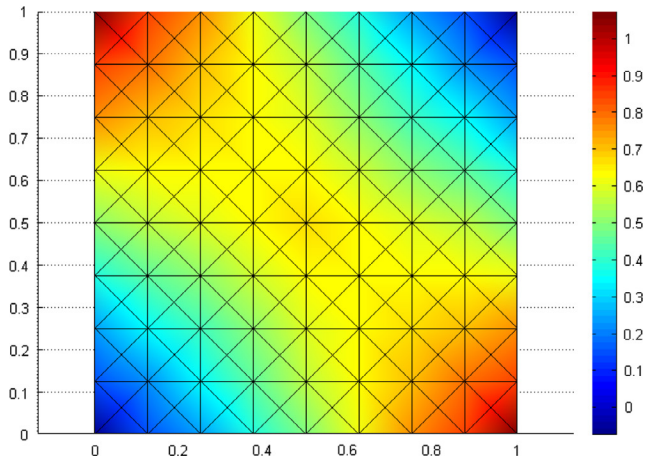
(iv) UoMFEC on $\widehat{T}_1$ (64 tiles on $\widehat{E}_0$)

Fig. 12. Contour temperature plots on tessellation with different methods applied to $\hat{T}_1$ with fixed wall temperatures.

where the total rate of energy input $\dot{Q}$ is determined from the dimensionless identity $\dot{Q}\ell_0^2/K_r\Delta T_r = 1$, which in this case gives $\dot{Q} = 400\,\mathrm{W/m^3}$ for $\Delta T_r = 1\,\mathrm{K}$.

However, prior to applying this identity and involving heat sources, it is convenient in the first instance to set $\dot{Q} = 0\,\mathrm{W/m^3}$ to ascertain the influence of different tessellations with the boundary conditions given in Table 4. One of the features of the UoMFEC is that it enforces specified temperature boundary conditions somewhat indirectly. It does this with a convective condition $\dot{q} = \hat{h}_r(T_r - T_{specified})$ and by stipulating a very high value of $\hat{h}_r$. The advantage of this approach is that the FE code is simplified and it generally transpires that most practical problems are convective. The disadvantage is that temperature differences at the boundary can result, which can be particularly significant when a coarse mesh is involved as is apparent in the following tests.

In order to test out the importance of different tessellation temperature contours for the analytical solution [36], ABAQUS and UoMFEC are depicted in Fig. 10. Temperatures along the diagonal line $x = y$ are sampled and shown in Fig. 11 and Table 5.

The temperature distributions on all the tessellations take the same form for the three approaches. The analytical and ABAQUS results match precisely, but errors are present for the UoMFEC results on the different tessellations considered. However, the maximum errors appear at the boundary as expected due to the convection condition applied (with an exceedingly high heat transfer coefficient). The results in Figs. 10 and 11 also reveal that these errors reduce with refinement of the tessellation. The tests reinforce the validity of the approach and also provide further validation for the UoMFEC.

6.2. Steady state analysis with heat sources

The analysis in Section 6.1 is repeated with heat sources applied to all internal edges in the tessellation. Temperatures are provided
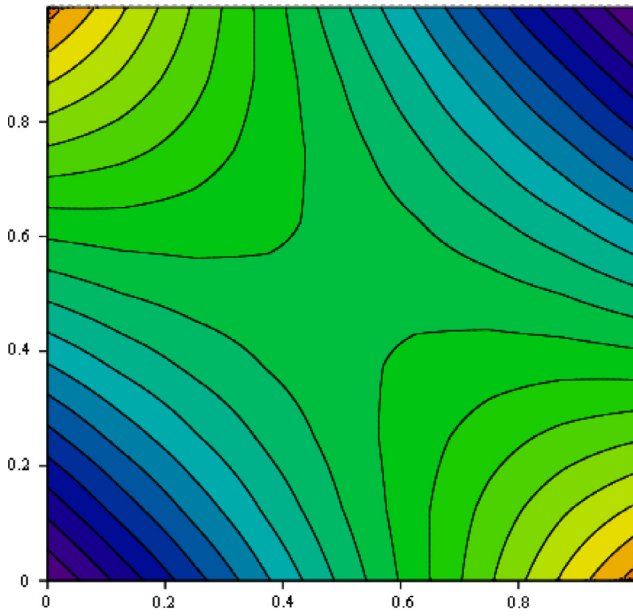
(i) Analytical on $\hat{T}_3$
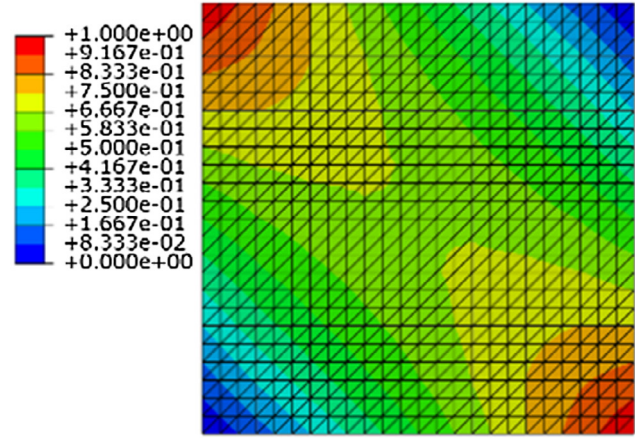
(ii) ABAQUS on $\hat{T}_3$
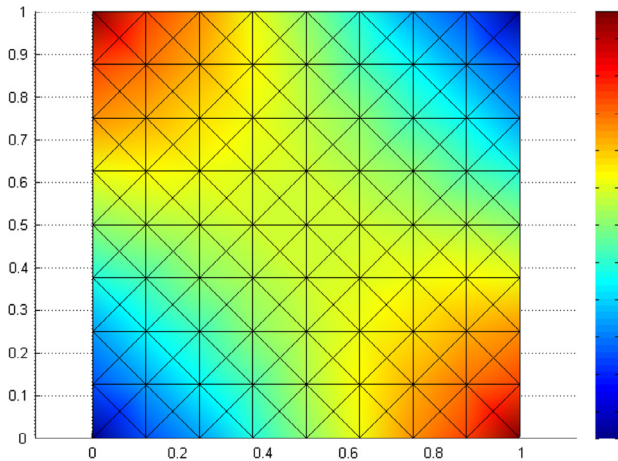
(iii) UoMFEC on $\hat{T}_3$ (4 tiles on $\hat{E}_0$)
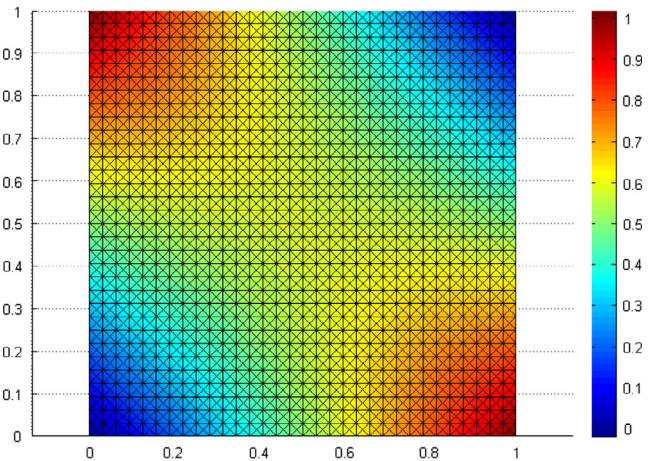
(iv) UoMFEC on $\hat{T}_3$ (64 tiles on $\hat{E}_0$)

Fig. 13. Contour temperature plots on tessellation with different methods applied to $\hat{T}_3$ with fixed wall temperatures.

on $\widehat{T}_k$ using the three approaches (analytical, ABAQUS, UoMFEC) and also on $\widehat{E}_k$ with mapped results from $\widehat{T}_k$ which are contrasted with ABAQUS applied directly to $\widehat{E}_k$. The two tessellations selected for the analysis are obtained with (a); no composition or (b); two initial compositions of $\boldsymbol{P}_{ij}(x,y)$, which produces (a); 4 or (b); $4 \times 4^2 = 64$ initial triangular tiles on $\widehat{E}_0$. Temperature contours on tessellations $\widehat{T}_1$ and $\widehat{T}_2$, are depicted in Figs. 12 and 13. Temperatures along the diagonal line $x = y$ are sampled and shown in Fig. 14 and Table 6.

The trends observed in Section 6.1 are observed here with near identical results for the analytical solution and ABAQUS on $\widehat{T}_k$, with the principal disparity for the UoMFEC occurring at the boundary for reasons already discussed.

6.3. Transient solution on a 2-D Cantor-dust

The transient equation on $\widehat{T}_k$ involving distribution terms to capture heat input at tile edges is

(a) On $\hat{T}_1$

(b) On $\hat{T}_3$
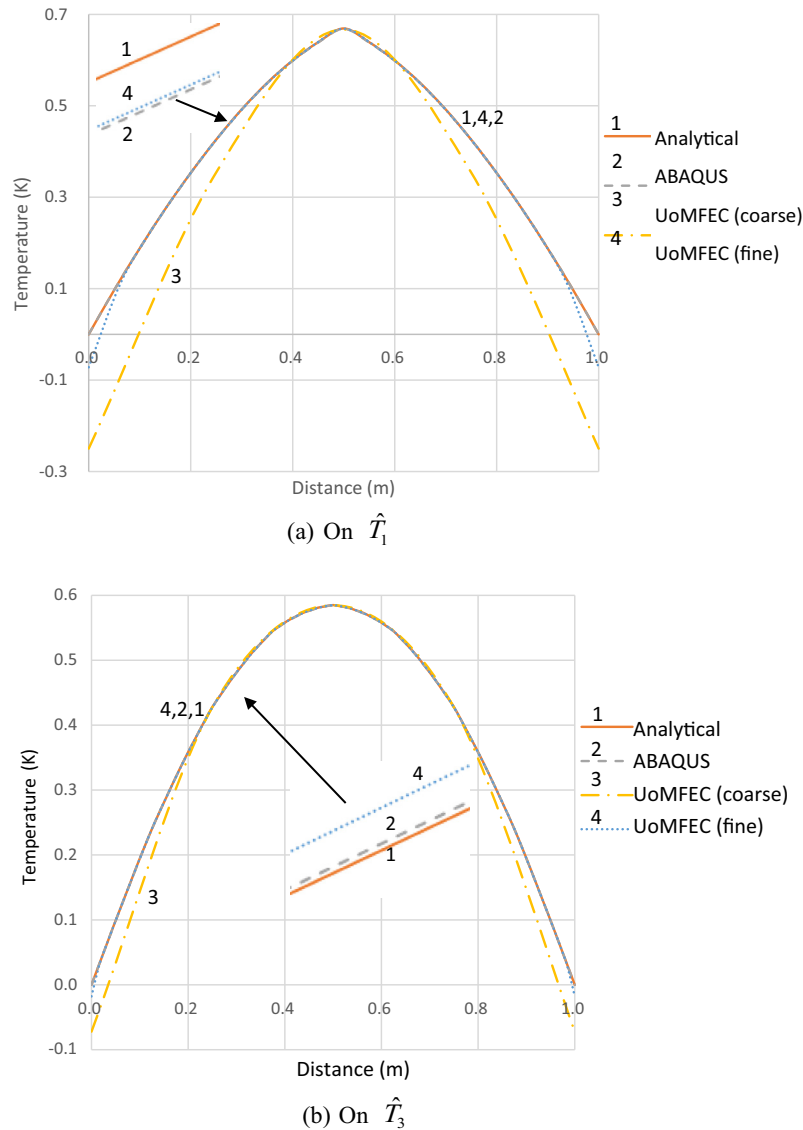
Fig. 14. Temperature plots along $x = y$ product dust on $\hat{T}_k$ with heat sources and fixed wall temperatures.

Table 6
Temperature differences along $x = y$: 2-D Cantor product with heat source.

|	Set	Number of tiles on $\widehat{E}_0$	Maximum difference (K)	Maximum difference (%)	Average difference (K)	Average difference (%)
UoMFEC	$\widehat{T}_1$	4	0.2499	24.9900	0.1250	16.6627
		64	0.0722	7.2165	0.0097	1.7255
	$\widehat{T}_2$	4	0.1428	14.2800	0.0571	5.7120
		64	0.0361	7.6070	0.0027	0.7605
	$\widehat{T}_3$	4	0.0721	7.2100	0.0290	2.9267
		64	0.0180	6.5801	0.0008	0.3234

$$\rho_r c_r \frac{\partial T}{\partial t} = K_r \left(\frac{\partial^2 T}{\partial x^2} + \frac{\partial^2 T}{\partial y^2} \right)$$
$$+ \frac{\dot{Q}}{2(2^k - 1)} \sum_{i=1}^{2^k - 1} \left(\delta \left(\frac{x}{\ell_0} - \frac{i}{2^k} \right) + \delta \left(\frac{y}{\ell_0} - \frac{i}{2^k} \right) \right), \qquad (37)$$

where it is assumed that edge-boundary conditions are identical to the steady-state problem above. Moreover, to conform with the analytical solution presented in Ref. [36], the initial condition is set as $T_r(x, y, 0) = x/\ell_0 + y/\ell_0 - 2xy/\ell_0^2$. The thermal histories on $\widehat{T}_k$ are given in Fig. 15. The transient behaviour is accurately captured and is quantified explicitly in Table 7 using Eqs. (26) and (27) for results obtained with UoMFEC and ABAQUS. Errors are apparent on $\widehat{T}_k$ for points close to the boundary with the UoMFEC due to the manner in which temperature boundary conditions are applied (using a high heat transfer coefficient).

Table 7
Average temperature differences on $\widehat{T}_k$.

Point on $\widehat{T}_k$	k	Analytical vs UoMFEC (4 tiles for each element) on $\widehat{T}_k$		Analytical vs UoMFEC (64 tiles for each element) on $\widehat{T}_k$		Analytical vs ABAQUS (fine) on $\widehat{T}_k$	
		$\overline{D}$ (K)	$\overline{D}_\%$ (%)	$\overline{D}$ (K)	$\overline{D}_\%$ (%)	$\overline{D}$ (K)	$\overline{D}_\%$ (%)
(0.5, 0.5)	1	0.0059	0.9343	0.0012	0.2023	0.0004	0.0634
	2	0.0124	2.1610	0.0004	0.0682	0.0010	0.1717
	3	0.0135	2.4076	0.0003	0.0524	0.0003	0.0507
(0.25, 0.25)	2	0.0061	1.4465	0.0003	0.0785	0.0007	0.1570
	3	0.0073	1.7486	0.0003	0.0610	0.0003	0.0597

7. Analysis on non-product tessellations

This section demonstrates that thermal analysis can be performed on more intricate pre-fractal geometries using the tessel-
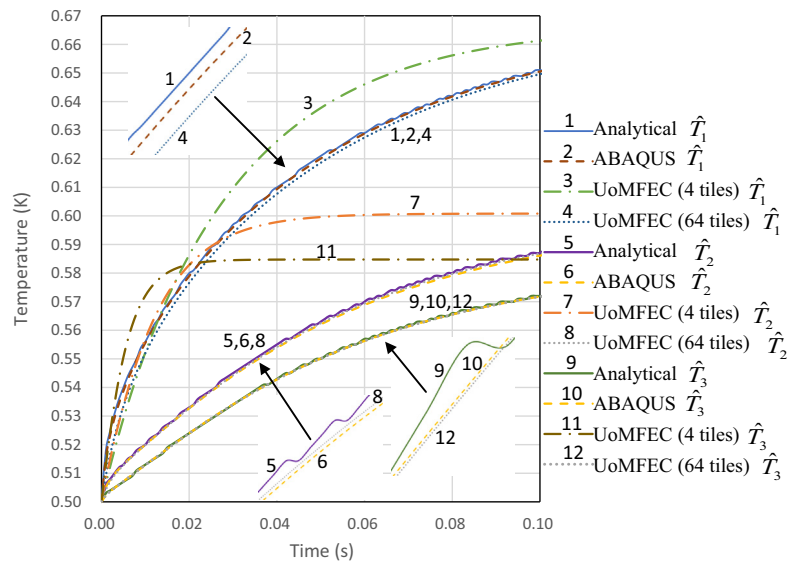
(a) For point (0.5, 0.5) on $\widehat{T}_k$
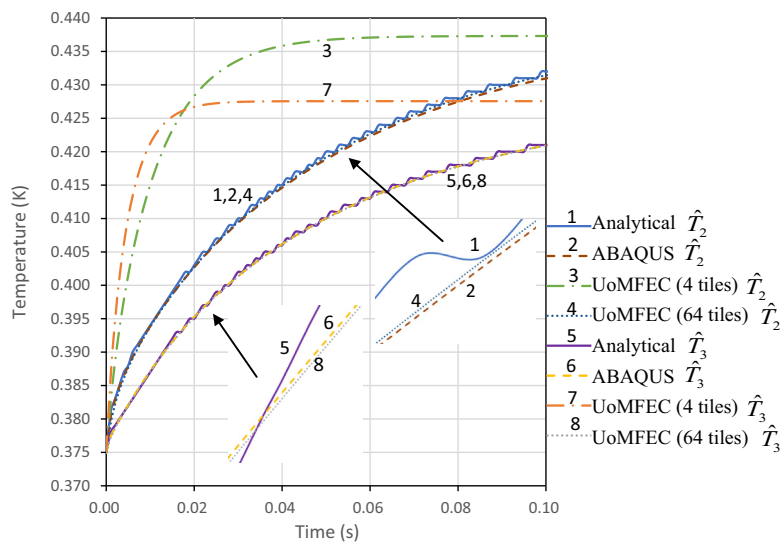
(b) For point (0.25, 0.25) on $\widehat{T}_k$

Fig. 15. Temperature plots for different points on $\widehat{T}_k$.

lated approach. A procedure for the creation of different tessellations with various levels of refinement is presented. This aspect is of some importance, particularly when a tessellation doubles up as a mesh, since mesh refinement is a necessary prerequisite for high levels of numerical accuracy. A particular concern however is that tessellations can become highly distorted. The distortion of a tile is intimately linked with the level of anisotropy in the material conductivity as discussed in Section 4. This coupling has the effect of mitigating deleterious effects resulting from tile distortion since in effect it is the behaviour on a pre-fractal that is ultimately being analysed.

7.1. Pre-fractals and tessellations for the Sierpinski gasket

The Sierpinski gasket is an example of a non-product fractal set and is constructed by the recursive application of the following three affine contraction maps:

$$S_1(x,y) = \left(\frac{x}{2}, \frac{y}{2}\right), S_2(x,y) = \left(\frac{\ell_0}{2} + \frac{x}{2}, \frac{y}{2}\right) \text{ and}$$

$$S_3(x,y) = \left(\frac{\ell_0}{4} + \frac{x}{2}, \frac{\sqrt{3}\ell_0}{4} + \frac{y}{2}\right), \tag{38}$$

where each S_i maps a triangular domain into a smaller triangular domain as deduced on inspection of Fig. 1.

The initial 6 tiles on $\widehat{E}_0$ provide a means to define the tessellation maps for the construction of $\widehat{T}_k$. The same number of tessellation maps are used as contraction maps (3 in this case). However, each tessellation map consists of a number of sub-maps with a number equal to the number of initial tiles on $\widehat{E}_0$ (6 in this case). Explicitly, the tessellation maps for the Sierpinski are illustrated in Table 8.

The tessellation maps produce a tessellated continuum free of the holes which are present in the corresponding pre-fractals. Their definition is evidently not unique with each affine sub-map P_{ij} taking the form of an expansion map; the triangular tiles must expand to remove holes. These maps are constrained in number and also

by the boundaries of the initiating triangular domain. The number of sub-maps P_{ij} depends on the initial number of tiles on $\widehat{E}_0$ but this can be increased in a simple manner. The tessellations produced in Fig. 1 are achieved by application of the tessellation maps to the previous tessellation. Evidently however any of these tessellations can be used as a starting tessellation on $\widehat{E}_0$. An example of this is depicted in Fig. 16, where the tessellation appearing in $\widehat{E}_1$ (and hence $\widehat{E}_0$) (Fig. 16) is the tessellation appearing in $\widehat{T}_2$ in Fig. 1. It is apparent on further examination of Fig. 1 (and 2) that all the tiles used in the tessellations are triangular. This simplifies the analysis considerably since $\boldsymbol{F}$ in Eq. (3) is constant on a triangular domain.

7.2. Thermal analysis of a Sierpinski gasket heat exchanger

The thermal problem considered involves water coolant flowing through the voids depicted in Fig. 1. Heat loading of the heat exchanger is achieved by loading pre-fractal elements from an external source in a manner than ensures that the volumetric heat loading $\dot{Q}_{tot} = 300 \text{ kW/m}^3$ appears uniform on the tessellated continuum. The heat exchanger is manufactured from copper with thermal conductivity $K_s = 400 \text{ W/mK}$, density $\rho_s = 8930 \text{ kg/m}^3$, specific heat $c_s = 385 \text{ J/kg K}$, and triangular edge length $\ell_0 = 1 \text{ m}$. The heat transfer coefficient h_{air} associated with air flowing external to the heat exchanger is taken to be $100 \text{ W/m}^2 \text{ K}$. The heat transfer coefficients $\hat{h}_s^{hole}$ pertaining to cooling channels are determined using empirical relationships found Appendix A. These vary depending on the hydraulic diameter d_s^{hole}, where $d_s^{hole} = 4\widehat{A}/\widehat{P}$, and where $\widehat{A}$ is cross sectional area and $\widehat{P}$ is the wetted perimeter. Values of $\hat{h}_s^{hole}$ for various sizes of d_s^{hole} pertinent to Sierpinski pre-fractals are tabulated in Table 9. These values must be scaled prior to application to edges in the corresponding tessellation in accordance with the theory presented in Section 2.

Temperature distributions on pre-fractal $\widehat{E}_3$ and $\widehat{T}_3$ for different tessellation refinements with results determined using the UoM-FEC are depicted in Fig. 17. The different tessellations are obtained

Table 8
Tessellation maps for the Sierpinski gasket.

$P_1(x,y)$	$P_{11}(x,y) = \left(\frac{x}{2} + \frac{y}{2\sqrt{3}}, \frac{2y}{3}\right)$	if $2x < \ell_0$ and $\sqrt{3}y < x$
	$P_{12}(x,y) = \left(\frac{3x}{4} - \frac{y}{4\sqrt{3}}, \frac{x}{4\sqrt{3}} + \frac{5y}{12}\right)$	if $\sqrt{3}y \leqslant \ell_0 - x$ and $\sqrt{3}y \geqslant x$
	$P_{13}(x,y) = \left(\frac{3x}{4} - \frac{y}{4\sqrt{3}}, \frac{x}{4\sqrt{3}} + \frac{5y}{12}\right)$	if $\sqrt{3}y > \ell_0 - x$ and $2x < \ell_0$
	$P_{14}(x,y) = \left(\frac{3x}{4} - \frac{y}{4\sqrt{3}}, \frac{x}{4\sqrt{3}} + \frac{5y}{12}\right)$	if $\sqrt{3}y \geqslant x$ and $2x \geqslant \ell_0$
	$P_{15}(x,y) = \left(\frac{x}{2} + \frac{y}{2\sqrt{3}}, \frac{2y}{3}\right)$	if $\sqrt{3}y > \ell_0 - x$ and $\sqrt{3}y < x$
	$P_{16}(x,y) = \left(\frac{x}{2} + \frac{y}{2\sqrt{3}}, \frac{2y}{3}\right)$	if $\sqrt{3}y \leqslant \ell_0 - x$ and $2x \geqslant \ell_0$
$P_2(x,y)$	$P_{21}(x,y) = \left(\frac{x}{2} + \frac{\ell_0}{4}, -\frac{x}{2\sqrt{3}} + \frac{2y}{3} + \frac{\sqrt{3}\ell_0}{4}\right)$	if $2x < \ell_0$ and $\sqrt{3}y < x$
	$P_{22}(x,y) = \left(\frac{x}{2} + \frac{\ell_0}{4}, -\frac{x}{2\sqrt{3}} + \frac{2y}{3} + \frac{\sqrt{3}\ell_0}{4}\right)$	if $\sqrt{3}y \leqslant \ell_0 - x$ and $\sqrt{3}y \geqslant x$
	$P_{23}(x,y) = \left(\frac{x}{2} + \frac{\ell_0}{4}, -\frac{x}{2\sqrt{3}} + \frac{2y}{3} + \frac{\sqrt{3}\ell_0}{4}\right)$	if $\sqrt{3}y > \ell_0 - x$ and $2x < \ell_0$
	$P_{24}(x,y) = \left(\frac{x}{2} + \frac{\ell_0}{4}, \frac{x}{2\sqrt{3}} + \frac{2y}{3} + \frac{\ell_0}{4\sqrt{3}}\right)$	if $\sqrt{3}y \geqslant x$ and $2x \geqslant \ell_0$
	$P_{25}(x,y) = \left(\frac{x}{2} + \frac{\ell_0}{4}, \frac{x}{2\sqrt{3}} + \frac{2y}{3} + \frac{\ell_0}{4\sqrt{3}}\right)$	if $\sqrt{3}y > \ell_0 - x$ and $\sqrt{3}y < x$
	$P_{26}(x,y) = \left(\frac{x}{2} + \frac{\ell_0}{4}, \frac{x}{2\sqrt{3}} + \frac{2y}{3} + \frac{\ell_0}{4\sqrt{3}}\right)$	if $\sqrt{3}y \leqslant \ell_0 - x$ and $2x \geqslant \ell_0$
$P_3(x,y)$	$P_{31}(x,y) = \left(\frac{x}{2} - \frac{y}{2\sqrt{3}} + \frac{\ell_0}{2}, \frac{2y}{3}\right)$	if $2x < \ell_0$ and $\sqrt{3}y < x$
	$P_{32}(x,y) = \left(\frac{x}{2} - \frac{y}{2\sqrt{3}} + \frac{\ell_0}{2}, \frac{2y}{3}\right)$	if $\sqrt{3}y \leqslant \ell_0 - x$ and $\sqrt{3}y \geqslant x$
	$P_{33}(x,y) = \left(\frac{3x}{4} + \frac{y}{4\sqrt{3}} + \frac{\ell_0}{4}, -\frac{x}{4\sqrt{3}} + \frac{5y}{12} + \frac{\ell_0}{4\sqrt{3}}\right)$	if $\sqrt{3}y > \ell_0 - x$ and $2x < \ell_0$
	$P_{34}(x,y) = \left(\frac{3x}{4} + \frac{y}{4\sqrt{3}} + \frac{\ell_0}{4}, -\frac{x}{4\sqrt{3}} + \frac{5y}{12} + \frac{\ell_0}{4\sqrt{3}}\right)$	if $\sqrt{3}y \geqslant x$ and $2x \geqslant \ell_0$
	$P_{35}(x,y) = \left(\frac{3x}{4} + \frac{y}{4\sqrt{3}} + \frac{\ell_0}{4}, -\frac{x}{4\sqrt{3}} + \frac{5y}{12} + \frac{\ell_0}{4\sqrt{3}}\right)$	if $\sqrt{3}y > \ell_0 - x$ and $\sqrt{3}y < x$
	$P_{36}(x,y) = \left(\frac{x}{2} - \frac{y}{2\sqrt{3}} + \frac{\ell_0}{2}, \frac{2y}{3}\right)$	if $\sqrt{3}y \leqslant \ell_0 - x$ and $2x \geqslant \ell_0$

(i) $\hat{E}_0$ with 18 elements

(ii) $\hat{T}_1$ with 3×18 elements

(iii) $\hat{E}_1$ with 3×18 elements

(iv) $\hat{E}_0$ with 3×162 elements

(v) $\hat{T}_1$ with 3×162 elements

(vi) $\hat{E}_1$ with 3×162 elements

Fig. 16. Pre-fractals and tessellations for the Sierpinski Gasket with different meshes.

by application of different numbers of tiles to the initial triangular domain $\hat{E}_0$, i.e. 6, $18 = 3 \times 6$, $54 = 3^2 \times 6$ and $162 = 3^3 \times 6$. The initial tessellations are obtained using an IFS with the maps defined in Table 9. Examination of the tessellated and pre-fractal domains in

Fig. 17 confirms convergence of the results. These results can be contrasted with those obtained by ABAQUS directly for the domain $\hat{E}_3$ depicted in Fig. 18. The meshing routine in ABAQUS provides a slightly different number of elements per pre-fractal element. It is

Table 9
Heat transfer coefficients for the Sierpinski gasket heat exchanger.

d_s^{hole} (m)	0.289	0.144	0.072	0.036	0.018
$\hat{h}_s^{hole}$ (W/m² K)	11823.4	5249.4	2330.6	1034.8	459.4

evident however on comparison of Figs. 17 and 18 that remarkably similar temperatures are obtained despite the continuity restriction placed on the results obtained from the UoMFEC. The results provide further confidence in the proposed methodology of using
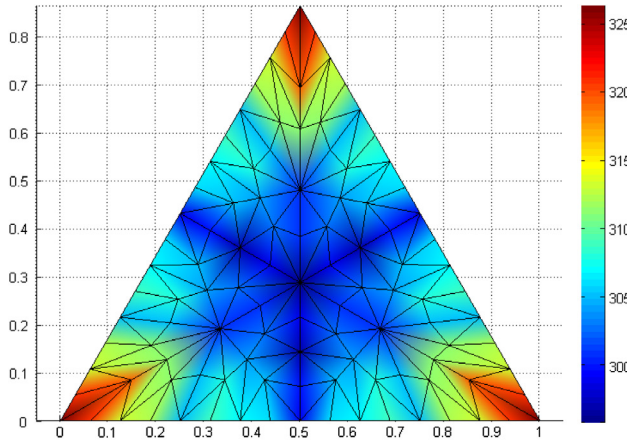
(i) $\hat{T}_3$ with 6 tiles on $\hat{E}_0$
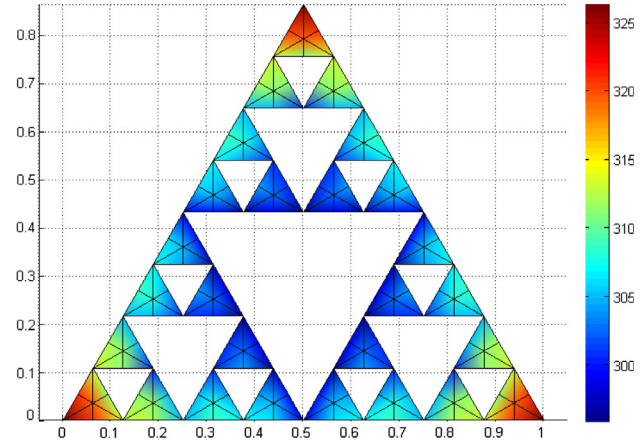
(ii) $\hat{E}_3$ with 6 tiles on $\hat{E}_0$
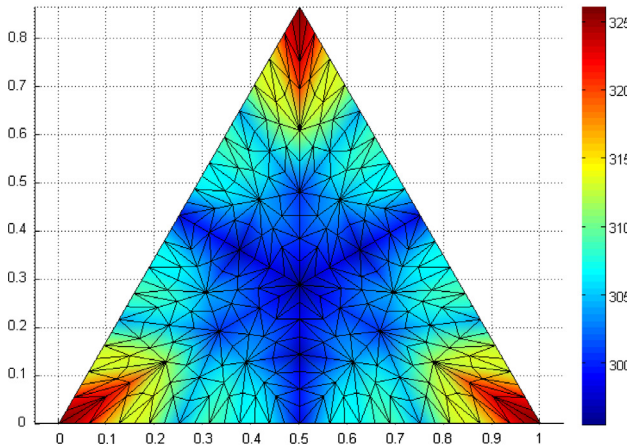
(iii) $\hat{T}_3$ with 18 tiles on $\hat{E}_0$
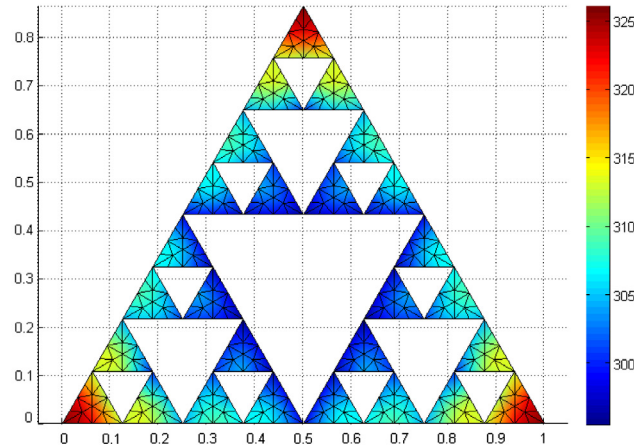
(iv) $\hat{E}_3$ with 18 tiles on $\hat{E}_0$
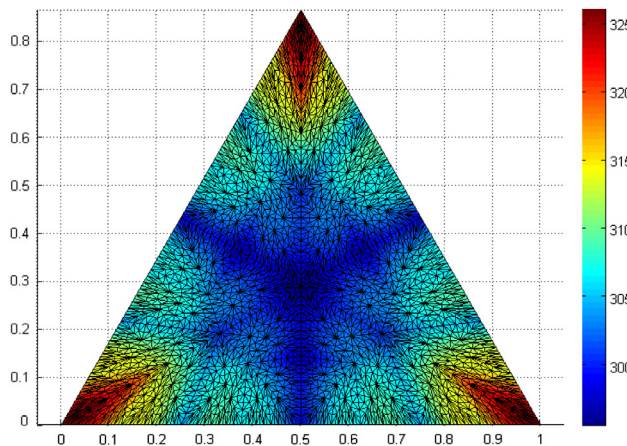
(v) $\hat{T}_3$ with 162 tiles on $\hat{E}_0$
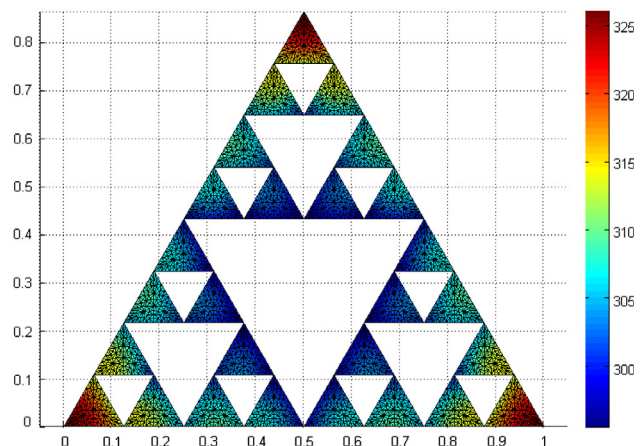
(vi) $\hat{E}_3$ with 162 tiles on $\hat{E}_0$

Fig. 17. UoMFEC contour temperatures on $\hat{T}_3$ and $\hat{E}_3$ with different meshes.
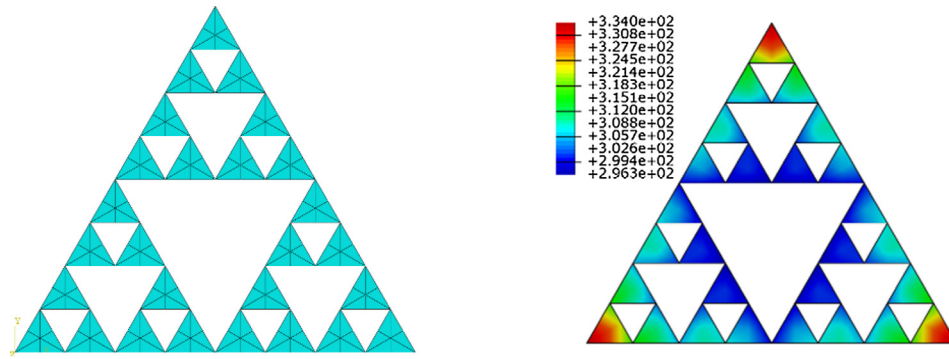
(i) $\hat{E}_3$ with 6 tiles per pre-fractal element
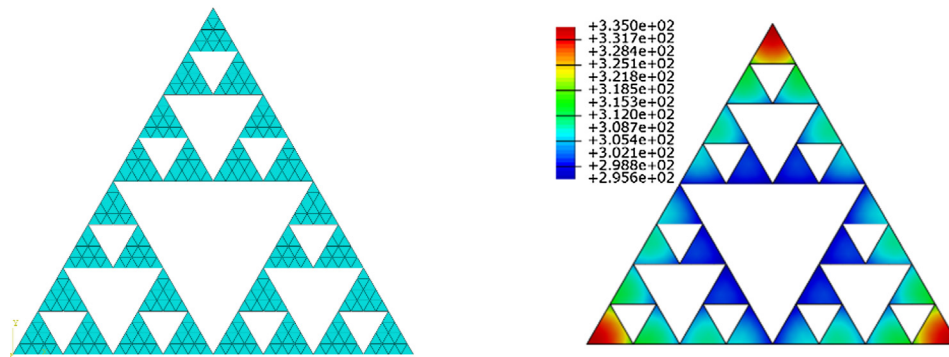
(ii) $\hat{E}_3$ with 16 tiles per pre-fractal element
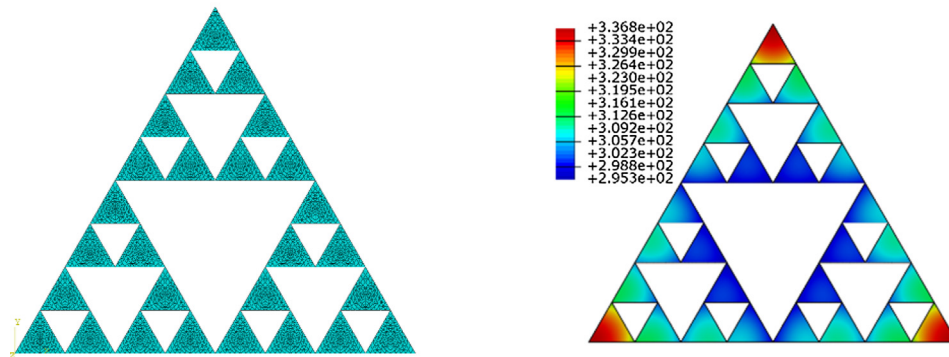
(iii) $\hat{E}_3$ with 150 tiles per pre-fractal element
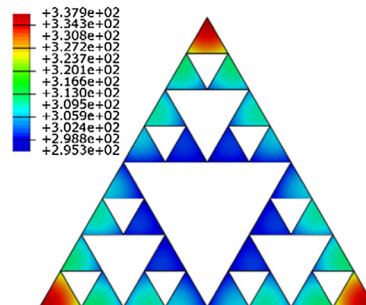
(iv) $\hat{E}_3$ with 1536 tiles per pre-fractal element

Fig. 18. ABAQUS contour temperature plots on $\hat{E}_3$ directly for various meshes.

Table 10
Average temperature errors on Sierpinski pre-fractals along $x = 0$.

k	Number of tiles on $\widehat{E}_0$	UoMFEC vs ABAQUS (coarse) on $\widehat{E}_k$		UoMFEC vs ABAQUS (fine) on $\widehat{E}_k$	
		$\overline{D}$ (K)	$\overline{D}_\%$ (%)	$\overline{D}$ (K)	$\overline{D}_\%$ (%)
1	6	2.2778	0.6049	5.5767	1.4025
	18	2.0637	0.5337	1.8220	0.4540
	162	0.4399	0.1156	0.2614	0.0694
2	6	2.7703	0.8155	3.3962	1.0166
	18	3.1598	0.9342	3.7012	1.0973
	162	3.6382	1.0788	3.9415	1.1770
3	6	2.3360	0.7138	3.7942	1.1506
	18	2.6484	0.8068	3.5763	1.0827
	162	3.1908	0.9680	3.4138	1.0353

a tessellated continuum to provide predictions on structures with lacunae. The average errors quantified using Eqs. (26) and (27) are provided in Table 10 for the edge $x = 0$. In addition, the temperature distribution on $\widehat{E}_1$ along the edge $x = 0$ is presented in Fig. 19.

Both Table 10 and Fig. 19 confirm good accuracy with results obtained using the UoMFEC on $\widehat{T}_k$ and subsequently mapped to $\widehat{E}_k$ and contrasted in ABAQUS results applied directly to $\widehat{E}_k$.

The average error obtained using Eq. (27) is recorded with mesh refinement in order to estimate the size of the modelling error, which is the error remaining on convergence. The modelling error is defined here to be the difference between results obtained from fully converged solutions from the UoMFEC and ABAQUS applied directly to the pre-fractal. The errors are presented in Table 11 and Fig. 20 on $\widehat{E}_k$ where mesh refinement is achieved by increasing

Table 11
Percentage errors on $\widehat{E}_k$ with mesh refinement.

$\ln(\ell/h)$		3.7274	4.8260	5.9246	7.0232	8.1218	9.2204
Error (%)	On $\widehat{E}_1$	10.2324	0.3111	0.1842	1.2603	1.2224	1.2224
	On $\widehat{E}_2$	3.2461	0.9576	0.9942	0.9113	0.9167	0.9230
	On $\widehat{E}_3$	1.1019	1.1031	1.0992	1.0947	1.0920	1.0917

(i) on $\hat{T}_1$

(ii) on $\hat{T}_3$
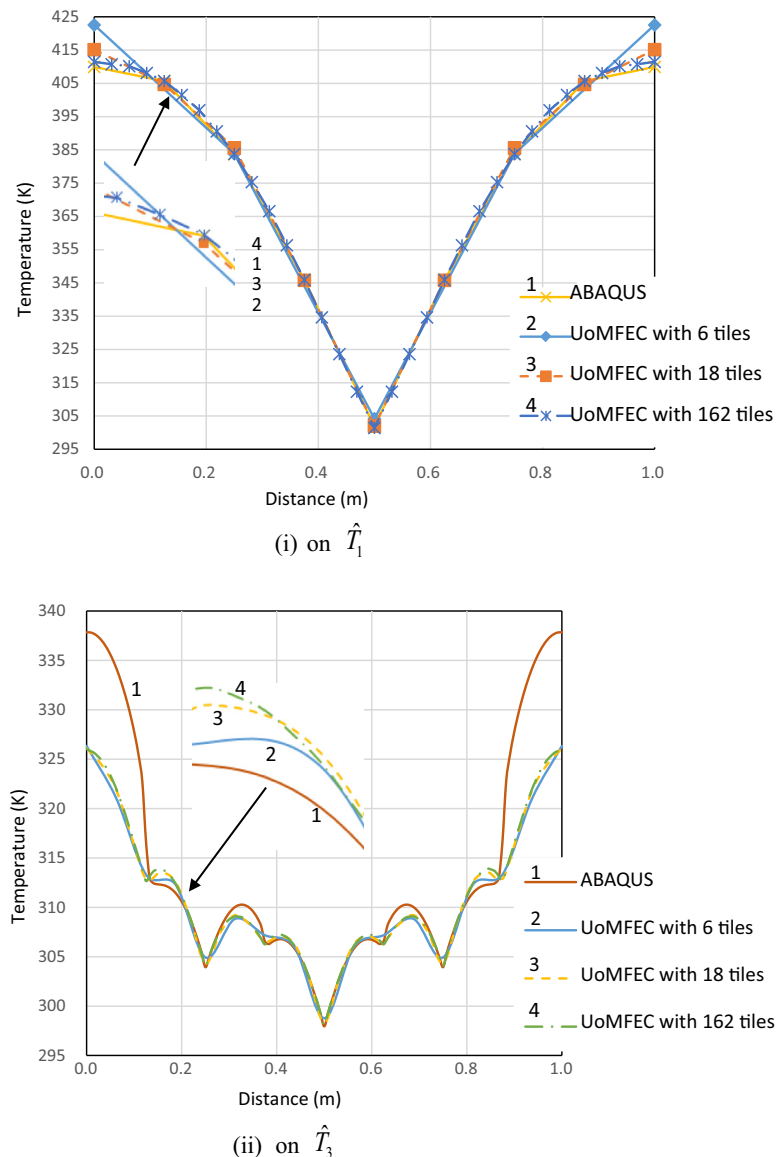
Fig. 19. Temperature plots along $x = 0$ on $\hat{T}_1$ for various tiles per pre-fractal element using ABAQUS and the UoMFEC.

Table 12
Heat transfer rates for Sierpinski pre-fractals with 162 tiles on $\widehat{E}_0$.

			Heat supplied to coolant on $\widehat{E}_k$					
			$\widehat{E}_1$	$\widehat{E}_2$	$\widehat{E}_3$	$\widehat{E}_4$	$\widehat{E}_5$	$\widehat{E}_6$
Cooling channel data	Heat transfer per hole (kW) Hydraulic Diameter (d_i)	d_1	284.80	126.39	91.89	78.68	72.24	68.71
		d_2		173.69	113.16	92.02	82.18	76.85
		d_3			98.52	79.03	69.91	65.02
		d_4				55.01	48.70	45.23
		d_5					32.25	29.97
		d_6						19.80
	The total correct energy transfer (kW)		284.80	299.44	302.81	303.79	304.05	304.05
	Total (kW)		284.80	300.08	303.57	304.74	305.28	305.58
	Incremental change in heat loss (kW)			15.28	3.49	1.17	0.54	0.30
	Percentage change in heat loss (%)			5.37	1.16	0.38	0.18	0.10
Heat loss to boundary (kW)			15.20	-0.08	-3.57	-4.74	-5.28	-5.58
Modelling error ε_∞ at the external boundary (kW)			0.02	0.83	0.86	1.03	1.30	1.59
Total heat loss (kW)			300.00	300.00	300.00	300.00	300.00	300.00
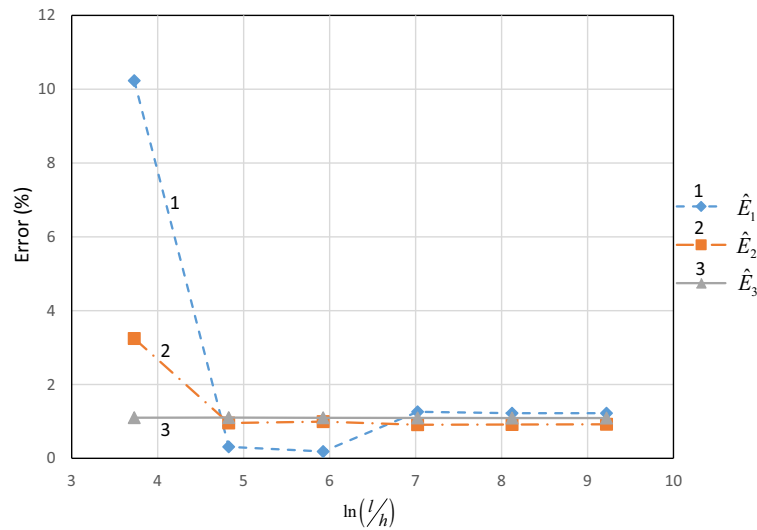
Fig. 20. Percentage error plots on $\widehat{E}_k$ showing magnitudes of modelling errors on convergence.

Table 13
Heat transfer coefficients for the Sierpinski carpet heat exchanger.

d_s^{hole} (m)	0.333	0.111	0.037	0.012	0.004
$\hat{h}_s^{hole}$ (W/m² K)	12735.0	1460.1	167.4	19.2	2.2

Table 14
Average temperature errors on Sierpinski pre-fractals along $x = 0$.

k	UoMFEC vs ABAQUS (coarse) on $\widehat{E}_k$		UoMFEC vs ABAQUS (fine) on $\widehat{E}_k$	
	$\overline{D}$ (K)	$\overline{D}_\%$ (%)	$\overline{D}$ (K)	$\overline{D}_\%$ (%)
1	3.1738	0.8647	5.1345	1.2330
2	3.2674	0.9123	3.2976	0.9053
3	4.6927	1.3354	5.0856	1.4442

the number of tiles on $\widehat{E}_0$. The table and plots confirm convergence but a small modelling error remains on each $\widehat{E}_k$.

From a thermal analysis perspective it is of interest to determine energy transfers on each pre-fractal. These can be found in Table 12 which confirm the stabilisation of transfer rates as k increases due to increasingly refined changes in $\widehat{E}_k$ and a diminishing cooling ability for holes of small hydraulic diameter. Also presented in Table 12 are the energy transfer rates to the cooling channels obtained from a converged ABAQUS model along with the corresponding modelling error calculated using

$$\varepsilon_\infty = \max \|X - X_{exact}\|_\infty \tag{39}$$

Errors in heat fluxes can be anticipated since these are represented with Robin boundary conditions at the pre-fractal holes involving heat transfer coefficients. In the tessellation these heat transfer coefficients are suitably scaled and applied to element edges and
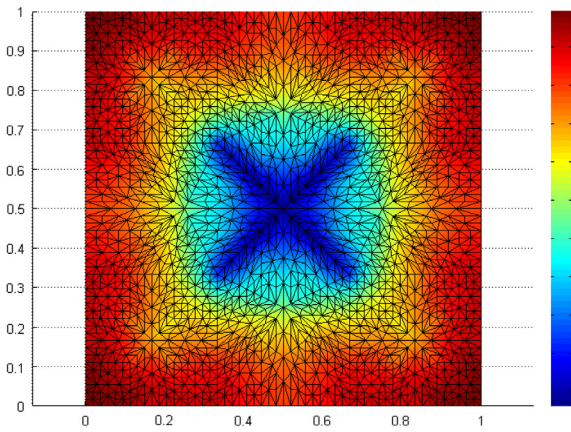
(i) UoMFEC on $\hat{T}_3$ with 8 tiles on $\hat{E}_0$
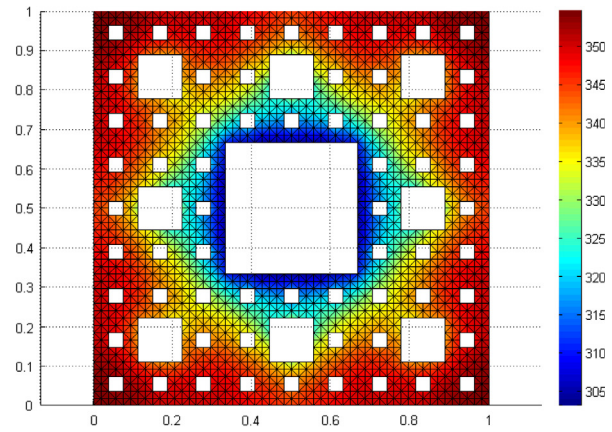
(ii) UoMFEC on $\hat{E}_3$ with 8 tiles on $\hat{E}_0$
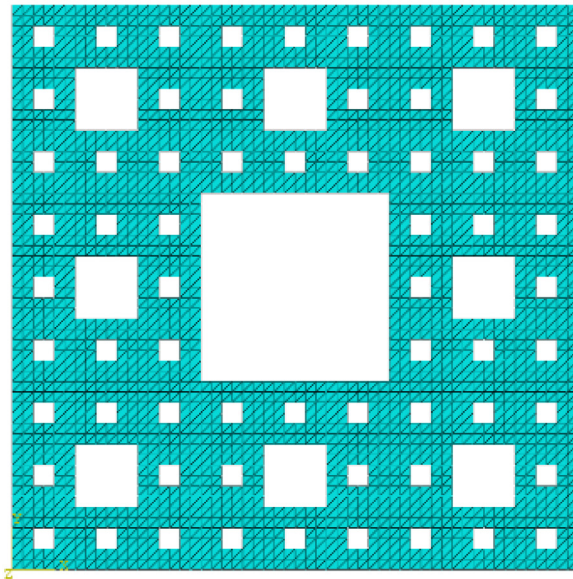
(iii) ABAQUS on $\hat{E}_3$ with 8 elements per pre-fractal element
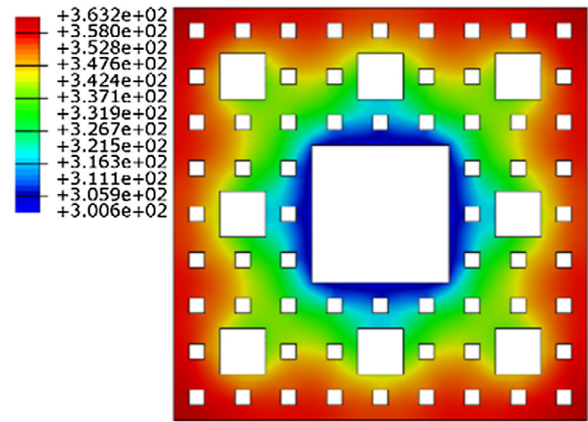
(iv) ABAQUS on $\hat{E}_3$ with 152 elements per pre-fractal element

Fig. 21. Contour temperature plots for $\hat{E}_3$ using the UoMFEC and ABAQUS.

there is no error involved in that aspect but because temperatures are assumed continuous the heat-fluxes are slightly different and hence a source of error. It is apparent on examination of Table 12 however that these errors are relatively small.
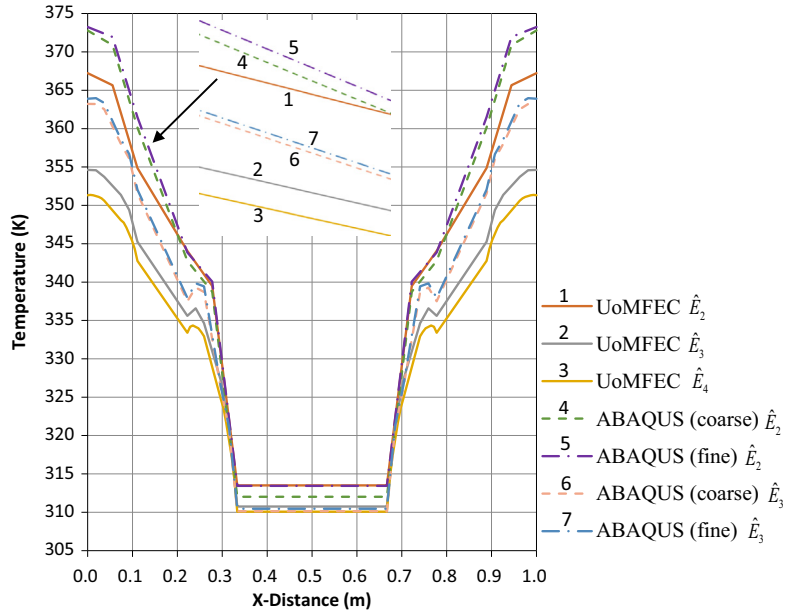
Fig. 22. Temperature plots along $x = y$ for pre-fractals $\hat{E}_3$ using the UoMFEC and ABAQUS.

Table 15
Material properties of water at temperature $T_{wat} = 293$ K [41].

Thermal conductivity (Wm^{-1} K^{-1})	598.4×10^{-3}
Viscosity (kg/ms)	1002×10^{-6}
Specific heat capacity (kJ/kg K)	4.183

Table 16
Contraction maps for Sierpinski carpet.

$S_1(x,y) = \left(\frac{x}{3}, \frac{y}{3}\right)$	$S_2(x,y) = \left(\frac{\ell_0}{3} + \frac{x}{3}, \frac{y}{3}\right)$
$S_3(x,y) = \left(\frac{2\ell_0}{3} + \frac{x}{3}, \frac{y}{3}\right)$	$S_4(x,y) = \left(\frac{x}{3}, \frac{\ell_0}{3} + \frac{y}{3}\right)$
$S_5(x,y) = \left(\frac{2\ell_0}{3} + \frac{x}{3}, \frac{\ell_0}{3} + \frac{y}{3}\right)$	$S_6(x,y) = \left(\frac{x}{3}, \frac{2\ell_0}{3} + \frac{y}{3}\right)$
$S_7(x,y) = \left(\frac{\ell_0}{3} + \frac{x}{3}, \frac{2\ell_0}{3} + \frac{y}{3}\right)$	$S_8(x,y) = \left(\frac{2\ell_0}{3} + \frac{x}{3}, \frac{2\ell_0}{3} + \frac{y}{3}\right)$

Table 17
Tessellation maps for Sierpinski carpet.

$P_2(x,y)$	$P_{21}(x,y) = \left(\frac{1}{3} + \frac{x}{3}, \frac{1}{3} + \frac{y}{3}\right)$	if $y \geqslant 2x$ and $2x \leqslant 1$
	$P_{22}(x,y) = \left(\frac{1}{3} + \frac{x}{3}, \frac{1}{3} - \frac{x}{3} + \frac{y}{3}\right)$	if $y \geqslant 2(1-x)$ and $2x > 1$
	$P_{23}(x,y) = \left(\frac{x}{2}, \frac{1}{3} + \frac{y}{3}\right)$	otherwise
$P_4(x,y)$	$P_{41}(x,y) = \left(\frac{1}{3} + \frac{x}{3}, \frac{1}{3} + \frac{y}{3}\right)$	if $2y \leqslant x$ and $2y \leqslant 1$
	$P_{42}(x,y) = \left(\frac{1}{3} + \frac{x}{3} - \frac{y}{3}, \frac{1}{3} + \frac{y}{3}\right)$	if $2y \geqslant (2-x)$ and $2y > 1$
	$P_{43}(x,y) = \left(\frac{x}{2}, \frac{1}{3} + \frac{y}{3}\right)$	otherwise
$P_5(x,y)$	$P_{51}(x,y) = \left(\frac{2}{3} + \frac{x}{3} - \frac{y}{3}, \frac{1}{3} + \frac{y}{3}\right)$	if $2y \leqslant 1 - x$ and $2y \leqslant 1$
	$P_{52}(x,y) = \left(\frac{1}{3} + \frac{x}{3} + \frac{y}{3}, \frac{1}{3} + \frac{y}{3}\right)$	if $2y \geqslant 1 - x$ and $2y > 1$
	$P_{53}(x,y) = \left(\frac{1}{2} + \frac{x}{2}, \frac{1}{3} + \frac{y}{3}\right)$	otherwise
$P_7(x,y)$	$P_{71}(x,y) = \left(\frac{1}{3} + \frac{x}{3}, \frac{2}{3} - \frac{x}{3} + \frac{y}{3}\right)$	if $y \leqslant 2 - 2x$ and $2x \leqslant 1$
	$P_{72}(x,y) = \left(\frac{1}{3} + \frac{x}{3}, \frac{1}{3} - \frac{x}{3} + \frac{y}{3}\right)$	if $y \leqslant -1 + 2x$ and $2x > 1$
	$P_{73}(x,y) = \left(\frac{1}{3} + \frac{x}{3}, \frac{1}{2} + \frac{y}{2}\right)$	otherwise

7.3. Thermal analysis of a Sierpinski carpet heat exchanger

The construction of pre-fractals and corresponding tessellations for Sierpinski carpet are relegated to Appendix B. The heat exchanger is manufactured from the same copper material used for the Sierpinske gasket with same surrounding conditions as described in Section 7.2, with water flowing through the voids shown in Fig. 2. A volumetric heat loading $\dot{Q}_{tot} = 500$ kW/m^3 is applied and appears uniform on the tessellation. Heat transfer coefficient

$\hat{h}_s^{hole}$ with different size of hydraulic diameter d_s^{hole} on Sierpinski carpet pre-fractals are tabulated in Table 13. The heat transfer coefficients on the effected edges in the corresponding tessellation are scaled prior to their application in accordance with the theory in Section 2.

Temperature distributions on $\widehat{E}_3$ and $\widehat{T}_3$ determined by the UoMFEC can be contrasted with those obtained by ABAQUS directly with different numbers of elements depicted in Fig. 20. Eqs. (26) and (27) are used to investigate the average temperature differences along the diagonal line $x = y$ and the results can be found in Table 14. In addition, temperature distributions along $x = y$ on $\widehat{E}_k$ from both the UoMFEC and ABAQUS are presented in Fig. 21. All the results provide confidence in the tessellated continuum methodology with good accuracy returned on $\widehat{E}_k$ (see Fig. 22).

8. Conclusions

This paper tests the hypothesis that heat transfer analysis on cellular structures can be performed with a new proposed form of continuum mechanics coupled to a Galerkin finite element method. The proposed method is validated through a series of tests on pre-fractals of increasing complexity. In establishing the tessellated finite-element approach for thermal analysis the following conclusions can be drawn:

- Transport equations can connect transport phenomena on pre-fractals to those on tessellated continua.
- Thermal analysis on pre-fractals can be achieved indirectly through analysis on a tessellated continuum using a Galerkin finite element method.
- The accuracy of the Galerkin finite element method is reasonable (less than a few percent for the examples considered) although requires reasonably high heat transfer coefficients to be applied to cooling channels to reduce modelling error.
- In order to capture the geometric complexity involved, the thermal conductivity on the tessellated continuum is manifestly different from the pre-fractal material. The principal directions for thermal conductivity on a tile are related to principal stretch directions for the hole-fill map.

Appendix A. Heat transfer coefficient calculation

It is assumed here that the flow is turbulent and fully developed and flowing out of the page in the non-product pre-fractals portrayed in Figs. 1 and 2. It is further assumed that the Dittus-Boelter equation [38] is applicable, i.e.

$$\frac{\hat{h}d}{k} = 0.023 \left(\frac{jd}{\mu}\right)^{0.8} \left(\frac{\mu c_p}{k}\right)^n \tag{40}$$

where $d = 4\hat{A}/\hat{P}$ is the hydraulic diameter, $\hat{A}$ is cross section area, $\hat{P}$ is the wetted perimeter, k is the thermal conductivity of the bulk fluid, μ is viscosity, $j = \rho\hat{A}v$ is mass flux rate, $n = 0.33$ [39] for cooling (wall hotter than the bulk fluid), v is average velocity, ρ is density, c_p specific heat capacity at constant pressure.

The Darcy-Weisbach equation [40] provides a relationship between average velocity v and pressure drop Δp along a channel and is of the form

$$\Delta p = \frac{0.316}{\left(\frac{\rho vd}{\mu}\right)^{1/4}} \left(\frac{L}{d}\right) \rho \left(\frac{v^2}{2}\right) \tag{41}$$

where L is the cooling channel length and fully developed for turbulent flow in the channel is assumed.

Substitution of Eq. (41) into Eq. (40) gives the required heat transfer coefficients for the pre-fractal holes, i.e.

$$\hat{h} = \left(0.0535 \frac{k^{0.67}\hat{A}^{0.8}\rho^{0.457}c_p^{0.33}}{\mu^{0.584}L^{0.457}}\right)\Delta p^{0.457}d^{0.371} \tag{42}$$

Consider then water flowing through the hole at temperature $T_{wat} = 293$ K, where pipe length $L = 1$ m and pressure drop $\Delta p = 50$ kPa. Using the physical parameters for water in Table 15 the heat transfer coefficients calculated using Eq. (42) can be found in Tables 9 and 12 for various hydraulic diameters.

Appendix B. Maps for the Sierpinski carpet

The Sierpinski carpet is a non-product fractal set is constructed by the eight affine contraction maps in Table 16.

Each contraction map, maps a rectangular domain into a smaller rectangular domain as deduced on inspection of Fig. 2. The initial number of tiles on $\widehat{E}_0$ in Fig. 2 is 6, which means that the 8 tessellation maps will each consist of 6 sub-maps although some are identical. The tessellation maps satisfy $P_1 = S_1$, $P_3 = S_3$, $P_6 = S_6$ and $P_8 = S_8$ with the remaining maps defined Table 17 but limited here to distinctive sub-maps.

References

[1] Ishizaki K, Komarneni S, Nanko M. Porous Materials: Process Technology and Applications Softcover reprint of the original, 1st ed.. 1998 ed. Springer; 2014.
[2] Narasimhan A. Essentials of heat and fluid flow in porous media. Boca Raton, Fla.; New Delhi, India: CRC Press; 2012.
[3] Coussy O. Poromechanics. 2Rev ed. Chichester, England; Hoboken, NJ: Wiley-Blackwell; 2003.
[4] Li Q, Flamant G, Yuan X, Neveu P, Luo L. Compact heat exchangers: a review and future applications for a new generation of high temperature solar receivers. Renew Sustain Energy Rev 2011;15(9):4855–75.
[5] Mancin S, Zilio C, Cavallini A, Rossetto L. Pressure drop during air flow in aluminum foams. Int J Heat Mass Transf 2010;53(15–16):3121–30.
[6] Boomsma K, Poulikakos D, Zwick F. Metal foams as compact high performance heat exchangers. Mech Mater 2003;35(12):1161–76.
[7] Yang Z, Cui J, Sun Y, Ge J. Multiscale computation for transient heat conduction problem with radiation boundary condition in porous materials. Finite Elem Anal Des 2015;102–103(Oct.):7–18.
[8] Rashidi S, Bovand M, Esfahani JA. Heat transfer enhancement and pressure drop penalty in porous solar heat exchangers: a sensitivity analysis. Energy Convers Manag 2015;103(Oct.):726–38.
[9] Su Y, Davidson JH. A Non-Dimensional Lattice Boltzmann Method for direct and porous medium model simulations of 240-tube bundle heat exchangers in a solar storage tank. Int J Heat Mass Transf 2015;85(Jun.):195–205.
[10] Bhadauria R, Sanghi T, Aluru NR. Interfacial friction based quasi-continuum hydrodynamical model for nanofluidic transport of water. J Chem Phys 2015;143(17):174702.
[11] Beex LAA, Rokoš O, Zeman J, Bordas SPA. Higher-order quasicontinuum methods for elastic and dissipative lattice models: uniaxial deformation and pure bending. GAMM-Mitteilungen 2015;38(2):344–68.
[12] Tremblay Y, Roberts AJ, Costa DP. Fractal landscape method: an alternative approach to measuring area-restricted searching behavior. J Exp Biol 2007;210(6):935–45.
[13] Tarasov VE. Continuous medium model for fractal media. Phys Lett A 2005;336(2–3):167–74.
[14] Tarasov VE. Fractional hydrodynamic equations for fractal media. Ann Phys 2005;318(2):286–307.
[15] Ostoja-Starzewski M. Towards thermoelasticity of fractal media. J Therm Stress 2007;30(9–10):889–96.
[16] Ostoja-Starzewski M. Extremum and variational principles for elastic and inelastic media with fractal geometries. Acta Mech 2009;205(1–4):161–70.
[17] Butera S, Di Paola M. A physically based connection between fractional calculus and fractal geometry. Ann Phys 2014;350:146–58.
[18] Alaimo G, Zingales M. Laminar flow through fractal porous materials: the fractional-order transport equation. Commun Nonlinear Sci Numer Simul 2015;22(1–3):889–902.
[19] Davey K, Prosser R, Jiang C. Heat transfer through fractal-like porous media: a tessellated continuum approach. Comput Struct 2015;151(Apr.):58–72.
[20] Oden JT, Prudhomme S. Estimation of modeling error in computational mechanics. J Comput Phys 2002;182(2):496–515.
[21] Kerfriden P, Alves Paladim D, Ródenas García JJ, Bordas SP-A. A posteriori error estimation for POD-based reduced order modelling with application in homogenisation. In: International conference on computational mechanics (CM13), Durham, United Kingdom; 2013. p. 1–6.
[22] Strouboulis T, Babuška I, Copps K. The design and analysis of the Generalized Finite Element Method. Comput Methods Appl Mech Eng 2000;181(1–3):43–69.
[23] An X, Ma G, Cai Y, Zhu H. A new way to treat material discontinuities in the numerical manifold method. Comput Methods Appl Mech Eng 2011;200(47–48):3296–308.
[24] Babuška I, Banerjee U. Stable generalized finite element method (SGFEM). Comput Methods Appl Mech Eng 2012;201–204(Jan.):91–111.
[25] Cockburn B, Shu C-W. Runge–Kutta discontinuous Galerkin methods for convection-dominated problems. J Sci Comput 2001;16(3):173–261.
[26] Krishna Murthy SVSSNVG, Kumar BVR, Nigam M. A parallel finite element study of 3D mixed convection in a fluid saturated cubic porous enclosure under injection/suction effect. Appl Math Comput 2015;269(Oct.):841–62.
[27] Ren B, Wen H, Dong P, Wang Y. Improved SPH simulation of wave motions and turbulent flows through porous media. Coast Eng 2016;107(Jan.):14–27.
[28] Rong F, Shi B, Cui X. Lattice Boltzmann simulation of heat and fluid flow in 3D cylindrical heat exchanger with porous blocks. Appl Math Comput 2016;276(Mar.):367–78.
[29] Tseng C-C, Li C-J. Numerical investigation of the inertial loss coefficient and the porous media model for the flow through the perforated sieve tray. Chem Eng Res Des 2016;106(Feb.):126–40.
[30] Valdés-Parada FJ, Álvarez Ramírez J, Ochoa-Tapia JA. Upscaling diffusion waves in porous media. Phys Stat Mech Its Appl 2016;448:57–67.
[31] Vondřejc J, Zeman J, Marek I. An FFT-based Galerkin method for homogenization of periodic media. Comput Math Appl 2014;68(3):156–73.
[32] Kerfriden P, Schmidt KM. Statistical extraction of process zones and representative subspaces in fracture of random composites. Int J Multiscale Comput Eng 2013;11(3):253–87.
[33] Kerfriden P, Goury O, Rabczuk T, Bordas SPA. A partitioned model order reduction approach to rationalise computational expenses in nonlinear fracture mechanics. Comput Methods Appl Mech Eng 2013;256(Apr.):169–88.
[34] Taguas FJ, Martín MA, Perfect E. Simulation and testing of self-similar structures for soil particle-size distributions using iterated function systems. In: JWC, Pachepsky WJRY, editors. Developments in Soil Science, vol. 27, Ed. Elsevier, 2000. p. 101–13.
[35] Darvizeh R, Davey K. Non-physical finite element modelling of high speed normal crushing of cellular materials. Int J Impact Eng 2015;82(Aug.):130–43.
[36] Davey K, Prosser R. Analytical solutions for heat transfer on fractal and pre-fractal domains. Appl Math Model 2013;37(1–2):554–69.
[37] Falconer K. Fractal geometry: mathematical foundations and applications.
[38] Dittus FW, Boelter LMK. Heat transfer in automobile radiators of the tubular type. Int Commun Heat Mass Transf 1985;12(1):3–22.
[39] Kreith F. The CRC handbook of thermal engineering. Springer-Verlag Berlin and Heidelberg GmbH & Co. KG; 2013.
[40] Mechanics Fluid. An introduction to the theory of fluid flows. 2008 ed. Berlin: Springer; 2008.
[41] Rogers GFC, Mayhew YR. Thermodynamic and Transport Properties of Fluids: S. I. Units. 5th ed. Oxford: Wiley-Blackwell; 1994.

Chapter 5.

Paper 3: A TESSELLATED CONTINUUM APPROACH TO THERMAL ANALYSIS: DISCONTINUITY NETWORKS

Due to the discontinuous behaviour of pre-fractals, discontinuity networks are introduced as described in this chapter. Although the strategy for closing holes in pre-fractals is changed, the structure and the material properties are the same between the tessellations with and without discontinuity networks. The Galerkin finite element method with discontinuity networks is then applied to investigate the thermal behaviour of pre-fractals.

The temperature distributions from the tessellated approach with and without discontinuity networks are nearly the same. However, the discontinuity networks can improve significantly the accuracy of the approach. Mesh refinement is achieved through increasing the number of tiles in the original set of pre-fractals. The results show that the modelling error is reduced from that of tessellations without discontinuity networks. Because the hole-fill maps are not unique, further tests are carried out to show that there is little impact on the mapped result from different tessellations.

The concept of discontinuity network was introduced by C. Jiang. The tests and the results presented in this chapter were designed and generated by C. Jiang. The manuscript was written by K. Davey and C. Jiang, with technical and editorial supervision and proofing provided by R. Prosser.

A tessellated continuum approach to
thermal analysis: discontinuity networks

C. Jiang, K. Davey & R. Prosser

A 20987

ONLINE FIRST

28

4

Continuum
Mechanics and
Thermodynamics
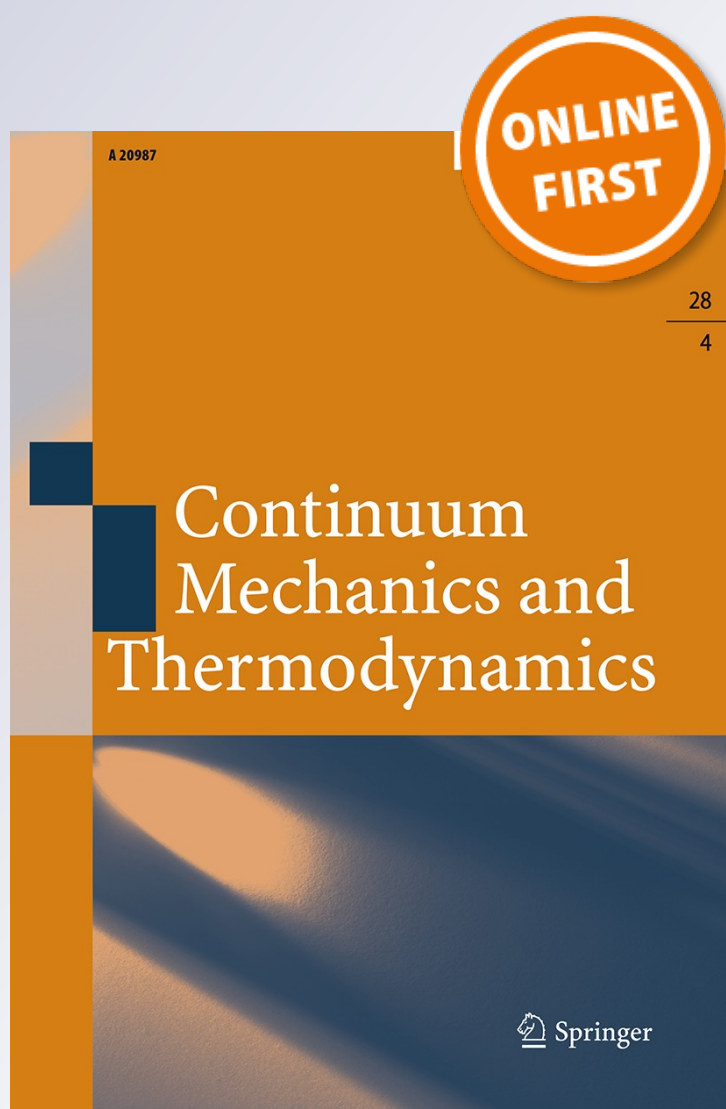
🔖 Springer

🔖 Springer

Springer

CrossMark

ORIGINAL ARTICLE

C. Jiang · K. Davey · R. Prosser

A tessellated continuum approach to thermal analysis: discontinuity networks

Abstract Tessellated continuum mechanics is an approach for the representation of thermo-mechanical behaviour of porous media on tessellated continua. It involves the application of iteration function schemes using affine contraction and expansion maps, respectively, for the creation of porous fractal materials and associated tessellated continua. Highly complex geometries can be produced using a modest number of contraction mappings. The associated tessellations form the mesh in a numerical procedure. This paper tests the hypothesis that thermal analysis of porous structures can be achieved using a discontinuous Galerkin finite element method on a tessellation. Discontinuous behaviour is identified at a *discontinuity network* in a tessellation; its use is shown to provide a good representation of the physics relating to cellular heat exchanger designs. Results for different cellular designs (with corresponding tessellations) are contrasted against those obtained from direct analysis and very high accuracy is observed.

Keywords Heat exchangers · Heat transfer · Transport theory · Porous fractals · Analytical solutions · Finite elements

1 Introduction

In the recently developed method of tessellated continuum mechanics, physics defined on fractal porous media is mapped to a corresponding continuum [1,2]. The classical Galerkin finite element method (GFEM) can then be combined with tessellated continuum mechanics to describe thermal physics in cellular structures. The drawback with the Galerkin approach, however, is that discontinuous behaviour arising from the closing of the pores during the mapping (which is pervasive on tessellations) cannot readily be accommodated. This paper extends the work in references [1,2] by incorporating a network of lines/surfaces on a tessellation at which discontinuous behaviour occurs. The discontinuities can be viewed as enforcing internal boundary conditions where (say) heat fluxes on different parts of a pore's surface are mapped to a single line. The new feature is called a *discontinuity network* and is designed to capture more completely the physics on cellular materials.

Many natural materials possess hierarchical microstructures extending over length scales that cover many orders of magnitude [3]. Those microstructures observed with geometric similarity over a range of scales are denoted as self-similar [4]. Self-similar objects possessing interesting mathematical properties have received the attention of researchers in many fields including mathematics, biology, chemistry and engineering. Analysis of these types of structures falls under the heading of multi-scale modelling [5], where physical self-similarity can in principle be used to describe scaling relationships connecting behaviours across a range of length scales.

C. Jiang · K. Davey (✉) · R. Prosser
School of Mechanical, Aerospace and Civil Engineering, The University of Manchester, Manchester, UK
E-mail: keith.davey@manchester.ac.uk

Of particular interest in this paper is the behaviour of self-similar porous structures subject to fluid-induced thermal loading.

The performance of heat exchangers involving thermo-fluids and cellular materials is an area of practical interest, designs of which can be found in everyday use for the cooling of printed circuit boards [6]. Self-similar porous materials that maximise fluid–solid contact areas offer potentially very high rates of heat transfer. This, when combined with high thermal conductivities and good enhancement of fluid mixing, may be exploited for heat exchanger designs [7]. Examples of commercial heat exchangers which incorporate a complex geometrical structure include miniature shell and tube heat designs [8]. Alternative configurations are honeycomb metallic structures [9], metallic foams [10] and plate-fin designs [8]. These designs play an important part in applications requiring high-density energy transfers, and growth in their use and application is expected [8]. Experimental evidence showcasing the benefits of cellular designs can be found in reference [11].

The complex geometries involved in porous/cellular heat exchangers raise particular challenges for analysis. These challenges include: the accurate representation of the geometry; the application of boundary conditions; meshing problems that arise with large and thin sections; and any computational constraints imposed by the large number of elements involved. The standard approach to the analysis of flow through porous heat exchangers would typically not include a direct description of the geometry of the porous media (see
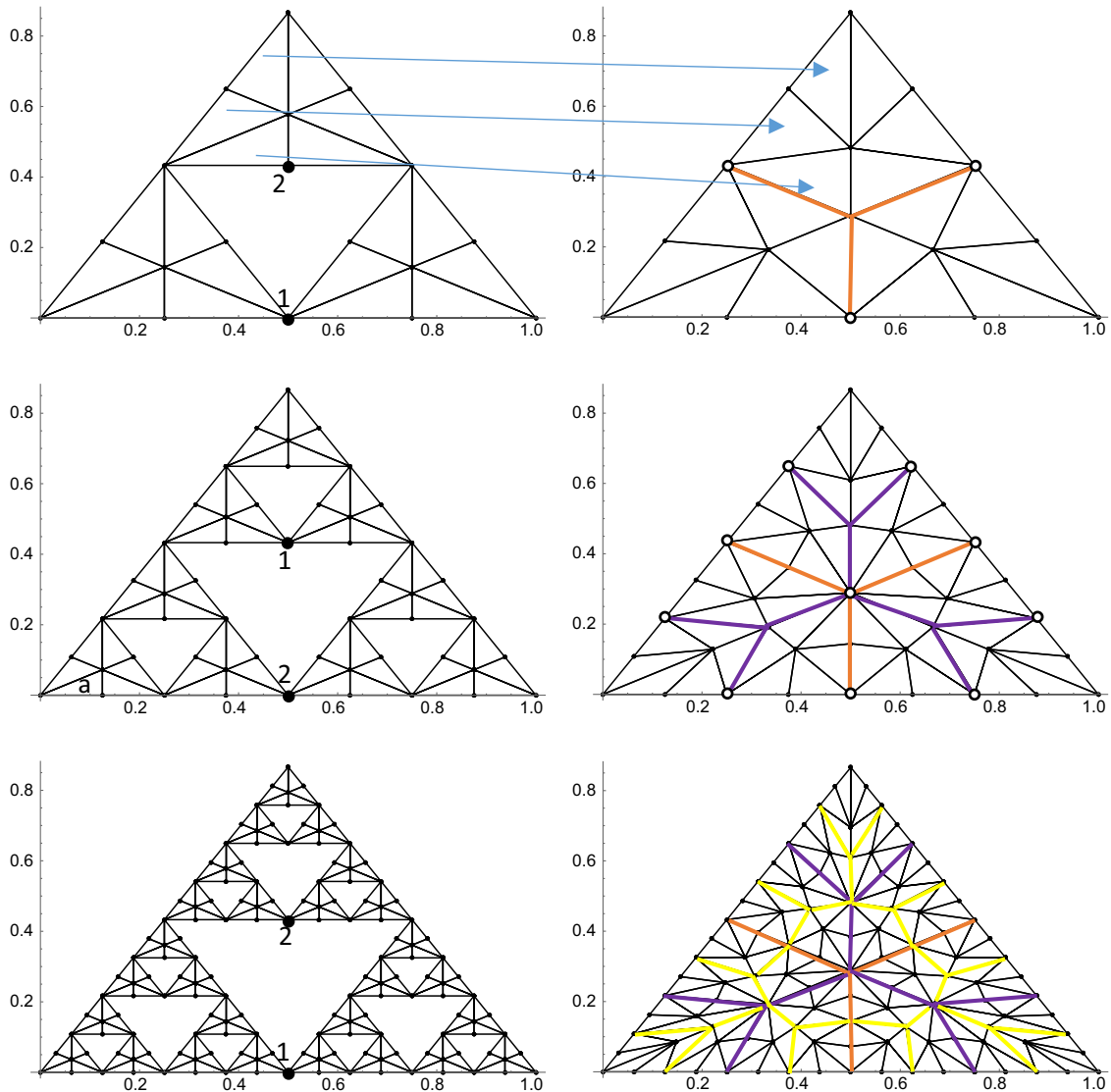
Fig. 1 Pre-fractal and corresponding tessellated domains containing discontinuity networks for the Sierpinski gasket

references [12–14]). Classical approaches founded on continuum equations, and involving coarse-grained geometrical parameters such as porosity and permeability [15] provide limited accuracy. Recent alternatives to these classical treatments include discrete techniques such as the lattice Boltzmann method (LBM), which is particularly attractive for low Reynolds number flows involving complex boundary conditions [16]. An example of pore-scale turbulent flow modelled using LBM is provided in [11], where four types of porous structures are considered. Unfortunately, despite the LBM offering some advantages, it still suffers in a similar manner to continuum approaches as a consequence of the complex geometries involved [17].

In order to represent better the types of complex geometries found in cellular material, the authors have investigated the use of fractals [2,18], which arise in many other areas of science [19] and play a part in describing a variety of behaviours in nonlinear systems [20]. Fractals can be constructed in a number of ways, but a particularly attractive procedure is by application of a small number of affine contraction maps [2,20,21]. Although complex geometries can readily be represented using fractals, their subsequent use in practical analysis is beset with difficulties. The principal concern is the lack of meaningful measures on the fractal, where traditional notions of length, area and volume are undefined as a consequence of non-integer Hausdorff fractal dimensions [22]. Consequently, traditional physical quantities such as fluxes (rates per unit area) and densities (per unit volume) are likewise ill-defined. Attempts to overcome these difficulties can be found in the literature [23,24]. One possible method to avoid the problem altogether is to use *pre-fractals*, which are
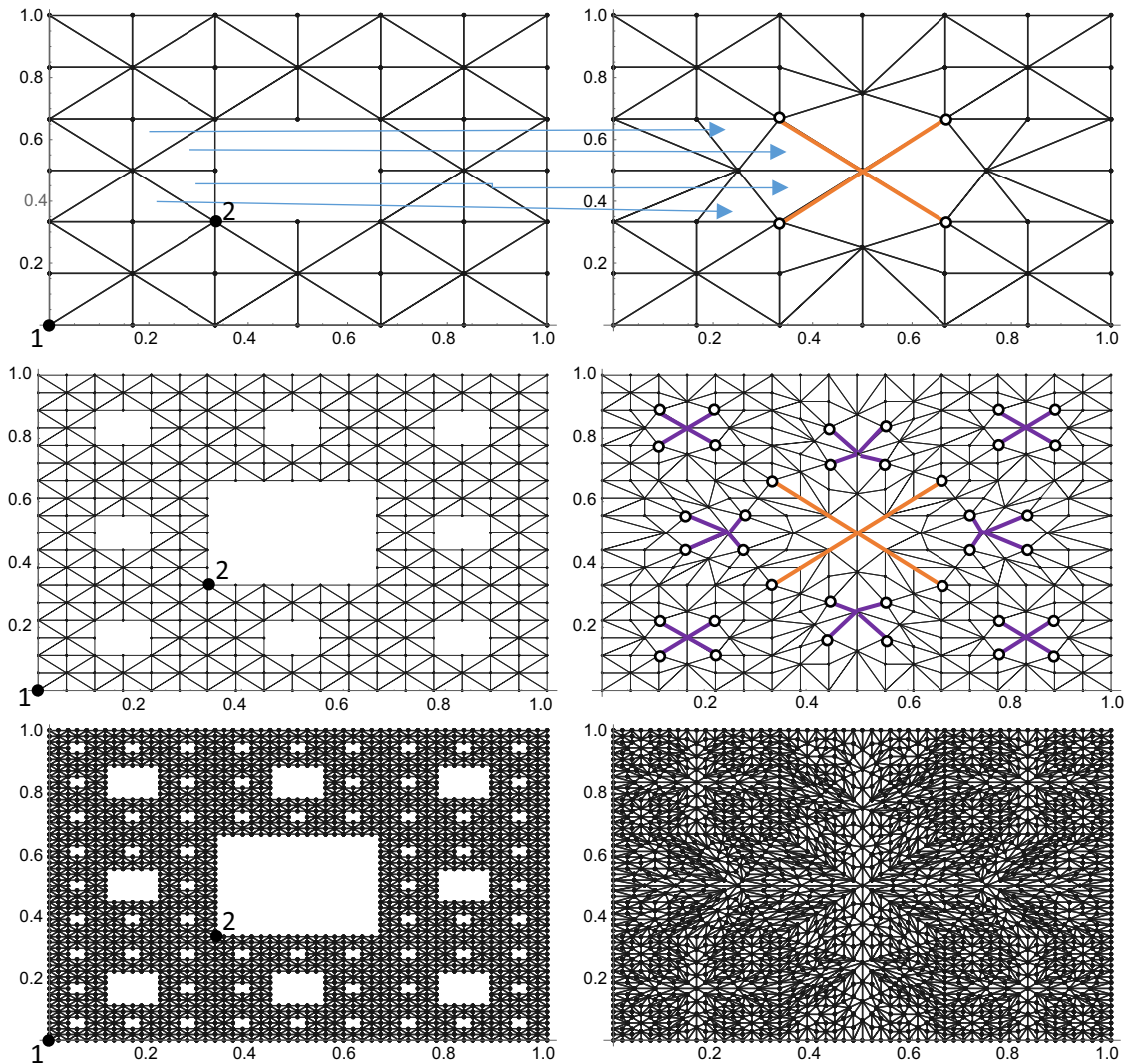
Fig. 2 Pre-fractal and corresponding tessellated domains containing discontinuity networks for the Sierpinski carpet

created with fractal construction procedures, but do not suffer from non-integer Hausdorff fractal dimensions. A popular indirect approach is through the use of fractional derivatives [25,26] in the governing equations describing the physics. An example is the fractional model considered in reference [27] for describing the flow of two incompatible liquids through homogenous porous media. The drawback of approaches of this type is that the governing equations are not directly derivable from the underlying physics. An alternative approach is to consider transport equations in their integral (Euler) form. A variant of this approach is considered by Tarasov [28,29] and underpins the fractional derivative approach outlined by Ostoja-Starzewski [30,31].

In this paper, the physics on the cellular material—whose geometry is represented by a pre-fractal—is linked to the physics on a tessellation by means of a *hole-fill* map. The map is identified as hole-filling because when applied to a pre-fractal it has the effect of closing the holes within the porous pre-fractal structure. Hole-fill maps can be constructed by means of function composition or by identifying corresponding elements in the pre-fractal and tessellation. Function composition is more suitable for analysis, so focus is directed towards the latter, which is preferred for the type of numerical work considered here.

A novel aspect of the work is the creation of a *discontinuity network*, which is a network of lines/surfaces where discontinuous behaviour is possible. The discontinuity network is simultaneously created during the formation of the fractal and associated tessellation, resulting in an elegant procedure controlled through a
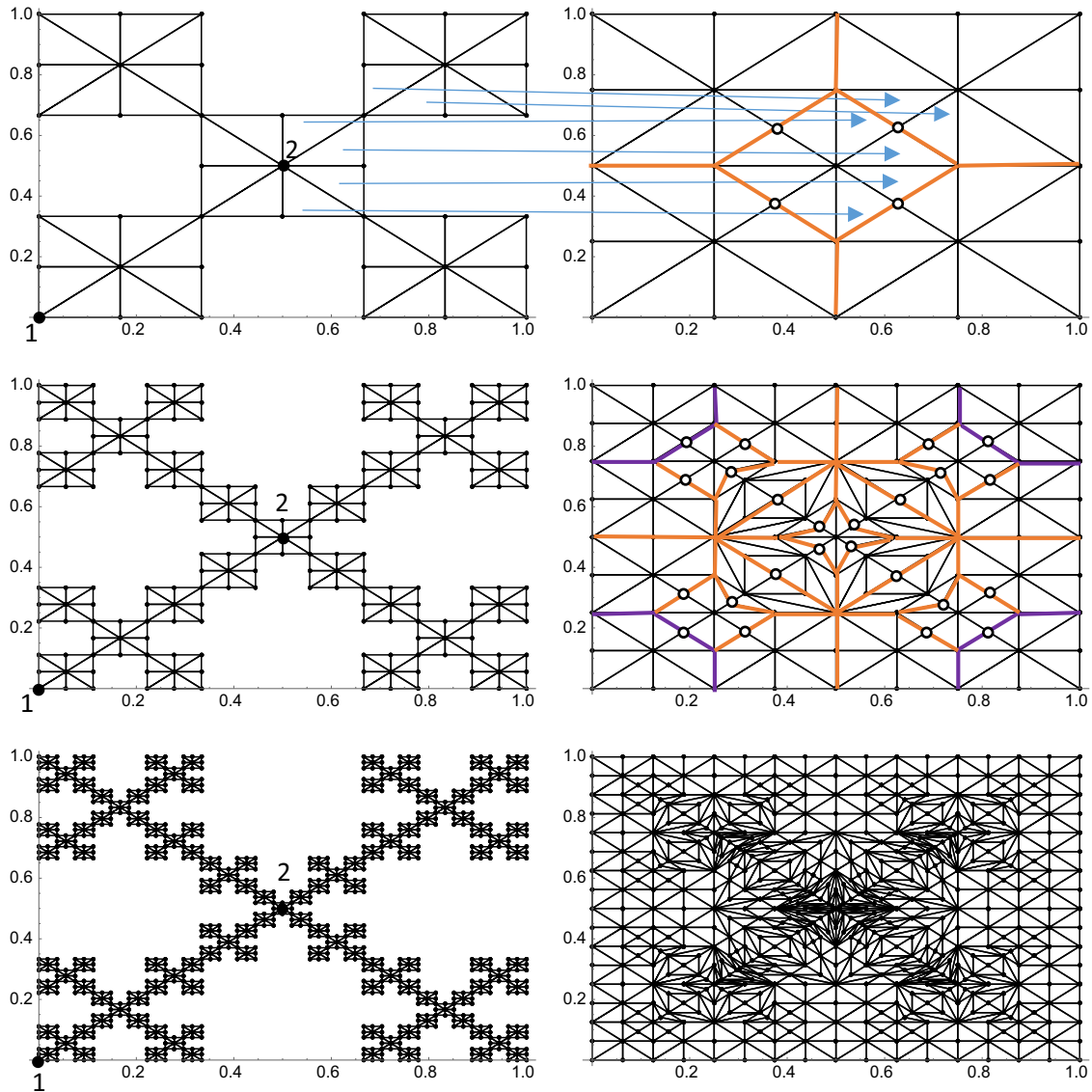
Fig. 3 Pre-fractal and corresponding tessellated domains containing discontinuity networks for a finger-like porous fractal

relatively small number of maps. The physics on the tessellations/pre-fractals is represented using weighted transport equations, which can be formulated directly without recourse to partial differential equations (PDEs). This aspect is important particularly if fractals (rather than pre-fractals) are involved, as the governing PDE in this latter case may not be obvious; indeed, it may not even be definable using traditional derivatives. The paper as a whole investigates how the finite element method can be applied to a tessellated mesh (where tiles double up as elements) incorporating a discontinuity network. A critical aspect of this work is that the physics on the porous structure are represented *exactly* in the continuum. This facilitates very precise analysis and is particularly important when high accuracy is required.

The procedures for construction of pre-fractals, tessellations and discontinuity networks for three classical fractals are presented in Sect. 2. The transport theory linking the tessellated space with the physical space is described in Sect. 3, with particular focus on heat transfer. This is followed by weighted transport equations in Sect. 4, which can be formulated directly and lead immediately to the finite element method. The role a discontinuity network plays in the finite element method is discussed. Transient and steady-state analytical solutions are given in Sect. 5 on a simple dust fractal and contrasted with numerical predictions. The role and importance of discontinuity networks are investigated in Sect. 6. In the absence of analytical results, numerical predictions—both with and without a discontinuity network—are compared with results obtained for a pre-fractal via the commercial package ABAQUS. The influence of different tessellation refinements is investigated in Sect. 7, where an efficient procedure for tessellation refinement is examined. Section 8 examines the influence of alternative expansion maps and confirms that they do not influence the accuracy of the numerical predictions.

2 Discontinuity network

Tessellated continuum mechanics is founded on the idea that physics described on a pre-fractal $\hat{E}_k$ can be exactly represented on a tessellation $\hat{T}_k$ at least down to the smallest element/domain considered. The construction of $\hat{E}_k$ is achieved by the recursive application (k times) of a relatively small number of contraction maps S_i, referred to as an iteration function scheme [11]. The recursive procedure starting from an initial domain $\hat{E}_0$ is described by $\hat{E}_k = \bigcup_i S_i \left(\hat{E}_{k-1} \right)$. One of the attractive aspects of the tessellated approach is that the tessellation is created in a corresponding fashion starting from $\hat{T}_0 = \hat{E}_0$ with the recursive relationship $\hat{T}_k = \bigcup_i P_i \left(\hat{T}_{k-1} \right)$, where in this case P_i are affine expansion maps. By design, the number of tiles in the

(a)

(b)
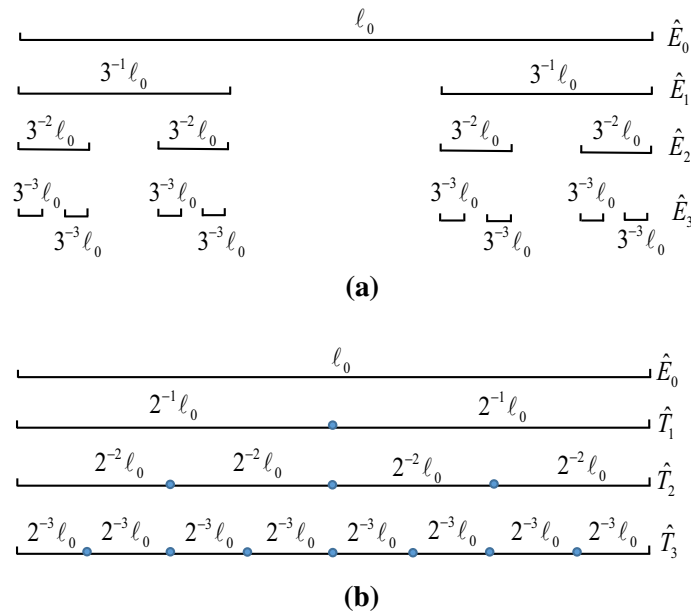
Fig. 4 Pre-fractals and tessellation for the Cantor dust. **a** Cantor dust. **b** Tessellations with discontinuity networks

tessellation $\hat{T}_k$ is exactly the same as the number of pre-fractal elements in $\hat{E}_k$; there is thus a one-to-one correspondence between tiles and pre-fractal elements, achieved by using an identical number of expansion and contraction maps. The one-to-one correspondence means that analysis results obtained on a tessellation $\hat{T}_k$ can be immediately lifted and returned to the corresponding pre-fractal $\hat{E}_k$.

Typical tessellations for some classical fractals are depicted in Figs. 1, 2 and 3 with affine contraction and tessellation maps provided in Appendices A–C. An aspect deduced on examination of Figs. 1, 2 and 3 is that $\hat{E}_0$ (not shown in figures) is supplied with an initial tessellation. The initial domain $\hat{E}_0$ has six tiles for the
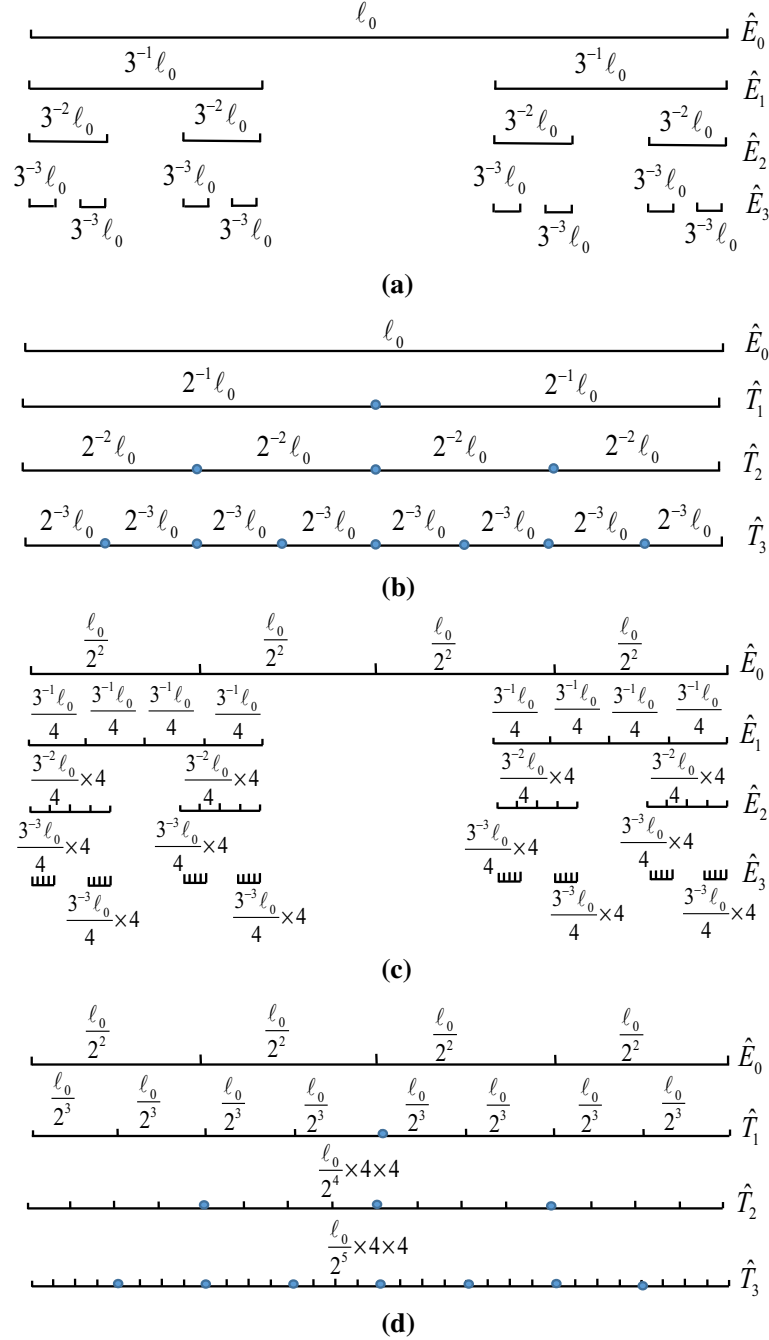
Fig. 5 Pre-fractals and tessellation for the Cantor dust with different meshes. **a** Coarse mesh on pre-fractals. **b** Coarse mesh on tessellations with discontinuity networks. **c** Fine mesh on pre-fractals. **d** Fine mesh on tessellations with discontinuity networks

pre-fractals in Fig. 1 and eight for those in Figs. 2 and 3, and each tile is purposely triangular. The initial tiling has two distinct functions: first it serves to form a piecewise linear hole-fill map and second it provides a means to modify the number of tiles in $\hat{T}_k$ for the purpose of numerical analysis.

The creation of pre-fractals and tessellations is achieved independently using bespoke iteration function schemes involving the (non-unique) maps given in "Appendices A–C". A hole-fill map—on application to a pre-fractal—has the effect of closing holes and producing the corresponding tessellation. Although it is possible to form a hole-fill map explicitly through composition of contraction and expansion maps (and their inverses), there is little merit in so doing. The independent creation of pre-fractals and tiles means that triangular elements in each domain are related. This relationship is shown explicitly in Figs. 1, 2 and 3 by means of arrows connecting a selection of tiles in each domain. A hole-fill map for a tile is simply a linear relationship which maps points from a pre-fractal element to a tile; the map is linear as a consequence of the triangular domains involved.

Figures 1, 2 and 3 also highlight a *discontinuity network* $\hat{D}_k$ in each tessellation $\hat{T}_k$. It is important to appreciate that like $\hat{T}_k$ and $\hat{E}_k$ a discontinuity network $\hat{D}_k$ is created recursively and satisfies the relationship $\hat{D}_k = \hat{D}_1 \cup \bigcup_i P_i \left(\hat{D}_{k-1} \right)$, $k \geq 2$. Thus a network is formed by forming a union with $\hat{D}_1$ and images of the previous network under the maps P_i. Examination of Figs. 1, 2 and 3 reveals that networks are associated with hole edges in pre-fractals. The closing of holes has the effect of bringing together the edges which appear on the discontinuity network in a tessellation. This makes clear why discontinuous behaviour is ubiquitous on any tessellation—there is little expectation that temperature and heat transfer rates are identical on opposite edges of a hole. The network $\hat{D}_1$ in $\hat{T}_1$, in Fig. 1 for example, is obtained from the boundary of $\hat{T}_0 = \hat{E}_0$, and the network $\hat{D}_2$ in $\hat{T}_2$ includes $\hat{D}_1$ and the three expansion maps $\{P_1, P_2, P_3\}$ (see "Appendix A") applied to $\hat{D}_1$, i.e. $\hat{D}_2 = \hat{D}_1 \cup P_1 \left(\hat{D}_1 \right) \cup P_2 \left(\hat{D}_1 \right) \cup P_3 \left(\hat{D}_1 \right)$. Similarly, the network $\hat{D}_3$ in $\hat{T}_3$ again includes $\hat{D}_1$ and the three expansion maps $\{P_1, P_2, P_3\}$ applied to the network $\hat{D}_2$ in $\hat{T}_2$ (i.e. $\hat{D}_3 = \hat{D}_1 \cup P_1 \left(\hat{D}_2 \right) \cup P_2 \left(\hat{D}_2 \right) \cup P_3 \left(\hat{D}_2 \right)$). It is thus apparent that creation of discontinuity networks parallels the recursive procedure for creation of a tessellation.

3 Transport theory

The ability to match physics on pre-fractals and tessellation was established in reference [2]. The basic idea is to describe the physics of interest in each domain on control volumes, which identify continuous spaces through which matter can flow. Control volumes are employed because they are concerned with the description of physics on a continuum (a continuous space) rather than on a discontinuous set. Thus, the difficulty posed by fractal geometry can in principle be overcome with physics described using traditional measures. Underpinning the approach adopted here is the continuum hypothesis (advanced by Cantor in 1878 [32]), which asserts that any infinite set (in 1-D) forms a bijection with either the set of natural numbers or the set of real numbers. The fact that the Cantor dust (for example) forms a bijection with the real line was proved by Cantor in 1883 [33]. The concept underpins the strategy adopted in this paper where pre-fractals (and in the limit, fractals) are mapped to continuous tessellations.

Table 1 Heat transfer coefficient (HTC) for pre-fractal holes on $\hat{E}_k$

k	d_s^{hole} (m)	$\hat{P}$ (m)	$\hat{h}_s^{\text{wat}}$ (W/m^2 K)
1	0.17	2.67	574.6
2	0.17	2.67	574.6
	0.02	2.22	46.9
3	0.17	2.67	574.6
	0.02	2.22	46.9
	2.62×10^{-3}	2.07	3.7
4	0.17	2.67	574.6
	0.02	2.22	46.9
	2.62×10^{-3}	2.07	3.7
	0.30×10^{-3}	2.02	0.3

Consider two control volumes Ω_s and Ω_r, with Ω_s located in the physical domain in which the cellular material resides (represented by $\hat{E}_k$); Ω_r is located in the tessellated space. For clarity, attention is restricted to heat transfer problems, although more complex physics is possible via the inclusion of additional transport equations. The transport equations for transient heat transfer through stationary control volumes (the latter again chosen for simplicity) are given by

$$\frac{\mathrm{d}}{\mathrm{d}t} \int_{\Omega_s} \rho_s h_s \mathrm{d}V_s = -\int_{\Gamma_s} \underline{\dot{q}}_s \cdot d\boldsymbol{\Gamma}_s + \int_{\Omega_s} \rho_s \dot{Q}_s \mathrm{d}V_s, \tag{1}$$
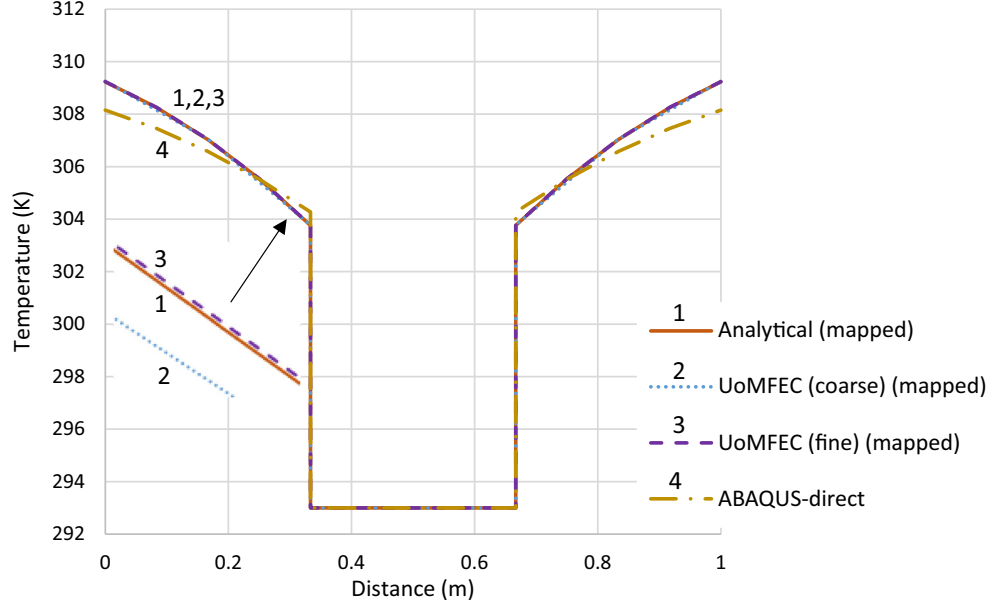
(a)
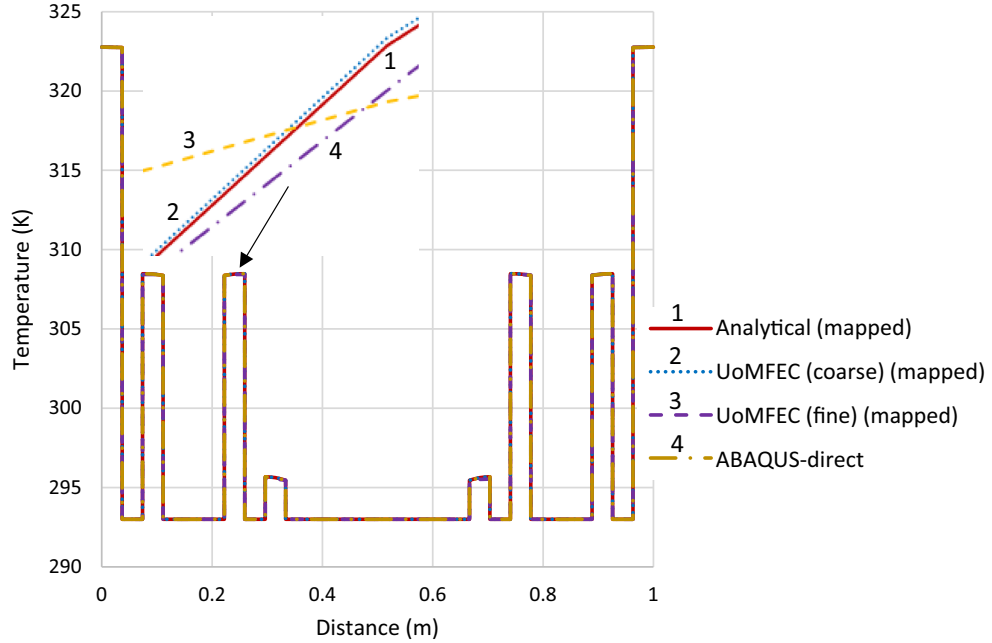
(b)

Fig. 6 Temperature plots for 1-D Cantor dust with steady-state solution on pre-fractal $\hat{E}_k$. **a** On pre-fractal $\hat{E}_1$. **b** On pre-fractal $\hat{E}_3$

Table 2 Temperature differences for Cantor dust: steady state measured on $\hat{E}_k$

k	Analytical versus UoMFEC (coarse)		Analytical versus UoMFEC (fine)		Analytical versus ABAQUS-lifted (fine)		Analytical versus ABAQUS-direct (fine)	
	$\bar{D}$ 10^{-2} K	$\bar{D}_\%$ 10^{-2} %	$\bar{D}$ 10^{-2} K	$\bar{D}_\%$ 10^{-2} %	$\bar{D}$ 10^{-2} K	$\bar{D}_\%$ 10^{-2} %	$\bar{D}$ 10^{-2} K	$\bar{D}_\%$ 10^{-2} %
1	1.95	0.64	0.51	0.17	0.04	0.01	5.722	18.62
2	0.35	0.12	0.09	0.03	0 00	0 00	15.75	5.17
3	0.14	0.05	0.05	0.02	0 00	0 00	3.95	1.31
4	0.05	0.01	0.13	0.04	0 00	0 00	64.98	82.19
5	0.07	0.02	0.09	0.03	0 00	0 00	51.24	45.31
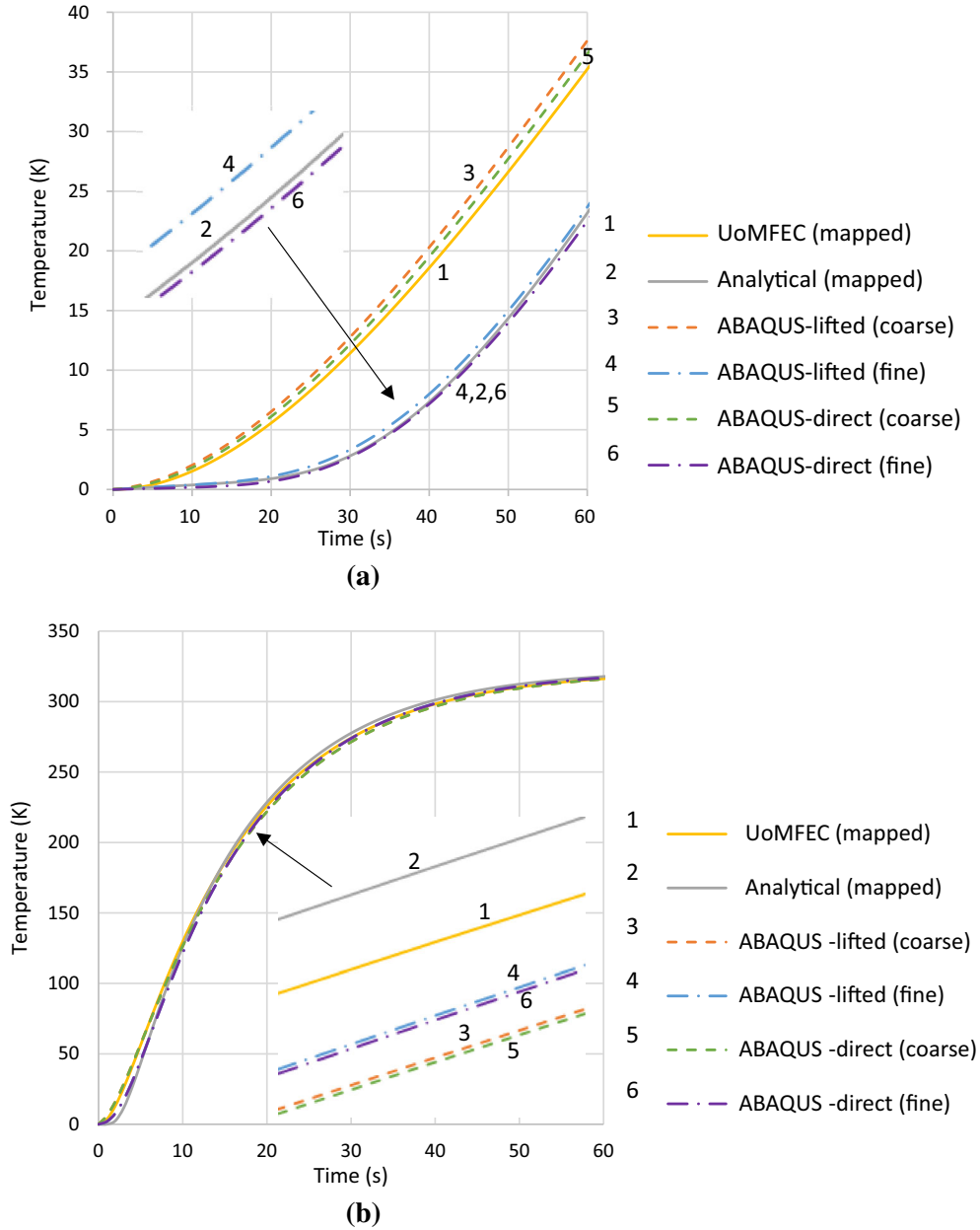
Fig. 7 Transient temperature plots for a 1-D Cantor dust. **a** Transient temperature plots for point 0.25 on $\hat{E}_1$. **b** Transient temperature plots for point 0.0625 on $\hat{E}_3$

and

$$\frac{\mathrm{d}}{\mathrm{d}t} \int_{\Omega_r} \rho_r h_r \mathrm{d}V_r = -\int_{\Gamma_r} \underline{\dot{q}}_r \cdot d\mathbf{\Gamma}_r + \int_{\Omega_r} \rho_r \dot{Q}_r \mathrm{d}V_r \tag{2}$$

where h is the specific enthalpy, $\dot{Q}$ is a heat source and the heat flux is defined as $\underline{\dot{q}} \cdot n = \hat{h}(T - T_\infty)$ with $\hat{h}$ a heat transfer coefficient and T_∞ is the bulk temperature of an external cooling/heating medium.

The differentials $\mathrm{d}V_s$ and $\mathrm{d}V_r$ are measures of volume on the two control volumes and are thus well defined. The tessellation is continuous and $\mathrm{d}V_r = \mathrm{d}V_{\text{tess}}$, where $\mathrm{d}V_{\text{tess}}$ is a volume measure on the tessellated set. Defining $\mathrm{d}V_{\text{frac}}$ as a measure of volume on a pre-fractal, $\mathrm{d}V_{\text{frac}} = \mu \mathrm{d}V_s$, where μ is a support function taking the value of zero or one. It follows from the discussion in Sect. 2, however, that hole-fill maps (being a material map) relate $\mathrm{d}V_{\text{frac}}$ to $\mathrm{d}V_{\text{tess}}$ with a relationship of the form $\mathrm{d}V_{\text{tess}} = |\mathbf{F}| \mathrm{d}V_{\text{frac}}$. This expression happens to be valid for precisely the situation where $\mathrm{d}V_r = \mathrm{d}V_{\text{tess}}$ and $\mathrm{d}V_s = \mathrm{d}V_{\text{frac}}$, and it follows that $\mathrm{d}V_r = |\mathbf{F}| \mathrm{d}V_s$. The interpretation placed on Eq. (1) therefore is that the integrands involved may not be defined for points off the pre-fractal, which is in fact an interpretation typical to classic control volume theory. In view of the continuous tessellation and the validity of the relationship $\mathrm{d}V_r = |\mathbf{F}| \mathrm{d}V_s$ almost everywhere on the tessellation, any support function is removable, as it takes the value of one. Substitution of Nanson's identities [34] $\mathrm{d}V_r = |\mathbf{F}| \mathrm{d}V_s$, $\mathrm{d}\mathbf{\Gamma}_r = |\mathbf{F}| \mathrm{d}\mathbf{\Gamma}_s \cdot \mathbf{F}^{-1}$, into Eq. (2), where $F_{ij} = \partial x_i / \partial s_j$, $\mathrm{d}\mathbf{\Gamma}_s = \underline{n}_s \mathrm{d}\Gamma_s$ and $\mathrm{d}\mathbf{\Gamma}_r = \underline{n}_r \mathrm{d}\Gamma_r$, and where the hole-fill map is of the form $x : s \mapsto x$, gives

$$\frac{\mathrm{d}}{\mathrm{d}t} \int_{\Omega_s} \rho_r h_r |\mathbf{F}| \mathrm{d}V_s = -\int_{\Gamma_s} |\mathbf{F}| \left(\mathbf{F}^{-1} \cdot \underline{\dot{q}}_r\right) \cdot \mathrm{d}\mathbf{\Gamma}_s + \int_{\Omega_s} \rho_r |\mathbf{F}| \dot{Q}_r \mathrm{d}V_s \tag{3}$$

which can be compared with Eq. (1).

Table 3 Temperature differences for Cantor dust: transient solution

	$x = 0.25$ on $\hat{T}_k$ and $k = 1$		$x = 0.125$ on $\hat{T}_k$ and $k = 2$		$x = 0.0625$ on $\hat{T}_k$ and $k = 3$	
	$\bar{D}$ (K)	$\bar{D}_\%$ (%)	$\bar{D}$ (K)	$\bar{D}_\%$ (%)	$\bar{D}$ (K)	$\bar{D}_\%$ (%)
Analytical versus UoMFEC (coarse) on $\hat{E}_k$	16.17	43.99	10.60	13.71	2.99	3.31
Analytical versus UoMFEC (fine) on $\hat{E}_k$	6.05	24.02	4.31	8.47	1.26	2.03
Analytical versus ABAQUS-lifted (fine) on $\hat{E}_k$	0.29	1.94	0.68	2.59	0.66	1.43
Analytical versus ABAQUS-direct (fine) on $\hat{E}_k$	1.83	6.41	0.84	2.41	0.68	1.44

Table 4 Heat transfer coefficients for the Sierpinski carpet heat exchanger on $\hat{E}_k$

k	d_s^{hole} (m)	$\hat{P}$ (m)	$\hat{h}_s^{\text{wat}}$ (W/m² K)
1	0.33	1.33	12,735.0
2	0.33	1.33	12,735.0
	0.11	0.44	1460.1
3	0.33	1.33	12,735.0
	0.11	0.44	1460.1
	0.04	0.15	167.4
4	0.33	1.33	12,735.0
	0.11	0.44	1460.1
	0.04	0.15	167.4
	0.01	0.05	19.2
5	0.33	1.33	12,735.0
	0.11	0.44	1460.1
	0.04	0.15	167.4
	0.01	0.05	19.2
	0.41×10^{-2}	0.02	2.2

Recognising that a mass-conserving map satisfies $\rho_r \mathrm{d}V_r = \rho_s \mathrm{d}V_s$, it follows that matching physics between the tessellated continuum and physical spaces is achieved with $\rho_r = |\boldsymbol{F}|^{-1} \rho_s$, $h_r = h_s$, $\dot{Q}_r = \dot{Q}_s$ and $\dot{\underline{q}}_r = |\boldsymbol{F}|^{-1} \boldsymbol{F} \cdot \dot{\underline{q}}_s$. The convective heat transfer boundary condition can be provided in the form of

$$\dot{\underline{q}}_r \cdot d\boldsymbol{\Gamma}_r = \hat{h}_r \left(T_r - T_\infty\right) d\Gamma_r = |\boldsymbol{F}|^{-1} \left(\boldsymbol{F} \cdot \dot{\underline{q}}_s\right) \cdot \left(|\boldsymbol{F}| \, d\boldsymbol{\Gamma}_s \cdot \boldsymbol{F}^{-1}\right) = \hat{h}_s \left(T_s - T_\infty\right) d\Gamma_s, \qquad (4)$$

which is satisfied for $T_r = T_s$ and $\hat{h}_r d\Gamma_r = \hat{h}_s d\Gamma_s$ giving $\nabla_s T_s = \boldsymbol{F}^T \cdot \nabla_r T_r$, and (in view of the identity $\dot{\underline{q}}_r = |\boldsymbol{F}|^{-1} \boldsymbol{F} \cdot \dot{\underline{q}}_s$) leads to $\dot{\underline{q}}_r = -\boldsymbol{K}_r \cdot \nabla_r T_r$. The relationship of thermal conductivity between tessellation and pre-fractal is

$$\boldsymbol{K}_r = |\boldsymbol{F}|^{-1} \boldsymbol{F} \boldsymbol{K}_s \boldsymbol{F}^T \qquad (5)$$

where $\boldsymbol{K}_r$ is the associated orthotropic conductivity tensor on the tessellated domain and $\boldsymbol{K}_s$ is the isotropic conductivity on the pre-fractal.

4 The finite element with discontinuity networks

In the absence of a governing partial differential equation, the finite element method can be applied directly to a transport equation via the inclusion of a weighting function [35]; such an approach applied to Eq. (1) gives

$$\frac{\mathrm{d}}{\mathrm{d}t} \int_{\Omega_s} W_s \rho_s h_s \mathrm{d}V_s = -\int_{\Gamma_s} W_s \dot{\underline{q}}_s \cdot \mathrm{d}\boldsymbol{\Gamma}_s + \int_{\Omega_s} \nabla_s W_s \cdot \dot{\underline{q}}_s \mathrm{d}V_s + \int_{\Omega_s} W_s \rho_s \dot{Q}_s \mathrm{d}V_s, \qquad (6)$$

where W_s is a weighting function which is assumed continuous at least up to the first derivative.
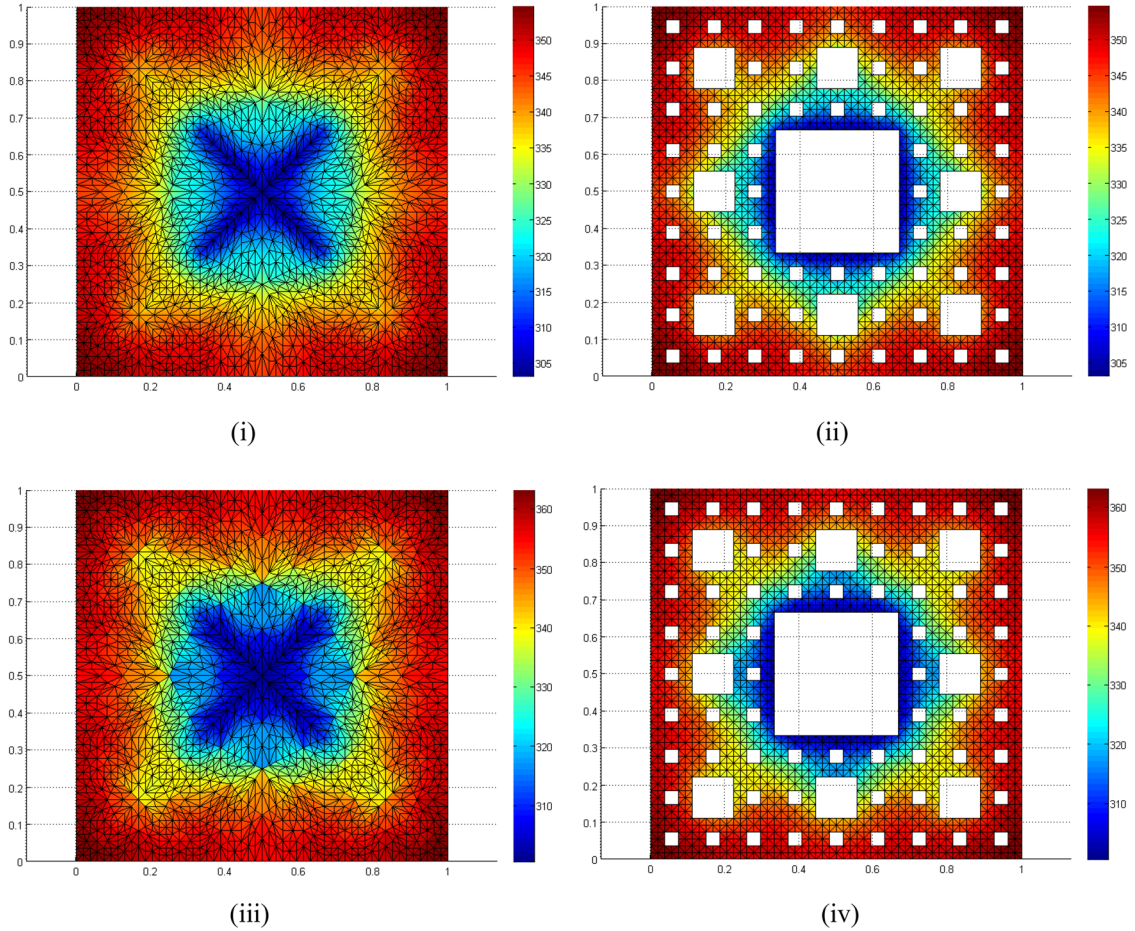
Fig. 8 Contour temperatures (UoMFEC) with and without a discontinuity network (DN). **i** On $\hat{T}_3$ without DN. **ii** On $\hat{E}_3$ without DN. **iii** On $\hat{T}_3$ with DN. **iv** On $\hat{E}_3$ with DN

The weighted transport equation for Eq. (2) is similar and takes the form

$$\frac{\mathrm{d}}{\mathrm{d}t} \int_{\Omega_r} W_r \rho_r h_r \mathrm{d}V_r = - \int_{\Gamma_r} W_r \dot{\underline{q}}_r \cdot \mathrm{d}\mathbf{\Gamma}_r + \int_{\Omega_r} \nabla_r W_r \cdot \dot{\underline{q}}_r \mathrm{d}V_r + \int_{\Omega_r} W_r \rho_r \dot{Q}_r \mathrm{d}V_r. \tag{7}$$

Substitution into Eq. (7) of the relationships established in Sect. 3 (i.e. $\rho_r = |\mathbf{F}|^{-1} \rho_s$, $h_r = h_s$, $\dot{Q}_r = \dot{Q}_s$, $\dot{\underline{q}}_r = |\mathbf{F}|^{-1} \mathbf{F} \cdot \dot{\underline{q}}_s$ and $\nabla_s \equiv \mathbf{F}^{-T} \cdot \nabla_r$ along with Nanson's identities) gives

$$\frac{\mathrm{d}}{\mathrm{d}t} \int_{\Omega_s} W_r \rho_s h_s \mathrm{d}V_s = - \int_{\Gamma_s} W_r \dot{\underline{q}}_s \cdot d\mathbf{\Gamma}_s + \int_{\Omega_s} \nabla_s W_r \cdot \mathbf{F}^{-1} \mathbf{F} \cdot \dot{\underline{q}}_s \mathrm{d}V_s + \int_{\Omega_s} W_r \dot{Q}_s \mathrm{d}V_s \tag{8}$$

which matches Eq. (6) on setting $W_r = W_s$.

The finite element method describing the physics on a tessellation $\hat{T}_k$ (and hence $\hat{E}_k$) is obtained by setting $W_r = W_s = N_i$ to give

$$\frac{\mathrm{d}}{\mathrm{d}t} \int_{\Omega_r^e} N_i \rho_r h_r \mathrm{d}V_r = - \int_{\Gamma_r^e} N_i \dot{\underline{q}}_r \cdot \mathrm{d}\mathbf{\Gamma}_r - \int_{\Omega_r^e} \nabla_r N_i \cdot \mathbf{K}_r \cdot \nabla_r T_r \mathrm{d}V_r + \int_{\Omega_r^e} N_i \rho_r \dot{Q}_r \mathrm{d}V_r \tag{9}$$

(i)

(ii)

(iii)
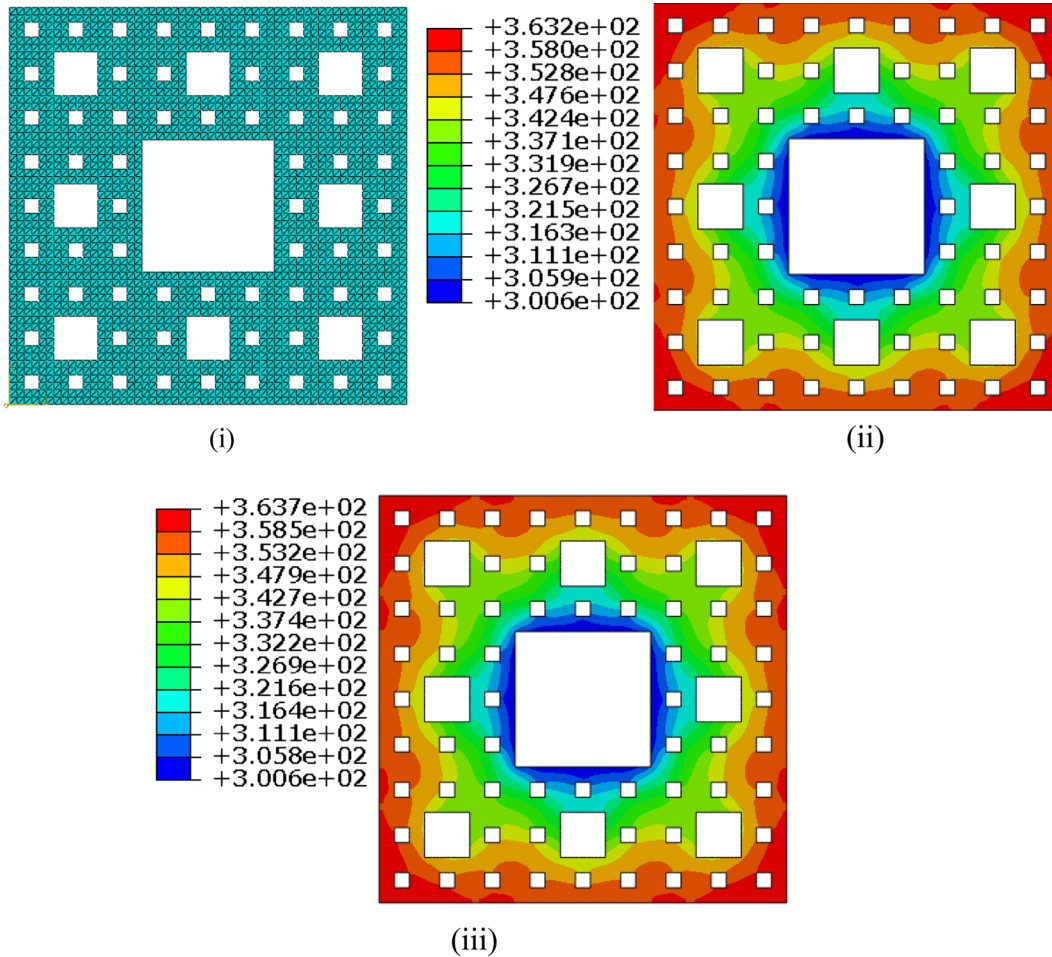
Fig. 9 Contour temperature plots for $\hat{E}_3$ using ABAQUS-direct. **i** Mesh on $\hat{E}_3$ with 8 elements per pre-fractal element. **ii** Temperature contours on $\hat{E}_3$ with 8 elements per pre-fractal element. **iii** Temperature contours on $\hat{E}_3$ with 152 elements per pre-fractal element

where N_i is a shape function and Ω_r^e is a tile in $\hat{T}_k$; the tiles by choice double up as elements in the proposed numerical procedure.

Three-noded triangular elements are used in the analysis of a tessellation, which reflects the restriction imposed by the retention of linear hole-fill maps. Those elements that share no edges with a discontinuity network are continuous in both W_r and T_r and are consistent with a standard Galerkin finite element method. For elements connected by an edge on a discontinuity network, continuity cannot be assumed. Each element in this case is subject to a mapped convective boundary condition from the associated hole in the corresponding pre-fractal in accordance with Eq. (4).

Table 5 Temperature differences on $\hat{E}_k$: influence of discontinuity network

k	1	2	3
No discontinuity network			
Coarse mesh			
$\bar{D}$ (K)	3.17	3.27	4.69
$\bar{D}_\%$ (%)	0.86	0.91	1.34
Fine mesh			
$\bar{D}$ (K)	5.13	3.30	5.09
$\bar{D}_\%$ (%)	1.23	0.91	1.44
With discontinuity network			
Coarse mesh			
$\bar{D}$ (K)	3.17	0.55	0.09
$\bar{D}_\%$ (%)	0.86	0.16	0.03
Fine mesh			
$\bar{D}$ (K)	5.13	0.67	0.47
$\bar{D}_\%$ (%)	1.23	0.19	0.13
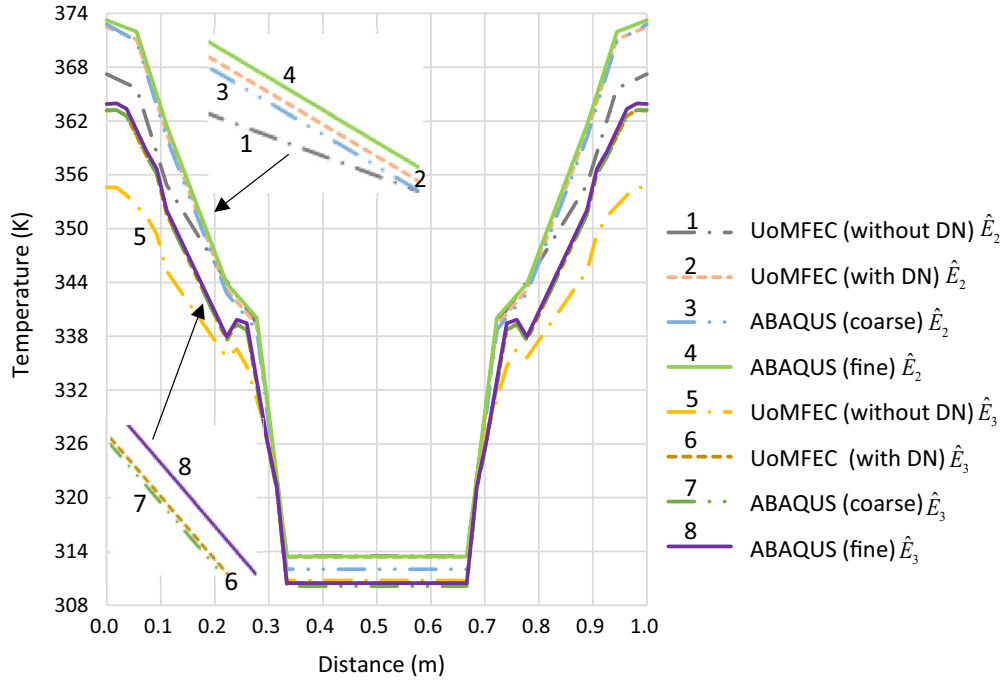
Fig. 10 Temperature plots along $x = y$ for pre-fractals $\hat{E}_k$ using UoMFEC and ABAQUS-direct

Table 6 Maximum temperature difference at $\hat{D}_k$ for the Sierpinski carpet

k	1	2	3
T_{diff} (K)	0	30.26	26.04

4.1 Numerical solution methods

The proposed finite element approach has been programmed into MATLAB at the University of Manchester (UoM). The code incorporates a facility for the creation of tessellations that double up as meshes along with
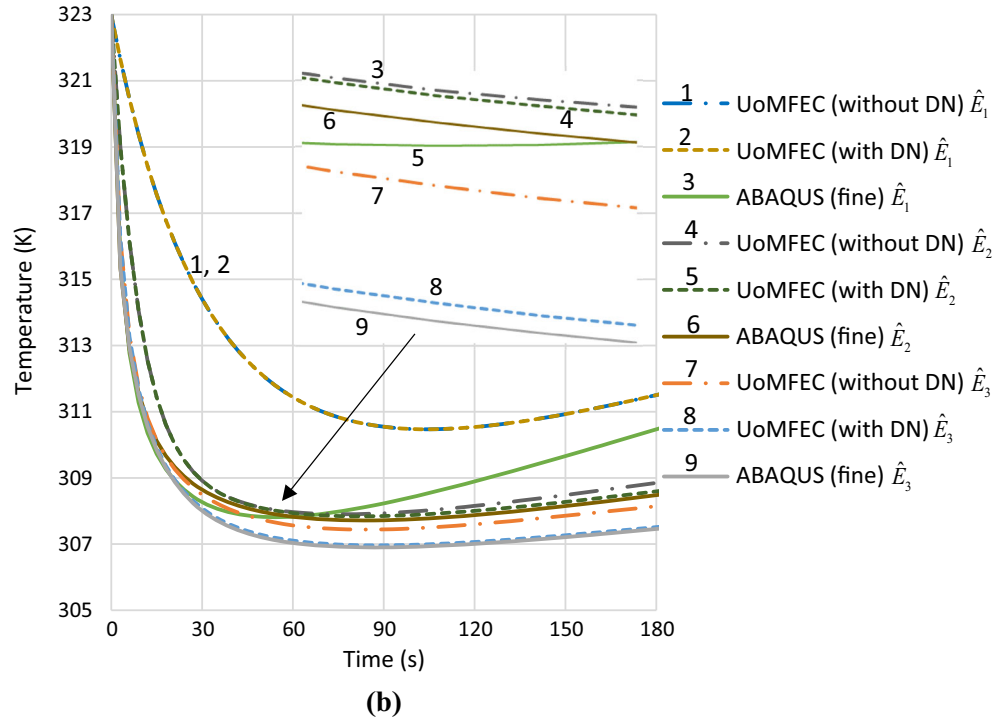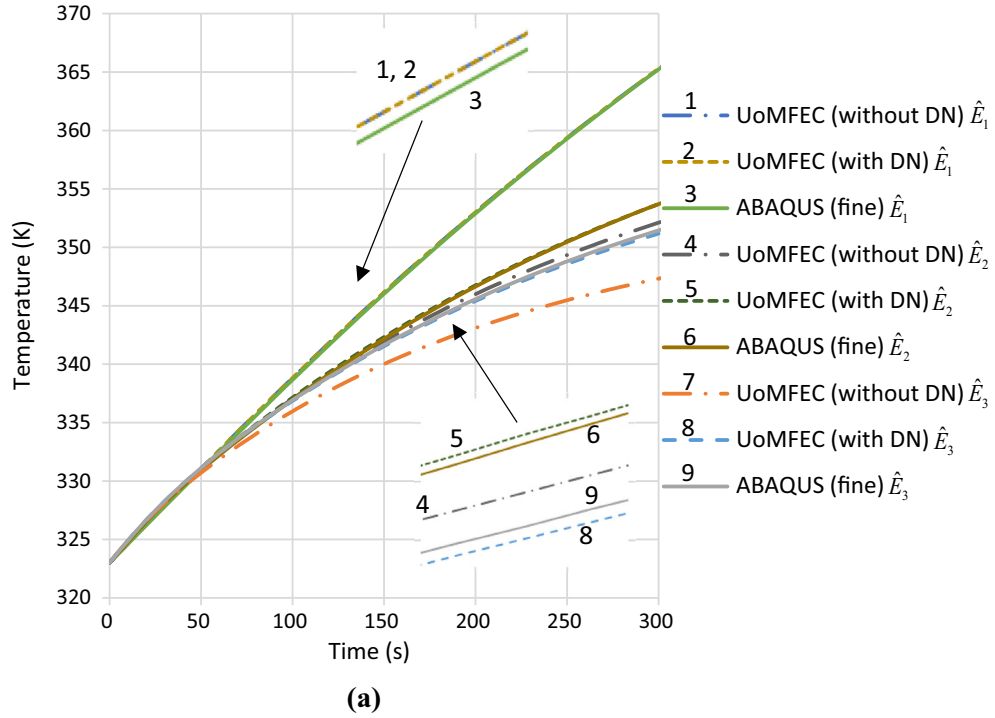
Fig. 11 Temperature plots for different points on $\hat{E}_k$ using UoMFEC and ABAQUS-direct. (a) For point $(0, 0)$ on $\hat{E}_k$. (b) For point $(1/3, 1/3)$ on $\hat{E}_k$

discontinuity networks for the purpose of numerical analysis with the UoM finite element code (termed here UoMFEC).

The commercial finite element package ABAQUS (version 6.13) has also been used for the purpose of confirming the validity of the theory. The methods proposed in the preceding sections do not directly analyse the pre-fractals but rather their tessellations. The ABAQUS code is able to analyse directly the pre-fractal and thus provide benchmark solutions. The elements selected for the analysis with ABAQUS are also linear three-noded elements.

It should be appreciated that the proposed work is aimed at very precise analysis on a continuum and takes advantage of the manner in which tessellations and pre-fractals are generated. The process is efficient in this regard involving recursive processes; tessellations, pre-fractals and discontinuity networks are all produced recursively. It is recognised, however, that the use of a tessellation, which is recursively produced, as a mesh, does place a constraint on the possible distribution of elements forming the mesh. This can possibly result in too few elements being located in regions of greatest need or equally too many in regions where there is no need.

Prior to testing out the full numerical theory on realistic fractals, however (as depicted in Figs. 1, 2, 3), it is of interest to test out the ideas initially on a relatively simple fractal on which analytical solutions can be developed.

5 Exact solutions on Cantor dusts

This section is concerned with the development of the analytical solution on the Cantor dust in one dimension, with internal heat source and convection boundary conditions. The exact solution is compared with the finite element method developed in the earlier sections. The governing partial differential equation arising from the heat transport Eq. (2) is of the form

$$\rho_r \frac{\partial h_r}{\partial t} = \mathrm{div}_r \left(\mathbf{K}_r \cdot \nabla_r T_r \right) + \dot{Q}_0 \tag{10}$$

where $\dot{Q}_0$ is a heat source loading density on tiles in any tessellation.

Table 7 Transient temperature differences on $\hat{E}_k$: influence of discontinuity network

Point 1 and 2 in Fig. 2	k	No discontinuity network		With discontinuity network	
		$\bar{D}$ (K)	$\bar{D}_\%$ (%)	$\bar{D}$ (K)	$\bar{D}_\%$ (%)
$(0, 0)$	1	1.88	0.43	1.88	0.43
	2	4.54	1.23	0.52	0.14
	3	7.67	2.14	0.60	0.17
$\left(\frac{1}{3}, \frac{1}{3}\right)$	1	1.64	0.50	1.64	0.50
	2	0.19	0.06	0.10	0.03
	3	0.41	0.13	0.02	0.01

Table 8 Heat transfer coefficients for the finger-like fractal heat exchanger on $\hat{E}_k$

k	d_s^{hole} (m)	$\hat{P}$ (m)	$\hat{h}_s^{\mathrm{wat}}$ (W/m^2 K)
1	0.33	1.33	12,735.0
2	0.30	2.00	15,344.0
	0.11	0.44	1460.0
3	0.24	2.67	15,145.0
	0.10	0.67	1759.0
	0.04	0.15	167.0
4	0.20	3.33	14,360.0
	0.08	0.89	1736.0
	0.03	0.22	202.0
	0.01	0.05	19.0
5	0.17	4.00	13,551.0
	0.07	1.11	1646.0
	0.03	0.30	199.0
	0.01	0.07	23.0
	0.41×10^{-2}	0.02	2.0

5.1 Pre-fractal and tessellation construction

The pre-fractals $\hat{E}_k$ for the Cantor dust and corresponding tessellations $\hat{T}_k$ with highlighted discontinuity networks (appearing as discontinuous points) are shown in Fig. 4. The contraction maps that produce $\hat{E}_k$ in Fig. 4 are

$$S_1(x) = \frac{x}{3} \quad \text{and} \quad S_2(x) = \frac{2\ell_0 + x}{3} \tag{11}$$

along with the expansion maps for $\hat{T}_k$ are

$$P_1(x) = \frac{x}{2} \quad \text{and} \quad P_2(x) = \frac{\ell_0 + x}{2} \tag{12}$$

with the original set $\hat{E}_0 = [0, \ell_0]$ used for both maps.

The expansion maps are not unique although those shown in Eq. (12) are a natural choice, producing tiles of equal size. When viewed as a mesh it is evident the maps in Eq. (12) provide the coarsest mesh possible originating from only one element on $\hat{E}_0$. Mesh refinement is possible and one approach is to supply an initial mesh to $\hat{E}_0$, where, for example, setting $\hat{E}_0 = [0, \ell_0/2] \bigcup [\ell_0/2, \ell_0]$ provides the two-element refinement in Fig. 5a, b. Equivalently, composition of the expansion maps can be used where, for example,

(i)

(ii)

(iii)

(iv)
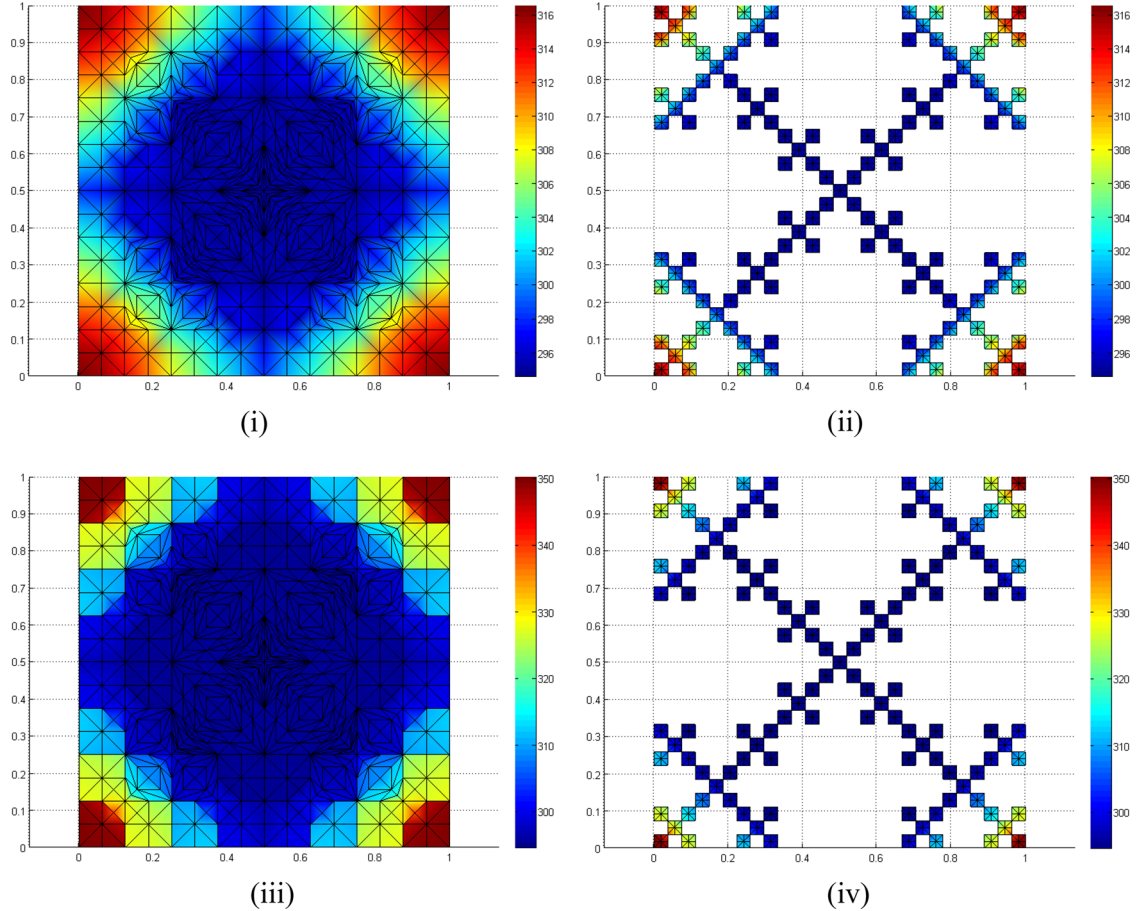
Fig. 12 Contour temperatures (UoMFEC) with and without a discontinuity network (DN). **i** Temperature contours on $\hat{T}_3$ without DN. **ii** Temperature contours on $\hat{E}_3$ without DN. **iii** Temperature contours on $\hat{T}_3$ with DN. **iv** Temperature contours on $\hat{E}_3$ with DN

$$P_1 \circ P_1\,(x) = \frac{x}{4}, \quad P_1 \circ P_2\,(x) = \frac{\ell_0 + x}{4}, \quad P_2 \circ P_1\,(x) = \frac{2\ell_0 + x}{4} \text{ and } P_2 \circ P_2\,(x) = \frac{3\ell_0 + x}{4} \quad (13)$$

which, when applied $\hat{E}_0$ produces four elements on $\hat{T}_1$ in Fig. 5c, d).

Examples of refined tessellations and corresponding pre-fractals are shown in Fig. 5. Observe also the discontinuity network $\hat{D}_k$ highlighted at particular points in the tessellations, which correspond to pre-fractal holes. The correspondence of elements means it is relatively straightforward to stipulate an hole-fill map between $\hat{E}_k$ and $\hat{T}_k$;

$$x_k\,(s) = x_k^{(i)} + \frac{x_k^{(i+1)} - x_k^{(i)}}{s_k^{(i+1)} - s_k^{(i)}}\left(s - s_k^{(i)}\right), \qquad (14)$$

where $s \in \left[s_k^{(i)}, s_k^{(i+1)}\right]$ and it is assumed here that nodes are enumerated from left to right, so that $s_k^{(i+1)} - s_k^{(i)} = \ell_k$ if $x_k^{(i+1)} \neq x_k^{(i)}$, with ℓ_k being the length of an element in $\hat{E}_k$ [1]. For this relatively simple case, the hole-fill map can be written in terms of a support function μ_k as [1]

(i)   (ii)

(iii)
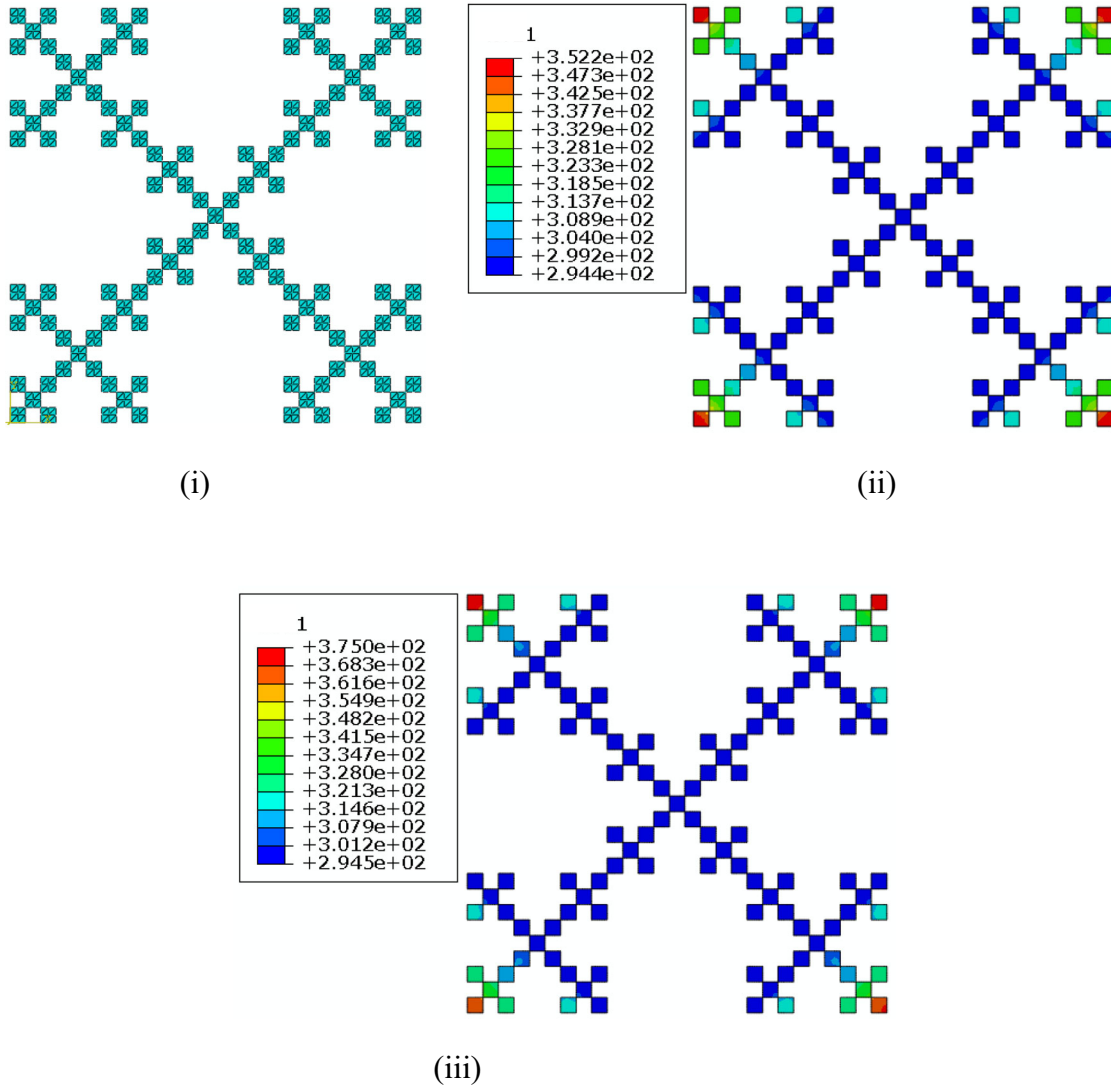
Fig. 13 Contour temperature plots for $\hat{E}_3$ using ABAQUS-direct. **i** Mesh on $\hat{E}_3$ with eight elements per pre-fractal element. **ii** Temperature contours on $\hat{E}_3$ with eight elements per pre-fractal element. **iii** Temperature contours on $\hat{E}_3$ with 152 elements per pre-fractal element

$$x_k(s) = \left(\frac{3}{2}\right)^k \int_0^s \mu_k(r)\,dr = \left(\frac{\ell_k}{\ell_0}\right)^{D_1-1} \int_0^s \mu_k(r)\,dr, \qquad (15)$$

where D_1 is the Hausdorff fractal dimension (see Ref. [36] for derivation).

The relationship between material on pre-fractals and tessellations is readily obtained with knowledge of the hole-fill map (Eq. (15)). Conservation of mass on $\hat{E}_k$ and $\hat{T}_k$ gives $\rho_r = |F|^{-1}\rho_s = \left(\ell_k\ell_0^{-1}\right)^{1-D_1}\rho_s$ with scalar K_s and K_r related by $K_r = |F|^{-1} F K_s F^T = \left(\ell_k\ell_0^{-1}\right)^{D_1-1} K_s$. Note that in view of the fact that ℓ_k is constant for each element of the kth pre-fractal, the density ρ_r and thermal conductivity K_r are homogenous for the corresponding tessellation.

Table 9 Temperature differences on $\hat{E}_k$: influence of discontinuity network

k	1	2	3
No discontinuity network			
Coarse mesh			
$\quad \bar{D}$ (K)	2.25	7.11	5.09
$\quad \bar{D}_\%$ (%)	0.66	2.14	1.57
Fine mesh			
$\quad \bar{D}$ (K)	3.64	8.50	7.05
$\quad \bar{D}_\%$ (%)	1.09	2.54	2.12
With discontinuity network			
Coarse mesh			
$\quad \bar{D}$ (K)	2.24	0.69	0.12
$\quad \bar{D}_\%$ (%)	0.65	0.22	0.04
Fine mesh			
$\quad \bar{D}$ (K)	3.28	1.71	2.15
$\quad \bar{D}_\%$ (%)	0.98	0.51	0.62
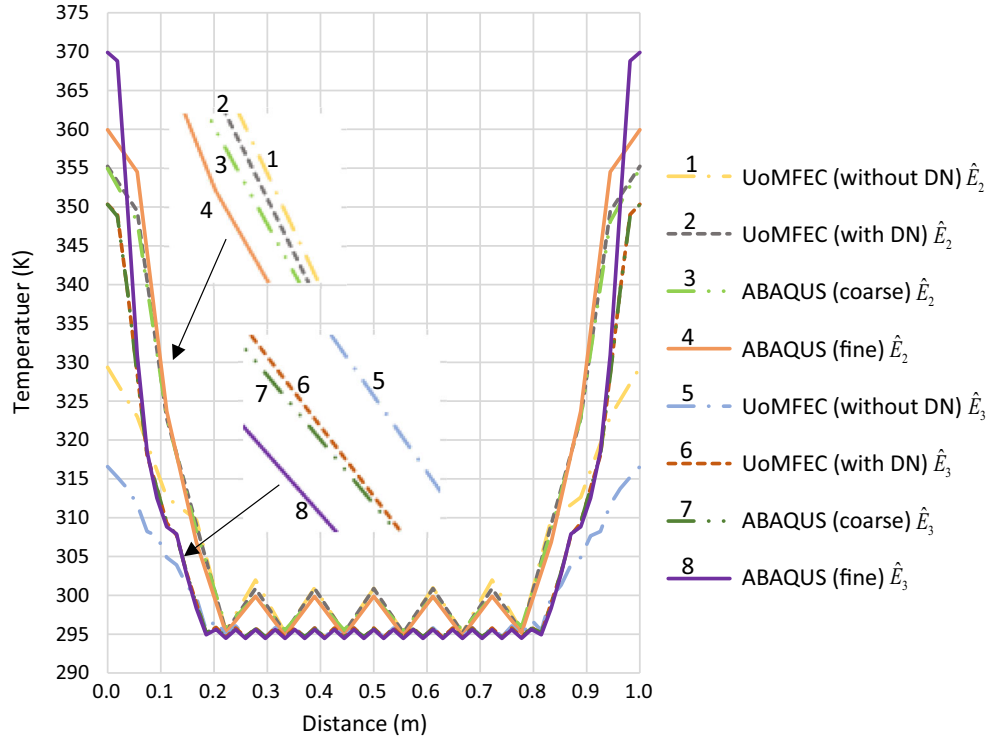
Fig. 14 Temperature plots along $x = y$ for pre-fractals $\hat{E}_k$ using the UoMFEC and ABAQUS-direct

5.2 Analytical solution for a 1-D Cantor dust model

In view of the ultimate objective to describe the behaviour of cellular heat exchangers, it is fitting to assume that coolant flows in a normal direction through the voids in the pre-fractals for the Cantor dust depicted in

Table 10 Maximum temperature difference at $\hat{D}_k$ for the finger fractal

k	1	2	3
T_{diff} (K)	0	33.72	24.65
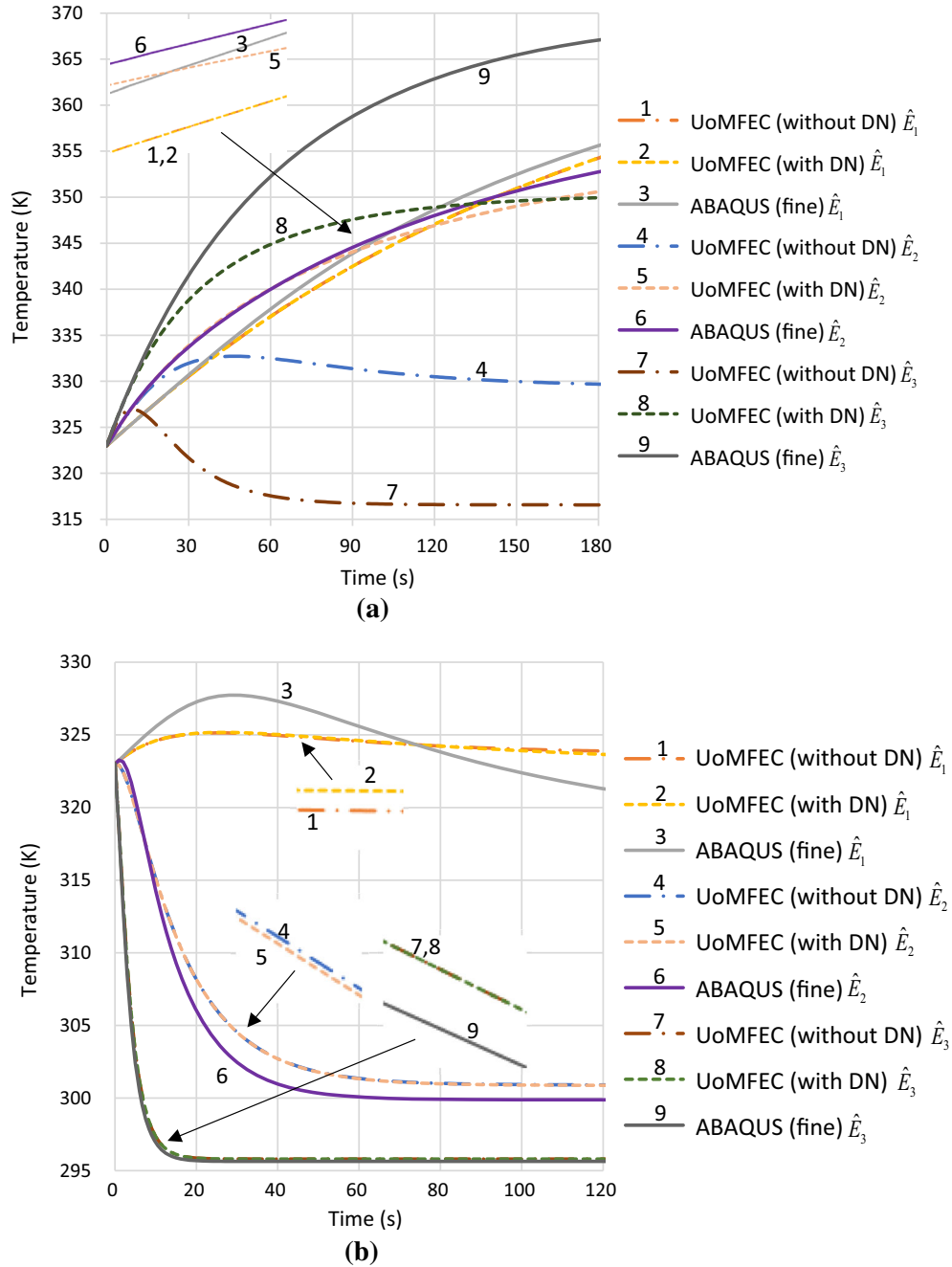
Fig. 15 Temperature plots for different points on $\hat{E}_k$ using UoMFEC and ABAQUS-direct. **a** For point $(0, 0)$ on $\hat{E}_k$. **b** For point $(0.5, 0.5)$ on $\hat{E}_k$

Figs. 4 and 5. A uniform heat source is applied to each pre-fractal element, defined to ensure that the total rate of energy supplied is constant on $\hat{E}_k$ (and consequently on $\hat{T}_k$). The loading appears as a constant value of $\dot{Q}_0$ in Eq. (10) as a consequence of the total volume remaining constant on a tessellation. At nodes in the discontinuity network, cooling is set as a boundary condition for each adjoining element and is of the form $\dot{q}_r = \hat{h}_x \left(T_r - T_{\text{wat}}\right)$, where T_{wat} is the bulk coolant temperature and $\hat{h}_x$ is a heat transfer coefficient associated with a pre-fractal hole. In this case, Eq. (4) gives $\dot{q}_r = \dot{q}_s$, i.e. the cooling experienced at a pre-fractal hole is also experienced at the discontinuity network. External surfaces are exposed to a heat flux of the form $\dot{q}_0 = \hat{h}_0 \left(T_r - T_\infty\right)$, where T_∞ is the ambient temperature of the surrounding medium and $\hat{h}_0$ is the associated heat transfer coefficient. To arrive at an analytical solution on the tessellated structure requires the union of solutions obtained on individual tiles in the tessellation.

5.2.1 Steady-state solution for a 1-D Cantor dust

According to Eq. (10), the governing equation on $\hat{T}_k$ is

$$K_r T_r'' + \dot{Q}_0 - \frac{2\hat{h}_0}{w} \left(T_r - T_\infty\right) = 0, \tag{16}$$

where w is the width of the bar and is part of an additional term to capture convective heat transfer from the top and bottom faces of the bar.

The form the solution takes on a tile can be assumed to be $T_r = T_{\text{cf}} + T_{\text{source}}$, where the complementary function is of the form $T_{\text{cf}}(x) = a\cosh(\alpha x) + b\sinh(\alpha x)$ and satisfies $K_r T_{\text{cf}}'' - 2\hat{h}_0 w^{-1} T_{\text{cf}} = 0$ with $\alpha = \left(2\hat{h}_0/wK_r\right)^{\frac{1}{2}}$, and where a and b are integration constants. The temperature T_{source} takes the form $T_{\text{source}} = T_\infty + 2^{-1}\hat{h}_0^{-1} w\dot{Q}_0$ (on assumption $\hat{h}_0$ is nonzero) and satisfies $K_r T_{\text{source}}'' + \dot{Q}_0 - 2\hat{h}_0 w^{-1} \left(T_{\text{source}} - T_\infty\right) = 0$, which is readily verified on substitution. The solution is

$$T_r(x) = a^i \cosh\left(\alpha\left(x - x_i\right)\right) + b^i \sinh\left(\alpha\left(x - x_i\right)\right) + T_{\text{source}} \tag{17}$$

where a^i and b^i are determined by two boundary conditions $\hat{h}_i \left(T_r^{x=x_i} - T_{\text{wat}}^i\right) = -K_r \left(\partial T_r/\partial x\right)_{x=x_i}$ and $\hat{h}_{i+1} \left(T_r^{x=x_{i+1}} - T_{\text{wat}}^{i+1}\right) = K_r \left(\partial T_r/\partial x\right)_{x=x_{i+1}}$, which applies at the edges of a tile.

5.2.2 Steady-state validation tests

The analytical solution is compared with results from ABAQUS and UoMFEC. The material properties for the Cantor dust material (copper) are: thermal conductivity $K_s = 400\,\text{W/mK}$, density $\rho = 8930\,\text{kg/m}^3$ and specific heat capacity $c_p = 385\,\text{J/kgK}$. The dimensions for the bar are taken to be: edge length $l_0 = 1\,\text{m}$ and width $w = 1\,\text{m}$. The ambient temperature of the surrounding medium is taken to be $T_\infty = 323\,\text{K}$, with the heat transfer coefficient $\hat{h}_0 = 200\,\text{W/m}^2\,\text{K}$. A uniform heat-loading rate $\dot{Q}_0 = 400\,\text{W/m}^3$ is applied to the bar as an internal heat source to account for thermal loading. The required heat transfer coefficients $\hat{h}_s^{\text{wat}}$ for the pre-fractal holes are determined using an empirical relationship obtained on combination of the Dittus–Boelter and the Darcy–Weisbach equations [37], which provides

$$\hat{h}_s^{\text{wat}} = \left(0.0535 \frac{k^{0.67} \hat{A}^{0.8} \rho^{0.457} c_p^{0.33}}{\mu^{0.584} L^{0.457}}\right) \Delta p^{0.457} \left(d_s^{\text{hole}}\right)^{0.371} \tag{18}$$

Table 11 Transient temperature differences on $\hat{E}_k$: influence of discontinuity network

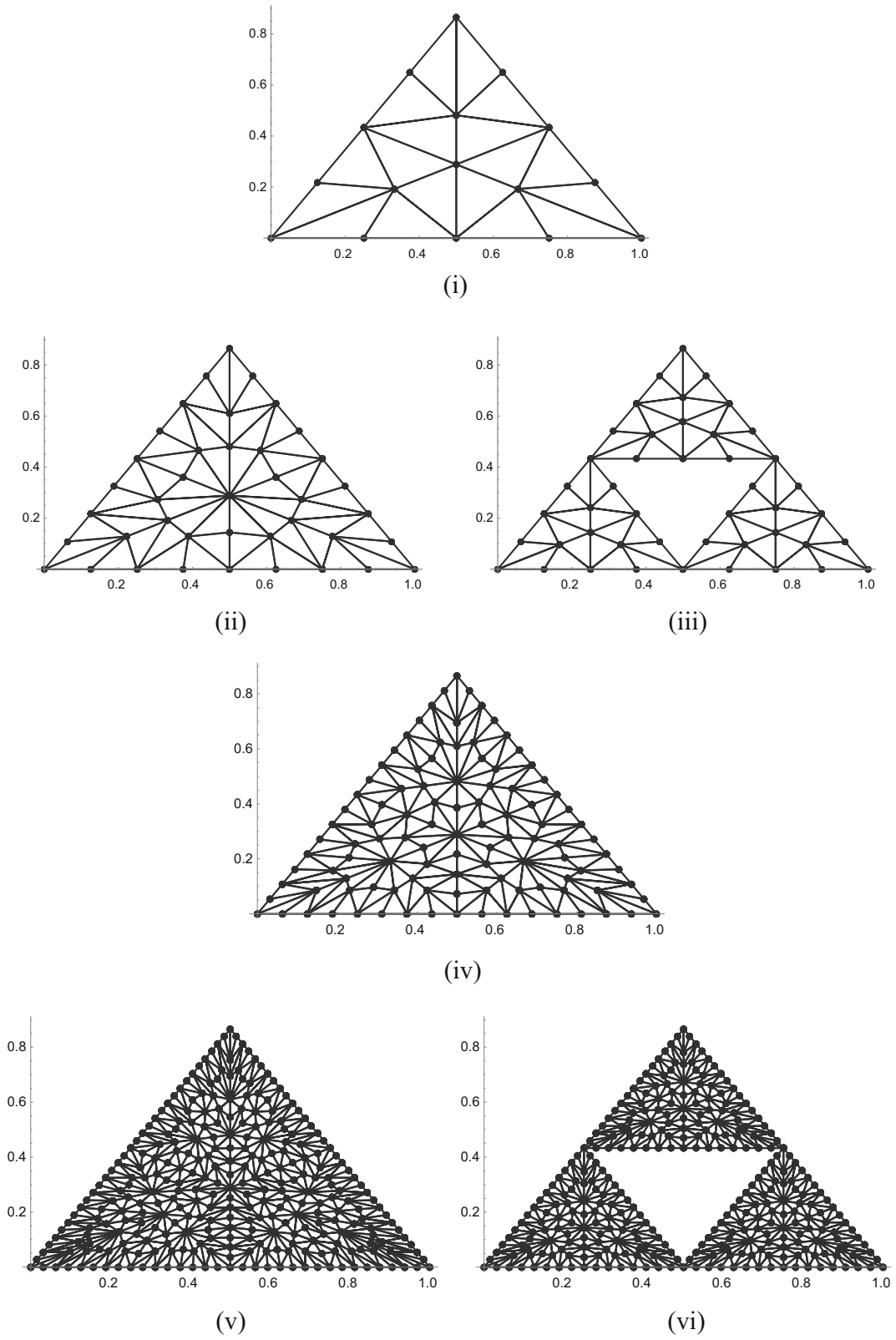| Point 1 and 2 in Fig. 3	k	No discontinuity network		With discontinuity network	
		$\bar{D}$ (K)	$\bar{D}_\%$ (%)	$\bar{D}$ (K)	$\bar{D}_\%$ (%)
(0, 0)	1	0.82	0.23	1.03	0.28
	2	25.88	7.53	3.49	0.98
	3	49.67	14.51	17.44	4.85
(0.5, 0.5)	1	5.84	1.81	3.96	1.23
	2	1.06	0.35	1.03	0.34
	3	0.22	0.07	0.22	0.07

Fig. 16 Pre-fractals and tessellations for the Sierpinski gasket with different meshes. **i** $\hat{E}_0$ with 18 tiles. **ii** $\hat{T}_1$ with 3×18 tiles. **iii** $\hat{E}_1$ with 3×18 elements. **iv** $\hat{E}_0$ with 162 tiles. **v** $\hat{T}_1$ with 3×162 tiles. **vi** $\hat{E}_1$ with 3×162 elements

where $d_s^{\text{hole}} = 4\,\hat{A}/\hat{P}$ is the hydraulic diameter, $\hat{A}$ is cross-sectional area, $\hat{P}$ is the wetted perimeter (in this case the perimeter of the cooling channel), k is the thermal conductivity of the bulk fluid, μ is the viscosity, ρ is the density and c_p is the specific heat capacity at constant pressure.

For water flowing through the hole at temperature $T_{\text{wat}} = 293$ K, with pipe length $L = 1$ m and pressure drop $\Delta p = 50$ kPa, the heat transfer coefficient $\hat{h}_s^{\text{wat}}$ with different sizes of d_s^{hole} on pre-fractals for the dust is calculated using Eq. (18) and given in Table 1.

Temperature plots on pre-fractals $\hat{E}_k$ for the analytical solution, for solutions from UoMFEC with different initial meshes on $\hat{E}_0$ and solutions from the commercial package ABAQUS are depicted in Fig. 6, with different values of k. The pre-fractal temperatures from the analytical solution and from UoMFEC are mapped from temperatures obtained on the corresponding tessellated structure $\hat{T}_k$. To obtain similar results from ABAQUS, two options are available for the Cantor dust: (i) indirect temperature determination via a tessellation with results lifted to the corresponding pre-fractal and (i.e. a procedure similar to that used by UoMFEC and termed ABAQUS-lifted) and (ii) temperatures obtained directly on the pre-fractal (termed ABAQUS-direct). Although not an issue for the Cantor dust (but certainly so for more complex fractals), the use of ABAQUS for the two approaches has particular drawbacks: with ABAQUS-lifted, complex orthotropic material properties for the tessellation have to be determined and input as a separate exercise; with ABAQUS-direct, complex geometries have to be loaded into the software.

The various approaches are tested on the pre-fractals and tessellation depicted in Fig. 5, where temperatures lifted from tessellations are of principal interest. The results are provided in Fig. 6 and Table 2 which, in general, establish the credibility of the tessellation strategy via the high accuracy returned. The averages $\bar{D}$ and $\bar{D}_\%$ given in Table 2 are obtained with the relationships

$$\bar{D} = \frac{1}{n}\sum_{i=1}^{n}\left|T_i^{(a)} - T_i^{(b)}\right| \tag{19}$$

and

$$\bar{D}_\% = \frac{2\times100}{n}\sum_{i=1}^{n}\left|\frac{T_i^{(a)} - T_i^{(b)}}{T_i^{(a)} + T_i^{(b)}}\right| \tag{20}$$

where superscripts (a) and (b) distinguish the methods (analytical solution, UoMFEC, ABAQUS-lifted and ABAQUS-direct) and n is the number of the data points.

Examination of Table 2 reveals relatively small errors, with the largest of these for ABAQUS-direct (i.e. for ABAQUS applied directly to the pre-fractals); this is a consequence of a modelling error arising from the approximate enforcement of continuity on a disconnected set.

Table 12 Heat transfer coefficients for the Sierpinski gasket heat exchanger on $\hat{E}_k$

k	d_s^{hole} (m)	$\hat{P}$ (m)	$\hat{h}_s^{\text{wat}}$ (W/m² K)
1	0.29	1.50	11,823.4
2	0.29	1.50	11,823.4
	0.14	0.75	5249.4
3	0.29	1.50	11,823.4
	0.14	0.75	5249.4
	0.07	0.38	2330.6
4	0.29	1.50	11,823.4
	0.14	0.75	5249.4
	0.07	0.38	2330.6
	0.04	0.19	1034.8
5	0.29	1.50	11,823.4
	0.14	0.75	5249.4
	0.07	0.38	2330.6
	0.04	0.19	1034.8
	0.02	0.09	459.4

5.2.3 Transient solution for a 1-D Cantor dust

The transient equation on the tessellated construction $\hat{T}_k$ with a discontinuity network for each tile is given by

$$\rho_r c_r \frac{\partial T_r}{\partial t} = K_r \frac{\partial^2 T_r}{\partial x^2} + \dot{Q}_0 - \frac{2\hat{h}_0}{w} (T_r - T_\infty)$$

(21)
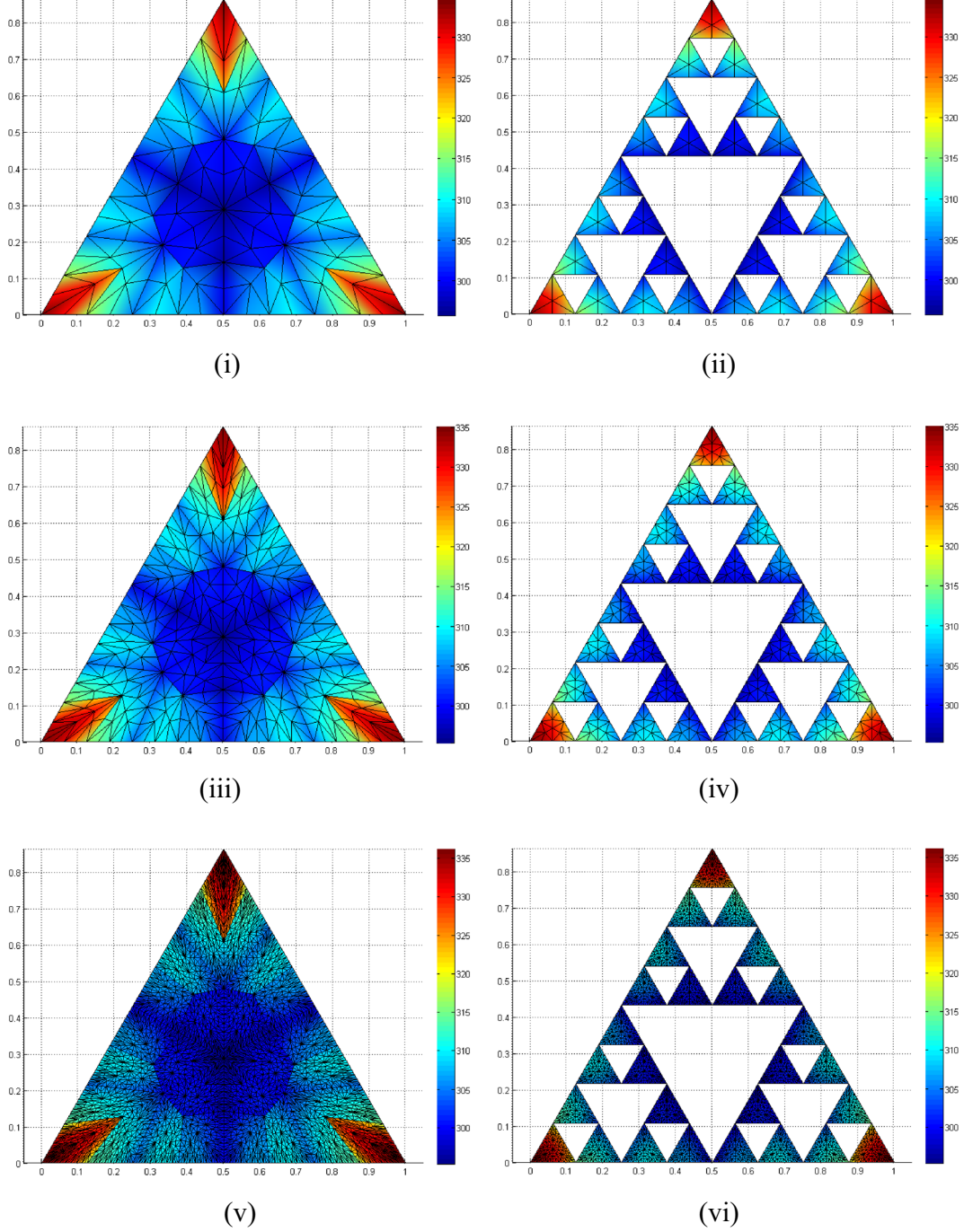
Fig. 17 Contour temperatures (UoMFEC) on $\hat{T}_3$ and $\hat{E}_3$ with different meshes. **i** Contours on continuum with six tiles on $\hat{E}_0$. **ii** Contours on corresponding pre-fractal with six tiles on $\hat{E}_0$. **iii** Contours on continuum with 18 tiles on $\hat{E}_0$. **iv** Contours on corresponding pre-fractal with 18 tiles on $\hat{E}_0$. **v** Contours on continuum with 162 tiles on $\hat{E}_0$. **vi** Contours on corresponding pre-fractal with 162 tiles on $\hat{E}_0$
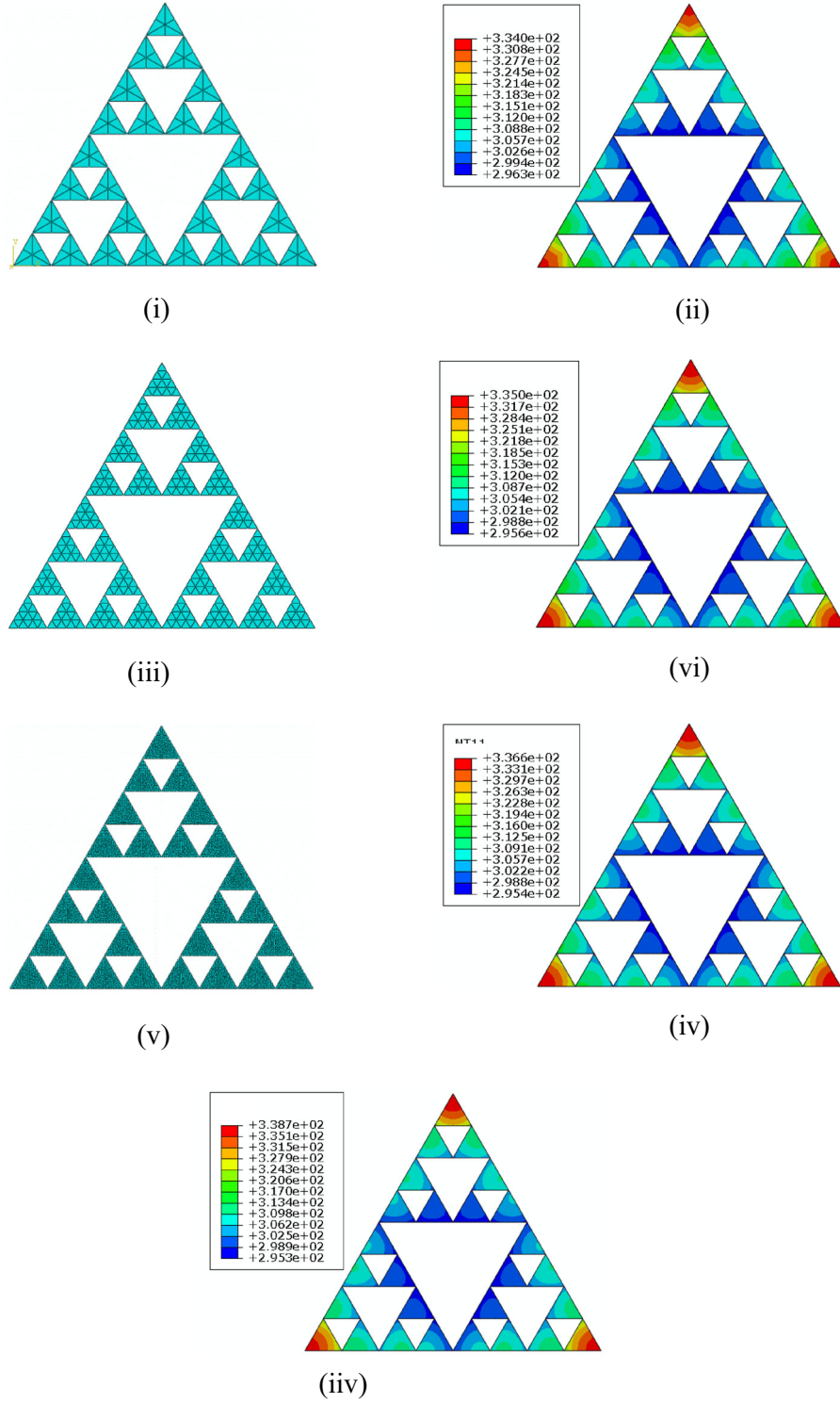
Fig. 18 ABAQUS-direct temperature plots on $\hat{E}_3$ directly for various meshes. **i** Mesh on $\hat{E}_3$ with six tiles per pre-fractal element. **ii** Contour temperature on $\hat{E}_3$ with six tiles per pre-fractal element. **iii** Mesh on $\hat{E}_3$ with 16 tiles per pre-fractal element. **iv** Contour temperature on $\hat{E}_3$ with 16 tiles per pre-fractal element. **v** Mesh $\hat{E}_3$ with 150 tiles per pre-fractal element. **vi** Contour temperature $\hat{E}_3$ with 150 tiles per pre-fractal element. **vii** Contour temperature $\hat{E}_3$ with 1536 tiles per pre-fractal element

in which it is assumed that steady-state temperatures are attained instantaneously at holes in pre-fractals with very high heat transfer coefficients. This assumption is an approximation but allows for an analytical solution of the form $T_r(x, t) = \mathcal{F}(x, t) + \mathcal{S}(x)$, where $\mathcal{S}(x)$ is the steady-state solution of Eq. (17) and $\mathcal{F}(x, t)$ satisfies

$$\rho_r c_r \frac{\partial \mathcal{F}}{\partial t} = K_r \frac{\partial^2 \mathcal{F}}{\partial x^2} - \frac{2\hat{h}_0}{w}\mathcal{F} \tag{22}$$

which, on assumption that $\mathcal{F}(x, t) = X(x)\,\tau(t)$ presents as

$$\frac{\rho_r c_r}{K_r} \frac{\dot{\tau}}{\tau} + \frac{2\hat{h}_0}{w K_r} = \frac{X''}{X} = -\omega^2. \tag{23}$$

This equation provides solutions with the transient part

$$\tau(t) = \exp(-\beta(\omega^2 + \alpha^2)t) \tag{24}$$

where $\beta = K_r/\rho_r c_r$ and $\alpha = \left(2\hat{h}_0/w K_r\right)^{\frac{1}{2}}$.

The tile considered here is $[x_i, x_{i+1}]$, so it is convenient to set the spatial part of the solution to

$$X(x) = A^i \cos(\omega(x - x_i)) + B^i \sin(\omega(x - x_i)). \tag{25}$$

To satisfy the specific temperatures as end conditions for each element, it is necessary for $A^i = 0$ and $\omega_n = 2^k n\pi/\ell_0$, with B^i unspecified, where use is made of the tile length $l_k = \ell_0/2^k$. It follows that solution on the interval $[x_i, x_{i+1}]$ is

$$T_r^i(x, t) = \mathcal{S}(x) + \sum_{n=1}^{\infty} B_n^i \sin(\omega_n(x - x_i)) \exp(-\beta(\omega^2 + \alpha^2)t) \tag{26}$$

where in the limit $t \to \infty$ the temperature $T_r^i(x, t) \to \mathcal{S}(x)$, i.e. steady-state conditions are obtained after a sufficient period of time.

For convenience, the initial condition along the bar is set to zero, i.e. $T(x, 0) = 0$, which means on $[x_i, x_{i+1}]$ the Fourier solution is required to satisfy

$$\sum_{n=1}^{\infty} B_n^i \sin(\omega_n(x - x_i)) = -\mathcal{S}(x) \tag{27}$$

which is a Fourier sine series representation of $-\mathcal{S}(x)$ on the interval $[x_i, x_{i+1}]$, where B_n^i are obtained from the Euler formulae

$$B_n^i = -\frac{2}{l_k} \int_{x_i}^{x_{i+1}} \mathcal{S}(x) \sin(\omega_n(x - x_i))\,.dx \tag{28}$$

The complete solution is obtained on joining solutions on tiles $[x_i, x_{i+1}]$ with $\bigcup_i [x_i, x_{i+1}] = [0, \ell_0]$.

Table 13 Temperature errors on the Sierpinski gasket pre-fractals along $y = 0$ on $\hat{E}_k$

k	No. of tiles on $\hat{E}_0$		Average difference comparing with ABAQUS-direct			
	UoMFEC	ABAQUS-direct with coarse mesh	With coarse mesh		With fine mesh	
			$\bar{D}$ (K)	$\bar{D}_\%$ (%)	$\bar{D}$ (K)	$\bar{D}_\%$ (%)
1	6	6	2.28	0.60	5.58	1.38
	18	16	2.07	0.53	1.82	0.45
	162	150	0.44	0.12	0.26	0.07
2	6	6	0.79	0.23	1.76	0.53
	18	16	0.58	0.17	0.76	0.23
	162	150	0.13	0.04	0.38	0.12
3	6	6	0.37	0.11	1.45	0.45
	18	16	0.29	0.09	1.20	0.37
	162	150	0.26	0.08	0.71	0.22

5.2.4 Transient validation tests

Transient results from the analytical solution are compared with results from UoMFEC and ABAQUS. The assumption adopted in Sect. 5.2.3—that temperatures in cooling channels immediately attain steady-state temperatures—makes the analytical solution approximate. The same meshes employed for the steady-state case are also employed for the transient analysis. Transient temperature plots for selected points on $\hat{E}_k$ are
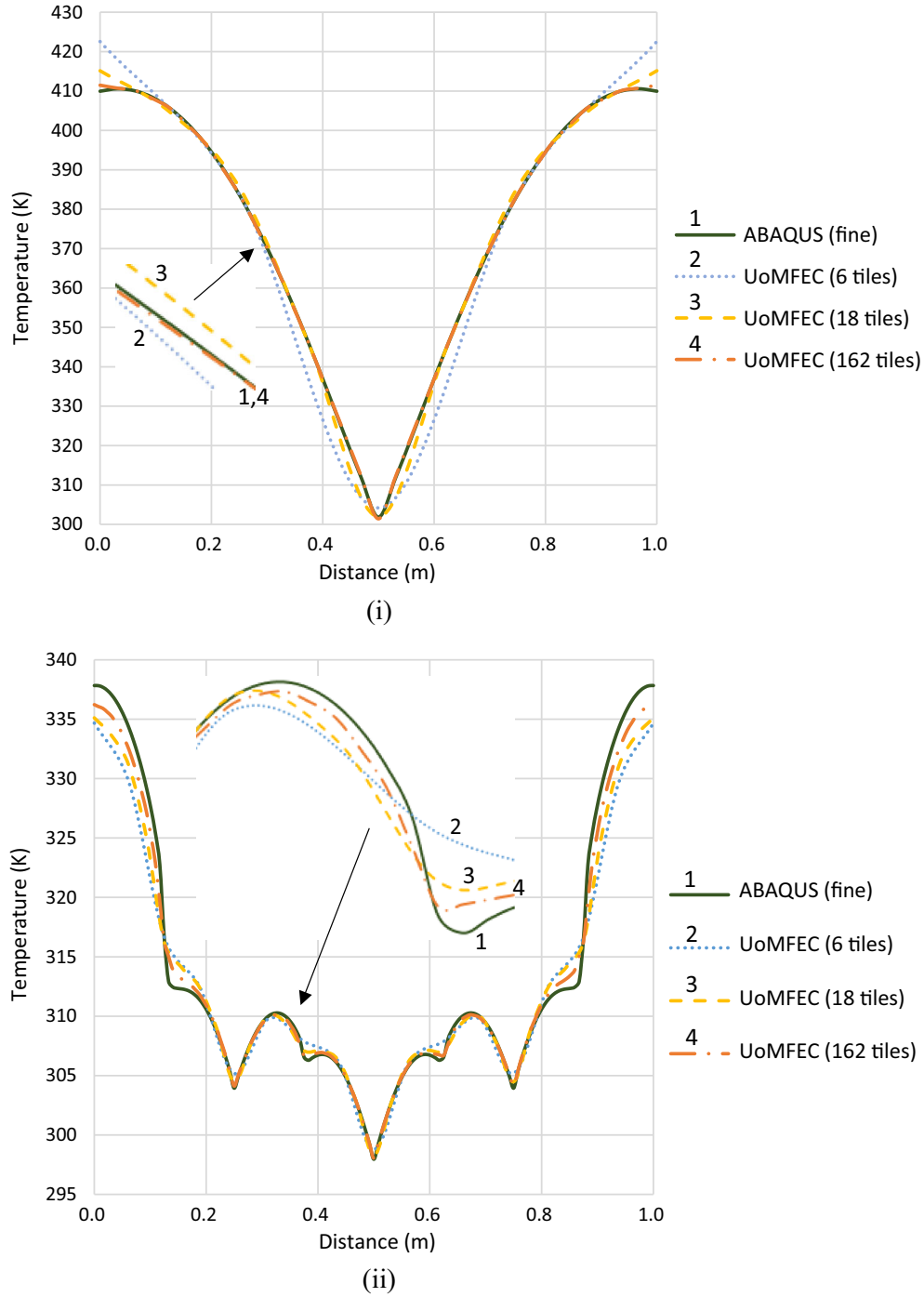

(i)

(ii)

Fig. 19 Temperature plots along $x = 0$ on $\hat{E}_k$ with different meshes using UoMFEC and ABAQUS-direct. **i** Temperature plots along $x = 0$ on $\hat{E}_1$. **ii** Temperature plots along $x = 0$ on $\hat{E}_3$

presented in Fig. 7, with average differences provided in Table 3; averages are again obtained using Eqs. (18) and (19).

Errors in results from UoMFEC and ABAQUS on the tessellations $\hat{T}_k$ and pre-fractals $\hat{E}_k$ are larger with lower values of k but reduce significantly as k increases. This trend is apparent on examination of Fig. 7 and Table 3. Increasing the value of k has the effect of increasing the number of elements involved, which appears to override deleterious effects coming from an increase in geometric complexity.

6 The importance of discontinuity networks

The results provided in reference [2] were performed without the use of a discontinuity network, which meant that temperature and heat transfer discontinuities could not be accommodated. It is of interest therefore to investigate the influence of discontinuity networks on the accuracy of predictions on realistic pre-fractals. In the absence of a network, cooling can be achieved along the edge of tiles by application of an appropriate heat sink as described in reference [2].

For the results presented in this section, the material selected for the heat exchangers is copper as used in Sect. 4 and the types of exchanger designs considered are limited to prismatic designs with cross sections represented by pre-fractals. The heat transfer coefficient $\hat{h}_{\mathrm{air}}$ associated with flowing air with temperature $T_{\mathrm{air}} = 323$ K around the pre-fractals is taken to be 100 W/m^2 K. Each pre-fractal has water flowing through the voids in order to match typical working conditions pertaining to heat exchangers and is subjected to a uniform heat loading with internal heat source $\dot{Q}_0 = 500\,\mathrm{kW/m^3}$.

6.1 Thermal analysis of a Sierpinski carpet heat exchanger

The Sierpinski carpet is selected to represent a closed-pore cellular material for the heat exchanger. The contraction and expansion maps for the pre-fractals and corresponding tessellations are provided in "Appendix B". It is assumed that the water coolant flows through the voids in the pre-fractal depicted in Fig. 2 with temperature $T_{\mathrm{wat}} = 293$ K. The heat transfer coefficients $\hat{h}_s^{\mathrm{wat}}$ for each hole in the pre-fractals (with different hole sizes and hydraulic diameters d_s^{hole}) are given in Table 4. Note that heat transfer coefficients in Table 4 are transferred to the corresponding edges in a tessellation but first must be scaled to satisfy Eq. (6).

Two different meshes are defined in ABAQUS as follows: (i) one is a coarse mesh with exactly the same number of tiles as used in UoMFEC and (ii) the other is a sufficiently fine mesh to provide a converged result. Temperature distributions obtained with UoMFEC on tessellation $\hat{T}_3$ with and without discontinuity networks, and with results subsequently mapped to pre-fractal $\hat{E}_3$ are depicted in Fig. 8. Similarly, results obtained
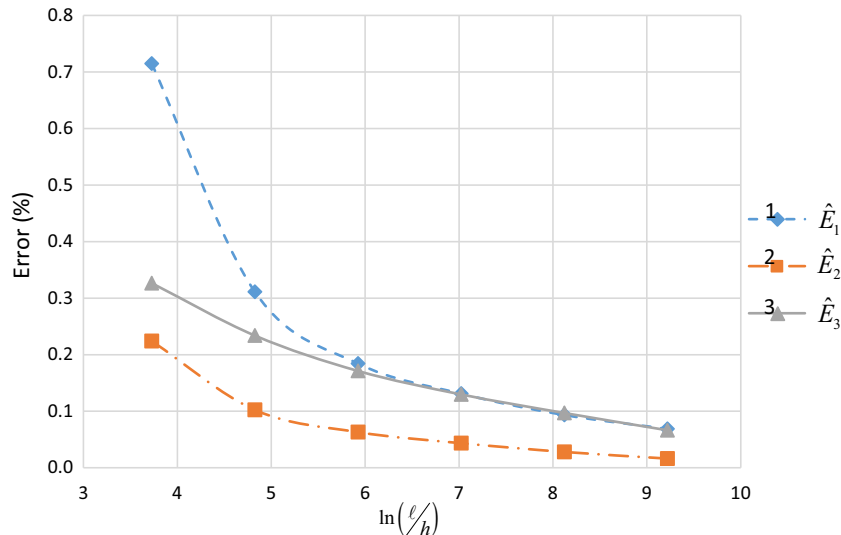
Fig. 20 Percentage error plots on $\hat{E}_k$ showing decay with mesh refinement

directly on $\hat{E}_3$ are obtained using ABAQUS (on two meshes) which are presented in Fig. 9. To provide a quantitate basis of comparison, the average errors (using the converged ABAQUS solution as a benchmark) are calculated using Eqs. (18) and (19) along the diagonal line $x = y$ on $\hat{E}_k$. These errors are given in Table 5,
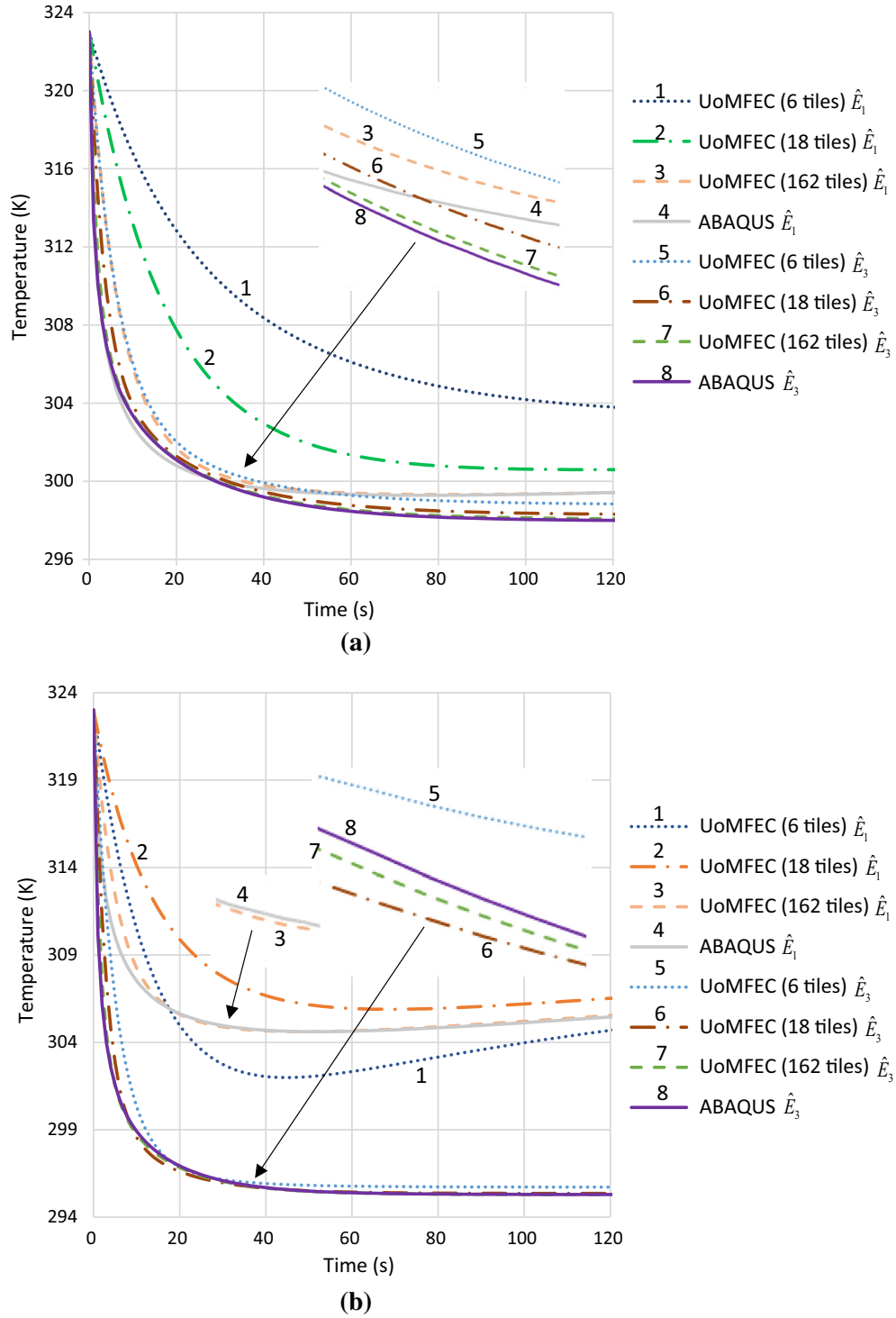
Fig. 21 Transient temperature plots for different points on $\hat{E}_k$ using UoMFEC and ABAQUS-direct. **a** Transient temperature plots for point (0.5, 0) on $\hat{E}_k$. **b** Transient temperature plots for point (0.5, 0.433) on $\hat{E}_k$

Table 14 Average transient temperature differences at points (see Fig. 1) on $\hat{E}_k$

k	No. of tiles on $\hat{E}_0$		Average difference comparing with ABAQUS (fine)			
	UoMFEC	ABAQUS-direct with coarse mesh	Point (0.5, 0)		Point (0.5, 0.433)	
			$\bar{D}$ (K)	$\bar{D}_\%$ (%)	$\bar{D}$ (K)	$\bar{D}_\%$ (%)
1	6	6	3.25	1.07	1.32	0.42
	18	16	0.74	0.24	1.26	0.41
	162	150	0.33	0.11	0.15	0.05
2	6	6	1.91	0.64	0.42	0.14
	18	16	0.73	0.24	0.43	0.14
	162	150	0.14	0.05	0.20	0.07
3	6	6	0.88	0.29	0.45	0.15
	18	16	0.33	0.11	0.08	0.03
	162	150	0.08	0.03	0.01	0.24×10^{-2}
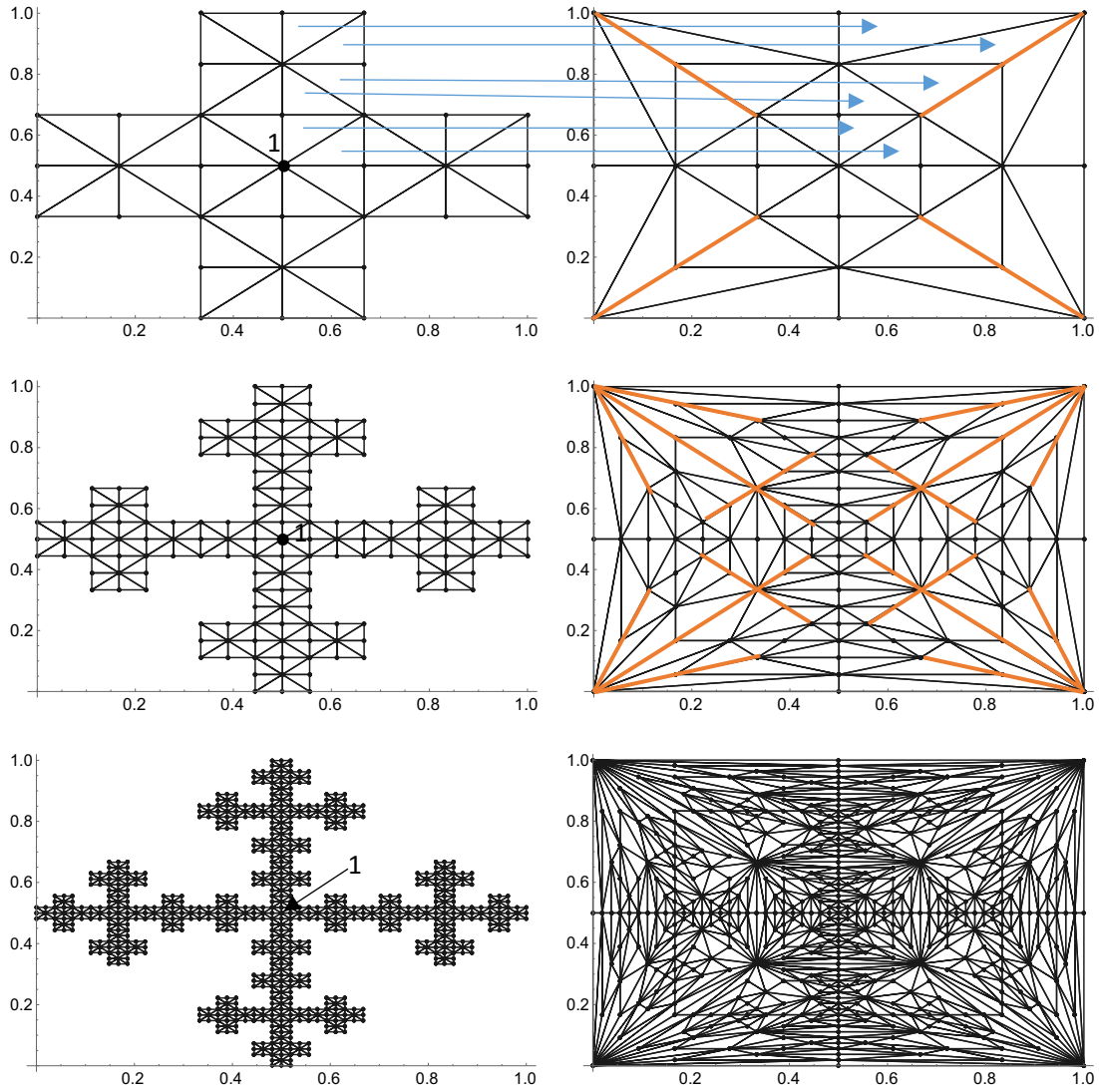
Fig. 22 Pre-fractal and corresponding tessellated domains containing discontinuity networks for a Vicsek fractal with hole-fill map formed with expansion map **(a)**

and corresponding temperature distributions are presented in Fig. 10. It can be seen that errors increase with an increase in k for the tessellated approach without discontinuity networks as a consequence of the unrealistic enforcement of continuity at cooling channel holes. Although in this case reasonable accuracy is obtained in the absence of a discontinuity network, higher accuracy is achieved with its inclusion.

Continuity assumptions are enforced on tessellations without discontinuity networks, which is equivalent to temperatures and heat transfer rates on opposite sides of pre-fractal holes having identical values. This lack of realism gives rise to problem-dependent modelling errors. It is of interest, however, to quantify the maximum temperature difference T_{diff} at a discontinuity network $\hat{D}_k$ to provide a direct indication of the significance of this aspect; T_{diff} is formally defined to be

$$T_{\text{diff}} = \max_{x \in \hat{D}_k} \left| T^+ (\boldsymbol{x}) - T^- (\boldsymbol{x}) \right| \tag{29}$$

where $T^+ - T^-$ is the jump in temperature across the discontinuity network $\hat{D}_k$.
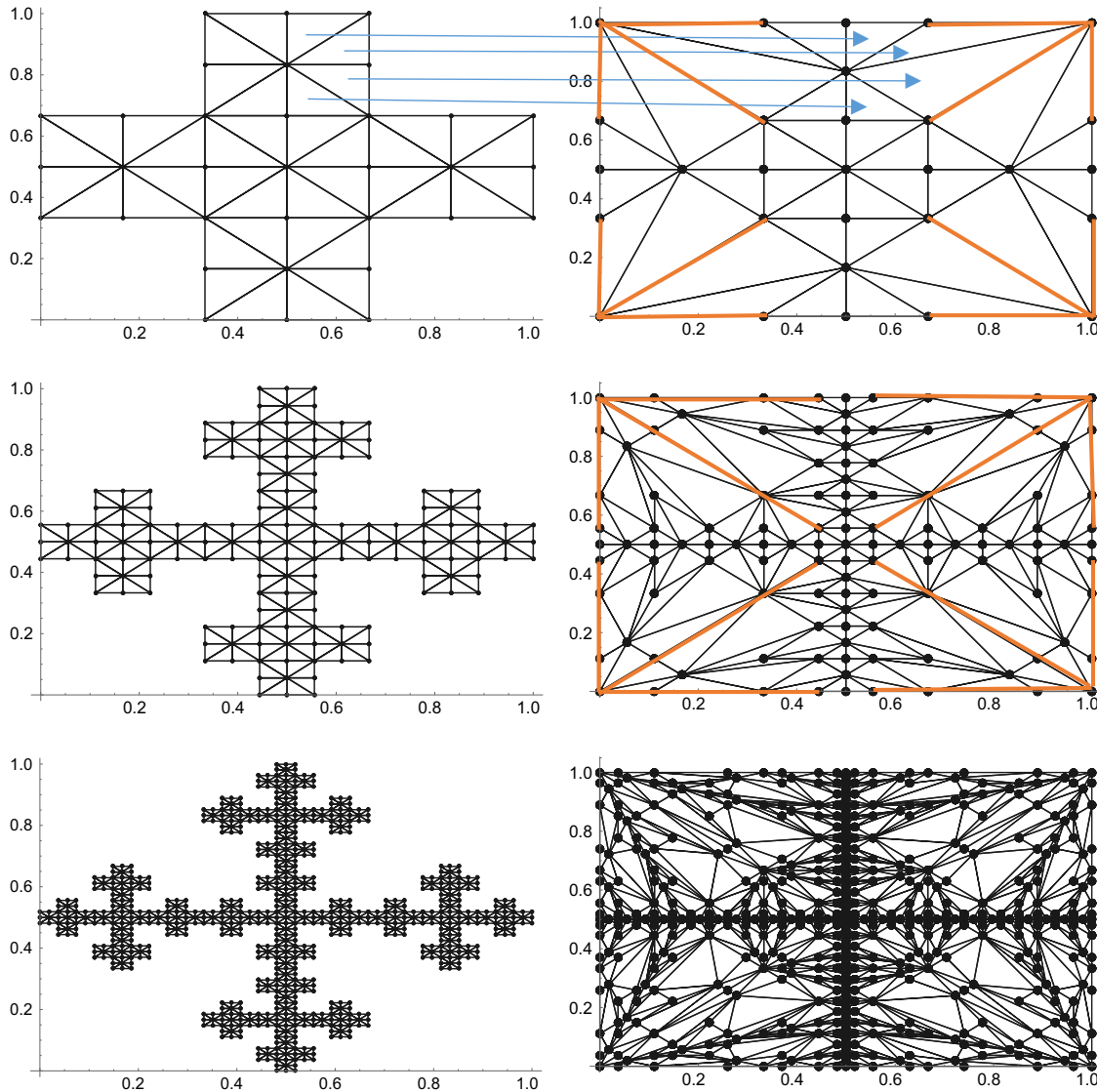

Fig. 23 Pre-fractal and corresponding tessellated domains containing discontinuity networks for a Vicsek fractal with hole-fill map formed with expansion map **(b)**

In the case of the Sierpinski carpet heat exchanger, the values for T_{diff} are presented in Table 6. The magnitude is significant on $\hat{D}_3$ and $\hat{D}_2$ but zero on $\hat{D}_1$ as a consequence of symmetric boundary conditions and the one symmetrically located hole.

Transient temperature plots mapped on $\hat{E}_k$ for the different points shown in Fig. 2 are provided in Fig. 11 for UoMFEC on two tessellations, which are compared with convergent ABAQUS-direct results (ABAQUS applied directly to the pre-fractals with fine mesh). In addition, average differences calculated by Eqs. (19) and (20) are given in Table 7 at two points in $\hat{E}_k$. Similar to the steady-state solution, the discontinuity network has little impact on transient results on $\hat{E}_1$. However, the influence of the network becomes obvious with increase in k, where its inclusion provides greater accuracy. Errors tend to be greatest at or close to boundaries of holes, and an increase in k provides a greater number of holes.

6.2 Finger-like fractal

It is of interest to investigate the open-pore structure depicted in Fig. 3 to represent a cellular heat exchanger. The open-pore structure is assumed to be placed in a close-fitting container to enforce the flow of coolant through the structure. The contraction and expansion maps for the pre-fractals and corresponding tessellations shown in Fig. 3 are provided in "Appendix C". The heat transfer coefficients $\hat{h}_s^{\text{wat}}$ associated with each hydraulic diameter d_s^{hole} in the pre-fractals are given in Table 8. Examination of Fig. 3 and Table 8 highlights a peculiar feature with higher heat transfer coefficients appearing at smaller holes on different tessellations. This is an unfortunate consequence of the rather irregular wetted perimeter used in the calculation for the hydraulic diameter.

Temperature distributions for the finger-like porous fractal are provided Figs. 12 and 13. Equations (19) and (20) are again used to determine the average errors (contrasted against the benchmark converged ABAQUS-direct results) along the diagonal line $x = y$ on $\hat{E}_k$. The temperature differences are presented in Table 9 with

Fig. 24 Principal thermal conductivity ratio (K_r/K_s) distribution for Vicsek fractal with hole-fill map formed with expansion map (a). **i** Contours on $\hat{T}_1$. **ii** Contours on $\hat{T}_2$. **iii** Contours on $\hat{T}_3$. **iv** Graph on $\hat{T}_1$. **v** Graph on $\hat{T}_2$. **vi** Graph on $\hat{T}_3$

corresponding temperature plots in Fig. 14. It is evident on examination in Table 9 and Fig. 14 that greater accuracy is achieved with the inclusion of a discontinuity network. Errors are observed to be particularly large for the continuous Galerkin approach at extreme corners and remain high despite higher values of k. Large error at the corners is an indication that insufficient elements are being placed there, which is a constraint imposed by tiles doubling up as elements with tessellations being created recursively.

Equation (29) is again employed to quantify the extent of the temperature differences on $\hat{D}_k$ for the finger fractal with the results given in Table 10. The results are similar to the results obtained for the Sierpinski gasket (see Table 6) with non-trivial differences on $\hat{D}_3$ and $\hat{D}_2$ but zero on $\hat{D}_1$ because of symmetric boundary conditions and the location of the (in this case) four holes.

Using the points illustrated in Fig. 3 on $\hat{E}_k$, transient temperatures are depicted in Fig. 15, obtained both from $\hat{T}_k$ (UoMFEC) and directly obtained with ABAQUS-direct with fine mesh. The average differences calculated by Eqs. (19) and (20) are provided in Table 11. The importance of including a discontinuity network is clear on examination of the results, with maximum errors appearing at corners. The temperatures produced by the continuous Galerkin method close to the corners are higher than those with a discontinuity network.

Comparing errors produced on the closed-pore structure (Sierpinski carpet) against the open-pore structure (finger-like fractal) reveals the latter structure's relative sensitivity to the inclusion of a discontinuity network.
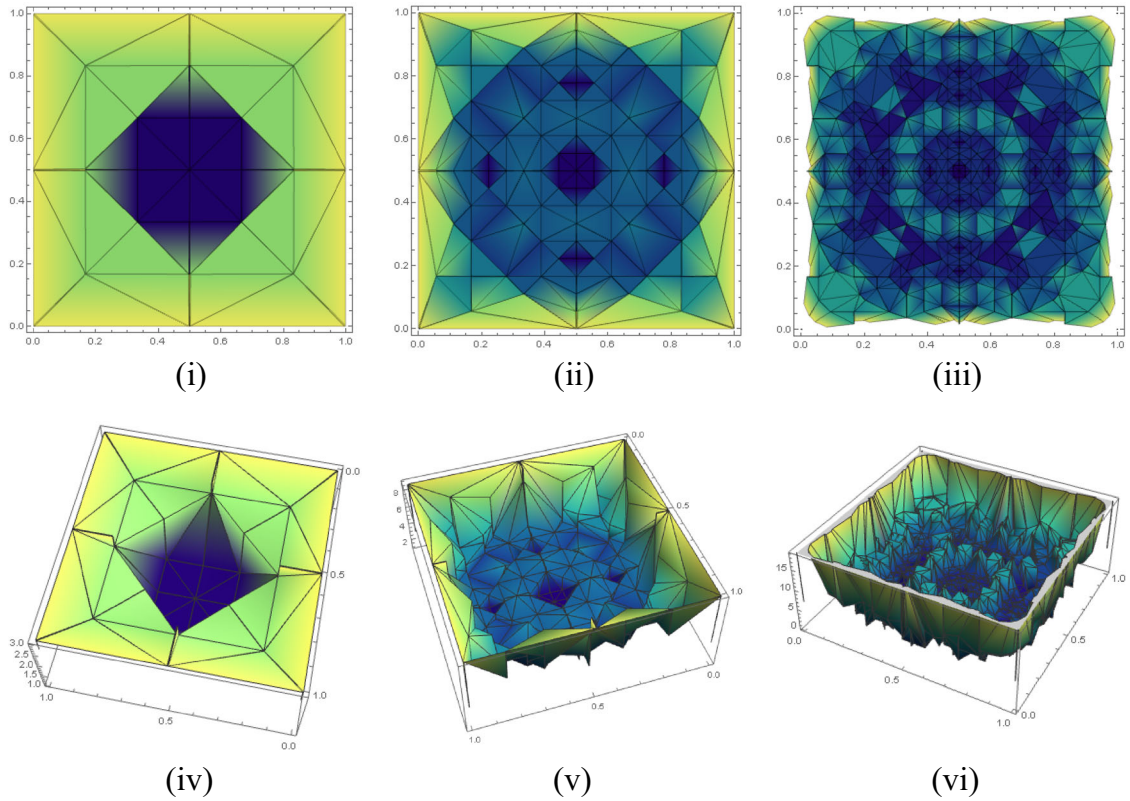

(i) (ii) (iii)

(iv) (v) (vi)
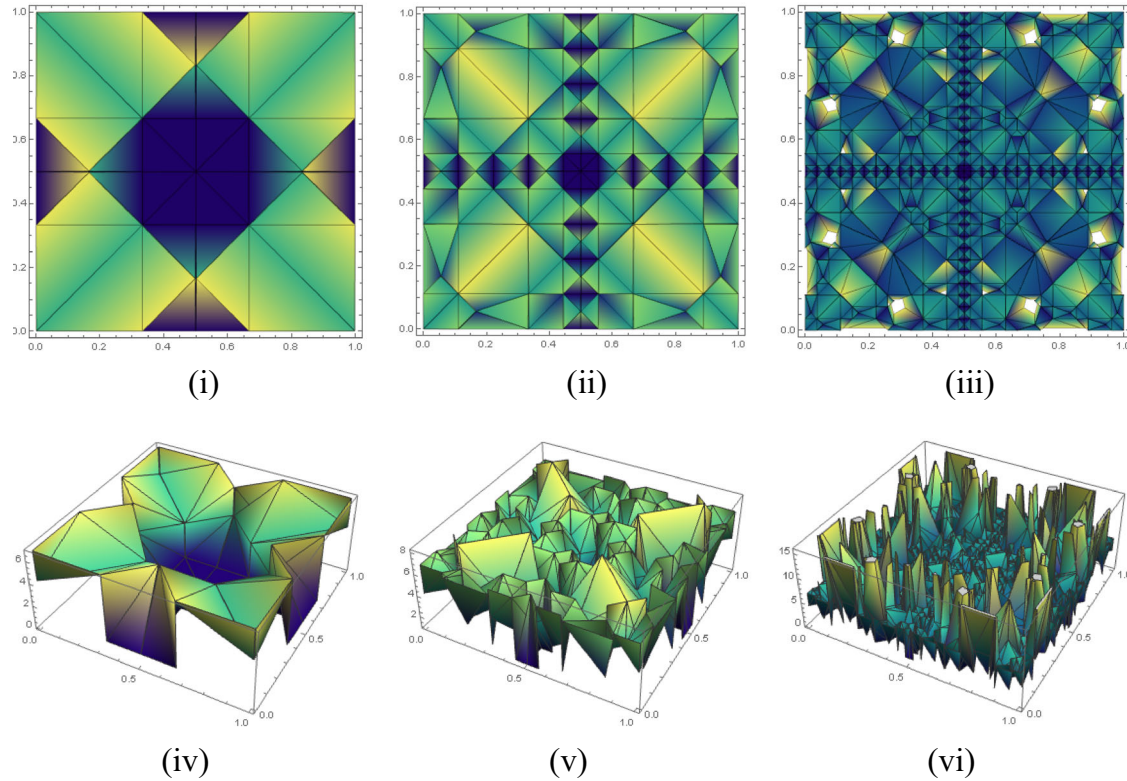
Fig. 25 Principal thermal conductivity ratio (K_r/K_s) distribution for Vicsek fractal with hole-fill map formed with expansion map (b). **i** Contours on $\hat{T}_1$. **ii** Contours on $\hat{T}_2$. **iii** Contours on $\hat{T}_3$. **iv** Graph on $\hat{T}_1$. **v** Graph on $\hat{T}_2$. **vi** Graph on $\hat{T}_3$

Table 15 Heat transfer coefficients for the Vicsek fractal heat exchanger on $\hat{E}_k$

k	d_s^{hole} (m)	$\hat{P}$ (m)	$\hat{h}_s^{\text{wat}}$ (W/m^2 K)
1	0.33	1.33	12,735.0
2	0.31	2.22	17,675.8
3	0.25	3.26	18,953.1
4	0.19	4.84	18,141.7
5	0.13	7.42	16,327.6

This is not unexpected, since enforcing continuity between points separated across holes is difficult to justify and is unrepresentative for open-pore constructions of the type depicted in Fig. 3.

7 The influence of mesh

It is apparent from the results in previous sections that UoMFEC provides improved accuracy in its mapped results when compared with results obtained from ABAQUS applied directly to pre-fractals. A feature of the tessellated approach, however, is that the tessellated mesh used in any analysis is related to the initial tessellation on $\hat{E}_0$; it is thus of interest to investigate the influence the initial tessellation has on the accuracy of predicted results.

Consider again the Sierpinski gasket with an initial tessellation of 6 elements on $\hat{T}_0 = \hat{E}_0$. Re-examination of Fig. 1 reveals tessellations on $\hat{T}_1$, $\hat{T}_2$ and $\hat{T}_3$ consisting of $18 = 3 \times 6$, $54 = 3^2 \times 6$ and $162 = 3^3 \times 6$ tiles. The tile numbers arise from the number of maps involved (i.e. 3) and the initial number of tiles (i.e. 6). Each of these tessellations is produced by the expansion maps provided in "Appendix A". These tessellations could all in principle be used as alternative initial tessellations on $\hat{E}_0$. The expansion maps now associated with these initial tessellations on $\hat{T}_0 = \hat{E}_0$ are obtained by function compositions of the maps in "Appendix A", but there is no requirement to formulate these explicitly because all tessellations can be produced from the original set of maps. This aspect is demonstrated in Fig. 16, which shows tessellations produced solely from the maps in "Appendix A", without recourse to composite functions. The different initial tessellations on $\hat{T}_1$ and $\hat{E}_1$ in Fig.

(i)   (ii)

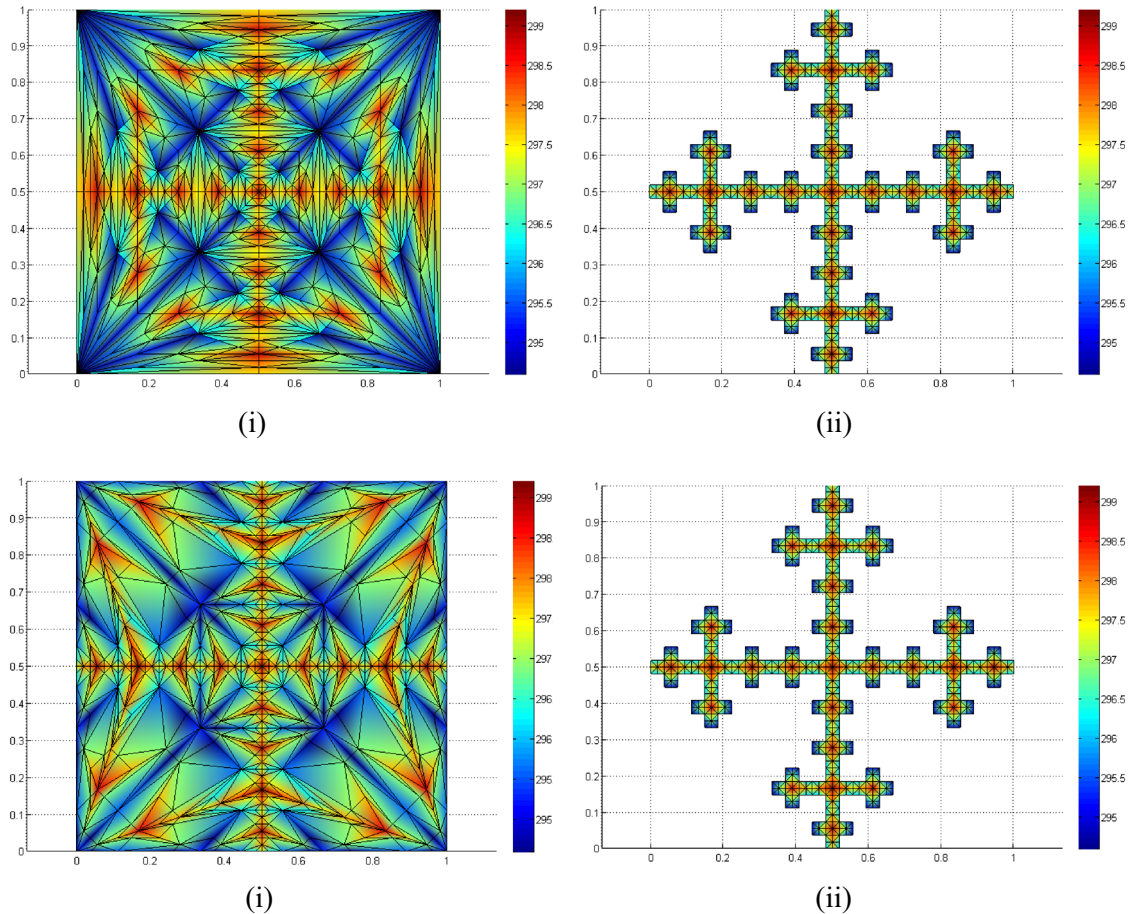(i)   (ii)

Fig. 26 Contour temperatures (UoMFEC) on $\hat{T}_3$ and $\hat{E}_3$ with hole-fill maps constructed with different expansion maps. i Contour temperatures on $\hat{T}_3$ with expansion map (a). ii Contour temperatures on $\hat{E}_3$ with expansion map (a). i Contour temperatures on $\hat{T}_3$ with expansion map (b). ii Contour temperatures on $\hat{E}_3$ with expansion map (b)

16 are obtained from different initial tessellations on $\hat{E}_0$, themselves formed from a tessellation consisting of six tiles. Thermal analysis performed on the Sierpinski carpet in Sect. 5 is repeated but on the gasket with an internal heat loading $Q_{tot} = 300\text{kW/m}^3$ and cooling-channel heat transfer coefficients given in Table 12, for the various hydraulic diameters involved.

Temperature distributions on $\hat{T}_3$ mapped to $\hat{E}_3$ as determined by UoMFEC are shown in Fig. 17. These are compared with results from ABAQUS-direct applied directly to $\hat{E}_3$ for a similar numbers of elements as presented in Fig. 18. All the temperatures from UoMFEC (all UoMFEC results are lifted from the tessellation) provide very close agreement with ABAQUS-direct results, providing further confidence in the tessellation method and discontinuity networks. The average errors determined using Eqs. (19) and (20) on the edge $y = 0$ are given in Table 13. The results correspond to temperatures presented in Fig. 19.

The average error (contrasting UoMFEC against a convergent ABAQUS-direct solution) obtained using Eq. (19) is recorded to give an indication on how error reduces with mesh refinement. Mesh refinement is achieved through the increasing the number of tiles on the original set $\hat{E}_0$. The recorded errors on $\hat{E}_k$ are depicted in Fig. 20, where convergent behaviour is observed.

Transient temperature profiles are shown in Fig. 21 along with average differences given in Table 14. Both steady-state and transient results confirm that accuracy improves with tessellated mesh refinement.
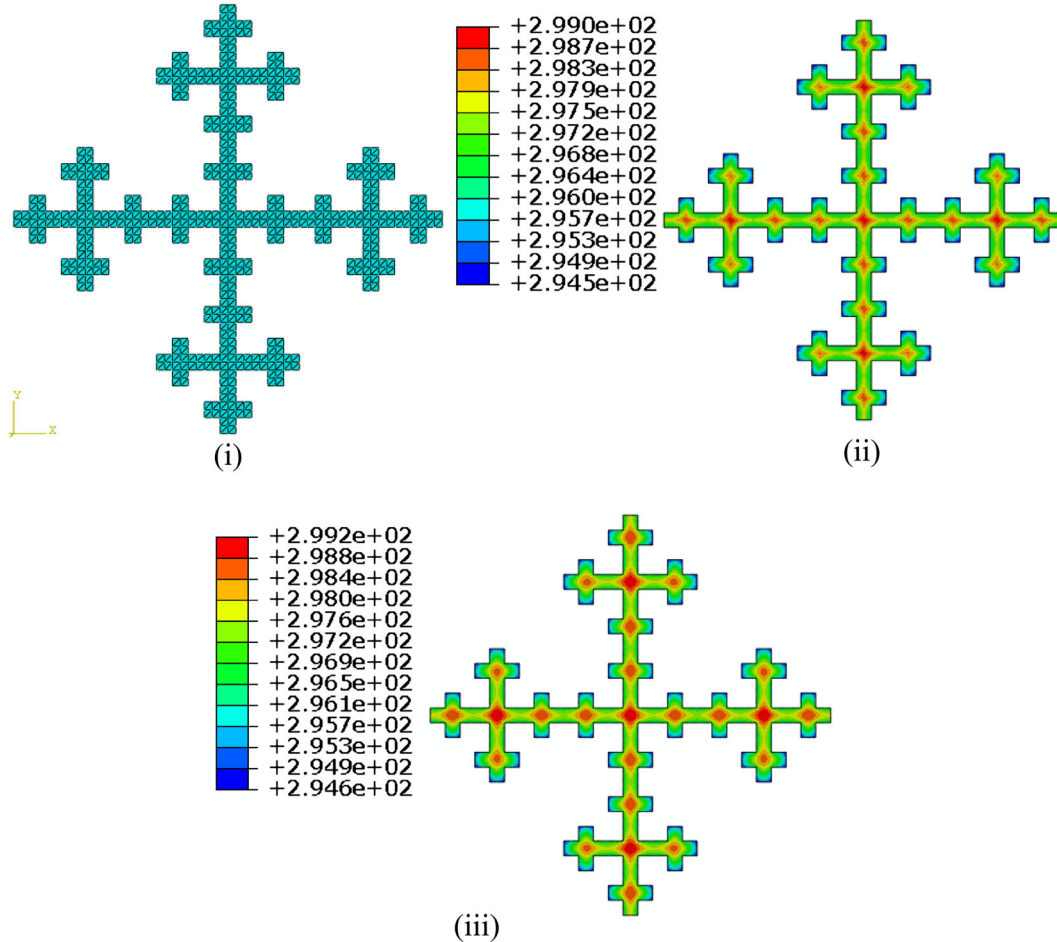

Fig. 27 Contour temperature plots (ABAQUS-direct) on $\hat{E}_3$ directly for various meshes. **i** Mesh on $\hat{E}_3$ with eight elements per pre-fractal element. **ii** Contour temperatures on $\hat{E}_3$ with eight elements per pre-fractal element. **iii** Contour temperatures on $\hat{E}_3$ with 152 elements per pre-fractal element

8 The influence of different hole-fill maps

One of the features of the tessellated approach is the non-uniqueness of the sub-expansion maps P_{ij} in the formation of on an expansion map P_i. This variability is reflected in changes in the tessellation on $\hat{T}_1$ and changes in P_i change the hole-fill map $x : s \mapsto x$ and influence the precise manner in which holes are closed. Recall that hole-fill maps relate points s on a pre-fractal to points x in a tessellation. Any temperature $T(x, t)$ calculated on a tessellation is related to a temperature on a pre-fractal through the hole-fill map $x : s \mapsto x$, i.e. $T(s, t) = T(x(s), t)$. Predictions on a pre-fractal are required to be invariant with respect to the non-unique choice of hole-fill map $x : s \mapsto x$. The explicit form the hole-fill map takes for a fixed set of contraction maps S_i depends on the choice of expansion maps P_i. It is of interest therefore to demonstrate explicitly the invariance of predictions for two significantly different hole-fill maps. It is also of interest to examine the effect distorted tiles have on the accuracy of predictions. These aspects are examined on pre-fractals for the classic Vicsek fractal, on tessellations formed with two distinct hole-fill maps.

8.1 Pre-fractal and tessellation construction

The Vicsek fractal is a non-product fractal, constructed by the recursive application of the affine contraction maps shown in Table 23, "Appendix D". Pre-fractals and two corresponding tessellations are shown in Figs. 22 and 23. These are formed from an initial tessellation on $\hat{E}_0$ consisting of eight-triangular tiles and are produced with expansion maps defined in Tables 24 and 25. The arrows depicted in Figs. 22 and 23 illustrate for a selection of triangles the effect of the two mappings.

Thermal conductivity contours using Eq. (5) for point-wise maximum thermal conductivities are shown in Figs. 24 and 25. Examination of the two figures reveals significant differences in the distributions; it should be appreciated that differences in the tessellated space can be expected but of principal concern is the retention of isotropy in the physical space.

8.2 Thermal analysis of a Vicsek fractal heat exchanger

The open-pore Vicsek structure is assumed to be placed in a close-fitting container to enforce the flow of coolant through the structure. Consider then water coolant flowing through the voids shown in Figs. 22 and 23; the
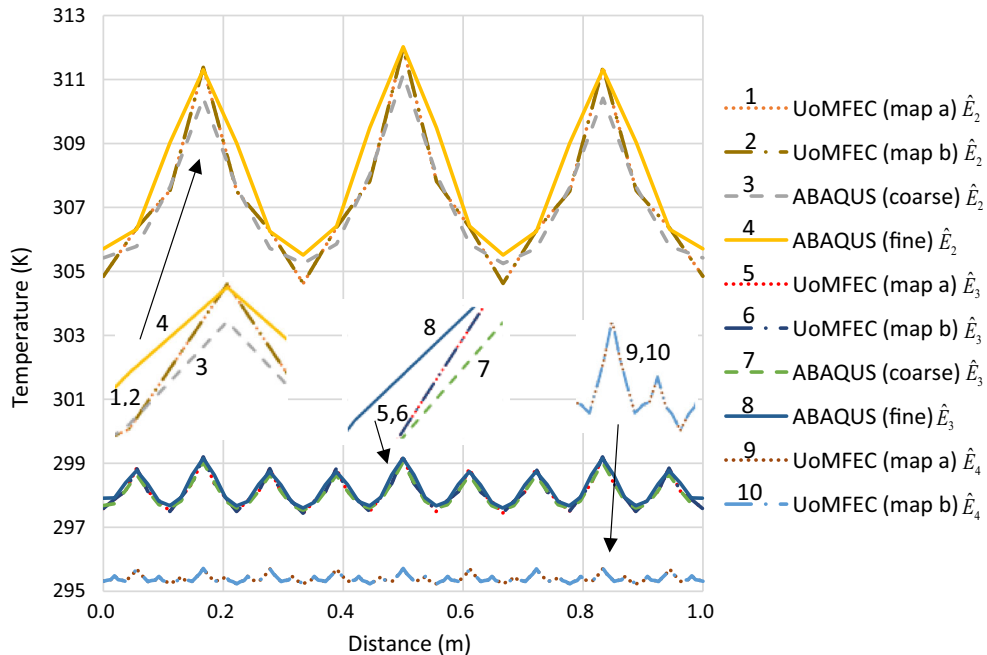

Fig. 28 Temperature plots along $y = 0.5$ for pre-fractals $\hat{E}_k$ using UoMFEC and ABAQUS-direct

heat exchanger is manufactured from the same copper material used in Sect. 5 with the exact same surrounding conditions. A uniform heat loading of $\dot{Q}_{tot} = 500\,\text{kW/m}^3$ is applied on each pre-fractal as an internal heat source. The cooling-channel heat transfer coefficients $\hat{h}_s^{\text{wat}}$ are provided in Table 15 for the hydraulic diameters met on the Vicsek fractal.

Temperature distributions on pre-fractal $\hat{E}_3$ and corresponding tessellation $\hat{T}_3$ determined by UoMFEC from the two different tessellation maps are shown in Fig. 26. These can compared against results obtained with ABAQUS-direct for two meshes as depicted in Fig. 27. Examination of Fig. 26 reveals stark differences in temperatures on the tessellation, yet almost identical results in the physical space. This result provides good evidence that the manner in which tessellations are created does not affect the final outcome as seen on pre-fractals in the physical space. To quantify the results more precisely, temperature distributions along $y = 0.5$ are shown in Fig. 28 for both ABAQUS-direct and UoMFEC. It is clear that the two sets of tessellations return high accuracy. The errors calculated via Eqs. (19) and (20) are also given in Table 16 and also confirm high accuracy.

Transient plots for Point 1 in Fig. 22 with coordinates (0.5, 0.5) on $\hat{E}_k$ are depicted in Fig. 29 along with the average differences calculated by Eq. (19) and (20) in Table 17. The results provided further evidence that different hole-fill maps have little impact on results viewed in the physical space.

Table 16 Average temperature errors on Vicsek fractal along $y = 0.5$ on $\widehat{E}_k$

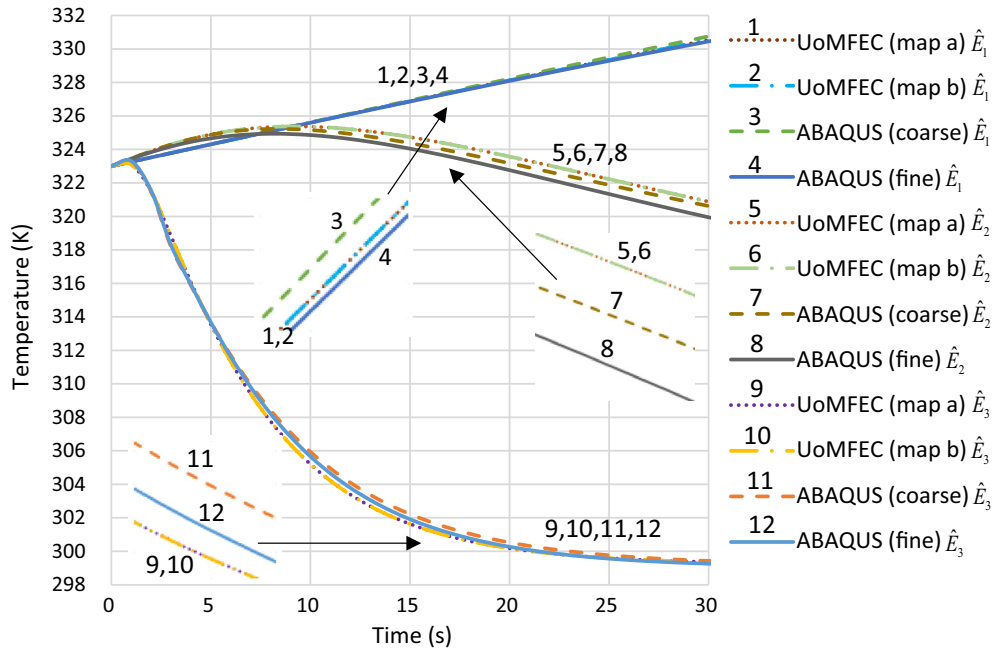| k	1	2	3
Results with hole-fill map formed with expansion map (a) in Table 24			
Coarse mesh			
$\bar{D}$ (K)	2.54	0.49	0.10
$\bar{D}_\%$ (%)	0.73	0.16	0.03
Fine mesh			
$\bar{D}$ (K)	4.03	0.70	0.13
$\bar{D}_\%$ (%)	1.16	0.23	0.05
Results with hole-fill map formed with expansion map (b) in Table 25			
Coarse mesh			
$\bar{D}$ (K)	2.54	0.49	0.10
$\bar{D}_\%$ (%)	0.73	0.16	0.03
Fine mesh			
$\bar{D}$ (K)	4.03	0.70	0.13
$\bar{D}_\%$ (%)	1.16	0.23	0.05

Fig. 29 Temperature plots for point (0.5, 0.5) on $\hat{E}_k$ using UoMFEC and ABAQUS-direct

Table 17 Transient temperature differences at point (0.5, 0.5) on Vicsek pre-fractals

k	1	2	3
Hole-fill map formed with expansion map (a) in Table 24			
Coarse mesh			
$\bar{D}$ (K)	0.75	0.06	0.06
$\bar{D}_\%$ (%)	0.21	0.02	0.02
Fine mesh			
$\bar{D}$ (K)	2.14	0.84	0.17
$\bar{D}_\%$ (%)	0.60	0.27	0.06
Hole-fill map formed with expansion map (b) in Table 25			
Coarse mesh			
$\bar{D}$ (K)	1.09	0.06	0.06
$\bar{D}_\%$ (%)	0.30	0.02	0.02
Fine mesh			
$\bar{D}$ (K)	1.80	0.84	0.17
$\bar{D}_\%$ (%)	0.50	0.27	0.06

It is worth noting that highly skewed tiles also have little impact on the accuracy of the results with the tessellated approach. This is expected because changes in thermal conductivities compensate to provide an analysis which is akin to doing calculations with the regular meshes appearing on the corresponding pre-fractals.

9 Conclusions

This paper tests the hypothesis that heat transfer analysis on porous media for cellular heat exchangers can be performed on a tessellation with new form of tessellated continuum mechanics using the finite element method. Thermal analysis of a relatively complex structures replicated by pre-fractals is demonstrated on corresponding tessellations incorporating discontinuity networks. In establishing the tessellated finite element approach for heat transfer on tessellations with discontinuity networks, the following conclusions can be drawn:

- Temperatures on tessellated structures have been shown to return the temperatures on pre-fractals in support of the contention that heat transfer analysis on pre-fractals can be achieved through analysis on tessellations with high accuracy.
- The accuracy of the tessellated approach with the finite element method can be significantly improved by incorporating discontinuity networks in tessellations.
- The use of highly skewed tiles and alternative expansion maps has little impact on the accuracy of the procedure.
- Increased accuracy can be obtained by refining the initial tessellation on the initial domain $\hat{T}_0 = \hat{E}_0$, which can be achieved very efficiently through multiple application of affine expansion maps.

Appendix A: Maps for the Sierpinski gasket

The Sierpinski gasket is an example of a non-product fractal set and is constructed by the recursive application of the following three affine contraction maps:

$$S_1(x, y) = \left(\frac{x}{2}, \frac{y}{2}\right), \quad S_2(x, y) = \left(\frac{\ell_0}{2} + \frac{x}{2}, \frac{y}{2}\right) \text{ and } S_3(x, y) = \left(\frac{\ell_0}{4} + \frac{x}{2}, \frac{\sqrt{3}\ell_0}{4} + \frac{y}{2}\right), \quad (28)$$

where each S_i maps a triangular domain into a smaller triangular as deduced on inspection of Fig. 1.
The initial six tiles on the triangular domain $\hat{E}_0$ provide a means to define the expansion maps for the construction of $\hat{T}_k$. Each expansion map consists of a number of sub-maps with a number equal to the number of initial tiles on $\hat{E}_0$ (6 in this case). Explicitly, the expansion maps for the Sierpinski are illustrated in Table 18.

Table 18 Expansion maps for Sierpinski

$P_1(x, y)$	$P_{11}(x, y) = \left(\frac{x}{2} + \frac{y}{2\sqrt{3}}, \frac{2y}{3}\right)$	if $2x < \ell_0$ and $\sqrt{3}y < x$
	$P_{12}(x, y) = \left(\frac{3x}{4} - \frac{y}{4\sqrt{3}}, \frac{x}{4\sqrt{3}} + \frac{5y}{12}\right)$	if $\sqrt{3}y \leq \ell_0 - x$ and $\sqrt{3}y \geq x$
	$P_{13}(x, y) = \left(\frac{3x}{4} - \frac{y}{4\sqrt{3}}, \frac{x}{4\sqrt{3}} + \frac{5y}{12}\right)$	if $\sqrt{3}y > \ell_0 - x$ and $2x < \ell_0$
	$P_{14}(x, y) = \left(\frac{3x}{4} - \frac{y}{4\sqrt{3}}, \frac{x}{4\sqrt{3}} + \frac{5y}{12}\right)$	if $\sqrt{3}y \geq x$ and $2x \geq \ell_0$
	$P_{15}(x, y) = \left(\frac{x}{2} + \frac{y}{2\sqrt{3}}, \frac{2y}{3}\right)$	if $\sqrt{3}y > \ell_0 - x$ and $\sqrt{3}y < x$
	$P_{16}(x, y) = \left(\frac{x}{2} + \frac{y}{2\sqrt{3}}, \frac{2y}{3}\right)$	if $\sqrt{3}y \leq \ell_0 - x$ and $2x \geq \ell_0$
$P_2(x, y)$	$P_{21}(x, y) = \left(\frac{x}{2} + \frac{\ell_0}{4}, -\frac{x}{2\sqrt{3}} + \frac{2y}{3} + \frac{\sqrt{3}\ell_0}{4}\right)$	if $2x < \ell_0$ and $\sqrt{3}y < x$
	$P_{22}(x, y) = \left(\frac{x}{2} + \frac{\ell_0}{4}, -\frac{x}{2\sqrt{3}} + \frac{2y}{3} + \frac{\sqrt{3}\ell_0}{4}\right)$	if $\sqrt{3}y \leq \ell_0 - x$ and $\sqrt{3}y \geq x$
	$P_{23}(x, y) = \left(\frac{x}{2} + \frac{\ell_0}{4}, -\frac{x}{2\sqrt{3}} + \frac{2y}{3} + \frac{\sqrt{3}\ell_0}{4}\right)$	if $\sqrt{3}y > \ell_0 - x$ and $2x < \ell_0$
	$P_{24}(x, y) = \left(\frac{x}{2} + \frac{\ell_0}{4}, \frac{x}{2\sqrt{3}} + \frac{2y}{3} + \frac{\ell_0}{4\sqrt{3}}\right)$	if $\sqrt{3}y \geq x$ and $2x \geq \ell_0$
	$P_{25}(x, y) = \left(\frac{x}{2} + \frac{\ell_0}{4}, \frac{x}{2\sqrt{3}} + \frac{2y}{3} + \frac{\ell_0}{4\sqrt{3}}\right)$	if $\sqrt{3}y > \ell_0 - x$ and $\sqrt{3}y < x$
	$P_{26}(x, y) = \left(\frac{x}{2} + \frac{\ell_0}{4}, \frac{x}{2\sqrt{3}} + \frac{2y}{3} + \frac{\ell_0}{4\sqrt{3}}\right)$	if $\sqrt{3}y \leq \ell_0 - x$ and $2x \geq \ell_0$
$P_3(x, y)$	$P_{31}(x, y) = \left(\frac{x}{2} - \frac{y}{2\sqrt{3}} + \frac{\ell_0}{2}, \frac{2y}{3}\right)$	if $2x < \ell_0$ and $\sqrt{3}y < x$
	$P_{32}(x, y) = \left(\frac{x}{2} - \frac{y}{2\sqrt{3}} + \frac{\ell_0}{2}, \frac{2y}{3}\right)$	if $\sqrt{3}y \leq \ell_0 - x$ and $\sqrt{3}y \geq x$
	$P_{33}(x, y) = \left(\frac{3x}{4} + \frac{y}{4\sqrt{3}} + \frac{\ell_0}{4}, -\frac{x}{4\sqrt{3}} + \frac{5y}{12} + \frac{\ell_0}{4\sqrt{3}}\right)$	if $\sqrt{3}y > \ell_0 - x$ and $2x < \ell_0$
	$P_{34}(x, y) = \left(\frac{3x}{4} + \frac{y}{4\sqrt{3}} + \frac{\ell_0}{4}, -\frac{x}{4\sqrt{3}} + \frac{5y}{12} + \frac{\ell_0}{4\sqrt{3}}\right)$	if $\sqrt{3}y \geq x$ and $2x \geq \ell_0$
	$P_{35}(x, y) = \left(\frac{3x}{4} + \frac{y}{4\sqrt{3}} + \frac{\ell_0}{4}, -\frac{x}{4\sqrt{3}} + \frac{5y}{12} + \frac{\ell_0}{4\sqrt{3}}\right)$	if $\sqrt{3}y > \ell_0 - x$ and $\sqrt{3}y < x$
	$P_{36}(x, y) = \left(\frac{x}{2} - \frac{y}{2\sqrt{3}} + \frac{\ell_0}{2}, \frac{2y}{3}\right)$	if $\sqrt{3}y \leq \ell_0 - x$ and $2x \geq \ell_0$

Appendix B: Maps for the Sierpinski carpet

The Sierpinski carpet is a non-product fractal set constructed by the eight affine contraction maps in Table 19. Each contraction map, maps a rectangular domain into a smaller rectangular domain as deduced on inspection of Fig. 2. The initial number of tiles on $\hat{E}_0$ in Fig. 2 is 6, which means that the eight expansion maps will each consist of six sub-maps although some are identical. The expansion maps satisfy $P_1 = S_1$, $P_3 = S_3$, $P_6 = S_6$ and $P_8 = S_8$ with the remaining maps defined in Table 20 but limited to distinctive sub-maps.

Table 19 Contraction maps for Sierpinski carpet

$S_1(x, y) = \left(\frac{x}{3}, \frac{y}{3}\right)$	$S_2(x, y) = \left(\frac{\ell_0}{3} + \frac{x}{3}, \frac{y}{3}\right)$
$S_3(x, y) = \left(\frac{2\ell_0}{3} + \frac{x}{3}, \frac{y}{3}\right)$	$S_4(x, y) = \left(\frac{x}{3}, \frac{\ell_0}{3} + \frac{y}{3}\right)$
$S_5(x, y) = \left(\frac{2\ell_0}{3} + \frac{x}{3}, \frac{\ell_0}{3} + \frac{y}{3}\right)$	$S_6(x, y) = \left(\frac{x}{3}, \frac{2\ell_0}{3} + \frac{y}{3}\right)$
$S_7(x, y) = \left(\frac{\ell_0}{3} + \frac{x}{3}, \frac{2\ell_0}{3} + \frac{y}{3}\right)$	$S_8(x, y) = \left(\frac{2\ell_0}{3} + \frac{x}{3}, \frac{2\ell_0}{3} + \frac{y}{3}\right)$

Table 20 Expansion maps for Sierpinski carpet

$P_2(x, y)$	$P_{21}(x, y) = \left(\frac{1}{3} + \frac{x}{3}, \frac{1}{3} + \frac{y}{3}\right)$	If $y \geq 2x$ and $2x \leq 1$
	$P_{22}(x, y) = \left(\frac{1}{3} + \frac{x}{3}, \frac{1}{3} - \frac{x}{3} + \frac{y}{3}\right)$	If $y \geq 2(1 - x)$ and $2x > 1$
	$P_{23}(x, y) = \left(\frac{x}{2}, \frac{1}{3} + \frac{y}{3}\right)$	Otherwise
$P_4(x, y)$	$P_{41}(x, y) = \left(\frac{1}{3} + \frac{x}{3}, \frac{1}{3} + \frac{y}{3}\right)$	If $2y \leq x$ and $2y \leq 1$
	$P_{42}(x, y) = \left(\frac{1}{3} + \frac{x}{3} - \frac{y}{3}, \frac{1}{3} + \frac{y}{3}\right)$	If $2y \geq (2 - x)$ and $2y > 1$
	$P_{43}(x, y) = \left(\frac{x}{2}, \frac{1}{3} + \frac{y}{3}\right)$	Otherwise
$P_5(x, y)$	$P_{51}(x, y) = \left(\frac{2}{3} + \frac{x}{3} - \frac{y}{3}, \frac{1}{3} + \frac{y}{3}\right)$	If $2y \leq 1 - x$ and $2y \leq 1$
	$P_{52}(x, y) = \left(\frac{1}{3} + \frac{x}{3} + \frac{y}{3}, \frac{1}{3} + \frac{y}{3}\right)$	If $2y \geq 1 - x$ and $2y > 1$
	$P_{53}(x, y) = \left(\frac{1}{2} + \frac{x}{2}, \frac{1}{3} + \frac{y}{3}\right)$	Otherwise
$P_7(x, y)$	$P_{71}(x, y) = \left(\frac{1}{3} + \frac{x}{3}, \frac{2}{3} - \frac{x}{3} + \frac{y}{3}\right)$	If $y \leq 2 - 2x$ and $2x \leq 1$
	$P_{72}(x, y) = \left(\frac{1}{3} + \frac{x}{3}, \frac{1}{3} - \frac{x}{3} + \frac{y}{3}\right)$	If $y \leq -1 + 2x$ and $2x > 1$
	$P_{73}(x, y) = \left(\frac{1}{3} + \frac{x}{3}, \frac{1}{2} + \frac{y}{2}\right)$	Otherwise

Appendix C: Maps for the finger-like fractal

The finger-like fractal is constructed by the five affine contraction maps in Table 21; the associated expansion maps are defined in Table 22.

Table 21 Contraction maps for finger-like fractal

$S_1(x, y) = \left(\frac{x}{3}, \frac{y}{3}\right)$	$S_2(x, y) = \left(\frac{2\ell_0}{3} + \frac{x}{3}, \frac{y}{3}\right)$
$S_3(x, y) = \left(\frac{\ell_0}{3} + \frac{x}{3}, \frac{\ell_0}{3} + \frac{y}{3}\right)$	$S_4(x, y) = \left(\frac{x}{3}, \frac{2\ell_0}{3} + \frac{y}{3}\right)$
$S_5(x, y) = \left(\frac{2\ell_0}{3} + \frac{x}{3}, \frac{2\ell_0}{3} + \frac{y}{3}\right)$	

Table 22 Expansion maps for finger-like fractal

$P_1(x, y)$	$P_{11}(x, y) = \left(\frac{x}{2} - \frac{y}{4} + \frac{1}{8}, \frac{y}{4} + \frac{1}{8}\right)$	If $2y \geq 1$ and $y \leq x$
	$P_{22}(x, y) = \left(\frac{x}{4} + \frac{1}{8}, -\frac{x}{4} + \frac{y}{2} + \frac{1}{8}\right)$	If $2x \geq 1$ and $y \geq x$
	$P_{13}(x, y) = \left(\frac{x}{2}, \frac{y}{2}\right)$	Otherwise
$P_2(x, y)$	$P_{21}(x, y) = \left(\frac{x}{2} - \frac{y}{4} + \frac{3}{8}, \frac{y}{4} + \frac{3}{8}\right)$	If $2y \leq 1$ and $y \geq x \, OR \, 2y \geq 1$ and $y \leq -x + 1$
	$P_{22}(x, y) = \left(\frac{x}{4} + \frac{3}{8}, -\frac{x}{4} + \frac{y}{2} + \frac{3}{8}\right)$	If $2x \leq 1$ and $y \leq x \, OR \, 2x \geq 1$ and $y \geq x$
	$P_{23}(x, y) = \left(\frac{x}{4} + \frac{3}{8}, \frac{x}{4} + \frac{y}{2} + \frac{1}{8}\right)$	If $2x \geq 1$ and $y \leq -x + 1 \, OR \, 2x \leq 1$ and $y \geq -x + 1$
	$P_{24}(x, y) = \left(\frac{x}{2} + \frac{y}{4} + \frac{1}{8}, \frac{y}{4} + \frac{3}{8}\right)$	If $2y \leq 1$ and $y \geq -x + 1 \, OR \, 2y \geq 1$ and $y \leq -x + 1$
$P_3(x, y)$	$P_{31}(x, y) = \left(\frac{x}{4} + \frac{5}{8}, \frac{x}{4} + \frac{y}{2} - \frac{1}{8}\right)$	If $2x \leq 1$ and $y \geq -x + 1$
	$P_{32}(x, y) = \left(\frac{x}{2} + \frac{y}{4} + \frac{3}{8}, \frac{y}{4} + \frac{1}{8}\right)$	If $2y \geq 1$ and $y \leq -x + 1$
	$P_{33}(x, y) = \left(\frac{x}{2} + \frac{1}{2}, \frac{y}{2}\right)$	Otherwise
$P_4(x, y)$	$P_{41}(x, y) = \left(\frac{x}{4} + \frac{1}{8}, \frac{x}{4} + \frac{y}{2} + \frac{3}{8}\right)$	If $2x \leq 1$ and $y \leq x$
	$P_{42}(x, y) = \left(\frac{x}{2} + \frac{y}{4} - \frac{1}{8}, \frac{y}{4} + \frac{5}{8}\right)$	If $2y \leq 1$ and $y \geq -x + 1$
	$P_{43}(x, y) = \left(\frac{x}{2}, \frac{y}{2} + \frac{1}{2}\right)$	Otherwise
$P_5(x, y)$	$P_{51}(x, y) = \left(\frac{x}{2} - \frac{y}{4} + \frac{5}{8}, \frac{y}{4} + \frac{5}{8}\right)$	If $2y \leq 1$ and $y \geq x$
	$P_{52}(x, y) = \left(\frac{x}{4} + \frac{5}{8}, -\frac{x}{4} + \frac{y}{2} + \frac{5}{8}\right)$	If $2x \leq 1$ and $y \leq x$
	$P_{53}(x, y) = \left(\frac{x}{2} + \frac{1}{2}, \frac{y}{2} + \frac{1}{2}\right)$	Otherwise

Appendix D: Maps for the Vicsek fractal

The Vicsek fractal is constructed by the five affine contraction maps in Table 23.

Table 23 Contraction maps for Vicsek fractal

$S_1(x, y) = \left(\frac{x}{3}, \frac{\ell_0}{3} + \frac{y}{3} \right)$	$S_2(x, y) = \left(\frac{\ell_0}{3} + \frac{x}{3}, \frac{\ell_0}{3} + \frac{y}{3} \right)$
$S_3(x, y) = \left(\frac{\ell_0}{3} + \frac{x}{3}, \frac{y}{3} \right)$	$S_4(x, y) = \left(\frac{2\ell_0}{3} + \frac{x}{3}, \frac{\ell_0}{3} + \frac{y}{3} \right)$
$S_5(x, y) = \left(\frac{\ell_0}{3} + \frac{x}{3}, \frac{2\ell_0}{3} + \frac{y}{3} \right)$	

Two sets of expansion maps termed (a) and (b) are defined in Tables 24 and 25, respectively. The effect of these maps is shown visually in Figs. 22 and 23, where disparate tessellations are displayed.

Table 24 Expansion maps (a) for Vicsek fractal

$P_1(x, y)$	$P_{11}(x, y) = \left(\frac{x}{3}, -\frac{x}{3} + \frac{2y}{3} + \frac{1}{3} \right)$	If $y \geq x$ and $y \geq -x + 1$
	$P_{12}(x, y) = \left(\frac{x}{3}, \frac{y}{3} + \frac{1}{3} \right)$	If $y \leq x$ and $y \geq -x + 1$
	$P_{13}(x, y) = \left(\frac{x}{3}, \frac{x}{3} + \frac{2y}{3} \right)$	If $y \leq x$ and $y \leq -x + 1$
	$P_{14}(x, y) = \left(\frac{x}{3}, y \right)$	If $y \geq x$ and $y \leq -x + 1$
$P_2(x, y) = \left(\frac{1}{3} + \frac{x}{3}, \frac{1}{3} + \frac{y}{3} \right)$		
$P_3(x, y)$	$P_{31}(x, y) = \left(\frac{x}{3} + \frac{1}{3}, \frac{y}{3} \right)$	If $y \geq x$ and $y \geq -x + 1$
	$P_{32}(x, y) = \left(\frac{2x}{3} - \frac{y}{3} + \frac{1}{3}, \frac{y}{3} \right)$	If $y \leq x$ and $y \geq -x + 1$
	$P_{33}(x, y) = \left(x, \frac{y}{3} \right)$	If $y \leq x$ and $y \leq -x + 1$
	$P_{34}(x, y) = \left(\frac{2x}{3} + \frac{y}{3}, \frac{y}{3} \right)$	If $y \geq x$ and $y \leq -x + 1$
$P_4(x, y)$	$P_{41}(x, y) = \left(\frac{x}{3} + \frac{2}{3}, \frac{x}{3} + \frac{2y}{3} \right)$	If $y \geq x$ and $y \geq -x + 1$
	$P_{42}(x, y) = \left(\frac{x}{3} + \frac{2}{3}, y \right)$	If $y \leq x$ and $y \geq -x + 1$
	$P_{43}(x, y) = \left(\frac{x}{3} + \frac{2}{3}, -\frac{x}{3} + \frac{2y}{3} + \frac{1}{3} \right)$	If $y \leq x$ and $y \leq -x + 1$
	$P_{44}(x, y) = \left(\frac{x}{3} + \frac{2}{3}, \frac{y}{3} + \frac{1}{3} \right)$	If $y \geq x$ and $y \leq -x + 1$
$P_5(x, y)$	$P_{51}(x, y) = \left(x, \frac{y}{3} + \frac{2}{3} \right)$	If $y \geq x$ and $y \geq -x + 1$
	$P_{52}(x, y) = \left(\frac{2x}{3} + \frac{y}{3}, \frac{y}{3} + \frac{2}{3} \right)$	If $y \leq x$ and $y \geq -x + 1$
	$P_{53}(x, y) = \left(\frac{x}{3} + \frac{1}{3}, \frac{y}{3} + \frac{2}{3} \right)$	If $y \leq x$ and $y \leq -x + 1$
	$P_{54}(x, y) = \left(\frac{2x}{3} - \frac{y}{3} + \frac{1}{3}, \frac{y}{3} + \frac{2}{3} \right)$	If $y \geq x$ and $y \leq -x + 1$

Table 25 Expansion maps (b) for Vicsek fractal

$P_1(x, y)$	$P_{11}(x, y) = \left(\frac{2x}{3} - \frac{y}{3}, -\frac{2x}{3} + y + \frac{1}{3}\right)$	If $2x \geq 1$ and $y \geq x$
	$P_{12}(x, y) = \left(\frac{2x}{3} + \frac{y}{3} - \frac{1}{3}, \frac{2x}{3} + y - \frac{1}{3}\right)$	If $2x \geq 1$ and $y \leq -x + 1$
	$P_{13}(x, y) = \left(\frac{y}{3}, -\frac{2x}{3} + y + \frac{1}{3}\right)$	If $2x \leq 1$ and $y \leq x$
	$P_{14}(x, y) = \left(-\frac{y}{3} + \frac{1}{3}, \frac{2x}{3} + y - \frac{1}{3}\right)$	If $2x \leq 1$ and $y \geq -x + 1$
	$P_{15}(x, y) = \left(\frac{x}{3}, \frac{y}{3} + \frac{1}{3}\right)$	Otherwise
$P_2(x, y) = \left(\frac{1}{3} + \frac{x}{3}, \frac{1}{3} + \frac{y}{3}\right)$		
$P_3(x, y)$	$P_{31}(x, y) = \left(x - \frac{2y}{3} + \frac{1}{3}, -\frac{x}{3} + \frac{2y}{3}\right)$	If $2y \geq 1$ and $y \leq x$
	$P_{32}(x, y) = \left(x + \frac{2y}{3} - \frac{1}{3}, -\frac{x}{3} + \frac{1}{3}\right)$	If $2y \leq 1$ and $y \geq -x + 1$
	$P_{33}(x, y) = \left(x - \frac{2y}{3} + \frac{1}{3}, \frac{x}{3}\right)$	If $2y \leq 1$ and $y \geq x$
	$P_{34}(x, y) = \left(x + \frac{2y}{3} - \frac{1}{3}, \frac{x}{3} + \frac{2y}{3} - \frac{1}{3}\right)$	If $2y \geq 1$ and $y \leq -x + 1$
	$P_{35}(x, y) = \left(\frac{x}{3} + \frac{1}{3}, \frac{y}{3}\right)$	Otherwise
$P_4(x, y)$	$P_{41}(x, y) = \left(\frac{y}{3} + \frac{2}{3}, -\frac{2x}{3} + y + \frac{1}{3}\right)$	If $2x \geq 1$ and $y \geq x$
	$P_{42}(x, y) = \left(-\frac{y}{3} + 1, \frac{2x}{3} + y - \frac{1}{3}\right)$	If $2x \geq 1$ and $y \leq -x + 1$
	$P_{43}(x, y) = \left(\frac{2x}{3} - \frac{y}{3} + \frac{2}{3}, -\frac{2x}{3} + y + \frac{1}{3}\right)$	If $2x \leq 1$ and $y \leq x$
	$P_{44}(x, y) = \left(\frac{2x}{3} + \frac{y}{3} + \frac{1}{3}, \frac{2x}{3} + y - \frac{1}{3}\right)$	If $2x \leq 1$ and $y \geq -x + 1$
	$P_{45}(x, y) = \left(\frac{x}{3} + \frac{2}{3}, \frac{y}{3} + \frac{1}{3}\right)$	Otherwise
$P_5(x, y)$	$P_{51}(x, y) = \left(x - \frac{2y}{3} + \frac{1}{3}, \frac{x}{3} + \frac{2}{3}\right)$	If $2y \geq 1$ and $y \leq x$
	$P_{52}(x, y) = \left(x + \frac{2y}{3} - \frac{1}{3}, \frac{x}{3} + \frac{2y}{3} + \frac{1}{3}\right)$	If $2y \leq 1$ and $y \geq -x + 1$
	$P_{53}(x, y) = \left(x - \frac{2y}{3} + \frac{1}{3}, -\frac{x}{3} + \frac{2y}{3} + \frac{2}{3}\right)$	If $2y \leq 1$ and $y \geq x$
	$P_{54}(x, y) = \left(x + \frac{2y}{3} - \frac{1}{3}, -\frac{x}{3} + 1\right)$	If $2y \geq 1$ and $y \leq -x + 1$
	$P_{55}(x, y) = \left(x, \frac{y}{3} + \frac{2}{3}\right)$	Otherwise

References

1. Davey, K., Prosser, R.: Analytical solutions for heat transfer on fractal and pre-fractal domains. Appl. Math. Model. **37**(1–2), 554–569 (2013)
2. Davey, K., Prosser, R., Jiang, C.: Heat transfer through fractal-like porous media: a tessellated continuum approach. Comput. Struct. **151**, 58–72 (2015)
3. Galvanetto, U.: Multiscale Modeling in Solid Mechanics: Computational Approaches. Imperial College Press, London (2009)
4. Mandelbrot, B.B.: The Fractal Geometry of Nature by Mandelbrot, Benoit B. (November 18, 1982) Hardcover. W.H.Freeman & Co Ltd, New York (1701)
5. Horstemeyer, M.F.: Integrated Computational Materials Engineering (ICME) for Metals: Using Multiscale Modeling to Invigorate Engineering Design with Science. Wiley, New Jersey (2012)
6. Khan, H.H., M, A.A., Sharma, A., Srivastava, A., Chaudhuri, P.: Thermal-hydraulic characteristics and performance of 3D wavy channel based printed circuit heat exchanger. Appl. Therm. Eng. **87**, 519–528 (2015)
7. Boomsma, K., Poulikakos, D., Zwick, F.: Metal foams as compact high performance heat exchangers. Mech. Mater. **35**(12), 1161–1176 (2003)
8. Li, Q., Flamant, G., Yuan, X., Neveu, P., Luo, L.: Compact heat exchangers: a review and future applications for a new generation of high temperature solar receivers. Renew. Sustain. Energy Rev. **15**(9), 4855–4875 (2011)
9. Bhouri, M., Goyette, J., Hardy, B.J., Anton, D.L.: Honeycomb metallic structure for improving heat exchange in hydrogen storage system. Int. J. Hydrog. Energy **36**(11), 6723–6738 (2011)
10. Mancin, S., Zilio, C., Cavallini, A., Rossetto, L.: Pressure drop during air flow in aluminum foams. Int. J. Heat Mass Transf. **53**(15–16), 3121–3130 (2010)
11. Kuwata, Y., Suga, K.: Large eddy simulations of pore-scale turbulent flows in porous media by the lattice Boltzmann method. Int. J. Heat Fluid Flow **55**, 143–157 (2015)

12. Rashidi, S., Bovand, M., Esfahani, J.A.: Heat transfer enhancement and pressure drop penalty in porous solar heat exchangers: A sensitivity analysis. Energy Convers. Manag. **103**, 726–738 (2015)
13. Dehghan, M., Valipour, M.S., Saedodin, S.: Temperature-dependent conductivity in forced convection of heat exchangers filled with porous media: A perturbation solution. Energy Convers. Manag. **91**, 259–266 (2015)
14. Chikh, S., Allouache, N.: Optimal performance of an annular heat exchanger with a porous insert for a turbulent flow. Appl. Therm. Eng. **104**, 222–230 (2016)
15. Nield, D.A., Kuznetsov, A.V.: 2 - Heat transfer in Bi-disperse porous media. In: Transport Phenomena in Porous Media III, pp. 34–59. Pergamon, Oxford (2005)
16. Rupert, H.B.C., Nash, W.: Choice of boundary condition for lattice-Boltzmann simulation of moderate Reynolds number flow in complex domains. Phys. Rev. E **89**(2), 1–13 (2012)
17. Mehrizi, A.A., Farhadi, M., Sedighi, K., Delavar, M.A.: Effect of fin position and porosity on heat transfer improvement in a plate porous media heat exchanger. J. Taiwan Inst. Chem. Eng. **44**(3), 420–431 (2013)
18. Liu, Y., Zhou, X., Wang, D., Song, C., Liu, J.: A diffusivity model for predicting VOC diffusion in porous building materials based on fractal theory. J. Hazard. Mater. **299**, 685–695 (2015)
19. Falconer, K.: Fractal Geometry: Mathematical Foundations and Applications, 2nd edn. Wiley, Chichester (2003)
20. Barnsley, M.F.: Fractals Everywhere, 2, Sub edn. Morgan Kaufmann Pub, Boston (1993)
21. Falconer, K.J.: The Hausdorff dimension of self-affine fractals. Math. Proc. Camb. Philos. Soc. **103**(2), 339–350 (1988)
22. Edgar, G.A.: Integral, Probability, and Fractal Measures. Springer, New York (2013)
23. Nakashima, Y., Nakano, T.: Steady-state local diffusive fluxes in porous geo-materials obtained by pore-scale simulations. Transp. Porous Media **93**(3), 657–673 (2012)
24. Keulen, J.V.: Density of porous solids. Matér. Constr. **6**(3), 181–183 (1973)
25. Alaimo, G., Zingales, M.: Laminar flow through fractal porous materials: the fractional-order transport equation. Commun. Nonlinear Sci. Numer. Simul. **22**(1–3), 889–902 (2015)
26. Blanc, E., Chiavassa, G., Lombard, B.: Wave simulation in 2D heterogeneous transversely isotropic porous media with fractional attenuation: A Cartesian grid approach. J. Comput. Phys. **275**, 118–142 (2014)
27. Choudhary, A., Kumar, D., Singh, J.: A fractional model of fluid flow through porous media with mean capillary pressure. J. Assoc. Arab Univ. Basic Appl. Sci. doi:10.1016/j.jaubas.2015.01.002
28. Tarasov, V.E.: Continuous medium model for fractal media. Phys. Lett. A **336**(2–3), 167–174 (2005)
29. Tarasov, V.E.: Fractional hydrodynamic equations for fractal media. Ann. Phys. **318**(2), 286–307 (2005)
30. Ostoja-Starzewski, M.: Towards thermoelasticity of fractal media. J. Therm. Stress. **30**(9–10), 889–896 (2007)
31. Ostoja-Starzewski, M.: Towards thermomechanics of fractal media. Z. Für Angew. Math. Phys. **58**(6), 1085–1096 (2007)
32. Reviews, C.T.: e-Study Guide for Elements of Advanced Mathematics, textbook by Steven G. Krantz: Mathematics, Mathematics. Cram101 Textbook Reviews (2012)
33. Peitgen, H.-O., Jürgens, H., Saupe, D.: Chaos and fractals: new frontiers of science. In: Chaos and Fractals: New Frontiers of Science, pp. 545–591. Springer, New York (2006)
34. Clayton, J.D.: Nonlinear Mechanics of Crystals. Springer, New York (2010)
35. Davey, K., Mondragon, R.: A non-physical enthalpy method for the numerical solution of isothermal solidification. Int. J. Numer. Methods Eng. **84**(2), 214–252 (2010)
36. Davey, K., Rasgado, M.T.A.: Analytical solutions for vibrating fractal composite rods and beams. Appl. Math. Model. **35**(3), 1194–1209 (2011)
37. Dittus, F.W., Boelter, L.M.K.: Heat Transfer in Automobile Radiators of the Tubular Type, vol. 2. University of California Press, Berkeley (1930)

Chapter 6.

Thermal Analysis on Pre-fractals

This chapter builds on the results presented in Chapters 5 and 6, and tests further the hypothesis that the thermal analysis of porous materials can be explored by using a finite element method on the corresponding tessellated construction through tessellated continuum mechanics. Tessellations with and without discontinuity networks (DN) are again considered to demonstrate thermal behaviour of pre-fractals. Thermal analysis is performed on heat exchangers with porous cross-sections in the form of classical pre-fractal designs. The results obtained are contrasted against direct pre-fractal solutions which, in general, show great accuracy for the tessellated approach. A weakness of the approach, however, is its focus on the physics of fractal elements (or tiles) over the surrounding matrix material (or holes). Any hole (or matrix material) which maps to an edge in a tessellation requires the associated physics to be represented using distribution-like functions. This feature is examined for two situations; one which is favourable to the tessellated approach, and the other where it is not.

6. 1 Introduction

Tessellated continuum mechanics is further tested on porous heat exchangers. The cellular structures presented in this chapter are represented in the usual way using pre-fractals, which are collapsed to tessellations using alternative hole-fill maps. This approach returns the analysis to the continuum but, in this case, the continuum is tessellated; each tile in the tessellation possesses thermal properties arising from the hole-fill map. The results selected for presentation in this chapter are obtained for classical fractal designs, but are chosen to test the limits of the tessellated approach. Results are contrasted against those obtained from direct analysis of the fractal heat exchangers to illustrate the higher accuracy achieved. The tessellated finite element method is tested in Section 6.2 on 2-D Cantor dust, where dust-like fractal elements

are embedded in a matrix material. This example provides a challenge for the tessellated approach as a consequence of the complex thermal response of the matrix material. The dust, however, benefits from the existence of an analytical solution which, along with the UoMFEC results, are represented on the tessellations and mapped to the corresponding pre-fractals. These are then compared with directly obtained ABAQUS results. It should be appreciated that an ABAQUS model of a pre-fractal takes account of the physics of the matrix material, so despite the matrix having a relatively high conductivity, this provides a source of difficulty for the tessellated approach. The thermal fields are assumed to be continuous and hence do not involve a discontinuity network.

The investigation performed in Section 6.2 is extended to classical non-product fractals in Section 6.3. However, in this section, discontinuity networks are included to highlight the added flexibility and accuracy these provide in the face of complex thermal responses of the matrix material.

The influence of boundary conditions and hole-fill maps are explored for the Viscek Fractal in Section 6.4. The lack of uniqueness of hole-fill maps (arising principally from the non-unique expansion maps) is a source of concern and therefore it is of interest to investigate what effects different maps provide when considered in conjunction with different boundary conditions. Traditionally, two forms of boundary conditions are applied to account for the presence of a cooling system; these are: i) a convection condition employing a heat transfer coefficient (considered in earlier chapters), and ii) a fixed temperature condition. These are applied in Section 6.4 to assess the influence of different alternative hole-fill maps. The tests confirm that there is little impact on the mapped pre-fractal results from different hole-filling maps.

6. 2   Solution on 2-D Product Cantor Dust

The same problem in [48] is selected again in this section to contrast against the ABAQUS direct result. The governing equations on a control volume are re-presented here for convenience. The equations for the physical and tessellated spaces are

$$\frac{d}{dt}\int_{\Omega_s}\rho_s h_s dV_s = -\int_{\Gamma_s}\dot{\underline{q}}_s\cdot d\Gamma_s + \int_{\Omega_s}\rho_s\dot{Q}_s dV_s\,,\tag{6.1}$$

and

$$\frac{d}{dt}\int_{\Omega_r}\rho_r h_r dV_r = -\int_{\Gamma_r}\dot{\underline{q}}_r\cdot d\Gamma_r + \int_{\Omega_r}\rho_r\dot{Q}_r dV_r\tag{6.2}$$

where $\dot{Q}$ is a heat source and the heat flux is defined as $\dot{\underline{q}}\cdot n = h(T - T_\infty)$.

The convective heat transfer boundary conditions in the two spaces are related by

$$\dot{\underline{q}}_r\cdot d\Gamma_r = h_r\left(T_r - T_\infty\right)d\Gamma_r = |F|^{-1}\left(F\cdot\dot{\underline{q}}_s\right)\cdot\left(|F|d\Gamma_s\cdot F^{-1}\right) = h_s\left(T_s - T_\infty\right)d\Gamma_s\,,\tag{6.3}$$

which is satisfied for $T_r = T_s$ and $h_r d\Gamma_r = h_s d\Gamma_s$ giving $\nabla_s T_s = F^T\cdot\nabla_r T_r$, and in view of the identity $\dot{\underline{q}}_r = |F|^{-1}F\cdot\dot{\underline{q}}_s$ leads to $\dot{\underline{q}}_r = -K_r\cdot\nabla_r T_r$.

The relationship of thermal conductivity between tessellation and pre-fractal is

$$K_r = |F|^{-1}FK_s F^T\tag{6.4}$$

where K_r is the associated orthotropic conductivity tensor for the tessellated domain and K_s is the isotropic conductivity for pre-fractal. Thus, the tessellated continuum for 2-D Cantor dust is isotropic, permitting a scalar K_r related by $K_r = K_s$.

It is assumed here that Cantor Dust is a material with thermal conductivity $K_s = 400W / mK$, density $\rho_s = 400 \text{kg/m}^3$, specific heat $c_s = 1000$ J/kgK and edge length $\ell_0 = 1$m, i.e. the analysis is performed on a unit square domain. The edge temperatures are fixed as $\hat{T}_k$ and the chosen values are consistent as defined in Table 6.1. Two different values of thermal conductivities are applied separately to the matrix material in the ABAQUS pre-fractal; i) an extremely high conductivity to simplify the problem, and ii) thermal conductivity of water $K_{water} = 0.58W / mK$. The matrix is supplied with a uniform heat source $\dot{Q} = 400W / m^3$ to match the energy input with the expression $\dot{Q}\ell^2 / K_0 \Delta T = 1$, where $K_0 = K_s$ and $\Delta T = 1K$.

Table 6.1. Edge-boundary temperatures on $\hat{T}_k$ (unit tessellated continuum)

| Boundary Edge (m)	$x = 0$	$y = 0$	$x = 1$	$y = 1$
Temperature (K)	$\hat{T}_k(0, y) = y$	$\hat{T}_k(x,0) = x$	$\hat{T}_k(1, y) = 1 - y$	$\hat{T}_k(x,1) = 1 - x$

The temperature distributions on tessellations $\hat{T}_k$ from the analytical solution and UoMFEC are mapped on to the corresponding pre-fractals $\hat{E}_k$; while ABAQUS obtains temperature distributions on $\hat{E}_k$ directly. Temperature contours on $\hat{E}_k$ are depicted in Figure 6.1 and 6.2 from the analytical solution, UoMFEC and ABAQUS.
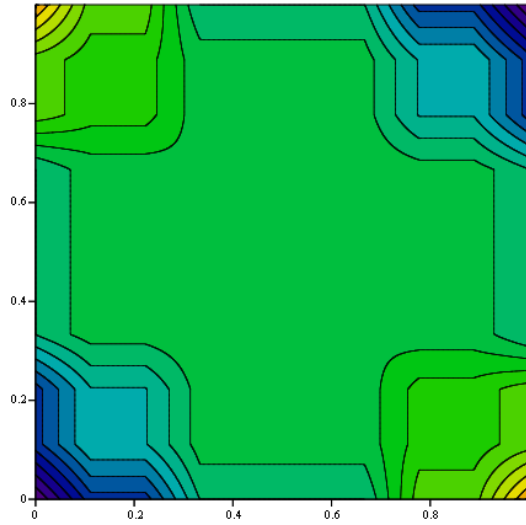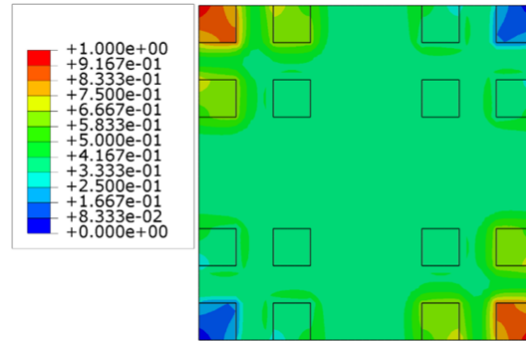
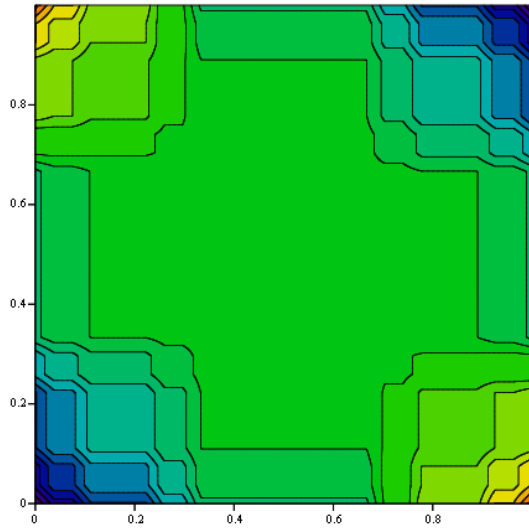i) Contours from analytical solution   ii) Contours from UoMFEC
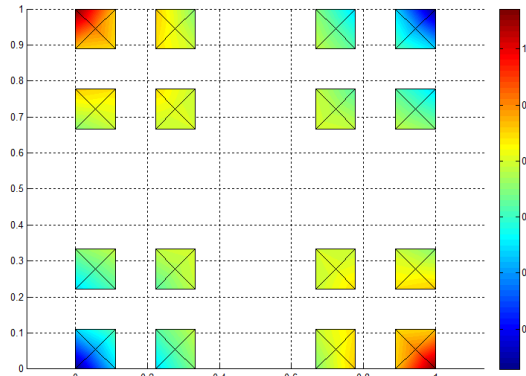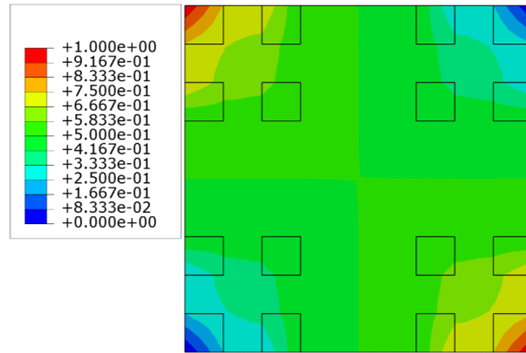
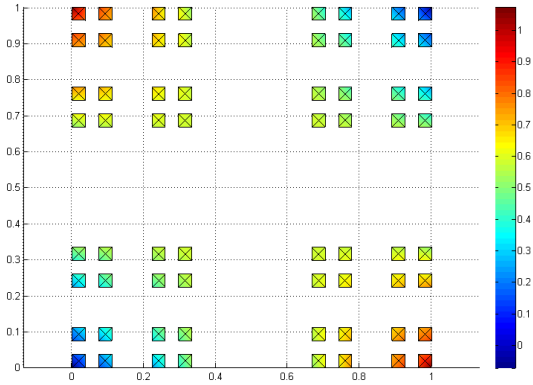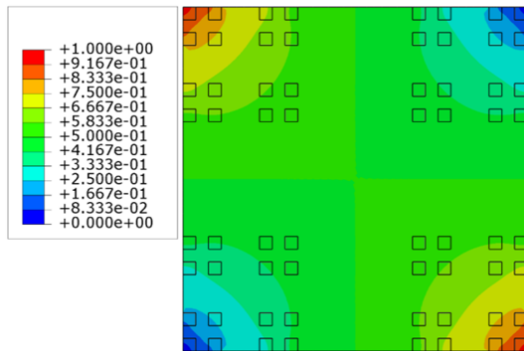iii) Contours from ABAQUS with high conductivity   iv) Contours from ABAQUS with low conductivity

Figure 6.1. Contour temperature plots for continuum and corresponding $\hat{E}_2$ with fixed wall temperatures from different methods
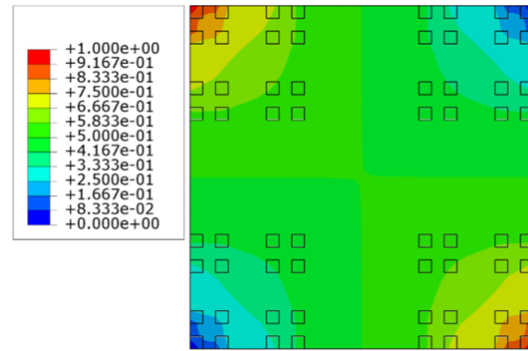
i) Contours from analytical solution

ii) Contours from UoMFEC

iii) Contours from ABAQUS with high conductivity

iv) Contours from ABAQUS with low conductivity

Figure 6.2. Contour temperature plots for continuum and corresponding $\hat{E}_3$ with fixed wall temperatures from different methods

The maximum differences in the solution giving by M and $M_{\%}$ are defined as follow

$$M = \max_i \left\{ \left| T_i^{(a)} - T_i^{(b)} \right| \right\} \tag{6.5}$$

and

$$M_{\%} = 100 \times \max_i \left\{ \left| \frac{T_i^{(a)} - T_i^{(b)}}{T_i^{(a)} + T_i^{(b)}} \right| \right\} \tag{6.6}$$

The average differences in the solution giving by $\bar{D}$ and $\bar{D}_{\%}$ are obtained from the relationships

$$\bar{D} = \frac{1}{n} \sum_{i=1}^{n} \left| T_i^{(a)} - T_i^{(b)} \right| \tag{6.7}$$

and

$$\bar{D}_{\%} = \frac{2 \times 100}{n} \sum_{i=1}^{n} \left| \frac{T_i^{(a)} - T_i^{(b)}}{T_i^{(a)} + T_i^{(b)}} \right| \tag{6.8}$$

where superscripts (a) and (b) distinguish the methods and n is the number of data points. Temperatures on $\hat{E}_k$ for $k = 2$ and $k = 3$ along the diagonal line $x = y$ are shown in Figure 6.3 with temperature differences in Table 6.2 calculated from Equations (6.5) to (6.8). Near identical results on $\hat{E}_k$ are observed for the analytical solution and ABAQUS, with the principal disparity for UoMFEC occurring at the boundary. The reason is the convection condition with an extremely high thermal conductivity applied along the boundaries in an attempt to match the fixed

temperatures. The magnitude of errors appearing in Table 6.2 is misleading. However, as it is apparent from the inspection of Figure 6.3, maximum errors are located entirely at the boundary with a good match elsewhere. Other large errors are located near the matrix, which confirms the limitation of the tessellated approach when faced with a complex thermal response of the matrix. It is important to appreciate however that a continuous temperature field is assumed for the tessellation. Applying a high value of conductivity to the matrix is found to reduce the errors. This is expected as an increase in conductivity provides a closer match with a continuous thermal field. This observation provides the motivation for the inclusion of a discontinuity network which is expected to offer greater accuracy.
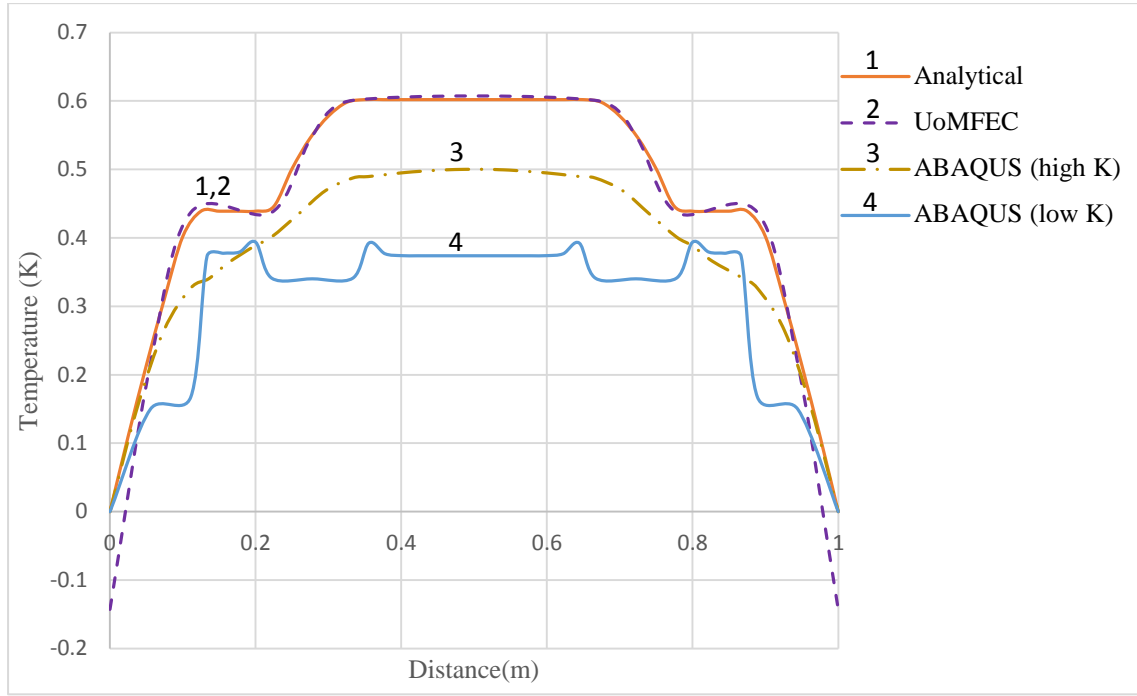
(a) On $\hat{E}_2$
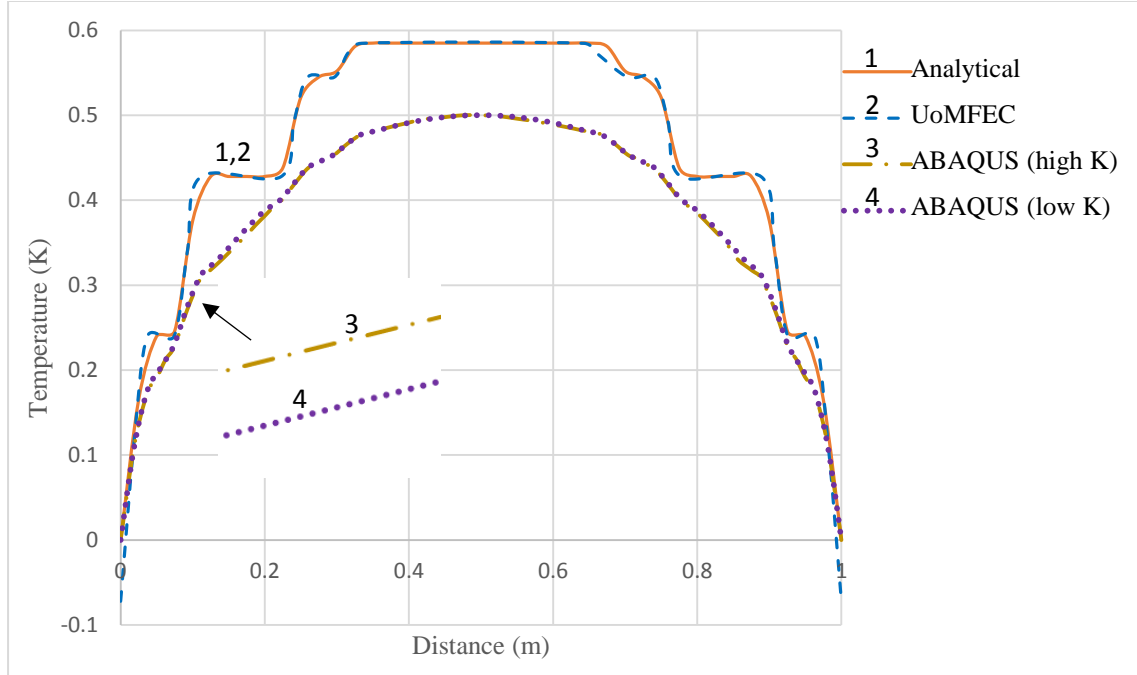
(b) On $\hat{E}_3$

Figure 6.3. Temperature plots along x=y for 2D Cantor Dust with heat source and fixed wall temperatures from different methods on $\hat{E}_k$

Table 6.2. Temperature differences along $x = y$:2-D Cantor product with heat source

		Maximum (K)	Maximum (%)	Average (K)	Average (%)
$\hat{E}_1$	Analytical vs UoMFEC (coarse)	0.2499	24.9900	0.1250	16.6627
	Analytical vs ABAQUS (high conductivity) (fine)	0.1690	28.9138	0.1382	23.7802
	Analytical vs ABAQUS (low conductivity) (fine)	32.0440	191.9837	18.1803	138.0075
$\hat{E}_2$	Analytical vs UoMFEC (coarse)	0.1428	14.l2800	0.0571	5.7120
	Analytical vs ABAQUS (high conductivity) (fine)	0.1144	27.7254	0.0809	16.5933
	Analytical vs ABAQUS (low conductivity) (fine)	0.2713	89.4151	0.1593	37.0760
$\hat{E}_3$	Analytical vs UoMFEC (coarse)	0.0721	7.2100	0.0290	2.9267
	Analytical vs ABAQUS (high conductivity) (fine)	0.1195	32.4823	0.0716	17.3644
	Analytical vs ABAQUS (low conductivity) (fine)	0.1166	31.5266	0.0775	17.3274

6. 3 Analysis on Non-Product Fractal

The results presented in this section are contrasted against those obtained from direct analysis of fractal heat exchangers to further test the limitations imposed by the complex thermal response of the matrix material in the tessellated approach. The Sierpinski Gasket is a non-product fractal set constructed by the pre-fractal affine maps presented in Chapter 5. The material selected for the heat exchanger is copper with thermal conductivity $K_s = 400$ W/mK, density $\rho_s = 8930$ kg/m^3 and specific heat $c_s = 385$ J/kgK. The heat transfer coefficient h^{surr} associated with flowing air with temperature $T_{air} = 323K$ around the pre-fractals is taken to be 100 W/m^{2}K. Heat loading of the heat exchanger is achieved by loading the pre-fractal elements from an external source in a manner than ensures the total heat loading $\dot{Q}_{tot} = 300kW$ is uniform on the tessellated continuum. Each pre-fractal has water flowing through the voids to match the working conditions pertaining to the heat exchanger presented in Figure 6.4. It is assumed that the material of the matrix is water with thermal conductivity $K_s = 0.58$ W/mK and the total heat loss $\dot{Q}_s^{loss}$ for each hole in the pre-fractals with different hole sizes and hydraulic diameters d_s^{hole} are shown in Table 6.3.

Table 6.3. Heat loss for the Sierpinski-Gasket heat exchanger

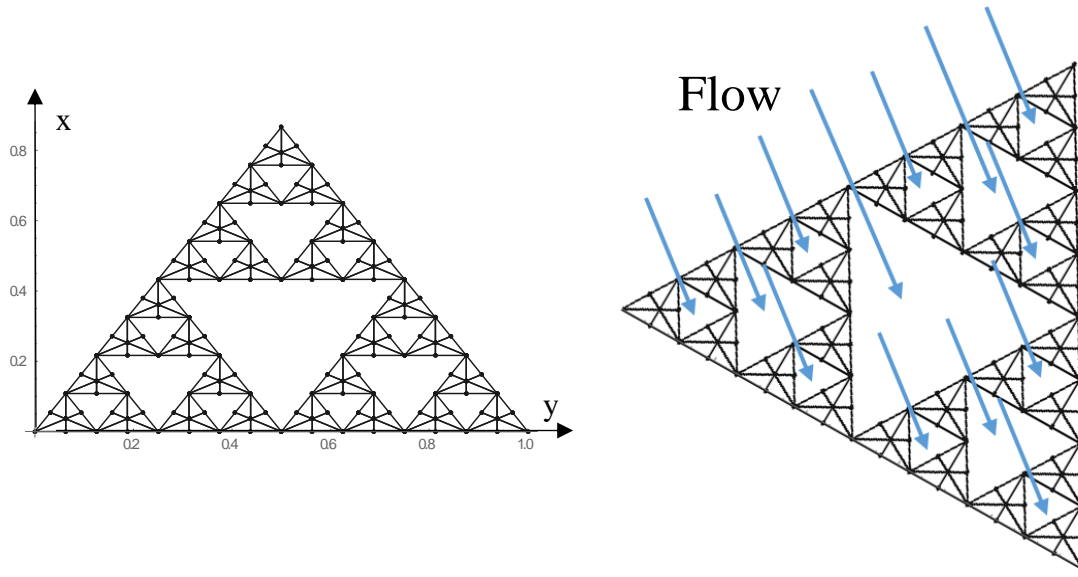| d_s^{hole} (m)	0.289	0.144	0.072	0.036
$\dot{Q}_s^{loss}$ (kW)	270	90	30	10

Figure 6.4. Operating condition for a Sierpinski Gasket heat exchanger

The temperature distributions on $\hat{T}_3$ and mapped on to the pre-fractal $\hat{E}_3$ from UoMFEC are depicted in Figure 6.5. The distributions on both tessellations and pre-fractals are quite different from each other. The temperature distributions from the tessellation with discontinuity networks illustrate discontinuous behaviour. The mapped temperatures are contrasted against an ABAQUS direct result on pre-fractal $\hat{E}_3$ in Figure 6.6. Here, two different meshes are considered in ABAQUS; a coarse mesh and a fine mesh with a convergent result.
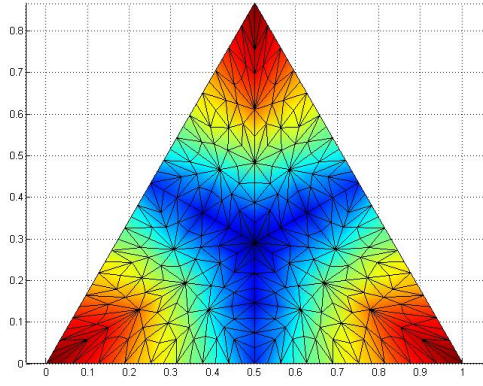
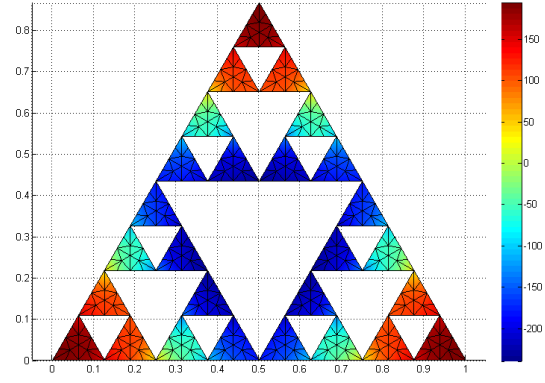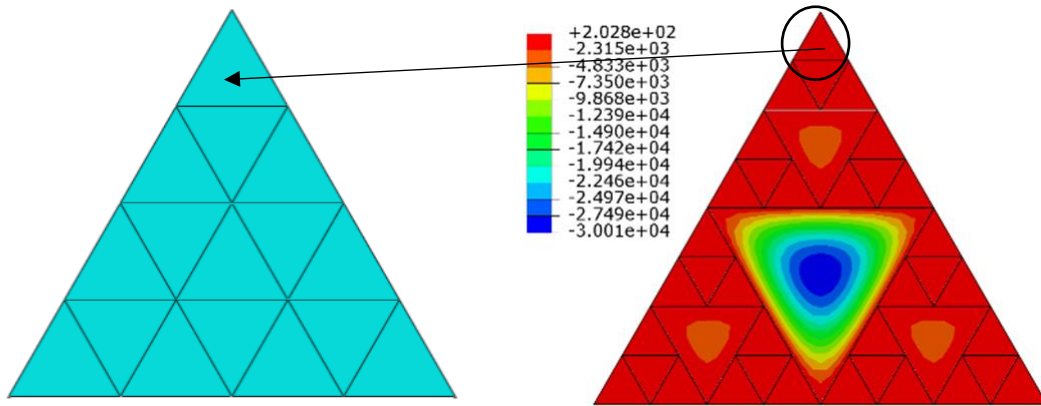(i) On $\hat{T}_3$ without DN
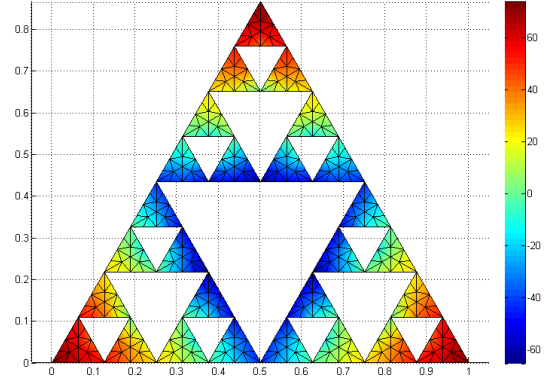
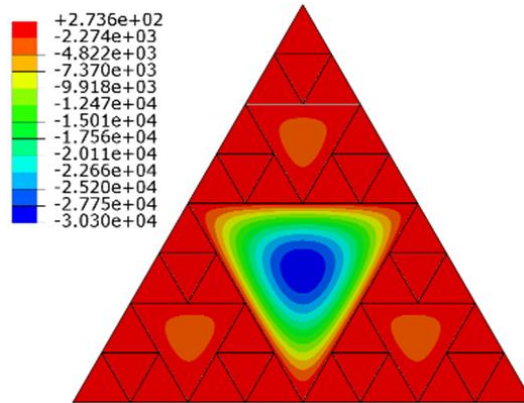(ii) On $\hat{E}_3$ without DN
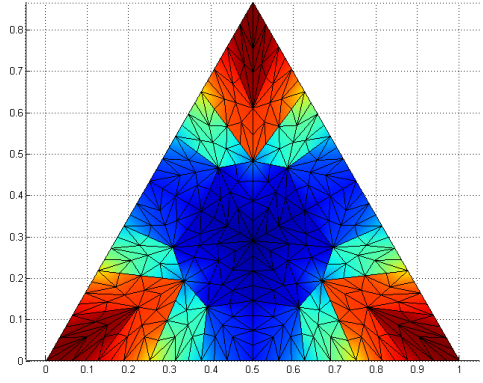
(iii) On $\hat{T}_3$ with DN

(iv) On $\hat{E}_3$ with DN

Figure 6.5. Contour temperatures (UoMFEC) with and without a discontinuity network (DN)

(i) On $\hat{E}_3$ with 16 elements per pre-fractal element

(ii) On $\hat{E}_3$ with 1536 elements per pre-fractal element

Figure 6.6. Contour temperature plots for $\hat{E}_3$ using ABAQUS

The temperature plots on $\hat{E}_k$ for $k = 2$ and $k = 3$ from UoMFEC and ABAQUS along the edge $y = 0$ are presented in Figure 6.7; average temperature differences are quantified using Equations (6.7) and (6.8) in Table 6.4. The largest errors are at the centre where the largest hole is located. The inaccuracy using tessellations without discontinuity networks increases with increasing k for results compared with ABAQUS with coarse mesh. This reduces on tessellations where a discontinuity network is incorporated. However, despite higher accuracy offered from a discontinuity network, low overall accuracy still remains. This illustrates the limitations of the tessellated approach arising from the complex thermal response of the matrix material.
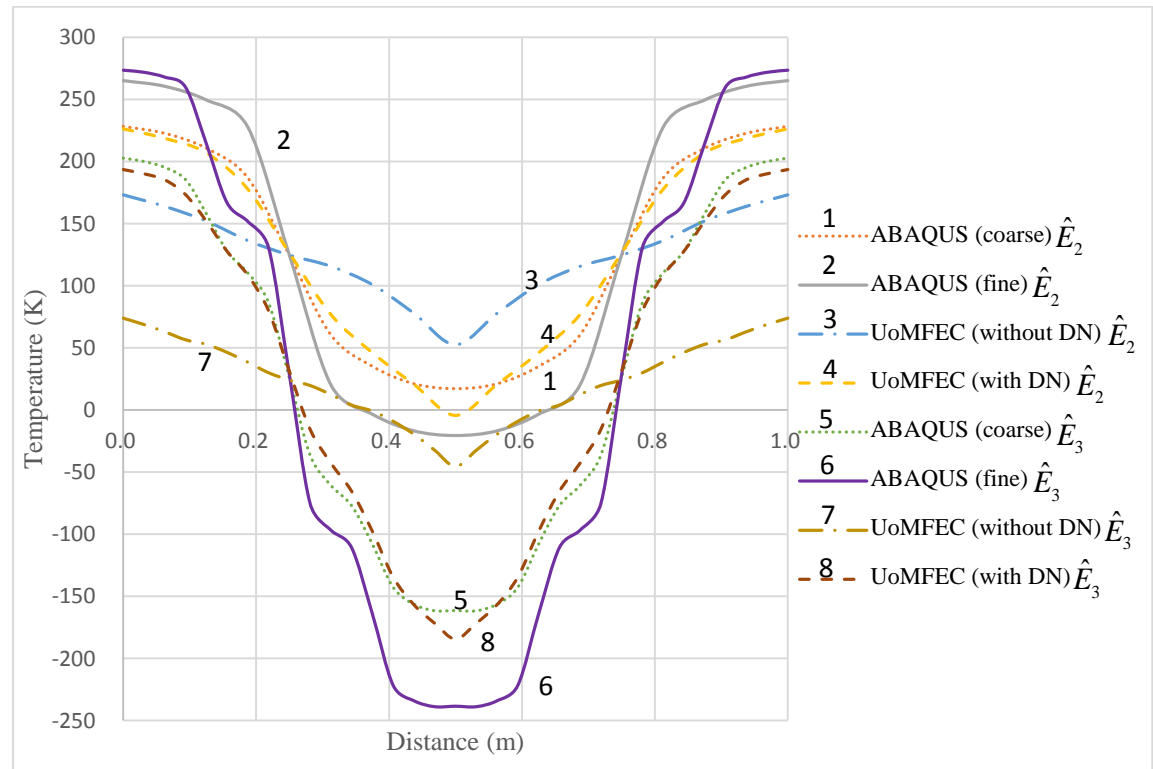

Figure 6.7. Temperature plots along $y = 0$ for pre-fractals $\hat{E}_k$ using UoMFEC and ABAQUS

Table 6.4. Temperature differences on $\hat{E}_k$

			$\hat{E}_1$	$\hat{E}_2$	$\hat{E}_3$
No discontinuity network	Coarse mesh	(K)	493.6781	49.2106	97.7378
		(%)	73.4401	52.4982	127.9979
	Fine mesh	(K)	492.8198	83.3381	152.9618
		(%)	73.3595	97.2703	142.6732
With discontinuity network	Coarse mesh	(K)	493.6781	6.9728	9.1684
		(%)	73.4401	27.3402	12.8828
	Fine mesh	(K)	492.8198	38.4049	61.4024
		(%)	73.3595	77.5928	44.9391

It is of interest to investigate the influence of different number of tiles on the initial tessellation $\hat{E}_0$ for tessellations with discontinuity networks. Mesh refinement of the previous $\hat{E}_0$ provides the tessellations on $\hat{T}_2$, $\hat{T}_3$, $\hat{T}_5$, $\hat{T}_6$ and $\hat{T}_7$ consisting of $54 = 3^2 \times 6$, $162 = 3^3 \times 6$, $1458 = 3^5 \times 6$ $4374 = 3^6 \times 6$ and $13122 = 3^7 \times 6$ tiles to explore the associated temperature distribution. The temperature plots on $\hat{E}_3$ along the edge $y = 0$ are shown in Figure 6.8 for both UoMFEC and ABAQUS direct results, with the average percentage difference tabulated in Table 6.5 through Equations (6.7) and (6.8). The average percentage error with mesh refinement is plotted in Figure 6.9 in order to estimate the modelling error on convergence. The modelling error is defined as the average difference between results obtained from fully converged solutions from UoMFEC and ABAQUS direct results. Figure 6.8 and Table 6.5 reveal that by increasing the number of tiles on the original set $\hat{E}_0$ accuracy can be improved, but high modelling errors remain as shown in Figure 6.9. Other two tests on Sierpinski Carpet and Finger-like Fractal are demonstrated in Appendix A and B respectively.

All the results show that the largest error is located close to the centre at the largest hole. This is not unexpected and reaffirms the limitation of the tessellated approach when matrix material is involved. These tests also provide evidence that tessellations incorporating discontinuity networks can provide greater accuracy. Mesh refinement

achieved by increasing the number of tiles on the initial domain $\hat{E}_0$ is also shown to reduce errors.
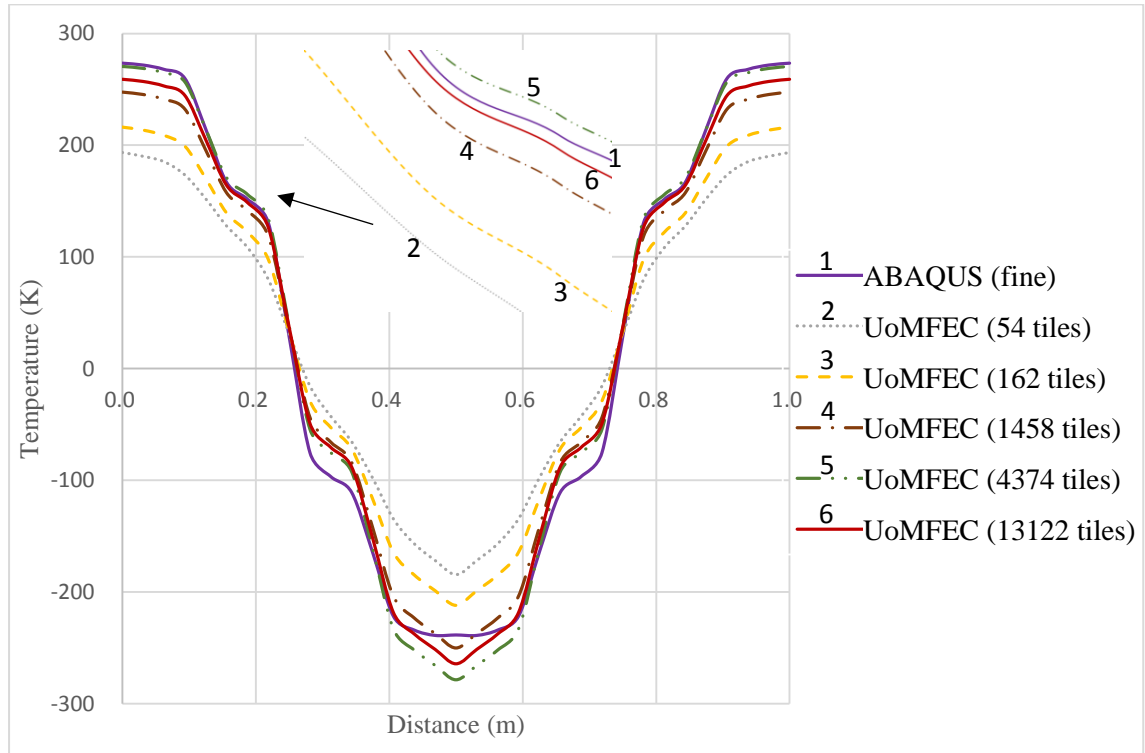

Figure 6.8. Temperature plots along $y = 0$ on $\hat{E}_3$ with different meshes

Table 6.5. Temperature errors on $\hat{E}_k$ along $y = 0$ with different meshes

| $\hat{E}_k$	No. of tiles on $\hat{E}_0$	$\ln(\ell/h)$	Average difference comparing with converge ABAQUS direct result	
			(K)	(%)
$\hat{E}_1$	54	4.8260	492.8198	53.5573
	162	5.9246	493.5616	53.6393
	1458	8.1218	494.3916	53.7301
	4374	9.2204	494.5287	53.7452
	13122	10.3190	494.5961	53.7527
$\hat{E}_2$	54	4.8260	38.4049	62.2946
	162	5.9246	25.8766	64.0147
	1458	8.1218	10.9919	24.7962
	4374	9.2204	5.6834	24.8059
	13122	10.3190	5.2827	22.1788
$\hat{E}_3$	54	4.8260	61.4024	44.9391
	162	5.9246	43.0810	30.6483
	1458	8.1218	18.9293	14.8747
	4374	9.2204	12.5721	10.7569
	13122	10.3190	10.5834	9.0919
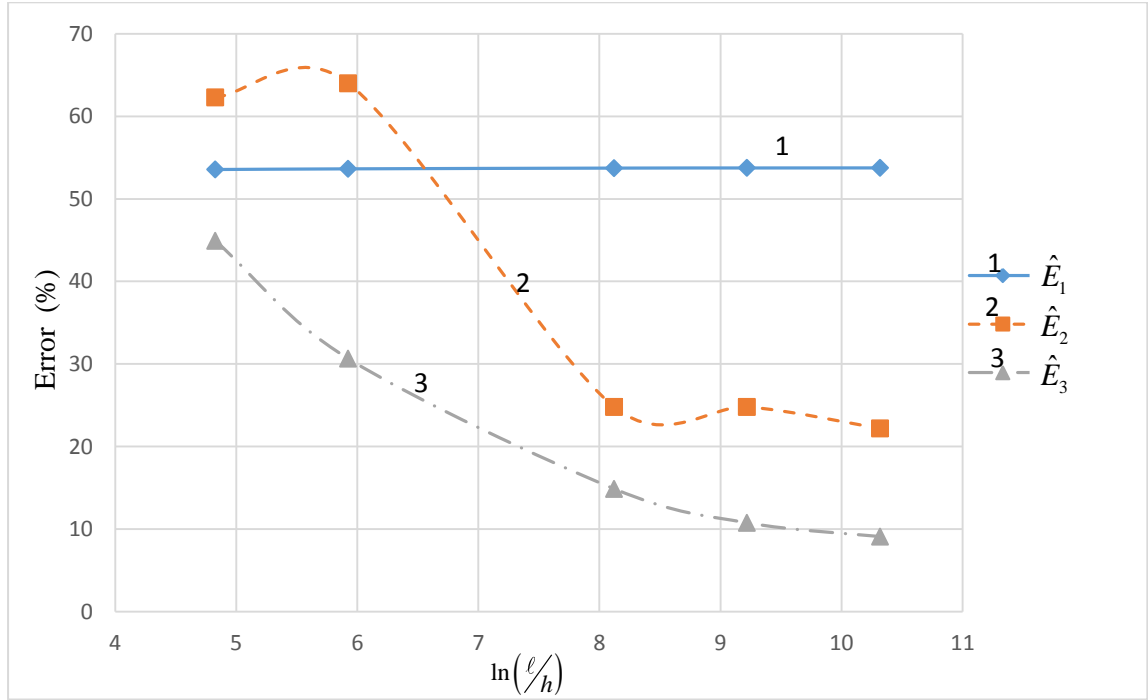
Figure 6.9. Percentage error plots on $\hat{E}_k$ showing magnitudes of modelling errors on convergence

6.4 The Independence of the Solution with Respect to the Expansion Maps

One of the features of the tessellated approach is the non-uniqueness of the sub-expansion maps $\mathbf{P}_{ij}$ in the formation of on an expansion map $\mathbf{P}_i$. This variability is reflected in changes in the tessellation on $\hat{T}_1$. Moreover, changes in $\mathbf{P}_i$ can affect the hole-filling map and influence the precise manner in which holes are closed. Thus, it is of interest to investigate the influence that different hole-fill maps and temperature boundary conditions have on the results. The Viscek Fractal is selected for the investigation and is constructed by the recursive application of the five affine contraction maps with two different hole-fill maps. The thermal conductivity distributions associated with the maps are provided in Chapter 5. The Viscek Fractal heat exchanger is manufactured from the same copper as in Section 6.3 with water coolant flowing through the voids. The heat transfer coefficient h_{air} associated with exterior flowing air of temperature $T_{air} = 323K$ is taken to be $100W/m^2K$. A total external heat source $\dot{Q}_{tot} = 500 \text{ k}W$ is applied uniformly on each pre-fractal. It is assumed that the fixed temperature at the edge of the voids is 293K to match the water cooling.

Depicted in Figure 6.10 are temperature distributions on $\hat{T}_3$ and $\hat{E}_3$ for the two hole-fill maps applied (i.e. map (a) and map (b)). These are compared with the results obtained by ABAQUS directly with two different meshes as depicted in Figure 6.11. Figure 6.10 reveals stark differences in temperature distributions on the two tessellations but the same distributions on the corresponding mapped pre-fractals.
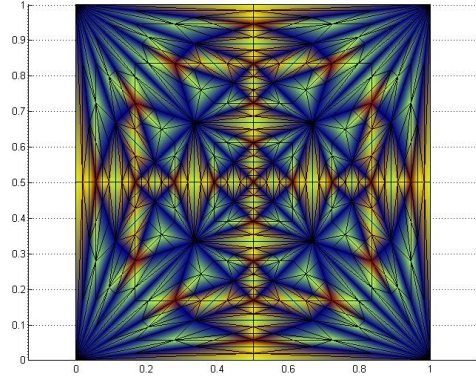
(i) On $\hat{T}_3$ with map (a)
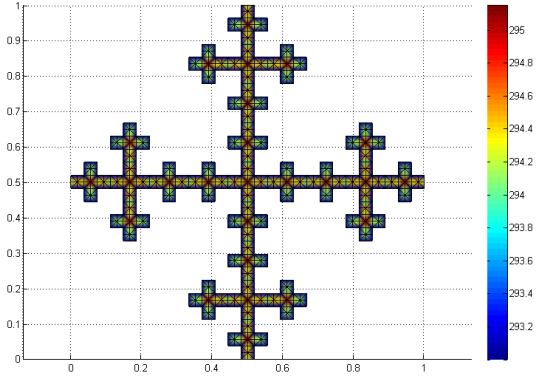
(ii) On $\hat{E}_3$ with map (a)
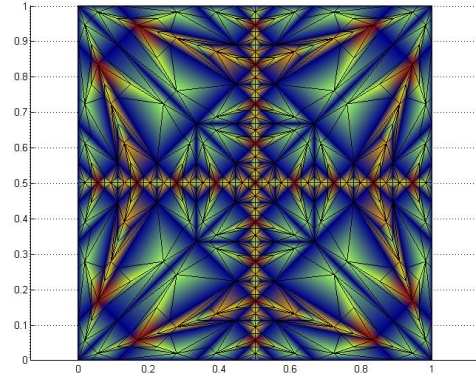
(i) On $\hat{T}_3$ with map (b)
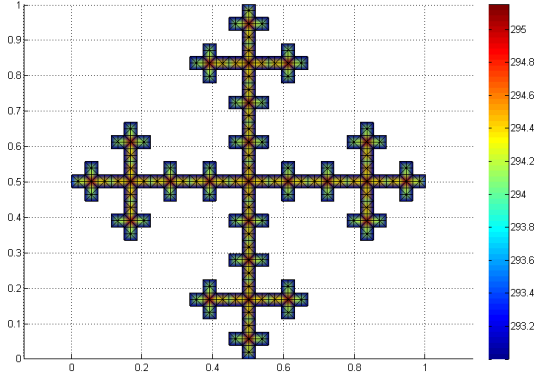
(ii) On $\hat{E}_3$ with map (b)

Figure 6.10. UoMFEC contour temperatures on $\hat{T}_3$ and $\hat{E}_3$ with different hole-filling maps

(i) On $\hat{E}_3$ with 8 elements per pre-fractal element

(ii) On $\hat{E}_3$ with 152 elements per pre-fractal element

Figure 6.11. ABAQUS directly contour temperature plots on $\hat{E}_3$ for various meshes

Temperature distributions along $y = 0.5$ on $\hat{E}_2$ and $\hat{E}_3$ are shown in Figure 6.12 from both UoMFEC and ABAQUS. The average errors calculated 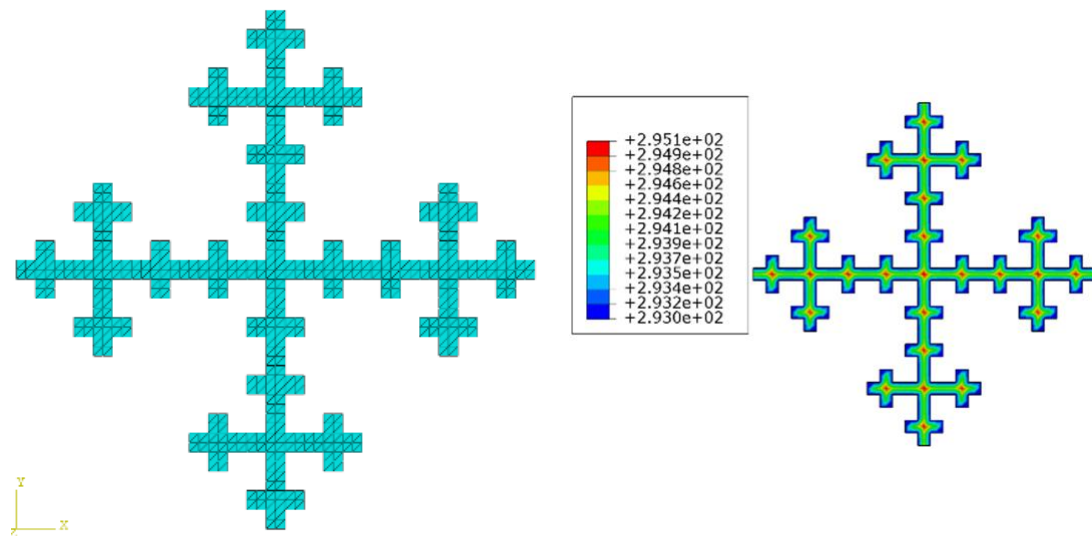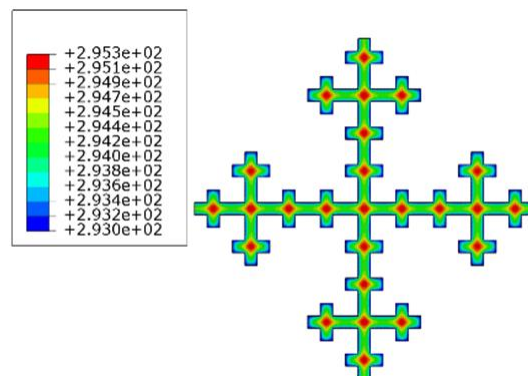through Equations (6.7) and (6.8) are tabulated in Table 6.6 along $y = 0.5$ on $\hat{E}_k$. It is clear that there is good agreement between the ABAQUS direct results and UoMFEC results. The involvement of two different hole-fill maps has little impact on the steady state temperatures on the pre-fractals. The hole-filling map (b) has a larger error on the mapped pre-fractal, because several bigger tiles are created on the original set $\hat{E}_0$. Figure 6.12 shows that the largest difference appears at or near the boundaries in the corresponding pre-fractals, due to the manner in which temperature is fixed with a convection condition with an exceedingly high heat transfer coefficient. According to the analysis performed in Chapter 5, these differences can be reduced through mesh refinement on the original set $\hat{E}_0$. However, the results provide further evidence that different hole-fill maps have little impact on results viewed in the physical space with fixed temperatures.
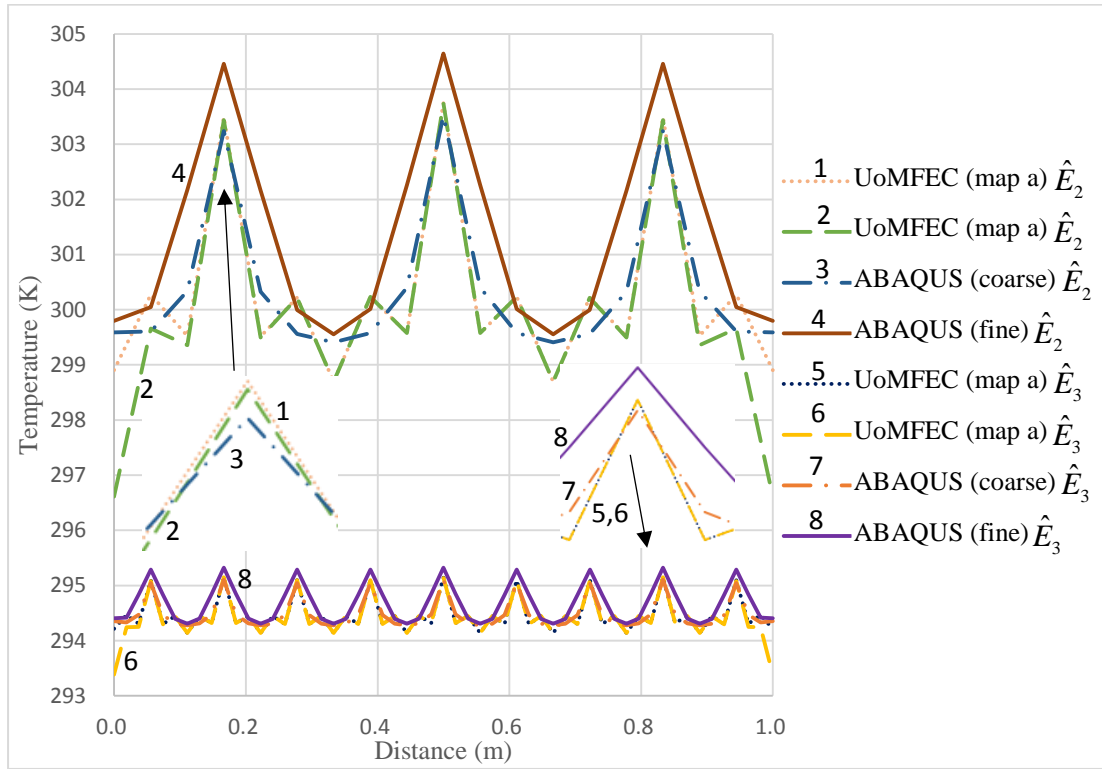
Figure 6.12. Temperature plots along $y = 0.5$ for pre-fractals $\hat{E}_k$ using UoMFEC and ABAQUS

Table 6.6. Average temperature errors on Viscek Fractal along $y = 0.5$

			$\hat{E}_1$	$\hat{E}_2$	$\hat{E}_3$
Result with (a) tessellation maps	Coarse mesh	(K)	3.2222	0.6522	0.1304
		(%)	0.9843	0.2174	0.0443
	Fine mesh	(K)	5.9679	1.2445	0.2502
		(%)	1.7958	0.4135	0.0849
Result with (b) tessellation maps	Coarse mesh	(K)	4.3508	0.8419	0.1605
		(%)	1.3422	0.2813	0.0545
	Fine mesh	(K)	7.3819	1.5270	0.2882
		(%)	2.2385	0.5083	0.0979

6. 5   Conclusions

The thermal analysis of complex cellular structures represented by the pre-fractals is demonstrated on the corresponding tessellations with and without discontinuity networks through the finite element method. In establishing the tessellated approach for heat transfer analysis on pre-fractals, the following conclusions can be drawn:

- The tessellated approach has limited applicability for problems where complex physics governs the surrounding matrix material. Large errors have been shown to occur in the vicinity of relatively large matrix domains.

- Tessellations incorporating discontinuity networks provide greater accuracy as they accommodate discontinuities that appear at tile boundaries. Their use offers improvements when accommodating complex material responses but errors can still be significant.

- The tessellation with discontinuity networks and a large number of titles on the original set $\hat{E}_0$ can reduce errors.

- Alternative expansion maps (and consequently hole-fill maps) have been shown to have little impact on the mapped temperatures for the problems considered despite the use of Dirichlet boundary conditions.

Appendix A: Thermal analysis of a Sierpinski Carpet heat exchanger

The pre-fractals and corresponding tessellations for Sierpinski Carpet are created by the affine maps shown in Chapter 5. The material selected for the Sierpinski Carpet heat exchanger is the same as in Section 6.3. Water with thermal conductivity $K_s = 0.58\,\text{W/mK}$ is considered to flow through the voids as cooling channels with total heat loss $\dot{Q}_s^{loss}$ for each hole in the pre-fractals with different hole sizes (and hydraulic diameters d_s^{hole}) are shown in Table 6.7. A total external heat source $\dot{Q}_{tot} = 500 kW$ is applied as uniform load on each pre-fractal.

Table 6.7. Heat loss for the Sierpinski-Carpet heat exchanger

$d_s^{hole}\ (m)$	0.333	0.111	0.037	0.012
$\dot{Q}_s^{loss}\ (kW)$	270	90	30	10

The tessellations with and without discontinuity networks are applied to UoMFEC. Temperature distributions obtained from UoMFEC on tessellation $\hat{T}_3$ and pre-fractal $\hat{E}_3$ are depicted in Figure 6.13. Similarly, results obtained directly on $\hat{E}_3$ are obtained using ABAQUS (on two different meshes) and are presented in Figure 6.14.

(i) On $\hat{T}_3$ without DN

(ii) On $\hat{E}_3$ without DN

(iii) On $\hat{T}_3$ with DN

(iv) On $\hat{E}_3$ with DN
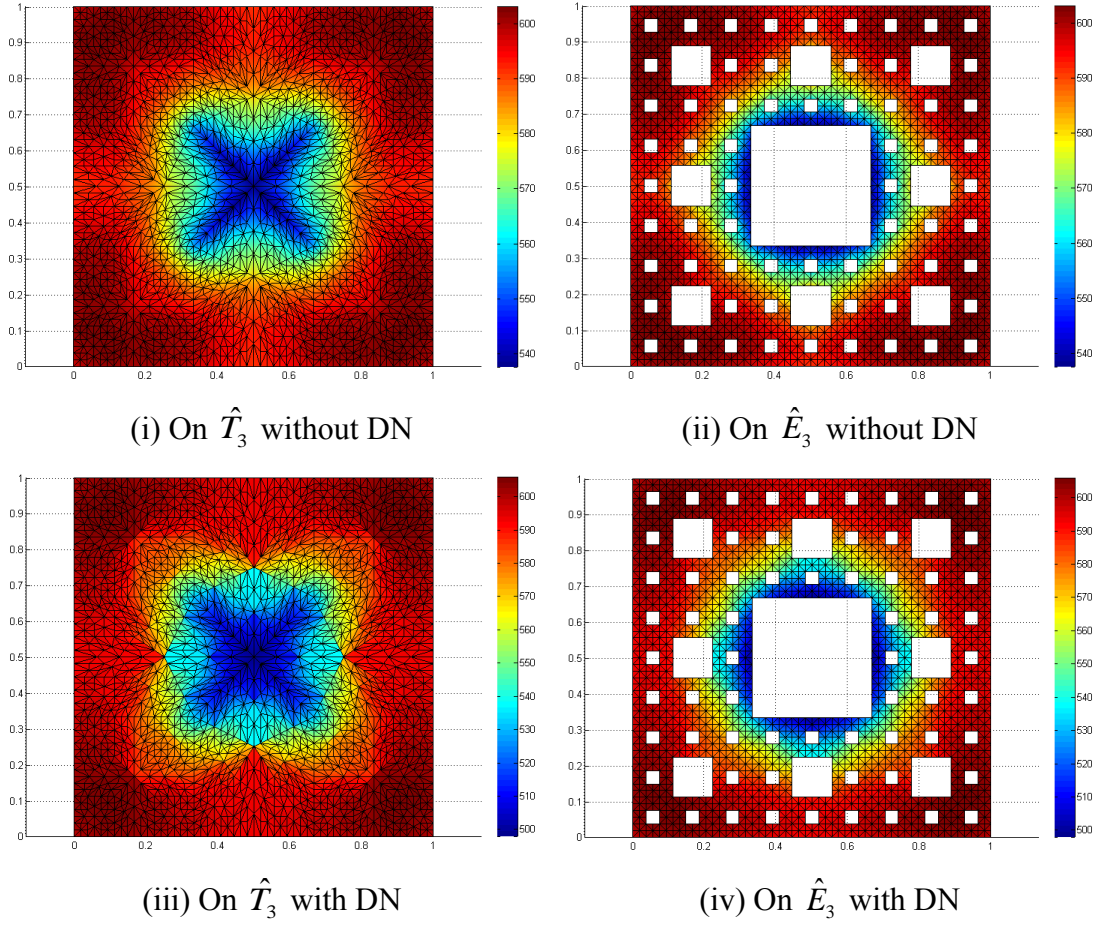
Figure 6.13. Contour temperatures (UoMFEC) with and without a discontinuity network (DN)
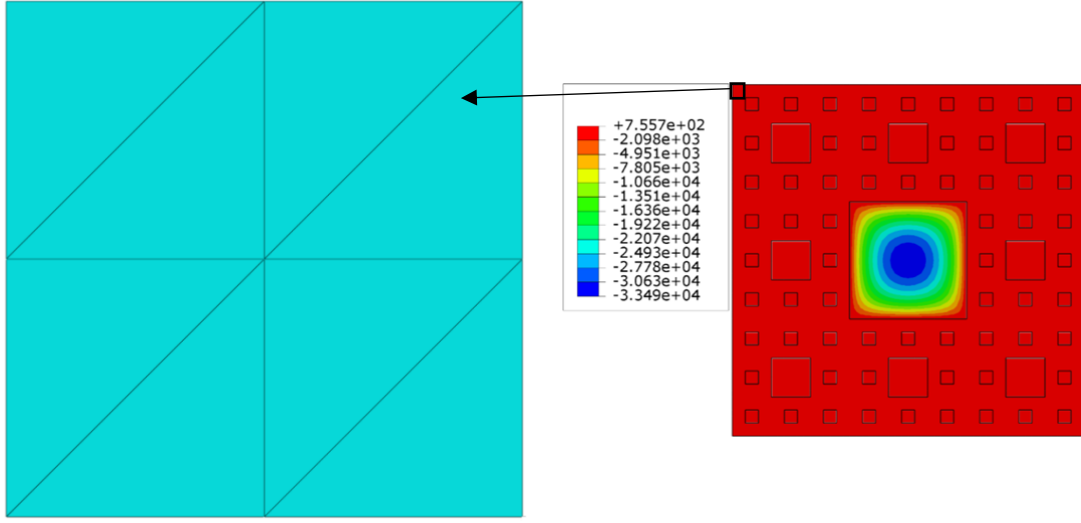
(i) On $\hat{E}_3$ with 8 elements per pre-fractal element
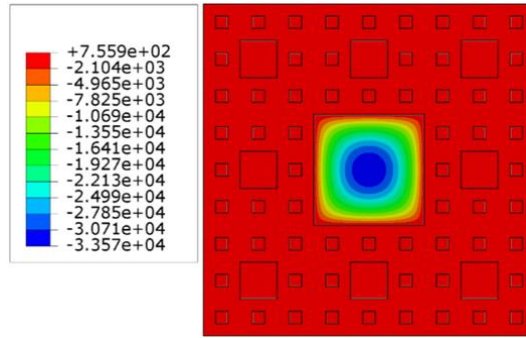
(ii) On $\hat{E}_3$ with 152 elements per pre-fractal element

Figure 6.14. Contour temperature plots for $\hat{E}_3$ using ABAQUS

The temperature distributions on $\hat{E}_k$ along the diagonal line $x = y$ from UoMFEC and ABAQUS are presented in Figure 6.15. The average errors quantified using Equations (6.7) and (6.8) are provided in Table 6.8. Figure 6.15 and Table 6.8 confirm low accuracy with results obtained using the UoMFEC on subsequently mapped to $\hat{E}_k$, (except $\hat{E}_1$) contrasted against ABAQUS direct results. The errors increase with the increase of k.
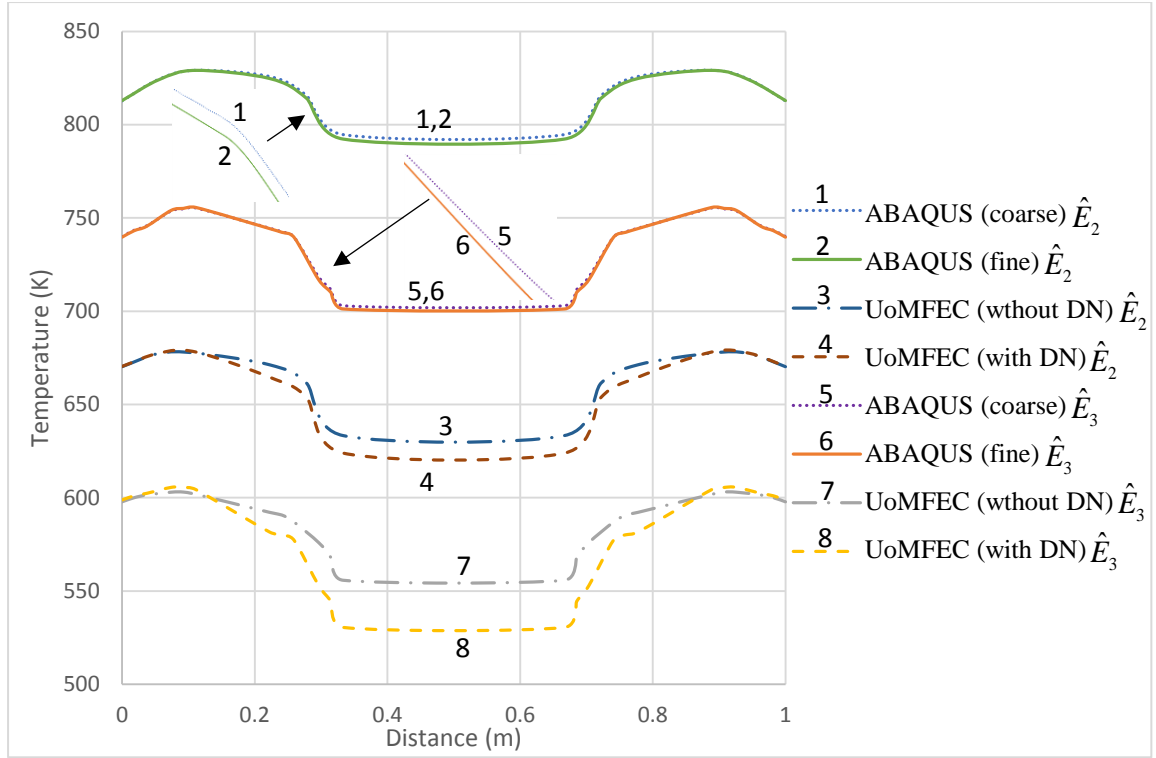
Figure 6.15. Temperature plots along $x = y$ for pre-fractals $\hat{E}_k$ using UoMFEC and ABAQUS

Table 6.8. Temperature differences on $\hat{E}_k$: Influence of discontinuity network

			$\hat{E}_1$	$\hat{E}_2$	$\hat{E}_3$
No discontinuity network	Coarse mesh	(K)	1.6962	151.8879	148.0265
		(%)	0.1889	20.5098	22.30919
	Fine mesh	(K)	4.2254	151.0374	147.5925
		(%)	0.4772	20.4057	22.24889
With discontinuity network	Coarse mesh	(K)	1.6962	155.6808	155.7153
		(%)	0.1889	21.0883	23.66428
	Fine mesh	(K)	4.2254	154.8303	155.2813
		(%)	0.4772	20.9843	23.6043

Appendix B: Thermal analysis of a Finger-like fractal heat exchange

The affine maps of pre-fractals and corresponding tessellations for Finger-like fractal are demonstrated in Chapter 5. The Finger-like Fractal heat exchanger is manufactured with the same copper as in Section 6.3. The total heat loss $\dot{Q}_s^{loss}$ from water flowing through the voids in the pre-fractals with different hole sizes (and hydraulic diameters d_s^{hole}) is illustrated in Table 6.9. The heat exchanger is subjected to a uniform heat loading with total external heat source $\dot{Q}_{tot} = 500 kW$.

Table 6.9. Heat loss for the Finger-like Fractal heat exchanger

$\hat{E}_k$	d_s^{hole} (m)	$\dot{Q}_s^{loss}$ (kW)
$\widehat{E}_1$	0.333	270
$\widehat{E}_2$	0.296	270
	0.111	90
$\widehat{E}_3$	0.241	270
	0.099	90
	0.037	30
$\widehat{E}_4$	0.198	270
	0.080	90
	0.033	30
	0.012	10

Temperature distributions for Finger-like porous fractal from UoMFEC and ABAQUS are presented in Figure 6.16 and Figure 6.17 respectively. The difference in temperature distributions are significant between tessellations with and without continuity networks. The discontinuous behaviour is clear by observed on the tessellation with discontinuity networks.

(i) On $\hat{T}_3$ without DN

(ii) On $\hat{E}_3$ without DN

(iii) On $\hat{T}_3$ with DN

(iv) On $\hat{E}_3$ with DN
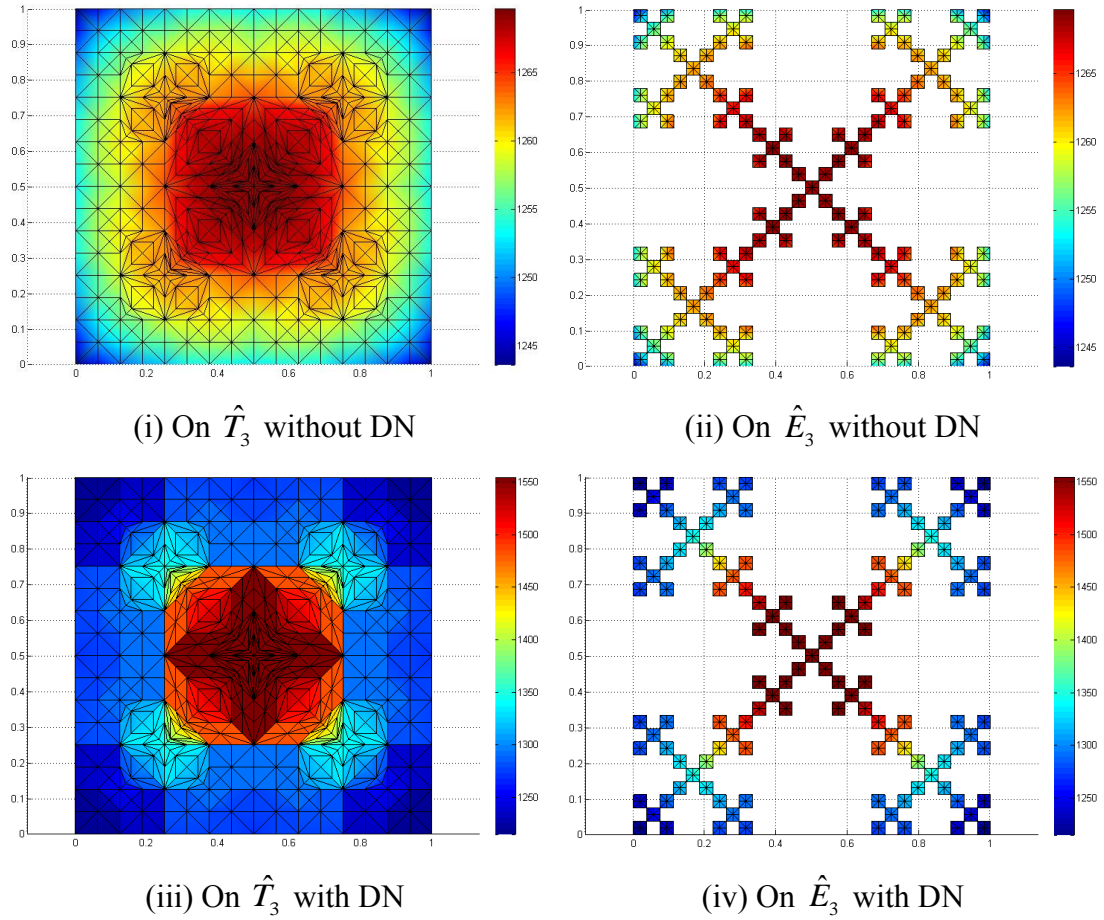
Figure 6.16. Contour temperatures (UoMFEC) with and without a discontinuity network (DN)
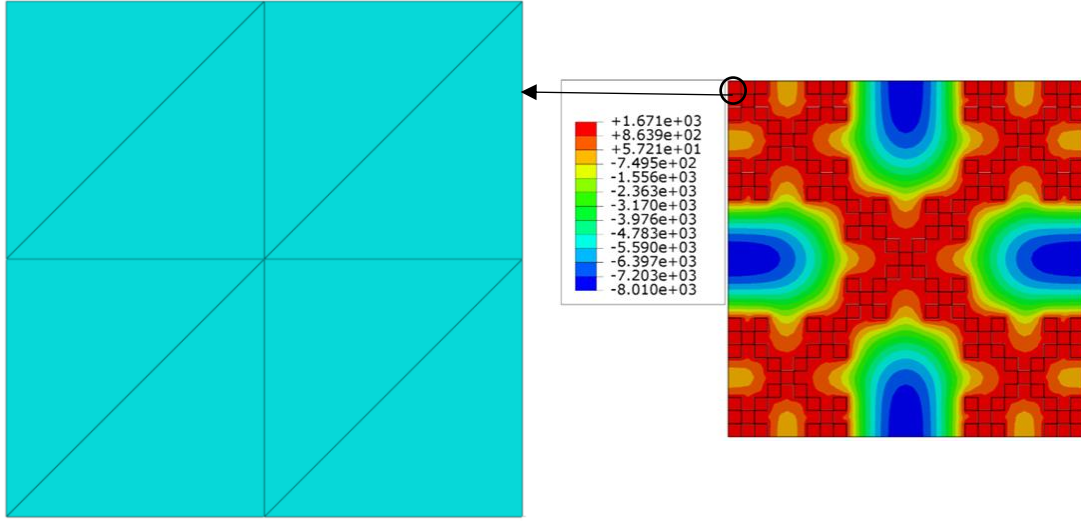
(i) On $\hat{E}_3$ with 8 elements per pre-fractal element
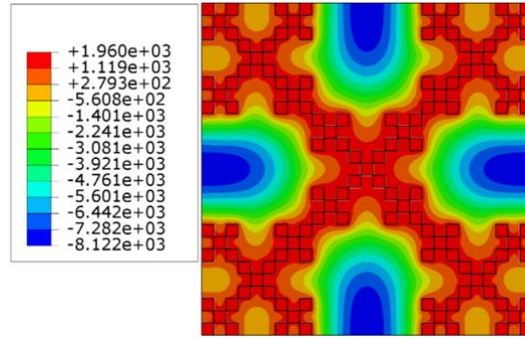
(ii) On $\hat{E}_3$ with 152 elements per pre-fractal element

Figure 6.17. Contour temperature plots for $\hat{E}_3$ using ABAQUS

The temperature plots on $\hat{E}_k$ from UoMFEC and ABAQUS along the diagonal line $x = y$ are illustrated in Figure 6.18 with the average errors in Table 6.10 quantified using Equations (6.7) and (6.8). The shortfall from tessellated approach increases with the increase of k comparing with the convergent ABAQUS direct results; but the errors from tessellation with discontinuity networks are reduced contrasted against the ABAQUS direct results with a coarse mesh.
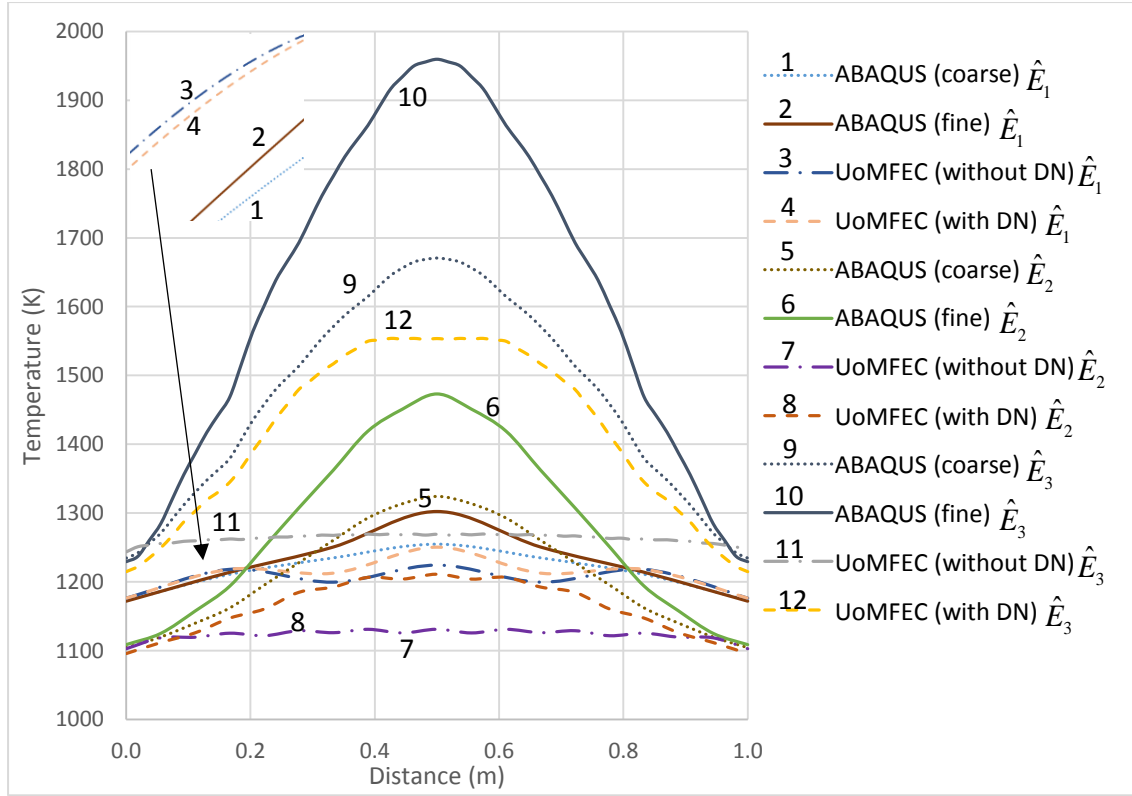
Figure 6.18. Temperature plots along $x = y$ for pre-fractals $\hat{E}_k$ using UoMFEC and ABAQUS

Table 6.10. Temperature differences on $\hat{E}_k$: Influence of discontinuity network

			$\hat{E}_1$	$\hat{E}_2$	$\hat{E}_3$
No discontinuity network	Coarse mesh	(K)	17.4464	85.5565	206.5515
		(%)	1.4299	7.1442	14.61262
	Fine mesh	(K)	28.2092	152.3123	357.4042
		(%)	2.2801	12.1931	23.56287
With discontinuity network	Coarse mesh	(K)	9.9754	46.7066	50.52511
		(%)	0.8184	3.8060	3.37318
	Fine mesh	(K)	20.7382	113.4623	200.6229
		(%)	1.6689	8.8739	12.40629

Chapter 7.

Conclusions and Future Work

Tessellated continuum mechanics can be extended to classical continuum mechanics to study thermo-mechanical behaviour of porous media. In this research, a novel tessellated approach for thermal analysis is developed to investigate temperature distributions on the cellular heat exchangers. The purpose of this approach is to enable thermal analysis to be performed on the corresponding tessellations as opposed to complex fractal structures. It is shown that the thermal behaviour on the related tessellated continua predicts the thermal behaviour of the pre-fractals with great accuracy.

7.1   Introduction

As a mathematical model, a fractal is chosen to represent the cellular structure of porous materials. A hole-fill map concept is introduced to construct a relative tessellation for pre-fractal. In order to analyse the material properties for the tessellations, transport equations and partial differential equations are considered. The Galerkin finite element method is applied to the related tessellations both with and without discontinuity networks in order to explore the thermal behaviour of the fractals. All the results confirm that the tessellated approach has great accuracy and discontinuity networks can reduce the error. However, there is a limitation in the approach when investigating a complex thermal response in the matrix material. Finally, some future work is recommended in order to extend this research.

7. 2   Conclusions

This research uses tessellated continuum mechanics to explore heat transfer problem in porous media. A hole-fill map concept is applied to build a related tessellated continuum for a pre-fractal to present cellular structure of a porous material. As closing the holes have the effect of bringing edges together, the discontinuity networks are introduced to the tessellations. They are applied to identify and describe the discontinuous behaviour of pre-fractals. Although the approach of creating hole-fill maps for tessellations with and without discontinuity networks are the same, the discontinuity networks can be used to better represent the physics of pre-fractals. Therefore, the tessellations both with and without discontinuity networks are considered in the process of creating hole-fill maps for pre-fractals.

Transport theory has been coupled to the tessellated approach. The transport equations are applied to both pre-fractal and corresponding tessellations in order to match the physics of the two structures and control volumes are used to describe the physics of the continuous set (rather than on a discontinuous set). Based on the transport theory, partial differential equations are defined on both pre-fractals and the corresponding tessellations in order to obtain the material properties of the relative tessellations. As the heat transfer coefficients and temperatures are the same for a pre-fractal and the related tessellation, the specific heats are the same. The density relationship for the tessellations is found to be $\rho_r = \left| \boldsymbol{F} \right|^{-1} \rho_s$ based on the scales in accordance with their volumes and areas. Thermal conductivity is the most complex property and scales as $\boldsymbol{K}_r = \left| \boldsymbol{F} \right|^{-1} \boldsymbol{F} \boldsymbol{K}_s \boldsymbol{F}^T$ on the corresponding tessellations. The thermal conductivity is inhomogeneous, anisotropic and discontinuous, so it is obtained from each tile of the tessellation and illustrated through the point-wise maximum value. Therefore, refined distribution of thermal conductivity for the tessellation is obtained from a large number of tiles. The distributions of thermal conductivity for a series of classical non-product fractals have been investigated to show how the geometric complexity present in the pre-fractals manifests in the material properties of the tessellations. The behaviour of thermal conductivity on the tessellation is explored and is found to depend on the principal stretch directions associated with the deformation tensor. Larger thermal conductivity is located at the tile with larger deformation. Due to the

same geometry, the tessellations with and without discontinuity network have the same material properties.

The Galerkin finite element method is applied on both the pre-fractals and the corresponding tessellations to obtain comparative numerical solutions. The commercial finite element package ABAQUS is chosen to obtain the pre-fractal results directly; a developed finite element code named UoMFEC is used to study the associated tessellations. The principal reason for the development of UoMFEC is to provide a convenient platform for the determination of element-conductivity matrices, which generally involve orthotropic conductivity tensors.

The hypothesis of this research is that the analysis of heat transfer for porous materials can be achieved through analysis on relative tessellated continuous structures. After the analysis of the hole-fill maps and material properties, thermal behaviour from analytical solution on fractal dusts and rings in 1-D and 2-D were tested. The results provided a means to test the accuracy of the tessellated approach.

Considering the operating conditions of cellular heat exchangers, analytical solutions for heat transfer problems are then defined for Cantor dusts. The governing partial differential equations are applied to obtain an analytical solution. The analytical results with steady state and transient solutions are contrasted against the numerical results from UoMFEC and the direct result from ABAQUS in order to prove the accuracy of the tessellated approach. Different tessellations were considered for the Cantor dust problem. Because of near-linear temperature distributions over pre-fractal elements for a 1-D Cantor dust, different tessellations have little impact on the results. Since continuity in the Galerkin method is enforced via the temperatures on the tessellations, the temperature differences between the tessellated approach and the direct result are located on the edges representing holes in the pre-fractals. Nevertheless, all the results demonstrate great accuracy of the method. More intricate pre-fractals such as Sierpinski gasket, Carpet and Finger-like fractals are chosen to represent porous materials found in cellular heat exchangers. The solutions from the tessellated approach were compared with the direct results from ABAQUS. The results further illustrate the great accuracy of the tessellated approach.

A procedure for the creation of different tessellations with various levels of refinement was presented. The mesh refinement was achieved by increasing the number of tiles on the original set of the pre-fractal. A modelling error defined as the difference between results obtained from fully converged solutions from UoMFEC and ABAQUS with a fine mesh applied directly to the pre-fractal was investigated. The results show that the tessellated approach provides a small modelling error which can be reduced with increasing refinement.

Discontinuity networks are applied on tessellations to analyse the thermal behaviour of cellular structures. An analytical solution to a heat transfer problem of Cantor Dust in one-dimension is derived considering both conduction and convection conditions. The temperatures from the analytical solution are compared with UoMFEC tessellated results and ABAQUS direct results. The tessellated approach using discontinuity networks are found to offer greater accuracy compared with the direct results. In contrast to tessellations without discontinuity networks, the accuracy of tessellations with discontinuity networks can be significantly improved with mesh refinement. Heat transfer on a series of classical non-product fractals was investigated on the corresponding tessellations with and without discontinuity networks to confirm the importance of discontinuity networks. The results have illustrated that the tessellations with discontinuity networks provide greater accuracy.

The influence of mesh refinement on the initial fractal set is explored for tessellations with discontinuity networks. Both steady state and transient results confirm that mesh refinement with a large number of tiles on the original set of the pre-fractal can improve accuracy. The modelling error is also much less than that found in tessellations without discontinuity networks.

The tessellated approach reuses non-unique sub-expansion maps in the form of a set of expansion maps. This variability is reflected in changes of the tessellation on the original set. The changes in an expansion map can affect the hole-fill maps and influence the precise manner in which holes are closed. Therefore, different hole-fill maps were considered to explore the influence of the tessellated approach on the thermal problem. The results show that different expansion maps have little impact on the mapped temperatures from alternative expansion maps with convection and temperature conditions.

The matrix is assumed to have a perfect conductivity, so further tests are undertaken to consider the thermal response of the matrix. Both analytical and numerical solutions from the tessellated approach without discontinuity networks on 2-D Cantor dust were contrasted against the pre-fractal direct results. Low accuracy is shown as large errors occur in the vicinity of relatively large matrix domains. Due to the consideration of two different thermal conductivities, high thermal conductivity applied to the matrix can increase the accuracy.

A series of classical non-product fractals were tested in order to extend simple Cantor dust case. Tessellations with and without discontinuity networks were applied to investigate the thermal behaviour of pre-fractals with consideration of thermal response of the matrix. Despite higher accuracy offered by a discontinuity network, low overall accuracy remains. The results illustrate that the largest error is located close to the biggest hole. Although mesh refinement can improve the accuracy, high modelling errors remain. All the results confirm that the tessellated approach provides limited applicability due to complex physics of the matrix material.

In this thesis, the thermal results obtained from tessellated approach are compared with the numerical results produced by ABAQUS. These two methods consider the same thermal conditions and both of them ignore the influence from the fluid flowing through the voids. Instead, they have applied convection conditions at the void edges to simulate the fluid flow. However, the results on the cellular structures from tessellated approach are returned from the results on the corresponding tessellations. The tessellated approach using UoMFEC makes effective use of recursion. Any thermal behaviour on the kth pre-fractal can be immediately obtained by specifying the value of k in the UoMFEC. ABAQUS on the other hand is not founded on recursion and consequently results are obtained on creating the geometry of the pre-fractal, each time. This latter approach is much more inefficient and cumbersome resulting in longer processing times than that required for the UoMFEC. Thus, the tessellated approach provides an effective means for efficiently investigating thermal behaviour for cellular structures on corresponding tessellations.

7. 3 Future Work

The possibilities of future work which are considered here has three main aspects. Firstly, the fluid mechanics of water flowing through the voids of the porous media can be analysed further in detail, secondly, the tessellated approach can be extended to more realistic porous materials in three dimensional cases, thirdly, the hole-fill maps can be created automatically for any geometry of the porous materials.

In this thesis, it is assumed that the water flowing through the voids of the porous media is turbulent and fully developed so that the Dittus-Boelter equation and the Darcy-Weisbach equation can be used to determinate the heat transfer coefficient for each void with different hydraulic diameter. However, it is clear that laminar flow will prevail with the decrease of the size of the voids in fractals. Reynolds number can be introduced to determine the type of the flow. Therefore, the heat transfer coefficient for the cooling channel should be more carefully calculated according to different flow conditions.

Furthermore, more realistic condition can be applied on the tessellations to simulate the fluid flowing through the voids. In this research, it is assumed (in the continuous Galerkin formulation) that any cooling medium passing through a porous structure is a perfect conductor which essentially means no temperature gradients are permitted perpendicular to the channel flow direction in this research. Presently, empirical heat transfer coefficients are used to capture the physics of cooling but this is recognised to be a limiting feature. This situation could be improved with the aid of Computational Fluid Dynamics (CFD), which can be used to investigate the fluid flowing through the pores of the cellular structure. The results can be compared with the previously obtained ABAQUS direct (and/or UoMFEC) results. The difference between these two methods can be analysed to determine the relative importance of different conditions applied in the CFD model. In this way the boundary conditions on the ABAQUS/UoMFEC model can be improved in order to reduce modelling errors.

It is proposed that the Lattice Boltzmann method providing greater accuracy can be examined with the objective of an improved representation of cooling involved. Some basic knowledge of Lattice Boltzmann method was introduced in the chapter on

literature review. This method can be employed to analyse fluid flow problems in complex geometries like porous media and it should be considered to investigate fluid flow in voids to improve the accuracy due to cooling channels in the tessellated approach. The Lattice Boltzmann method can at least in principle, be applied to the cellular structures to explore the nature of the fluid flowing through the voids. Influence factors can then be considered for the tessellated approach on the edges representing cooling channels. In this way it is envisaged that the accuracy of the approach can be improved to replicate more completely realistic operational conditions. Similar to the approach adopted in this thesis the Lattice Boltzmann method can be first tested on simple 1-D fractals to establish a route to do the further exploration on non-product fractals.

Secondly, this thesis is mainly focused on thermo-mechanics of 2-D classical fractals. An extension of this work would implement the tessellated approach for thermal analysis in more realistic porous media. Typical 3-D fractals such as Menger Sponge can be investigated for a start. Then, the geometry of several real porous materials can be considered. They can be represented through micro-CT scanner which is introduced in the literature review chapter. Therefore, more complex hole-fill maps are needed. Due to the geometry, the real flow dynamics through the voids during heat exchanger operation will be extremely complex. Future work will concentrate on better representation of this flow complexity.

Once a model from micro-CT for a complex realistic porous material is developed, it will be difficult to construct the relative tessellations manually. The two main types of voids (closed and open pore) should be further considered along with their corresponding hole-fill maps. If the hole is a closed pore, a new programme should be created to find the central point of the hole and divide the hole with uniform area for 2D fractals or volume for 3D cellular structures. After that, the hole can be filled by the elements around. If the hole is an open pore, then the axis of symmetry needs to be established together with the central point to build the hole-fill maps. Then, a corresponding tessellation can be obtained immediately with the input of the geometry of the porous materials.

REFERENCE

[1]   Q. Li, G. Flamant, X. Yuan, P. Neveu, and L. Luo, "Compact heat exchangers: A review and future applications for a new generation of high temperature solar receivers," *Renew. Sustain. Energy Rev.*, vol. 15, no. 9, pp. 4855–4875, Dec. 2011.

[2]   D. W. Bruce, D. O'Hare, and R. I. Walton, Eds., *Porous Materials*, 1 edition. Wiley, 2011.

[3]   J. J. Timothy and G. Meschke, "A cascade continuum micromechanics model for the effective elastic properties of porous materials," *Int. J. Solids Struct.*, vol. 83, pp. 1–12, Apr. 2016.

[4]   R. W. Serth, "3 - HEAT EXCHANGERS," in *Process Heat Transfer*, Oxford: Academic Press, 2007, pp. 85–125.

[5]   H. Peng and X. Ling, "Optimal design approach for the plate-fin heat exchangers using neural networks cooperated with genetic algorithms," *Appl. Therm. Eng.*, vol. 28, no. 5–6, pp. 642–650, Apr. 2008.

[6]   K. Boomsma, D. Poulikakos, and F. Zwick, "Metal foams as compact high performance heat exchangers," *Mech. Mater.*, vol. 35, no. 12, pp. 1161–1176, Dec. 2003.

[7]   M. Bhouri, J. Goyette, B. J. Hardy, and D. L. Anton, "Honeycomb metallic structure for improving heat exchange in hydrogen storage system," *Int. J. Hydrog. Energy*, vol. 36, no. 11, pp. 6723–6738, Jun. 2011.

[8]   V. E. Tarasov, "Continuous medium model for fractal media," *Phys. Lett. A*, vol. 336, no. 2–3, pp. 167–174, Mar. 2005.

[9]   V. E. Tarasov, "Fractional hydrodynamic equations for fractal media," *Ann. Phys.*, vol. 318, no. 2, pp. 286–307, Aug. 2005.

[10]   M. Ostoja-Starzewski, "Towards Thermoelasticity of Fractal Media," *J. Therm. Stress.*, vol. 30, no. 9–10, pp. 889–896, Aug. 2007.

[11]   M. Ostoja-Starzewski, "Towards thermomechanics of fractal media," *Z. Für Angew. Math. Phys.*, vol. 58, no. 6, pp. 1085–1096, Aug. 2007.

[12] B. H. Lee and S. K. Lee, "Effects of specific surface area and porosity on cube counting fractal dimension, lacunarity, configurational entropy, and permeability of model porous networks: Random packing simulations and NMR micro-imaging study," *J. Hydrol.*, vol. 496, pp. 122–141, Jul. 2013.

[13] E. B. W. V. L. Streeter, *Fluid Mechanics*, 7th Revised edition edition. New York: McGraw Hill Higher Education, 1985.

[14] J. Tian, T. Kim, T. J. Lu, H. P. Hodson, D. T. Queheillalt, D. J. Sypeck, and H. N. G. Wadley, "The effects of topology upon fluid-flow and heat-transfer within cellular copper structures," *Int. J. Heat Mass Transf.*, vol. 47, no. 14–16, pp. 3171–3186, Jul. 2004.

[15] A. H. Kim and R. A. Guyer, "Hysteresis in Porous Materials," in *Hysteresis in Porous Materials*, John Wiley & Sons, 2014, p. 127.

[16] I. Kroupová, F. Radkovský, P. Lichý, and V. Bednářová, "Manufacturing of Cast Metal Foams with Irregular Cell Structure," *Arch. Foundry Eng.*, vol. 15, no. 2, pp. 55–58, 2015.

[17] G. Q. Lu, *Nanoporous Materials, Science and Engineering*. Imperial College Press, 2005.

[18] O. Coussy, *Poromechanics*, 2nd ed. Chichester: Wiley, 2004.

[19] O. Coussy, *Mechanics of porous continua / Olivier Coussy ; translated from the French in collaboration with Franz Ulm.* Chichester: Wiley, 1995.

[20] K. Mattila, T. Puurtinen, J. Hyväluoma, R. Surmas, M. Myllys, T. Turpeinen, F. Robertsén, J. Westerholm, and J. Timonen, "A prospect for computing in porous materials research: Very large fluid flow simulations," *J. Comput. Sci.*, vol. 12, pp. 62–76, Jan. 2016.

[21] X. Li, Y. Du, S. Zhang, Q. Duan, and B. A. Schrefler, "Meso-hydro-mechanically informed effective stresses and effective pressures for saturated and unsaturated porous media," *Eur. J. Mech. - ASolids*, vol. 59, pp. 24–36, Sep. 2016.

[22] A. Narasimhan, *Essentials of Heat and Fluid Flow in Porous Media*. Boca Raton, Fla.; New Delhi, India: CRC Press, 2012.

[23] S. Bhaskar, J. G. Park, K. S. Lee, S. Y. Kim, and I. J. Kim, "Thermal and mechanical behavior of ZrTiO4-TiO2 porous ceramics by direct foaming," *Ceram. Int.*, vol. 42, no. 13, pp. 14395–14402, Oct. 2016.

[24] M. Dehghan, M. S. Valipour, and S. Saedodin, "Microchannels enhanced by porous materials: Heat transfer enhancement or pressure drop increment?," *Energy Convers. Manag.*, vol. 110, pp. 22–32, Feb. 2016.

[25] K. Ishizaki, S. Komarneni, and M. Nanko, *Porous Materials: Process Technology And Applications*, Softcover reprint of the original 1st ed. 1998 edition. Springer, 2014.

[26] S. Rashidi, M. Bovand, and J. A. Esfahani, "Heat transfer enhancement and pressure drop penalty in porous solar heat exchangers: A sensitivity analysis," *Energy Convers. Manag.*, vol. 103, pp. 726–738, Oct. 2015.

[27] M. L. Hunt and C. L. Tien, "Effects of thermal dispersion on forced convection in fibrous media," *Int. J. Heat Mass Transf.*, vol. 31, no. 2, pp. 301–309, Feb. 1988.

[28] D. Angirasa, "Experimental investigation of forced convection heat transfer augmentation with metallic fibrous materials," *Int. J. Heat Mass Transf.*, vol. 45, no. 4, pp. 919–922, Feb. 2002.

[29] G. Hetsroni, M. Gurevich, and R. Rozenblit, "Sintered porous medium heat sink for cooling of high-power mini-devices," *Int. J. Heat Fluid Flow*, vol. 27, no. 2, pp. 259–266, Apr. 2006.

[30] D. Angirasa, "Forced convective heat transfer in metallic fibrous materials," *J. Heat Transf.*, vol. 124, no. 4, pp. 739–745, 2002.

[31] S. Mancin, C. Zilio, A. Cavallini, and L. Rossetto, "Pressure drop during air flow in aluminum foams," *Int. J. Heat Mass Transf.*, vol. 53, no. 15–16, pp. 3121–3130, Jul. 2010.

[32] Y. Wang, F. W. Bai, Z. F. Wang, H. Kiriki, M. X. Han, and S. Kubo, "Experimental Research of the Heat Transfer Characteristics using a Packed-bed of Honeycomb Ceramic for High Temperature Thermal Storage System," *Energy Procedia*, vol. 69, pp. 1059–1067, May 2015.

[33] D. F. Merriam, *Random Processes in Geology*. Springer Science & Business Media, 2012.

[34] B. B. Mandelbrot, *The Fractal Geometry of Nature by Mandelbrot, Benoit B. (November 18, 1982) Hardcover*. W.H.Freeman & Co Ltd, 1701.

[35] J.-F. Gouyet, *Physics and Fractal Structures by Jean-Francois Gouyet*, 1 edition. Springer, 1996.

[36] H. M. Hastin, *Fractals: A User's Guide for the Natural Sciences*. Oxford ; New York: Oxford University Press, USA, 1994.

[37] A. L. Mehaute, *Fractal Geometries Theory and Applications*. CRC Press, 1991.

[38] M. Ostoja-Starzewski, "On turbulence in fractal porous media," *Z. Für Angew. Math. Phys.*, vol. 59, no. 6, pp. 1111–1117, Dec. 2007.

[39] H. Joumaa and M. Ostoja-Starzewski, "On the wave propagation in isotropic fractal media," *Z. Für Angew. Math. Phys.*, vol. 62, no. 6, pp. 1117–1129, Jun. 2011.

[40] M. Ostoja-Starzewski and J. Li, "Fractal materials, beams, and fracture mechanics," *Z. Für Angew. Math. Phys.*, vol. 60, no. 6, pp. 1194–1205, Nov. 2009.

[41] L. E. Scriven, "Porous media: Geometry and transport by Pierre M. Adler, butterworth-heinemann, stoneham, ma, 1992, 544 pp.," *AIChE J.*, vol. 40, no. 2, pp. 380–381, Feb. 1994.

[42] B. Yu, J. Li, Z. Li, and M. Zou, "Permeabilities of unsaturated fractal porous media," *Int. J. Multiph. Flow*, vol. 29, no. 10, pp. 1625–1642, Oct. 2003.

[43] Y. Chen, C. Shen, P. Lu, and Y. Huang, "Role of pore structure on liquid flow behaviors in porous media characterized by fractal geometry," *Chem. Eng. Process. Process Intensif.*, vol. 87, pp. 75–80, Jan. 2015.

[44] G. Pia and U. Sanna, "Case studies on the influence of microstructure voids on thermal conductivity in fractal porous media," *Case Stud. Therm. Eng.*, vol. 2, pp. 8–13, Mar. 2014.

[45] X. Huai, W. Wang, and Z. Li, "Analysis of the effective thermal conductivity of fractal porous media," *Appl. Therm. Eng.*, vol. 27, no. 17–18, pp. 2815–2821, Dec. 2007.

[46] P. M. Barnsley, *Fractals Everywhere*, 2nd Revised edition edition. Boston: AP Professional, 1993.

[47] R. Engelking, *Dimension Theory*. North-Holland Publishing Company, 1978.

[48] K. Davey and R. Prosser, "Analytical solutions for heat transfer on fractal and pre-fractal domains," *Appl. Math. Model.*, vol. 37, no. 1–2, pp. 554–569, Jan. 2013.

[49] J. C. Elliott and S. D. Dover, "X-ray microtomography," *J. Microsc.*, vol. 126, no. 2, pp. 211–213, May 1982.

[50] B. Otsuki, M. Takemoto, S. Fujibayashi, M. Neo, T. Kokubo, and T. Nakamura, "Pore throat size and connectivity determine bone and tissue ingrowth into porous implants: Three-dimensional micro-CT based structural analyses of porous bioactive titanium implants," *Biomaterials*, vol. 27, no. 35, pp. 5892–5900, Dec. 2006.

[51] Z. Yang and P. Xiaofeng, "Micro-CT scanning analysis for inner structure of porous media," *Heat Transfer—Asian Res.*, vol. 36, no. 4, pp. 208–214, Jun. 2007.

[52] I.-C. S. Daniel Chappard, "Porosity imaged by a vector projection algorithm correlates with fractal dimension measured on 3D models obtained by microCT," *J. Microsc.*, vol. 258, no. 1, 2014.

[53] Z. Liu and H. Wu, "Pore-scale study on flow and heat transfer in 3D reconstructed porous media using micro-tomography images," *Appl. Therm. Eng.*, vol. 100, pp. 602–610, May 2016.

[54] Q. Li, "Carbon nanotube reinforced porous magnesium composite: 3D nondestructive microstructure characterization using x-ray micro-computed tomography," *Mater. Lett.*, vol. 133, pp. 83–86, Oct. 2014.

[55] *Transport Phenomena in Biological Systems*, 2 edition. Upper Saddle River, N.J: Prentice Hall, 2009.

[56] *Transport Phenomena, Revised 2nd Edition*, 2nd edition. New York: John Wiley & Sons, Inc., 2006.

[57] G. E. Kapellos and T. S. Alexiou, "Chapter 1 - Modeling Momentum and Mass Transport in Cellular Biological Media: From the Molecular to the Tissue Scale A2 - Becker, Sid M.," in *Transport in Biological Media*, A. V. Kuznetsov, Ed. Boston: Elsevier, 2013, pp. 1–40.

[58] J. J. Duderstadt, W. R. Martin, and J. J. Dunderstadt, *Transport Theory*. New York: John Wiley & Sons Inc, 1979.

[59] T. R. Blake and S. K. Garg, "On the species transport equation for flow in porous media," *Water Resour. Res.*, vol. 12, no. 4, pp. 748–750, Aug. 1976.

[60] J. Tian and D. Tong, "The flow analysis of fiuids in fractal reservoir with the fractional derivative*," *J. Hydrodyn. Ser B*, vol. 18, no. 3, pp. 287–293, Apr. 2006.

[61] M. Ostoja-Starzewski, "Extremum and variational principles for elastic and inelastic media with fractal geometries," *Acta Mech.*, vol. 205, no. 1–4, pp. 161–170, Apr. 2009.

[62] A. P. S. Selvadurai, *Partial Differential Equations in Mechanics 2*. Springer Science & Business Media, 2013.

[63] L. Pipes, *Applied Mathematics for Engineers and Physicists: Third Edition*, 3rd Revised edition edition. Mineola, New York: Dover Publications Inc., 2014.

[64] G. Kulasiri and I. Woodhead, "On modelling the drying of porous materials: analytical solutions to coupled partial differential equations governing heat and moisture transfer," 2005.

[65] H. Ali, Y. Shi, D. Khazanchi, M. Lees, G. D. van Albada, J. Dongarra, P. M.A. Sloot, J. Dongarra, S. Sun, A. Salama, and M. F. El-Amin, "An Equation-Type Approach for the Numerical Solution of the Partial Differential Equations Governing Transport Phenomena in Porous Media," *Procedia Comput. Sci.*, vol. 9, pp. 661–669, Jan. 2012.

[66] M. D. Graham and P. H. Steen, "Plume formation and resonant bifurcations in porous-media convection," *J. Fluid Mech.*, vol. 272, pp. 67–90, Aug. 1994.

[67] D. Ingham, A. Bejan, E. Mamut, and I. Pop, *Emerging Technologies and Techniques in Porous Media*. Springer Science & Business Media, 2012.

[68] S. J. Kim and K. Vafai, "Analysis of natural convection about a vertical plate embedded in a porous medium," *Int. J. Heat Mass Transf.*, vol. 32, no. 4, pp. 665–677, Apr. 1989.

[69] D. Parris and B. Landrum, "Effect of Tube Geometry on Regenerative Cooling Performance," in *41st AIAA/ASME/SAE/ASEE Joint Propulsion Conference & Exhibit*, American Institute of Aeronautics and Astronautics, 2005.

[70] C. Li, L. Zheng, X. Zhang, and G. Chen, "Flow and heat transfer of a generalized Maxwell fluid with modified fractional Fourier's law and Darcy's law," *Comput. Fluids*, vol. 125, pp. 25–38, Feb. 2016.

[71] T. Chevalier, C. Chevalier, X. Clain, J. C. Dupla, J. Canou, S. Rodts, and P. Coussot, "Darcy's law for yield stress fluid flowing through a porous medium," *J. Non-Newton. Fluid Mech.*, vol. 195, pp. 57–66, May 2013.

[72] J. Marro and R. Dickman, *Nonequilibrium Phase Transitions in Lattice Models*. Cambridge University Press, 2005.

[73] S. Kirkpatrick, "Percolation and Conduction," *Rev. Mod. Phys.*, vol. 45, no. 4, pp. 574–588, 1973.

[74] I. Balberg, "Recent developments in continuum percolation," *Philos. Mag. B Phys. Condens. Matter Stat. Mech. Electron. Opt. Magn. Prop.*, vol. 56, no. 6, pp. 991–1003, 1987.

[75] A. N. Beris, D. L. Miller, S. Chen, S. P. Dawson, G. D. Doolen, D. R. Janecky, and A. Lawniczak, "Lattice methods and their applications to reacting systems," *Comput. Chem. Eng.*, vol. 19, no. 6, pp. 617–646, Jun. 1995.

[76] A. Vigliotti and D. Pasini, "Stiffness and strength of tridimensional periodic lattices," *Comput. Methods Appl. Mech. Eng.*, vol. 229–232, pp. 27–43, Jul. 2012.

[77] F. Xiao and X. Yin, "Geometry models of porous media based on Voronoi tessellations and their porosity–permeability relations," *Comput. Math. Appl.*, vol. 72, no. 2, pp. 328–348, Jul. 2016.

[78] D. Asahina, K. Ito, J. E. Houseworth, J. T. Birkholzer, and J. E. Bolander, "Simulating the Poisson effect in lattice models of elastic continua," *Comput. Geotech.*, vol. 70, pp. 60–67, Oct. 2015.

[79] P. S. Ghoshdastidar and I. Chakraborty, "A coupled map lattice model of low boiling in a horizontal tube," *J. Heat Transf.*, vol. 129, no. 12, pp. 1737–1741, 2007.

[80] J. Xu, Y. Wu, Y. Zhang, and J. Zhang, *Fluid Machinery and Fluid Mechanics: 4th International Symposium (4th ISFMFE)*. Springer Science & Business Media, 2010.

[81] Z.-G. Feng and E. E. Michaelides, "The immersed boundary-lattice Boltzmann method for solving fluid–particles interaction problems," *J. Comput. Phys.*, vol. 195, no. 2, pp. 602–628, Apr. 2004.

[82] H. B. C. Rupert W. Nash, "Choice of boundary condition for lattice-Boltzmann simulation of moderate Reynolds number flow in complex domains," *Phys. Rev. E*, vol. 89, no. 2, 2012.

[83] Y. Kuwata and K. Suga, "Large eddy simulations of pore-scale turbulent flows in porous media by the lattice Boltzmann method," *Int. J. Heat Fluid Flow*, vol. 55, pp. 143–157, Oct. 2015.

[84] J. Cai and X. Huai, "Study on fluid–solid coupling heat transfer in fractal porous medium by lattice Boltzmann method," *Appl. Therm. Eng.*, vol. 30, no. 6–7, pp. 715–723, May 2010.

[85] Y. Su and J. H. Davidson, "A Non-Dimensional Lattice Boltzmann Method for direct and porous medium model simulations of 240-tube bundle heat exchangers in a solar storage tank," *Int. J. Heat Mass Transf.*, vol. 85, pp. 195–205, Jun. 2015.

[86] P. A. Skordos, "Initial and boundary conditions for the lattice Boltzmann method," *Phys. Rev. E*, vol. 48, no. 6, pp. 4823–4842, Dec. 1993.

[87] S. Chen and G. D. Doolen, "Lattice Boltzmann Method for Fluid Flows," *Annu. Rev. Fluid Mech.*, vol. 30, no. 1, pp. 329–364, 1998.

[88] V. E. Tarasov, "Possible Experimental Test of Continuous Medium Model for Fractal Media," *Phys. Lett. A*, vol. 341, no. 5–6, pp. 467–472, Jun. 2005.

[89] V. E. Tarasov, *Fractional Dynamics: Applications of Fractional Calculus to Dynamics of Particles, Fields and Media*. Springer Science & Business Media, 2011.

[90] V. E. Tarasov, "Elasticity of fractal materials using the continuum model with non-integer dimensional space," *Comptes Rendus Mécanique*, vol. 343, no. 1, pp. 57–73, Jan. 2015.

[91] A. Carpinteri and P. Cornetti, "A fractional calculus approach to the description of stress and strain localization in fractal media," *Chaos Solitons Fractals*, vol. 13, no. 1, pp. 85–94, Jan. 2002.

[92] A. Carpinteri, B. Chiaia, and P. Cornetti, "The elastic problem for fractal media: basic theory and finite element formulation," *Comput. Struct.*, vol. 82, no. 6, pp. 499–508, Mar. 2004.

[93] A. Carpinteri, B. Chiaia, and P. Cornetti, "Static–kinematic duality and the principle of virtual work in the mechanics of fractal media," *Comput. Methods Appl. Mech. Eng.*, vol. 191, no. 1–2, pp. 3–19, Nov. 2001.

[94] A. Carpinteri, P. Cornetti, and A. Sapora, "Static-kinematic fractional operators for fractal and non-local solids," *ZAMM - J. Appl. Math. Mech. Z. Für Angew. Math. Mech.*, vol. 89, no. 3, pp. 207–217, Mar. 2009.

[95] A. S. Balankin, "Stresses and strains in a deformable fractal medium and in its fractal continuum model," *Phys. Lett. A*, vol. 377, no. 38, pp. 2535–2541, Nov. 2013.

[96] J. Reddy, *An Introduction to the Finite Element Method*, 3 edition. New York, NY: McGraw-Hill Education, 2005.

[97] M. Bruneau and C. Potel, Eds., *Materials and Acoustics Handbook*, 1 edition. Wiley-ISTE, 2013.

[98] Q. Liu, Z. Lu, Z. Hu, and J. Li, "Finite element analysis on tensile behaviour of 3D random fibrous materials: Model description and meso-level approach," *Mater. Sci. Eng. A*, vol. 587, pp. 36–45, Dec. 2013.

[99] Z. Lu, Q. Liu, H. Han, and D. Zhang, "Experiment and modeling on the compressive behaviors for porous silicon nitride ceramics," *Mater. Sci. Eng. A*, vol. 559, pp. 201–209, Jan. 2013.

[100] T. Strouboulis, I. Babuška, and K. Copps, "The design and analysis of the Generalized Finite Element Method," *Comput. Methods Appl. Mech. Eng.*, vol. 181, no. 1–3, pp. 43–69, Jan. 2000.

[101] I. Babuška and U. Banerjee, "Stable Generalized Finite Element Method (SGFEM)," *Comput. Methods Appl. Mech. Eng.*, vol. 201–204, pp. 91–111, Jan. 2012.

[102] B. Cockburn and C.-W. Shu, "Runge–Kutta Discontinuous Galerkin Methods for Convection-Dominated Problems," *J. Sci. Comput.*, vol. 16, no. 3, pp. 173–261, Sep. 2001.